



THE HONG KONG
POLYTECHNIC UNIVERSITY

香港理工大學

Pao Yue-kong Library

包玉剛圖書館

Copyright Undertaking

This thesis is protected by copyright, with all rights reserved.

By reading and using the thesis, the reader understands and agrees to the following terms:

1. The reader will abide by the rules and legal ordinances governing copyright regarding the use of the thesis.
2. The reader will use the thesis for the purpose of research or private study only and not for distribution or further reproduction or any other purpose.
3. The reader agrees to indemnify and hold the University harmless from and against any loss, damage, cost, liability or expenses arising from copyright infringement or unauthorized usage.

IMPORTANT

If you have reasons to believe that any materials in this thesis are deemed not suitable to be distributed in this form, or a copyright owner having difficulty with the material being included in our database, please contact lbsys@polyu.edu.hk providing details. The Library will look into your claim and consider taking remedial action upon receipt of the written requests.

**ACOUSTIC BLACK HOLE PLATES FOR VIBRATION AND
SOUND RADIATION MITIGATION**

**LI MA
PhD**

The Hong Kong Polytechnic University

2020

The Hong Kong Polytechnic University
Department of Mechanical Engineering

**Acoustic black hole plates for vibration and sound radiation
mitigation**

Li Ma

**A thesis submitted in partial fulfillment of the requirements for the
degree of Doctor of Philosophy**

September 2019

CERTIFICATE OF ORIGINALITY

I hereby declare that this thesis is my own work and that, to the best of my knowledge and belief, it reproduces no material previously published or written, nor material that has been accepted for the award of any other degree or diploma, except where due acknowledgement has been made in the text.

Li Ma

(Signed)

(Name of student)

To my beloved family

Abstract

This thesis proposes an efficient, flexible and versatile 2D semi-analytical model for the vibration and sound radiation analyses of Acoustic Black Hole (ABH) plates. The proposed model, along with the associated wavelet-based solution procedure, is intended to overcome major technical difficulties which are specific to ABH structures: the non-uniform wavelength distribution and ABH-induced wave compressions at the high frequency range in a realistic structure of finite size. Under the general Rayleigh-Ritz framework, Daubechies wavelet (DW) scaling functions are used for expressing the transverse displacement of the ABH plates. The accuracy of the propose model is thoroughly validated using Finite Element simulations and experiments. Results show that the model allows an accurate prediction of various vibration and sound radiation parameters and provides a truthful description of the typical ABH phenomena.

Vibration analyses on the ABH plates show a drastic increase in structural damping, by using only a small amount of damping material. ABH local modes are shown to be dominant in the damping increase which leads to remarkably reduced vibration responses above the cut-on frequency. Meanwhile, ABH plates exhibit broadband sound power and sound radiation efficiency reduction, compared with uniform plates. Below the critical frequency, the reduced radiation efficiency is caused by the weakening of the structural stiffness due to the ABH indentation. Above the critical frequency, a subsonic region inside the ABH cell containing acoustically slow structural waves may appear. This region,

confined within a transonic boundary, is due to the ABH-specific phase velocity reduction of the bending waves. Visualization of the supersonic acoustic intensity allows identifying the effective sound radiation regions of ABH plates and their relationship with the transonic boundaries at different frequencies.

Sound radiation analyses show that damping layers also increase the sound radiation efficiency of ABH plates due to their additional stiffness. The conflicting effect of damping layers in the increase of both structural damping and sound radiation efficiency calls for a balanced and meticulous design of their deployment to draw the best possible vibration or acoustic benefit. To tackle the problem, by combining the proposed model with an optimizer, the sound radiation of an ABH plate into a free space is minimized through adjusting the damping layer layout.

Finally, an alternative ABH profile that is different from the standard ABH profiles is proposed for structural damping enhancement. Results show that a plate with optimized ABH profile entails significantly increased structural damping compared with a standard ABH plate. Local $(n, 1)$ and $(n, 2)$ modes that have n half waves in the circumferential direction and 1 or 2 half waves in the radial direction of the indentation dominate the modal damping increase. The optimized plate exhibits larger energy density ratio between the ABH portion and the uniform portion, which entails better energy dissipation. Also, a reduction in the sound radiation is observed which is confirmed by reduced energy level of the supersonic vibration components in wavenumber domain.

Publications Arising from the Thesis

Journal papers

1. **Ma L**, Zhang S, Cheng L. A 2D Daubechies wavelet model on the vibration of rectangular plates containing strip indentations with a parabolic thickness profile. *Journal of Sound and Vibration*, 2018, 429:130-146.
2. **Ma L**, Cheng L. Sound radiation and transonic boundaries of a plate with an acoustic black hole. *Journal of the Acoustical Society of America*, 2019, 145(1):164-172.
3. **Ma L**, Cheng L. Topological optimization of damping layout for minimized sound radiation of an acoustic black hole plate. *Journal of Sound and Vibration*, 2019, 458:349-364.
4. **Ma L**, Cheng L. Numerical and experimental benchmark solutions on vibration and sound radiation of an acoustic black hole plate. Submitted to *Applied Acoustics* (in revision)

Conference papers

1. **Ma L**, Zhang S, Cheng L. Vibration of plates with a power-law-profiled thickness variation by wavelet decomposed Rayleigh-Ritz method. 46th International Congress and Exposition on Noise Control Engineering, Hong Kong, China, 27-30, August 2017.

2. **Ma L**, Cheng L. Sound radiation of plates with embedded circular acoustic black hole indentations. 47th International Congress and Exposition on Noise Control Engineering, Chicago, USA, 26-29, August 2018.

Acknowledgements

Firstly, I would like to sincerely express my special thanks to my supervisor Prof. Li Cheng for his continuous support and encouragement of my PhD study and research work. His immense knowledge, excellent guidance and advice have inspired me a lot whenever I encounter some difficulties in my research.

Also, I would like to thank my group members. Many thanks to Dr. Su Zhang for willingly answering my dumbest questions about Daubechies wavelet functions without yelling at me and for providing me the codes for analyses of uniform plates. Without his help, I would not finish my PhD thesis smoothly. Thanks to Dr. Shengbo Shan and Mr. Xiaoqi Zhang for providing me much help with great patience during the past three years. Thanks to Mr. Xudong Tian and Mr. E Fan for helping me understand parallel computing in Linux system. Thanks to Dr. Liling Tang, Mr. Tong Zhou and Ms Linli Zhang for their inspirations to my research work. Taking this opportunity, I would like to thank Dr. Stephen, Mr. Fuzhen Wen, Mr. Tong Zhou, Ms. Linli Zhang, Mr. Xiaoqi Zhang, Dr. Shengbo Shan, Dr. Zhongyu Hu, Dr. Shancheng Cao and Dr. Qi Xu for their help in the acoustic experiments.

Finally, for providing unconditional love, I thank my parents and my siblings. Last but not the least, I thank my longtime and beloved boyfriend for his unconditional support for my decisions in my study and in my life.

Table of Contents

1	Chapter 1 Introduction	1
1.1	Background	1
1.2	Traditional measures for structural damping	3
1.3	Literature review on acoustic black holes.....	5
1.3.1	Acoustic black hole theory	5
1.3.2	Numerical analyses of acoustic black hole structures	7
1.3.2.1	Wave reflection from ABH edges.....	8
1.3.2.2	Modelling of vibration and sound radiation from ABH structures ..	11
1.3.2.3	Energy harvesting.....	16
1.3.3	Experimentally investigations of acoustic black hole structures.....	17
1.3.3.1	Wave reflection from ABH edges.....	17
1.3.3.2	Vibration of ABH structures.....	18
1.3.3.3	Sound radiation of ABH structures	21
1.3.3.4	Sound transmission loss	22
1.3.4	Potential applications of acoustic black hole structures	23
1.3.5	Improvements to enhance acoustic black hole performance	26
1.4	Research objectives	29
1.5	Overview of the thesis.....	31
2	Chapter 2 2D Daubechies wavelet semi-analytical model	36

2.1	Introduction.....	36
2.2	Semi-analytical modelling and formulation	39
2.2.1	Modelling	39
2.2.2	Daubechies wavelet scaling functions.....	44
2.2.3	Connection coefficients	47
2.2.4	Sound radiation model.....	50
2.2.4.1	Sound power and sound radiation efficiency	50
2.3	Summary.....	53
3	Chapter 3 Model validations	55
3.1	Introduction.....	55
3.2	Vibration validations by FE simulations	57
3.2.1	Determination of DW parameters and vibration validations.....	57
3.3	Sound field Verifications by analytical solutions	63
3.4	Experimental validations	67
3.4.1	Manufacturing of ABH test sample.....	67
3.4.1.1	Manufacturing method	68
3.4.1.2	Measurement of the manufactured ABH profile	70
3.4.2	Experimental setup	72
3.4.2.1	Measurement of vibration characteristics.....	72
3.4.2.2	Measurement of the radiated sound power.....	74

3.4.3	Experimental results	77
3.4.3.1	Eigen-frequencies and mode shapes.....	77
3.4.3.2	Cross point mobility	92
3.4.3.3	Radiated sound power	96
3.5	Summary.....	98
4	Chapter 4 A 2D Daubechies wavelet model on the vibration of rectangular plates containing strip indentations with a parabolic thickness profile	100
4.1	Introduction.....	100
4.2	Numerical Analyses and discussions	101
4.2.1	ABH phenomena and vibration benefit.....	101
4.2.2	Modal loss factors.....	106
4.2.3	Strip ABH versus circular ABH	109
4.3	Summary.....	113
5	Chapter 5 Sound radiation and transonic boundaries of a plate with a circular acoustic black hole indentation.....	115
5.1	Introduction.....	115
5.2	Supersonic acoustic intensity in spatial domain.....	116
5.3	Model implementation and numerical analyses.....	118
5.3.1	Vibration and sound fields of ABH plates.....	118
5.3.2	Phenomena assertion by experiments.....	124

5.3.3	Sound radiation mechanism analyses	126
5.3.3.1	Stiffness-controlled sound radiation efficiency	126
5.3.3.2	Sound radiation within the transonic boundary	127
5.3.3.3	Sound radiation efficiency with transonic boundary changes	129
5.3.3.4	Verification of Supersonic acoustic intensity	131
5.3.3.5	Numerical illustration of the supersonic acoustic intensity	132
5.4	Summary	136
6	Chapter 6 Topological optimization of damping layers	138
6.1	Introduction	138
6.1.1	Formulation of topological optimization	142
6.1.2	Sensitivity analysis for optimization	144
6.1.3	Validation examples	147
6.2	Numerical analyses	149
6.2.1	Effect of damping layers on the vibration and sound radiation of ABH plates	149
6.2.2	Topological optimization for the minimization of sound power	152
6.2.3	Vibration minimization versus sound power minimization	159
6.2.4	Minimization of sound power within a frequency band	162
6.3	Summary	165
7	Chapter 7 Optimization for alternative ABH profiles	168

7.1	Introduction.....	168
7.2	Formulation and procedures of the optimization	170
7.2.1	Objective function and constraints	170
7.2.2	Constraint-handling NSGA II.....	172
7.2.3	Lagrange interpolation polynomials for profile generation.....	175
7.3	Numerical analyses and discussions	177
7.3.1	Damping performance	177
7.3.2	Vibration and sound radiation characterizations	186
7.4	Summary.....	192
8	Chapter 8 Conclusions and future research.....	195
8.1	Conclusions.....	195
8.2	Suggestions for future research	199
	Appendix A Formulas for M, K, and F for a plate embedded with a strip ABH	
	indentation.....	202
	Appendix B Formulas for M and K for a plate embedded with a circular ABH	
	indentation.....	205
	References.....	209

List of Figures

Figure 1.1 Graded impedance interface at the edge of a steel bar [6].	4
Figure 1.2 Elastic wedge of power law profile [7].	7
Figure 1.3 Three typical ray trajectories illustrating propagation of bending waves over a pit of power law profile: the ray below is trapped by the acoustic black hole, which means that the reflection from it can be neglected [20].	9
Figure 1.4 Model of an acoustic black hole. The tube with rings whose inner radius $r(x)$ decreases to zero [21].	10
Figure 1.5 A composite panel enclosed with circular indentations.	20
Figure 1.6 2D ABH with manufacturing defects [84].	21
Figure 1.7 A tapered bar of circular cross-section with the radius described by a power-law profile and with the Sharp end covered by a thick absorbing layer (a); such a device forms a one-dimensional acoustic black hole that can be used for suppression of impact-induced resonant vibrations in the main structure of tennis racquets (only part of which close to the grip is shown) (b).	23
Figure 1.8 Flow visualization diagram for (a): reference fan blade; (b) fan blade with power- law wedge; (c) fan blade with power-law wedge with single damping layer; (d) fan blade with power-law wedge with shaped damping layer.	24
Figure 1.9 ABH engine cover (top view) and locations of accelerometers on reference engine cover [92].	25
Figure 1.10 Plate with an ABH of an Archimedean [93].	26

Figure 2.1 Plate model with a strip ABH indentation: (a) plate with symmetrical power-law thickness profiles; (b) ABH portion in vertical view; (c) cross-section of the ABH portion; (d) modeling of the boundary conditions.	41
Figure 2.2 Plate model with a circular ABH indentation.	42
Figure 2.3 Daubechies scaling functions with $L=12$, $m=2$, $i=-3, -2, \dots, 2, 3$	47
Figure 2.4 Coordinate system for the baffled plate.	51
Figure 3.1 Comparisons with FEM analyses for the first 100 eigen-frequencies: FEM (solid line); $L=12$, $m=6$ (short dash line); $L=12$, $m=7$ (short dot line); $L=12$, $m=8$ (short dash dot line).	60
Figure 3.2 Percent errors for the first 100 eigen-frequencies obtained by the present model with $L=12$: $m=6$ (circle dot); $m=7$ (square dot) and $m=8$ (triangle dot).	60
Figure 3.3 Percent errors for the first 100 eigen-frequencies obtained by the present model with $m=7$: $L=12$ (square dot); $L=14$ (circle dot) and $L=16$ (triangle dot).	61
Figure 3.4 Mode shape comparisons: present model (left); FEM (right). (a) 1 st mode; (b) 50 th mode; (c) 79 th mode; (d) 98 th mode.	62
Figure 3.5 Mean square velocity: ABH portion (left); uniform portion (right).	63
Figure 3.6 Radiated sound power obtained by the present theoretical model and analytical solution.	65
Figure 3.7 Radiation efficiencies of the first six low-order modes: present model (solid line); analytical solution (dash line).	66
Figure 3.8 Half thickness profile: (a) measuring points; (b) top side; (c) bottom side; (d) averaged manufactured profile and predesigned profile.	72

Figure 3.9 Experimental setup: (a) ABH test sample; (b) excitation with electromagnetic shaker and force transducer.....	74
Figure 3.10 Anechoic chamber for radiated sound power tests: (a) position of the ABH test sample in relation to the rigid baffle; (b) coverage of the viscoelastic material F9473PC; (c) measuring points projected on the floor (red dot); (d) microphone positions over the hemispherical surface [120].....	76
Figure 3.11 Eigen-frequencies of the first 120 modes: DW model (short dash line); experiment (short dot line).....	78
Figure 3.12 Relative errors of eigen-frequencies of the first 120 modes obtained from the DW model and experiments.....	79
Figure 3.13 Comparison of 6 th mode shape: (a) DW model (left), $f_n = 105.2$ Hz ; (b) experiment (right), $f_n = 105.0$ Hz .	80
Figure 3.14 Comparison of 24 th mode shape: (a) DW model (left), $f_n = 767.7$ Hz ; (b) experiment (right), $f_n = 746.6$ Hz .	81
Figure 3.15 Comparison of 30 th mode shape: (a) DW model (left), $f_n = 1025.8$ Hz ; (b) experiment (right), $f_n = 1014.0$ Hz .	82
Figure 3.16 Comparison of 48 th mode shape: (a) DW model (left), $f_n = 1736.1$ Hz ; (b) experiment (right), $f_n = 1721.9$ Hz .	83
Figure 3.17 Comparison of 49 th mode shape: (a) DW model (left), $f_n = 1759.6$ Hz ; (b) experiment (right), $f_n = 1759.4$ Hz .	84

Figure 3.18 Comparison of 50 th mode shape: (a) DW model (left), $f_n = 1801.4$ Hz ; (b) experiment (right), $f_n = 1782.5$ Hz	85
Figure 3.19 Comparison of 60 th mode shape: (a) DW model (left), $f_n = 2252.1$ Hz ; (b) experiment (right), $f_n = 2246.9$ Hz	86
Figure 3.20 Comparison of 63 rd mode shape: (a) DW model (left), $f_n = 2329.6$ Hz ; (b) experiment (right), $f_n = 2318.8$ Hz	87
Figure 3.21 Comparison of 74 th mode shape: (a) DW model (left), $f_n = 2788.9$ Hz ; (b) experiment (right), $f_n = 2766.0$ Hz	88
Figure 3.22 Comparison of 79 th mode shape: (a) DW model (left), $f_n = 3001.8$ Hz ; (b) experiment (right), $f_n = 2992.0$ Hz	89
Figure 3.23 Comparison of 83 rd mode shape: (a) DW model (left), $f_n = 3163.5$ Hz ; (b) experiment (right), $f_n = 3135.0$ Hz	90
Figure 3.24 Comparison of 118 th mode shape: (a) DW model (left), $f_n = 4552.1$ Hz ; (b) experiment (right), $f_n = 4510.9$ Hz	91
Figure 3.25 Comparison of 119 th mode shape: (a) DW model (left), $f_n = 4593.7$ Hz ; (b) experiment (right), $f_n = 4556.3$ Hz	92
Figure 3.26 Cross point mobility of the ABH plate: (a) ABH center (0.3,0.25) m; (b) an arbitrary point (0.0375, 0.25) m on the uniform portion; (c) drive point at (0.518, 0.165) m.	94
Figure 3.27 Comparison of cross point mobility at (0.0375, 0.25) m with damping layers: (a) present model (solid line); (b) experiment (dot line). DL denotes damping layer.	95

Figure 3.28 Radiated sound power: (a) without damping layer; (b) with damping layer. DL denotes damping layer. 97

Figure 4.1 Typical ABH features: (a) decreased wavelength towards the center of ABH portion; (b) ratio of the mean square velocity between the ABH portion and that of the uniform portion. 103

Figure 4.2 Reference plate and ABH plate coated with the same amount of damping layers. Coating area $x_{d1} \sim x_{d2}=0.25\sim 0.31$ m, $y_{d1} \sim y_{d2}=0\sim 0.56$ m and thickness $h_d=2h_0$: (a) Reference plate; (b) ABH plate. Dark gray area denotes the area coated with damping layers. 103

Figure 4.3 Mean square velocity of uniform portion: reference plate with damping layers (dot line); strip ABH plate with damping layers (solid line). 105

Figure 4.4 Mean square velocity of the uniform portion of reference plates: without damping layers (dot line); with damping layers (solid line). 105

Figure 4.5 Mean square velocity of the uniform portion of strip ABH plates: without damping layers (dot line); with damping layers (solid line). 106

Figure 4.6 Plates and modal loss factors: (a) bare reference plate (upper); reference plate with damping layers (middle); ABH plate with damping layers (lower); (b) reference plate (square dot); reference plate with damping layers (circular dot); ABH plate with damping layers (triangular dot). 107

Figure 4.7 Modal loss factors of the strip ABH plate coated with damping layers: (1, n) ABH cell modes (dots with hollow lower part); (2, n) ABH cell modes (dots with hollow upper part); global modes (solid dots). 109

Figure 4.8 Plates with two types of ABH indentations: strip (left); circular (right). Dark gray area denotes the area coated with damping layers. 111

Figure 4.9 Comparison of the ratio of the mean square velocity between the ABH portion and that of the uniform portion without damping layers: strip ABH plate (solid line); circular ABH plate (dot line). 111

Figure 4.10 Comparison of the modal loss factors of the strip ABH plate and the circular ABH plate with damping layers: strip ABH plate (square dot); circular ABH plate (circular dot). 112

Figure 5.1 Comparisons between the reference plate and the ABH plate: (a) space-averaged mean square velocity; (b) radiated sound power. DL denotes damping layers..... 120

Figure 5.2 Comparisons of the sound radiation efficiencies between the reference plates and the ABH plates. DL denotes damping layers. 122

Figure 5.3 Effect of the stiffness and mass of the damping layers on the sound radiation efficiency of ABH plate. 124

Figure 5.4 Measured cross point mobility at (0.0375, 0.25) m on the uniform portion of the test samples: (a) without damping material (solid line); (b) with damping material FP9473 (dot line); (c) with damping material SD40PSA (dash line). DL denotes damping layer..... 125

Figure 5.5 Measured radiated sound power of test samples: (a) without damping material (solid line); (b) with damping material FP9473 (dot line); (c) with Damping material SD40PSA (dash line). DL denotes damping layer. 126

Figure 5.6 Sound power radiated from the region inside the area with a radius of 118.4 mm, corresponding to the transonic boundary at 4000Hz.	128
Figure 5.7 Diagram of investigated ring on the ABH plate.	129
Figure 5.8 Radiation efficiency of rings around transonic boundary of ABH plate compared with those of reference plate at different frequencies: (a) Reference plate; (b) ABH plate.	130
Figure 5.9 Supersonic intensity of normal modes: (a) (11, 3) mode at $ka=17.92$; (b) (11, 9) mode at $ka=12$	132
Figure 5.10 (Color on-line) Acoustic intensity maps: (a-b-c) $f=2000$ Hz; (d-e-f) $f=4200$ Hz; (g-h-i) $f=7300$ Hz. (a-d-g) supersonic acoustic intensity of the reference plate; (b-e-h) supersonic acoustic intensity of the ABH plate; (c-f-i) acoustic intensity of the ABH plate. The dot circle denotes the ABH periphery and the dash circle the transonic boundary. SSI indicates the supersonic acoustic intensity; SI the acoustic intensity and SWL the total radiated sound power.	135
Figure 6.1 Optimized layout of damping layers.	142
Figure 6.2 Optimal layout of damping layers at different frequencies: Present model with OC method (a_1 - a_2 - a_3); Results from [135] with MMA method (b_1 - b_2 - b_3).	149
Figure 6.3 Comparison between ABH plate (dot line) and ABH plate with damping layers (solid line): (a) Radiated sound power; (b) Mean square velocity; (c) Radiation efficiency. DL denotes damping layer.	152
Figure 6.4 Convergence of iteration process at $f = 3480$ Hz. The outer dot circle represents the ABH peripheral circle, and the inner dash circle represents the circular	

coverage of damping layers. DL denotes damping layer and W the radiated sound power. Step 1 is the initial starting configuration.	154
Figure 6.5 Comparison between initial case (square symbol) and the case of optimized sound power (circular symbol) at single frequencies: (a) Sound power; (b) Mean square velocity; (c) Radiation efficiency. DL denotes damping layer, and W the radiated sound power.	157
Figure 6.6 Wavenumber spectra of ABH plates at 3480 Hz: (a) ABH plate with no damping layers; (b) ABH plate with damping layers coated inside a central circle; (c) ABH plate with optimized damping layers. The solid circle indicates the normalized radiation circle with radius of $r=1$	158
Figure 6.7 Comparison of the coverage ratios W_{rad} : Sound power optimization (circular dot); MSV: mean square velocity optimization (star dot).....	162
Figure 7.1 The design variables (shown in pink color) that determine the ABH profile.	172
Figure 7.2 The flow chart of NSGA-II.	174
Figure 7.3 The first 16 individuals in the randomly generated initial population.	177
Figure 7.4 Objective values for the initial population.	178
Figure 7.5 Steps of optimization process: (a) objective values of the best individual in each step; (b) optimal profile in each step.....	179
Figure 7.6 Plates with different ABH profiles: (a) the standard profile and optimized profile in 1D view; (b) a plate with an indentation of standard ABH profile; (c) a plate with an indentation of optimized profile.	181
Figure 7.7 Mode shapes of a plate embedded with an indentation of optimized profile.	183

Figure 7.8 Comparison of modal loss factors: (a) standard profile (square dot); (b) optimized profile (circular dot)..... 185

Figure 7.9 Ratio of energy density between the ABH portion and the uniform portion: (a) standard profile (solid line); (b) optimized profile (dot line)..... 186

Figure 7.10 Comparisons between a plate of uniform thickness (dash line) and plates embedded with an indentation of standard ABH profile (solid line) and optimized profile (dot line): (a) space-averaged mean square velocity; (b) radiated sound power; (c) sound radiation efficiency..... 188

Figure 7.11 Comparisons between the standard ABH plate and the optimized ABH plate in one third octave band: (a) space-averaged mean square velocity; (b) radiated sound power; (c) sound radiation efficiency..... 190

Figure 7.12 Wavenumber spectra of uniform plate (left), ABH plates embedded with an indentation of standard profile (middle) and optimized profile (right) at different frequencies: (a) 2250 Hz; (b) 3390 Hz. The dash circle indicates the normalized radiation circle with radius $r=1$ 191

List of Tables

Table 3.1 Geometrical and material parameters of a plate embedded with a trip indentation	58
Table 3.2 Geometrical parameters of the experimental sample of an ABH plate.....	68
Table 3.3 Material parameters of experimental ABH sample and the damping layers.....	68
Table 5.1 Geometrical and material parameters of a plate with a circular ABH indentation	119
Table 6.1 Comparison of optimal layouts of damping layers under different objective functions. The outer dot circle represents the ABH peripheral circle, and the inner dash circle represents the circular coverage of damping layers.	161
Table 6.2 Characteristics of sound radiation under different frequency bands. Solid line represents the reference circular case, the dot line the optimized case, and the dash line the uniform plate.....	164

Nomenclature

Symbol	Meaning
$h(x)$	Local thickness for a strip ABH indentation
$h(r)$	Local thickness for a circular ABH indentation
ε	A constant
γ	power law index
Ψ	Aggregated wave phase
$k(x)$	Structural wavenumber
x_0	Truncation thickness
R_0	Reflection coefficient
h_d	Thickness of damping layers
a	Length of plates
b	Width of plates
h	Thickness of the uniform portion
(x_c, y_c)	ABH center
x_{d1}, x_{d2}	Position of Damping layers in x direction
y_{d1}, y_{d2}	Position of Damping layers in y direction
h_0	Minimum thickness of ABH indentations
R_{ABH}	Radius of ABH indentations

R_d	Radius of damping layers
k_i, c_i	Translational and rotational spring stiffness, respectively
E_0	Young's modulus of plates
E_d	Young's modulus of damping layers
η_0	Loss factor of plates
η_d	Loss factor of damping layers
η_n	Modal loss factors
w	Transverse displacement of ABH plates
\mathbf{A}	Unknown complex coefficients
$\varphi_i(\bar{x}),$	Daubechies wavelet scaling functions in x direction
$\varphi_j(\bar{y})$	Daubechies wavelet scaling functions in y direction
\mathcal{L}	Lagrangian operator
E_k	Kinetic energy
E_p	Potential energy
W_f	Work done by external forces
ρ_0	Density of plates
ρ_d	Density of damping layers
ν_0	Poisson's ratio of plates

ν_d	Poisson's ratio of damping layers
(\bar{x}_f, \bar{y}_f)	Location of the excitation force
M	Global mass matrix
K	Global stiffness matrix
F	Vector of excitation force
ω_n	Undamped natural angular frequency
L	Even integer
m	Resolution
\mathbf{I}_x	Connect coefficient in x direction
\mathbf{I}_y	Connect coefficient in y direction
p	Sound pressure
ρ_a	Density of air
W_{rad}	Radiated sound power
c_a	Speed of sound
$f_{critical}$	Critical frequency
L_w	Sound power level
\bar{L}_p	Surface time-averaged sound pressure level
f_{cuton}	Cut-on frequency
$\langle v_{ABH}^2 \rangle$	Mean square velocity of the ABH portion
$\langle v_{uniform}^2 \rangle$	Mean square velocity of the uniform portion

$p^{(s)}$	Supersonic pressure
$v^{(s)}$	Supersonic normal velocity
$I^{(s)}$	Supersonic acoustic intensity
R_t	Transonic boundary
C	Objective function
f_v	Prescribed volume fraction
ρ_e	Relative density
v_e	Volume of damping materials for element e
\tilde{p}, \tilde{q}	Penal factors
\mathbf{W}	Complex displacement vector
\mathbf{V}	Complex velocity vector
P_t	Parent population
Q_t	Offspring population

Abbreviations

Terminology	Explanation
DW	Daubechies wavelet function
AI	Acoustic intensity
SSI	Supersonic acoustic intensity
OC	Optimality Criteria
SIMP	Solid isotropic material with penalization
AVM	Adjoint variable method
MSV	Mean square velocity
CR	Coverage ratio
NSGA	Nondominated sorting genetic algorithm

Chapter 1

Introduction

1.1 Background

Structural vibration is one of the main causes for noise generation and damage of thin-walled structures that are widely used in aircraft fuselages, ship hulls and vehicles. Also, unwanted vibration affects the comfort, durability and security of engineering structures in many applications. Therefore, mitigation of unwanted vibration has been a long-lasting issue and has attracted an ever-increasing attention from scientific community for decades.

Vibration control can be implemented in either active or passive means. Despite their attractive features in terms of adaptability, active approaches are still perceived as cost prohibitive, complex and less robust in some applications. Therefore, passive methods, exemplified by damping enhancement in structures still remain popular for vibration and noise mitigations. However, traditional passive measures, such as surface damping treatment for vibration energy dissipation or graded impedance interface for reducing reflections of flexural waves from structural edges, are either uneconomical or difficult to achieve, thus hampering their wide use in industry. Therefore, seeking lightweight and cost-effective solutions which allow structural damping enhancement for vibration control is of practical significance.

In the past decades, Acoustic Black Hole (ABH) has been proven to be a promising passive means for vibration and noise mitigations [ADDIN EN.CITE \[错误!未定义书签\]](#) , thereby attracting increasing attention over the years from the scientific and engineering community [ADDIN EN.CITE \[错误!未定义书签\]](#) . The great merit of the ABH is that only a small amount of damping material is needed to achieve a substantial increase in the overall structural damping, in contrast to traditional approaches. This attractive feature is of practical significance for the design of lightweight, yet highly damped structures in aeronautical and automotive industry. Despite the intensifying effort during the past few years, the study on ABH is still in its infancy. Among several important issues that will be discussed in detail later in this thesis, the lack of appropriate simulation tools is one of the bottlenecking problems in the ABH studies. In fact, due to the lack of analytical solutions, a large proportion of ABH studies resorts to the Finite Element Method (FEM) and experiments. While recognizing their ability in handling complex structures, they are not conducive to system analyses and optimization. As opposed to FEM analyses and experimental investigations, modelling based on energy principle might be a more flexible tool. Therefore, in this thesis, we propose an accurate semi-analytical wavelet model based on the Kirchhoff-Love thin plate theory under the framework of Rayleigh-Ritz method. The proposed model allows for accommodating fully coupled damping layers which play an indispensable role in the realization of ABH effect. The model is then exploited to explore various physical phenomena pertinent to ABH structures and to achieve structural optimizations from both vibration and sound radiation viewpoints.

1.2 Traditional measures for structural damping

Considering the importance of the damping in vibration control, persistent effort has been made to develop various ways to increase system damping, among which two major measures are viscoelastic coating over the structural surface and wave reflection control from structural boundaries.

Covering structural surface with highly energy-dissipating materials, such as polymer viscoelastic layers, to dissipate flexural waves is the most commonly used passive approach to achieve vibration attenuation, proven to be very efficient and successful [1-4]. In addition to the unconstrained configuration, the utilization of constrained damping layer has been shown to further increase the damping enhancement effect. However, due to the dispersive nature of the energy over structures, a large amount of viscoelastic material is usually needed to increase the overall structural damping to an appreciable level, thus giving rise to extra weight to the structure that may be unacceptable in many applications. Among many adverse consequences, increased weight of machines and vehicles would definitely lead to more fuel consumption and emissions [5]. These drawbacks make this traditional measure a major obstacle in its implementation into industrial world for which economic and ecological considerations are of crucial importance.

Reducing reflections of propagating waves from structural edges is another well-known approach for vibration mitigation [4, 6]. For example, a graded impedance interface may consist of different materials of uniform thickness (shown in Figure 1.1), terminated with composite materials at the free edge of a structure. The decreasing impedance leads to the slowing-down of propagating waves and increased vibration amplitude towards the edge, which enables appreciable energy dissipation by terminated composite materials. Reflectivity analyses of a steel bar show that up to 60-80% of vibration energy can be dissipated upon proper design [6]. However, the efficiency strongly depends on the large vibration amplitude resulting from impedance gradation which is difficult to be attained.

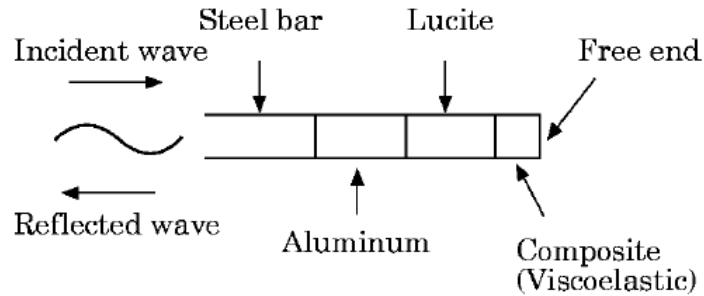


Figure 1.1 Graded impedance interface at the edge of a steel bar [6].

As an alternative option to reduce wave reflection from edges, a recently developed concept of the so-called acoustic black hole [7] constitutes an efficient and economical way to largely reduce reflections of flexural waves from edges over a broad frequency band with the utilization of only a small amount of damping material. The discovered

appealing features of the ABH have stimulated great interest of researchers. In the following sections, a literature review on various aspects pertinent to ABHs is presented.

1.3 Literature review on acoustic black holes

The concept of the black holes in astrophysics was initially proposed by Laplace [8], who stated that if an object can be compressed into a small enough radius, the escape velocity of that object would be even faster than light. The path of other objects passing around that object will be redirected towards the singularity point. Acoustic black hole (ABH) in vibration and acoustics can be regarded as the counterpart of the well-known astrophysical black hole. Pekeris [9] observed the phenomenon of decreasing sound velocity with increased depth in shallow zone in a half-space media. Analogously, Mironov [10] showed that, for a thin-walled structure whose thickness is tailored following a power-law profile, the phase speed of incident flexural waves would gradually slow down towards the thin edge tip alongside a simultaneous reduction of the wavelengths and an amplification of the vibration amplitude of vibration at the taper end. In an ideal scenario, *i.e.*, the local thickness is smoothly decreased to zero at the edge tip, waves would stop propagating and never reach the end, giving rise to zero reflection from the edge. Consequently, vibration energy is accumulated and focalized at the extremity region of the taper. A small amount of damping material coated at the extremity region would allow for effective energy focalization and dissipation [7].

1.3.1 Acoustic black hole theory

To gain physical insights into the ABH phenomena, the geometrical acoustics theory [10] has been utilized for the illustration of flexural wave propagation in elastic beams and plates whose thickness ideally varies and gradually reduces to zero according to a power-law relationship. Taking a simple beam containing an ABH wedge (as shown in Figure 1.2) as an example, the local thickness is progressively decreased following $h(x) = \varepsilon x^\gamma$, where ε is a constant, γ the power law index, and x the distance measured from the wedge tip. Under the assumption of geometrical acoustics theory, the aggregated wave phase Ψ from an arbitrary point x to the wedge tip writes [7]

$$\Psi = \int_0^x k(x) dx \quad (1.1)$$

where $k(x) = 12^{1/4} k_p^{1/2} (\varepsilon x^\gamma)^{-1/2}$ is the local wavenumber, $k_p = \omega/c_p$. The phase velocity is associated with the shear wave velocity c_t and longitudinal wave velocity c_l as $c_p = 2c_t (1 - c_t^2/c_l^2)^{1/2}$. Integration in Equation (1.1) tends to diverge if γ is equal or larger than two, *i.e.*, $\gamma \geq 2$ [11] for free wedges, and $\gamma \geq 5/3$ [10] for immersed wedges. The divergence suggests that the wave phase is infinite and the wave will never reach the wedge tip, resulting in zero reflection of waves from the edge. With proper dissipation, the combined process (energy focalization and dissipation) constitutes the Acoustic Black Hole (ABH) phenomenon.

However, in real world, zero thickness at the wedge tip is impossible to achieve, thus a truncation thickness always exists at the end of the power-law profile, which will adversely increase wave reflections and compromise the energy focalization at the same time. Equation (1.1) implies that even with a small truncation thickness (truncated at

coordinate x_0), reflections occur. In fact, the reflection coefficient of flexural waves would be as large as 50-70% [7]. To counter this, a piece of damping layer deposited over the surface of the wedge was proposed by Krylov, which entailed a sharp decrease of the reflection coefficient to typically 1-3% upon the deployment of the damping materials, as demonstrated both numerically and experimentally [7, 12].

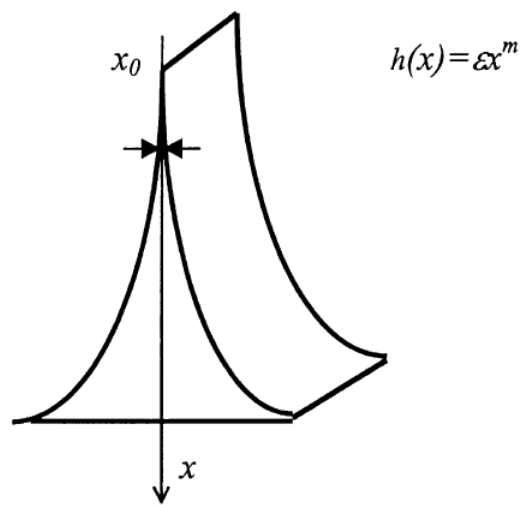


Figure 1.2 Elastic wedge of power law profile [7].

Wedges (1D acoustic black hole) exposed at the ends of beams or plates are fragile and prone to tearing, posing safety and health risks. One way to address the issue is to move the wedge to the inside of structures like plates. Similarly, plates embodied with circular indentations/pits (2D acoustic black hole) have been explored and also shown robust ABH effect [13-15].

1.3.2 Numerical analyses of acoustic black hole structures

1.3.2.1 Wave reflection from ABH edges

The reflection coefficient of flexural waves from an edge is perceived as a direct descriptor of the ABH effect and has been widely used in the literature. Employing the geometrical acoustics approach [7, 12, 16-19], the reflection coefficient of propagating flexural waves from the edge of elastic wedges was analytically derived and numerically calculated. In this regard, expressions of wavenumbers are considered in different ways, depending on the relative thickness of the damping layer to the truncation thickness of the wedge. For a relatively thin damping layer thickness compared to the truncation thickness of a quadratic wedge, the resulting reflection coefficient R_0 can be analytically derived as

$$R_0 = \exp(-2\mu_1 - 2\mu_2) \quad (1.2)$$

where

$$\mu_1 = \frac{12^{1/4} k_p^{1/2} \eta_w}{4\varepsilon^{1/2}} \ln\left(\frac{x}{x_0}\right) \quad (1.3)$$

and

$$\mu_2 = \frac{3 \times 12^{1/4} k_p^{1/2} \eta_d h_d}{4\varepsilon^{3/2}} \frac{E_2}{E_1} \frac{1}{x_0^2} \left(1 - \frac{x_0^2}{x^2}\right) \quad (1.4)$$

in which η_w and η_d are the loss factors of the wedge and that of the damping layer, respectively. E_1 and E_2 stand for their respective Young's moduli. h_d is the thickness of the damping layer. The extension of the analyses to a smaller truncation thickness necessitates the consideration of wedges covered with damping layer of arbitrary thickness. This work was undertaken in Ref. [7] under some simplifications. However,

the integration involved requires numerical calculations. Also under the framework of the geometrical acoustics approach, wave reflection and ray trajectories [20] (see Figure 1.3) were calculated, revealing energy trapping effect of both 1D and 2D ABHs.

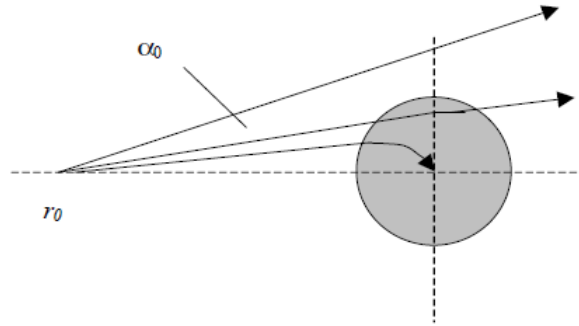


Figure 1.3 Three typical ray trajectories illustrating propagation of bending waves over a pit of power law profile: the ray below is trapped by the acoustic black hole, which means that the reflection from it can be neglected [20].

Using Wentzel-Kramers-Brillouin (WKB) approximation, Mironov [21] also conceptually showed the possibility of the total energy absorption in a narrow waveguide (see Figure 1.4) which exhibits a vanishing acoustic wave velocity towards the termination. Karlos *et al.* [22] estimated the reflection from wedges of power-law profile exhibiting different thicknesses using WKB approximation.

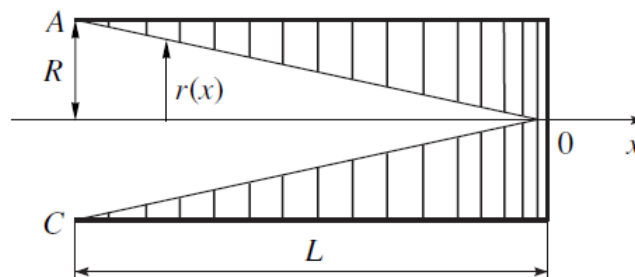


Figure 1.4 Model of an acoustic black hole. The tube with rings whose inner radius $r(x)$ decreases to zero [21].

Meanwhile, the high-order Wentzel-Kramers-Brillouin (WKB) method and FEM simulations were utilized by Karlos *et al.* [23] to characterize the reflection coefficient of a plate with a wedge of power-law profile. Guasch [24] calculated the reflection coefficients of acoustic black holes of linear and quadratic forms in duct terminations using the transfer matrix method and results were compared with those obtained from analytical solutions. Meanwhile, the influence of the number of rings, their thickness and damping on wave reflection were analyzed. Integrating the Riccati equation resulted in the impedance matrix from which reflection coefficients of flexural waves in a 1D ABH beam and 2D elliptical plate were numerically resolved by Georgiev *et al.* [13, 14].

Predictions of flexural ray trajectories and power flow in time domain were performed by Huang *et al.* [25, 26]. Lee and Jeon [27] analytically derived the displacement expression of an Euler-Bernoulli ABH beam. The reflection coefficient at the interface of the uniform portion and the ABH portion of the beam was analytically derived and numerically calculated and agrees with that obtained by geometrical acoustics approach. All the investigations showed largely reduced reflecting waves from edges covered with a small amount of damping material, as compared with bare edges and uniform counterparts with the same deposition of damping materials.

Based on the abovementioned numerical analyses, the impaired wave reflections of ABH were exploited and implemented in some engineering scenarios. Through a parametric study of key parameters on 1D beams using FE models, a trade-off between the maximum modal density and minimum wave reflection was reached by Hook *et al.* [28]. Motivated by the appealing feature of ABH with low reflecting waves from wedges of power-law profile, a taper tip was implemented by Yang and Thompson [29] into FE models to represent a non-reflecting boundary. Reflection analyses quantified by the wave/FE superposition method show that the utilization of a taper tip is more effective than its uniform counterpart. Also, the application of a tapered tip into a FE train track model generates analogous point mobility to an analytical infinite track model, albeit smaller size of model was adopted. Inspired by artificial cochleae, a waveguide consisting of two ducts partitioned by a plate was designed for the observation of propagating waves. The plate exhibits varying width and is terminated with an ABH acting as an anechoic end. Immersed in fluid media, the feature of low reflectivity of ABH characterized using WKB method [30] was utilized to improve the quality of measuring tonotopy [31].

1.3.2.2 Modelling of vibration and sound radiation from ABH structures

For both ABH beams and plates, analytical solutions are scarce. Therefore, much works related to ABH structures rely on numerical simulations, mainly including the FE method, the semi-analytical method, and the impedance method.

1) FE/BE model

The Finite Element Method (FEM) can readily handle structures of very complex geometries and irregular shapes. Also, complex boundary conditions, material properties and loading conditions can be easily taken care of using the FEM. Therefore, the FEM is universally popular among engineering community. However, FEM has its own disadvantages. In particular, the meshing and computation time involved in the solution of problems are intensive. Also, examining system response to changes in various parameters is tedious using the FEM, such as optimization problems. Despite of this, due to the absence of other alternatives, the FEM is by far still the most widely used method for ABH studies.

Using the FEM method, Zhou and Cheng [32] proposed and numerically modelled a so-called ABH featured resonant beam damper that entails broadband vibration attenuation. Tang and Cheng [33] observed band gaps in beams containing double-leaf acoustic black hole using FE models. It is shown that bending waves cannot propagate with the so-called band gaps, thus leading to considerable vibration attenuations within a broad frequency range. Furthermore, through FEM simulations, Gao *et al.* [34] designed V-folded beams that exhibit complete attenuation of flexural waves and

longitudinal waves. Due to conversion of longitudinal waves to flexural waves, a complete band gap was attained below 1 kHz, resulting in the considerably improved efficiency of ABH effect at low frequencies. Furthermore, the formation of 2D acoustic lenses in plates based on periodic acoustic black holes [35-37], and the improvement of effect of these acoustic lenses utilizing gradient-index local inhomogeneity [38] were observed or demonstrated using FE simulations.

Vibration characteristics of plates embedded with ABHs were extensively examined. Using FE/BE models, Conlon *et al.* [39] examined damping loss factors, vibration level and sound power of rectangular plates embedded with arrays of ABHs. Results show substantially increased damping and largely reduced sound power of a plate with ABHs as compared to a reference uniform plate. Meanwhile, possibilities for the enhancement of ABH effect at low frequencies were also explored [40]. Through FEM simulations, damping level of turbofan blades incorporating an ABH profile covered with non-polymeric damping materials was assessed [41]. Using FE models, Feurtado and Conlon [42, 43] characterized ABH behaviors at low, mid and high frequencies respectively. The low frequency performance of the ABH effect on damping was associated with low-order modes. Different damping layouts, such as the spatial coverage and the thicknesses of the damping layers over the ABH cell, were analyzed, with results suggesting that damping layers are beneficial to low frequency performance due to mass loading effect. On the other hand, an excessive thick damping layer on the sharp edge of wedges would probably impair damping increase because of the wave

reflection. Zhao and Semperlotti [44] modelled a plate embedded with multiple 2D ABHs mounted with piezoelectric transducers network. Dynamic behaviors of the model were quantitatively analyzed, showing broadband vibration attenuation performance. Meanwhile, an ABH plate combined with a dynamic absorber was numerically analyzed, showing substantial vibration reduction as compared with a uniform plate [45].

2) Impedance method

Not restricted to the hypotheses of the geometrical acoustic theory, Georgiev *et al.* analyzed the dynamic behaviors of ABH beams that follow Euler-Bernoulli assumptions and elliptical plates with indentations of power-law profile using the impedance method [13, 14] which allows taking evanescent waves into account. Additionally, the proposed model enables the accommodation of damping films which play a crucial role in vibration attenuation.

3) Semi-analytical model

Under the Rayleigh-Ritz framework, vibration characteristics pertinent to ABH beams were explored by Tang *et al.* [46] using a Mexican wavelet (MW) model. The predicted vibration field was experimentally validated. Meanwhile, the influence of damping layers of different configurations and an extended platform [47] at the ABH taper end on structural damping were investigated. In particular, the loss of ABH effect [48] was observed. Locally resonant band gaps in periodic beams [49] for vibration

mitigation were also studied employing the MW model. The aforementioned studies are limited to 1D cases.

Based on the Rayleigh-Ritz approach, investigations into vibration characteristics of ABH plates have been conducted in several works. With simple sinusoidal functions used as the trial functions to describe the displacement field of a rectangular plate embedded with a power-law profiled groove (1D ABH), O'Boy and Krylov [50] examined damping loss factors for roughly the first 20 modes. Deng *et al.* [51] employed Gaussian expansion functions to describe the transverse vibration displacement of a plate embedded with circular ABH indentations [52]. All these analyses demonstrated the damping enhancement of ABH structures using a moderate amount of damping layers. Power flow or structural intensity is another useful tool to get physical insights into ABH phenomena. Using Fourier series with supplementary auxiliary functions to approximate the transverse displacement of an ABH beam, Wang *et al.* [53] explored the distribution of structural intensity for an ABH beam under a point force excitation. Results show that structural intensity experiences a sharp decrease entering the coated area, confirming that the coated area of the taper tip acts as an energy sink. This analysis enriches the understanding of utilization of damping materials to enhance ABH effect.

In addition to several main approaches used to explore ABHs as abovementioned, other techniques such as the bending plate model, the wave model, the transfer matrix method, the image source approach, and the WKB method were also used for ABH

studies. O'Boy *et al.* [54] investigated the damping level of a plate with a wedge of power-law profile using a numerical bending plate model. The damping increase and the vibration reduction were clearly observed in the presence of damping material. O'Boy and Krylov [55] calculated the vibration response of a circular plate with a tapered central hole of quadratic power-law profile using a wave model. Using the transfer matrix method [56], vibration and sound radiation properties of a beam terminated with a wedge of power-law profile were investigated. Using a model based on the image source approach [57], Cuenca *et al.* investigated the damping efficiency of polygonal plates containing an circular ABH indentation. Exploiting the WKB method to characterize the fluid and solid fields, Zhou and Yu [58] numerically investigated the effectiveness of traditional Helmholtz Resonator (HR) combined with an ABH incorporated flexible plate. Magnified energy absorption and dissipation as well as enlarged working frequency were observed, suggesting that ABH is a viable solution to radically improve the efficiency of traditional HRs for noise mitigations.

1.3.2.3 Energy harvesting

Instead of converting strain energy to heat using damping material, piezo transducers deposited at the structural surface enables conversion of mechanical energy to electrical energy. Embracing the idea, Zhao *et al.* [59, 60] numerically established a fully coupled electro-mechanical model of an ABH plate. An indentation of power-law profile was incorporated in a plate with transducers mounted on the flat surface of the

indentation. The indentation undergoes wavelength sweep and exhibits high-density energy, leading to drastically increased efficiency in energy conversion (characterized by dissipated power) compared to traditional structures, regardless of steady-state excitation or transient excitation. It was concluded that ABHs exhibit progressive wavelength sweep and high-level energy density in the tapered region, thus making them a good candidate for vibration-based energy harvesting with mounted piezo-transducers. The numerically observed efficiency of mechanical-electrical energy conversion was also experimentally evidenced [61].

1.3.3 Experimentally investigations of acoustic black hole structures

1.3.3.1 Wave reflection from ABH edges

A Kundt-like method was proposed by Denis *et al.* [62] to experimentally measure the reflection coefficient of beams with an ABH termination. This technique allows for the consideration of thick damping layer. The resulting reflection coefficient, to some extent, agrees with those obtained from the geometrical acoustic approach [7], the impedance method [63] and a plate model [64]. Hook *et al.* [28] experimentally evidenced the trends of bands of low wave reflection of ABH beams in parametric studies.

The feature of the minimal reflection of propagating waves from the edges of elastic wedges makes ABH a good candidate to gain high Signal-Noise-Ratio (SNR)

direct Acoustic Emission (AE) waves [64], practically excluding wave reflection from structural boundaries. For example, in AE experiments, it is difficult to distinguish the characteristic information of noise source from received signal because of the interference of reflected wave components from structural boundaries. Inspired by the unique ABH feature of minimal wave reflection, Wang *et al.* [64] experimentally proved that the incorporation of an ABH into a disk is a viable option to lower wave reflection, yielding direct waves of high quality for AE tests.

1.3.3.2 *Vibration of ABH structures*

Vibration benefits drawn from the ABHs have been experimentally demonstrated in beams and plates. Experimental modal analyses on a beam with a power-law profiled termination and covered with damping materials were performed by Denis *et al.* [63]. Considerably increased modal overlap factors were observed compared against those of a uniform counterpart, suggesting reduced resonant behaviors of the beam with an ABH termination. The greatly attenuated vibration response observed in the so-called V-folded beams [34] using FEM simulations was also experimentally confirmed.

Rods with high damping offer a variety of possible applications in civil engineering and transportation industries. A steel rod featuring in a quadratic power-law profile covered by adhesive damping materials was proposed by Krylov [65] to damp vibrations. The observed reduction in mobility ensures that such a geometry combined with a small

amount of damping material represents an efficient damping system, pointing at its potential applications in the mitigation of impact-generated flexural vibrations frequently occurred in tennis racquets and golf clubs [66]. Extensive studies of vibration attenuation of 1D ABH beams can be found in Refs. [32, 46, 47, 56, 67, 68].

Vibration characteristics of plates with a wedge of power-law profile (1D ABH) were first experimentally [69] investigated by Krylov and Winward. Applying a point excitation force to the uniform portion, it was observed that peaks of mobilities of investigated plates in the vicinity of the wedge end covered with one adhesive strip were heavily damped, in comparison with those of uncovered ABH plates or covered uniform plates. However, increasing the number of adhesive strips shows little increase in the reduction of vibration peaks, which experimentally confirmed the theoretical calculation [7] that utilization of thicker damping material would not necessarily increase the structural damping, and even would be detrimental to ABH effect. It was concluded that a very small amount of damping material is sufficient to induce substantial damping of ABH structures, which is a remarkable feature of the ABHs. Adverse effect of the excessive use of damping material has also been evidenced in Refs. [43, 54, 70]. Bowyer *et al.* [71, 72] experimentally analyzed the damping performance of composite plates embedded with power-law slots. The potential application of wedges of power-law profile into turbofan blades for vibration attenuation was also experimentally attempted by E. Bowyer [73, 74]. Other experimental investigations into plates with 1D ABHs can be found in Refs. [54, 71, 75-78].

2D ABH Circular indentations were first experimentally examined in an elliptical plate by Gautier *et al.* [15]. An indentation located at one focus was covered by resins. Results show that the input mobility at the other focus exhibits a significant reduction at high frequencies, compared with that of a uniform elliptical plate completely covered with resins. Investigations of multiple-hole ABHs [79-81] embedded in a plate have also been carried out experimentally, showing that increased number of indentations will result in improved damping performance. The influence of the diameter of the indentations and the size of central holes on vibration attenuation were also examined [79]. Zhao and Semperlotti [44] experimentally demonstrated obvious broadband vibration attenuation characteristics based on multiple ABHs mounted with piezoelectric transducers. To attain improved damping performance, glass fibre composite panels [82, 83] encased with different configurations of power-law profiles were explored. Experimental results show that, with high-level intrinsic loss factor, composite panels embodied with multiple ABHs can result in effective damping performance with the absence of additional damping material, whilst maintaining similar surface texture as original sandwich panels as shown in Figure 1.5.

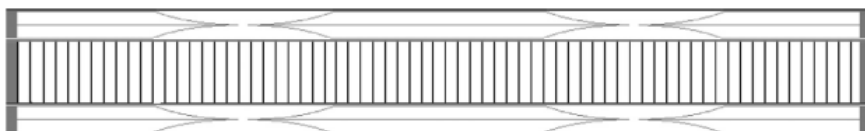


Figure 1.5 A composite panel enclosed with circular indentations.

Other experimental observations of damping vibration of plates embedded with circular indentations can be found in Refs. [13, 42, 43, 57, 71]. Furthermore, experimental investigations show that robust ABH effect is still visible even with the presence of geometrical defects (see Figure 1.6) [77, 84], such as curling at the wedge tips [84].

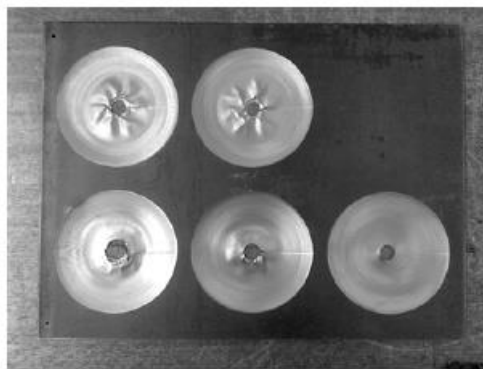


Figure 1.6 2D ABH with manufacturing defects [84].

1.3.3.3 *Sound radiation of ABH structures*

As opposed to vibration analyses, explorations of sound radiation properties of ABH structures are scarce. Experimental investigations into sound radiation characteristics pertinent to ABH plates were firstly carried out by Bowyer and Krylov [85]. Results show that the reduction of vibration level over the plate surface of uniform thickness necessarily leads to considerably reduced sound power level, despite the largely amplified vibration level at the ABH indentation center. The sound power was determined following ISO 3744 which requires the use of a rigid baffle with the test

sample. In this regard, the results obtained [85] may involve some errors at low frequencies because of the acoustic short circuiting resulted from free edges and the absence of the acoustic baffle. Feurtado and Conlon [43] also experimentally observed that a plate embodied with twenty circular indentations exhibits largely reduced sound power, compared with a uniform plate. The transformation of experimentally measured vibration velocity into wavenumber domain by Feurtado and Conlon [86, 87] offers useful physical insights into ABH behaviors. This wavenumber transform analysis reveals that ABHs are beneficial to redistribute vibration of supersonic components into subsonic components, subsequently the radiation efficiency was reduced. These analyses indicate that ABHs represent efficient means for noise mitigation.

1.3.3.4 Sound transmission loss

Sound transmission properties of structures constitute one of the main concerns in noise control application. The application of ABH concept for noise transmission control has also been attempted in the literature. ABH plate embedded with multiple circular ABH indentations was experimentally tested in a reverberant chamber by Feurtado and Conlon [88]. The measured transmission loss subjected to a diffuse sound field agrees with its numerically predicted results. Experimentally results show that a damped ABH plate containing 5×4 rectangular array of ABHs exhibits an increase of 6-9 dB in transmission loss over a uniform plate, achieved using less mass.

1.3.4 Potential applications of acoustic black hole structures

Taking advantage of the ABH effects, rods of a circular cross section that follows a power-law profile were successfully exploited by Krylov [65, 66] to damp impact-generated flexural vibration in tennis racquets and golf clubs (see Figure 1.7) that are supposed to be the major paths to transmit impact energy to arms [89, 90]. With narrow strips of energy absorbing materials coated at the taper areas, a large reduction in cross mobility was observed, compared with bare rods.

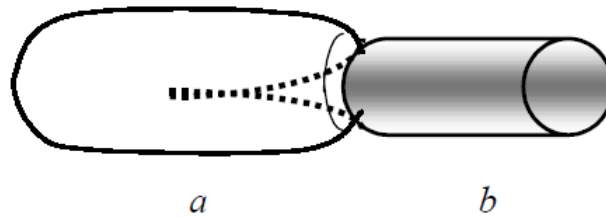


Figure 1.7 A tapered bar of circular cross-section with the radius described by a power-law profile and with the Sharp end covered by a thick absorbing layer (a); such a device forms a one-dimensional acoustic black hole that can be used for suppression of impact-induced resonant vibrations in the main structure of tennis racquets (only part of which close to the grip is shown) (b).

Another potential application of ABH is suggested for turbofan blades whose trailing edge exhibits a power-law profiled thickness. Bowyer *et al.* [73, 74, 91] experimentally analyzed accelerations of straight and twisted turbofan blades of power-law profile under air-flow excitations (shown in Figure 1.8). With moderate damping layers coated at trailing edges to produce original turbofan blades, separation of air flow

was eliminated and smaller vibration level was experimentally observed, which suggests that utilization of ABHs in trailing edges is a viable approach to damp structural vibration in engine fan blades. Using FE models, Bayod [41] numerically investigated the efficiency of abovementioned turbofan blades with a varying thickness of power-law profile. Results show a reduction in vibration response of turbofan blades with the tapered areas coated with non-polymeric damping materials.

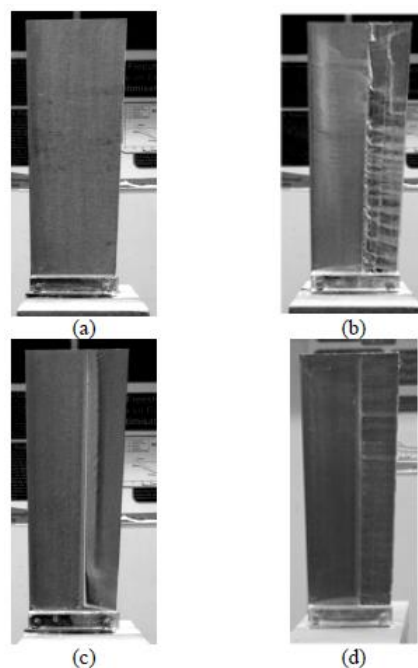


Figure 1.8 Flow visualization diagram for (a): reference fan blade; (b) fan blade with power-law wedge; (c) fan blade with power-law wedge with single damping layer; (d) fan blade with power-law wedge with shaped damping layer.

An automotive application of the ABHs into engine covers was exploited by Bowyer *et al.* [92]. The ABHs were boned into a standard engine cover (see Figure 1.9). Both vibration response and sound power were experimentally tested and compared

with those of a standard engine. Results indicate that the integration of ABHs into standards engines enabled a reduction of the total sound power by an average of 6.5 dB.



Figure 1.9 ABH engine cover (top view) and locations of accelerometers on reference engine cover [92].

Investigations suggested that, with fixed minimum thickness at ABH taper ends, increased ABH length would give rise to increased damping performance. However, in practice, due to the limitation of space, the length of ABH should be restricted. To solve the problem, a so-called curvilinear shaped ABH (shown in Figure 1.10) was proposed by Lee and Jeon [93]. Numerical analyses in terms of driving point mobility and radiated sound power were conducted using the commercial finite element software ANSYS. Results are similar to those of a standard ABH, which indicates that the compact spiral ABH can be a replacement for a standard ABH. Meanwhile, more effective ABH performance is expected as the length of the ABH is no longer a major constraint.

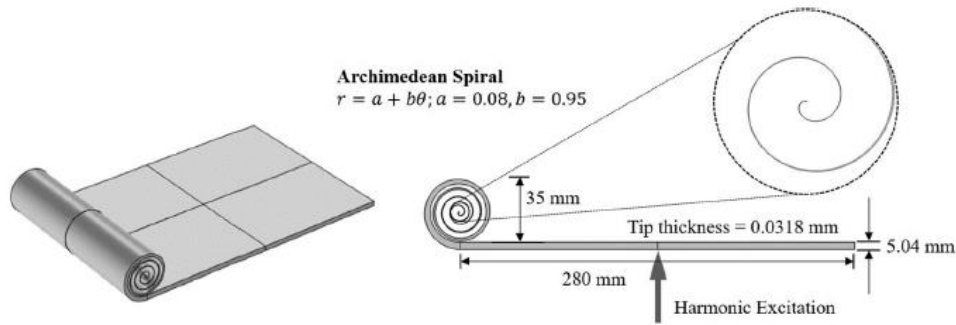


Figure 1.10 Plate with an ABH of an Archimedean [93].

Targeting a different application, plates with wedges of power-law profile were experimentally explored by Anderson *et al.* [94] for improved efficiency of ultrasonic sound radiation with a frequency span of 20-100 kHz. This idea was proposed by Remillieux *et al.* [95, 96] to ensure that ultrasonic sound radiates efficiently into air, which was experimentally evidenced by Anderson. Results reveal that a plate with a cubic power-law profile mounted with piezoelectric transducers is an extremely efficient means to ultrasonic radiation, thus suggesting its implementation as main sources in a Time Reversal Acoustic Non-Contact Excitation (TRANCE) source [97].

1.3.5 Improvements to enhance acoustic black hole performance

As aforementioned, ABH structures could act as efficient vibration absorbers. On the other hand, ABHs show little effect on damping enhancement at relative low frequencies, which is a major drawback of ABHs. To overcome the low frequency limit, some preliminary attempts were made, which are summarized in the following.

1) *Nonlinear effect*

Most of the theoretical and numerical investigations into ABH behaviors are based on linear assumptions. However, the large amplitude of vibration displacement at the end of ABH tapers, as compared to the minimum thickness, is highly likely to yield nonlinear effect in which linear eigenmodes are coupled. Such coupling enables energy transfer from a low frequency range to a high frequency range where ABH effect is very efficient, which may lower the effective frequency range of the ABH. Denis *et al.* [98] experimentally evidenced the energy transfer between low and high frequency ranges, and numerically illustrated the competing effect between nonlinearity and damping. To gain improved efficiency at low frequencies, power density spectrums of velocity response of a number of ABH beams with/without damping layers were calculated, giving rise to a compromise between the profile thickness and the moderate length of the damping layer. This work is probably the first one to focus on the nonlinear effect present in ABH structures that had been overlooked in the literature but is of crucial importance. However, the gain in the efficiency was rather limited, which later on motivated the exploration of the vibro-impact mechanism [67] to ensure more effective energy transfer. Numerically simulations show that the strongly nonlinear vibration of an ABH beam can lead to significant improvement of the ABH performance. Also, nonlinear acoustic absorption was theoretically explored by Gusev *et al.* [99], showing that acoustic waves in most wedges exhibiting acoustic black holes are completely attenuated. These analyses also ascertained the existence of ABH effect beyond

geometrical acoustics assumptions and the possible implementations of ABHs into nondestructive evaluation of micro-inhomogeneous materials.

2) Optimization of damping layer and ABH profile

For the purpose of enhancing ABH effect, optimizations of ABH layout has been carried out. Rothe *et al.* [100] optimized the position of an ABH indentation to minimize the vibration level of a plate. ABHs of high taper power are expected to exhibit totally low reflection coefficients of flexural waves thus induce better ABH performance. On the other hand, a high taper power index is likely to violate the smooth assumptions required by better ABH effect. To compromise the competing effects, parameters of power-law profiles including the minimum thickness, the end thickness, the taper power and the length of tapers were used as design variables to achieve an optimized profile that takes both vibration suppression and the smooth condition into account. A pareto optimality curve associated with abovementioned two objectives was estimated under the framework of the evolutionary search [101]. In addition, to gain increased ABH performance, parameters of power-law profiles were also investigated in Refs. [10, 12, 25, 28, 46, 47, 58, 64, 102-104].

3) Gradient thermal load

Also in Ref. [104], Cuenca *et al.* imposed a temperature gradient to a beam, which leads to a varying Young's modulus gradient along the distance, thus resulting in decreased structural wave velocity. Peaks of the reference input impedance were

practically eliminated, compared with their counterparts in the absence of gradient thermal load.

4) Negative capacitance shunted piezoelectric transducers

Beck and Cunefare [105] proposed to use shunted piezoelectric patches near the end of ABH tapers to increase the absorption of vibration energy. ABH, in turn, improved the efficiency of piezoelectric shunt control. In terms of the reduction in kinetic energy and reflection coefficient, the combination of negative capacitance shunted piezoelectric transducers with an ABH taper shows superiority over the traditional damping treatment coated at the ABH taper end.

Other numerical simulations and experimental investigations associated with improved ABH effect in terms of reflection coefficients, damping vibration and noise mitigation can be found in the literature, *e.g.* functionally graded ABH [106], sandwich plate with periodic ABH circular indentations covered by constrained layers [107] and compound ABH beams [68]. More detailed descriptions can be referred to a few recent review papers [92, 108-110].

1.4 Research objectives

Existing attempts on various aspects pertaining to ABH effects are presented above. As a summary, the reflection coefficient is perceived as a main intrinsic indicator/descriptor for assessing ABH effect of a structure. With a small amount of

damping material coating on the ABH taper end, the reflection coefficient undergoes a large decrease, entailing pronounced strain energy focalization/focusing at the extremity region of ABH tapers with proper dissipation, thus making the entire structure an efficient damping system. Investigations into energy harvesting show that, piezoelectric transducers mounted at ABH tapers allows for efficient conversion from mechanical energy to electrical energy, subsequently, vibration level of ABH structures was largely reduced. Additionally, the great potential of ABH plates in transmission loss applications was also experimentally observed. These works point at promising application of the ABH-based technology, as initially demonstrated by a few application cases.

Despite the progress made, however, the underlying mechanism of ABH effect, as well as its optimal design to cater for particular application scenario, has not been fully revealed, probably due to a lack of flexible simulation and optimization tools. While the vibration analyses of ABH structures are extensively reported as summarized in the [Section 1.3](#), the explorations in sound radiation properties of ABH structures are still relatively limited. Also, it can be surmised that optimizations of damping layers and ABH profiles may potentially enhance ABH performance, which has not practically been materialized. The ultimate solution to tackle these problem calls for flexible tools that enable examination of ABH behaviors in a versatile manner. This thesis attempts to contribute to the above-mentioned aspects.

The objectives of the thesis are as follows:

- 1) Develop a semi-analytical model for the prediction of the vibration and sound radiation of realistic ABH plates of finite size up to a high frequency range. Add-on components such as damping layers should be integrated into the model in a fully coupled manner.
- 2) Carry out experimental validations of the proposed model and demonstrate ABH effects on structural vibration and sound radiation.
- 3) Carry out systematic investigations and exploration of underlying physics behind the vibration and sound radiation of ABH plates with the help of the established model.
- 4) Optimize the layouts of the add-on damping layers for given targets such as minimization of structural vibration, and sound power.
- 5) Propose other possible ABH thickness profiles through optimizations. The optimized profile is expected to increase the damping performance of ABH plates while respecting other constraints such as minimum structural thickness that can possibly be achieved by the current state-of-the-art manufacturing technology.

1.5 Overview of the thesis

To achieve the objectives described above, the remaining thesis is organized as follows.

[Chapter 2](#) focuses on mathematical formulations of a 2D Daubechies wavelet (DW) model and the calculations of scaling functions and connection coefficients involved in the modelling. Additionally, the established vibration model is extended to sound radiation calculation. In [Chapter 3](#), the accuracy of the proposed model in terms of various vibration and sound radiation metrics is experimentally verified. [Chapter 4](#) is dedicated to the analyses of the vibration characteristics of a plate embedded with a strip indentation (1D ABH). [Chapter 5](#) explores the sound radiation properties of a plate containing a circular ABH indentation. [Chapter 6](#) investigates the optimal layouts of topologically optimized damping layers mainly for minimization of radiated sound power. [Chapter 7](#) proposes a profile that is different from the standard ABH profile with increased structural damping in an ABH plate. [Chapter 8](#) concludes the thesis and gives suggestions for future ABH studies. Detailed description of each chapter are as follows:

In [Chapter 2](#), a model based on the Kirchhoff-Love thin plate theory is developed under the Rayleigh-Ritz framework. The damping layer covering the surface of the ABH indentation is integrated with the plate in a fully coupled manner. Values of DW scaling functions are recursively calculated. General expression of the connection coefficients involved in the mass and stiffness matrices are derived. Furthermore, the proposed model is extended to sound radiation field. Both far field and near field methods for sound radiation analyses are presented.

Subsequently in [Chapter 3](#), the accuracy of the proposed model is thoroughly validated. Two key parameters, compactly supported length L and resolution m , that relevant to Daubechies wavelet scaling functions are carefully determined. The vibration field is verified through FE simulations, and the sound field is verified using a simply supported uniform plate for which analytical solutions are available. Furthermore, a rectangular plate embedded with a circular ABH indentation is successfully manufactured. The vibration parameters such as eigen-frequencies, mode shapes and mobilities, as well as the sound radiation parameters are experimentally measured to validate the proposed model.

Based on the DW model developed in [Chapter 2](#), vibration characteristics of a rectangular plate embedded with a strip indentation (1D ABH) are investigated in [Chapter 4](#). Based on the model, effects of different configurations of damping layers coated at the ABH indentation on damping enhancement are quantitatively analyzed. The obtained damping loss factors are classified into three groups that are associated with ABH local modes. The vibration attenuation performance of ABH plates is assessed by comparing against that of uniform reference plates.

In [Chapter 5](#), reductions in the radiated sound power of ABH plates are quantitatively analyzed. Effect of the stiffness due to the add-on damping layer on the increase of sound radiation efficiency is revealed and qualitatively investigated, both for ABH plates and uniform plates. To understand the underlying mechanism for sound

radiation reduction, sound radiation properties of ABH plates along with transonic boundary of the ABH plate is examined. The effective radiation regions on ABH plates are identified using the supersonic intensity theory.

Considering the competing effects of the damping layer on reduction of vibration level and reduced radiation efficiency, the damping layout of the viscoelastic coating over the surface of the ABH indentation is topologically optimized in [Chapter 6](#). The optimization is carried out using either the mean square velocity over the entire ABH surface or the radiated sound power as objective functions. Differences in optimal layouts obtained under the two different objectives and the corresponding radiation efficiencies are compared and analyzed. Additionally, the averaged sound power within a frequency band is minimized and results are compared against those of an ABH plate with damping layer centrally covering ABH indentation and a bare uniform plate.

In [Chapter 7](#), subjecting to the satisfaction of the smooth conditions, ABH thickness profiles are optimized using the Non-dominant Sorting Genetic Algorithm II (NSGA II) method. The objective function is the maximization of the sum of the first one hundred modes. The damping level of the convergent profile is compared with that of a standard profile with a taper power of four. Furthermore, physical mechanisms leading to the damping increase in the optimized profile are analyzed.

Major conclusions are drawn and summarized in [Chapter 8](#), with discussions and suggestions on possible future ABH work.

Chapter 2

2D Daubechies wavelet semi-analytical model

2.1 Introduction

The design of effective ABH structures relies on a good understanding of the underlying physics and a meticulous setting of the design parameters, be it material or geometrical. This can only be achieved with the help of efficient simulation and optimization tools. Up to now, extensive work has been carried out, predominantly using numerical tools such as finite element methods and experiments [39, 69, 79, 85]. To a much less degree, effort has also been made to develop more physical models, aimed at capturing the fundamental features of the ABH phenomena using basic configurations, as reviewed in [Chapter 1](#). Pros and cons of these methods have been extensively discussed in previous works [7, 46], among which geometrical and boundary restrictions of the structure as well as the applicable frequency range are the main concerns. More recently, structural modelling which considers more realistic structural features such as finite size, realistic structural boundaries and add-on damping layers has also been attempted, but mainly limited to 1D cases [46].

The modelling of the ABH structures is technically challenging due to the ABH-specific features, which are mainly twofold: a) structural wavelength varies significantly over a structure with embedded ABH elements. At any given frequency, bending waves

experience a continuous wavelength variation and are severely compressed inside the ABH cells, while remaining relatively even over the uniform part of the structure; b) ABH effects start to systematically show only above the so-called cut-on frequency [39], when the structural wave length starts to be comparable with the characteristic dimension of the ABH cells. Therefore, simulation methods should be able to reach the relatively high frequency range while being able to accommodate the significant wavelength variations over the structure. Along with these challenges, there is also the need in accommodating various structural changes such as add-on damping layers [46] or energy harvesting elements [59], as well as a better versatility and flexibility in coping with the structural design and optimizations. All these add further difficulties to the modelling task.

The use of wavelets under the Rayleigh-Ritz framework may provide a solution to cope with the abovementioned problems. In a previous work, a wavelet decomposed Rayleigh-Ritz method was proposed to model thin-walled structures with a constant thickness [111]. Results showed that the wavelet-based model can reach a much higher frequency range than the conventional Rayleigh-Ritz methods using admissible functions such as simple polynomials, Chebyshev series or trigonometric functions, which are prone to problems like numerical instability, ill condition or slow convergence [112, 113]. Meanwhile, the unique features of the wavelets such as flexible scaling, compact support and strong fitting capability are shown to be conducive to the handling of ABH-specific wavelength variations. The idea was tested on a 1D beam using

Mexican Hat Wavelets (MHWs) [46]. The formulation was rather straightforward since 1D configuration is relatively simple and MHWs can be analytically expressed. It was shown that the MHW-based Rayleigh-Ritz model allowed a good description of the ABH phenomena by accurately predicting the system dynamics at relatively high frequencies. Up to now, however, semi-analytical modelling of 2D ABH structures is scarce with the exception of a very recent work by O'Boy and Krylov [50]. That work follows the same Rayleigh-Ritz framework using trigonometric series as the admissible functions. The reported frequency range, however, is relatively low, typically covering the first twenty structural modes.

Inspired by our previous work on 1-D ABH beams [114] and the success in high frequency simulation on uniform structures [111], this paper proposes a 2D semi-analytical ABH model using Daubechies wavelet scaling functions. Compared with the MHWs which are smooth and analytically expressible, DWs are expected to better respond to the local variations of the ABH phenomena. However, as DW scaling functions have no closed form expressions, a proper recursive procedure needs to be worked out to deal with various operations on the scaling functions. In the present work, the same configuration used in O'Boy and Krylov [50] is adopted with an intention of improving that model to reach the effective ABH zone at much higher frequencies.

In this chapter, a versatile semi-analytical model is proposed based on the Kirchhoff-Love thin plate theory. The proposed semi-analytical model is first developed

for a plate embedded with strip/circular ABH indentations in [Section 2.2](#). In the formulation, DW scaling functions are chosen as the admissible functions for flexural displacement decomposition under the general Rayleigh-Ritz framework. Solutions to the derivatives of DW scaling functions and the connection coefficients are derived. The formation of matrices of mass and stiffness involves the calculation of connection coefficients that are integrals of DW functions and their derivatives in a finite interval. The integration can be performed using 1D Gaussian integration method for 1D ABH indentations (strip indentations) and 2D Gaussian integration method for 2D ABH indentations (circular ABH indentations), respectively. Furthermore, the proposed vibration model is extended to sound radiation field.

2.2 Semi-analytical modelling and formulation

2.2.1 Modelling

The modelling of 2D ABH plates is carried out for both strip and circular ABH indentations. Due to the similarity in the modelling approach, more details are given using strip case as an example. As shown in [Figure 2.1\(a\)](#), the investigated structure is a thin plate (with a dimension of a , b , and h), which contains a strip ABH indentation, symmetrically coated with damping layers on both sides. The strip ABH indentation featuring a thickness variation along one direction of the plate. [Figure 2.1\(b\)](#) gives the top view of the plate and [Figure 2.1\(c\)](#) the cross-sectional thickness profile. The plate consists of two portions. The region containing the ABH strip is referred to as ABH portion, and the one with a constant thickness the uniform portion. The ABH portion is

bounded by the range (x_1, x_2) and (y_1, y_2) , centered at (x_c, y_c) , featuring a thickness variation in x direction according to a power law relationship, *i.e.* $h(x) = \varepsilon(|x - x_c| + \delta_0)^\gamma$ with ε being a constant, γ a power law index and δ_0 a parameter which determines the termination thickness in the thinnest middle part of the strip. Along the center at $x = x_c$, the ABH indentation has the smallest thickness $\varepsilon\delta_0^\gamma$. Damping layers with a thickness h_d are coated within an area from x_{d1} to x_{d2} in x direction and from y_{d1} to y_{d2} in y direction.

As to a plate embedded with a circular ABH indentation (see [Figure 2.2](#)), it has a radius of R_{ABH} , centered at (x_c, y_c) . The thickness of the circular ABH indentation changes according to $h(x, y) = \varepsilon\left(\sqrt{(x - x_c)^2 + (y - y_c)^2}\right)^\gamma + h_0$, where h_0 is the smallest thickness of the indentation. The central portion of the ABH indentation within a radius R_d is covered with the damping layer. Other materials can be found in [Appendix B](#).

The boundary conditions of the plates are shown in [Figure 2.1\(d\)](#). A set of springs working in translation and rotation are uniformly distributed along the edges of the plate [115] (k_i for translational spring stiffness and c_i for rotational spring stiffness with $i=1, 2, 3, 4$ representing the edge number of the plate). The use of the springs allows various boundary conditions to be simulated through adjusting their stiffness values. Meanwhile, it allows a flexible choice of the admissible functions which are required to only satisfy

the geometrical boundary conditions. The inherent material damping of the plate and that of the damping layers are introduced through complex Young's modulus $E_0 = E_0(1+i\eta_0)$ and $E_d = E_d(1+i\eta_d)$, respectively, where η_0 and η_d are the corresponding loss factors. The damping layer is explicitly modeled as an integrate part of the ABH plate, with both its stiffness and mass included in the global matrices of stiffness and mass of the whole system.

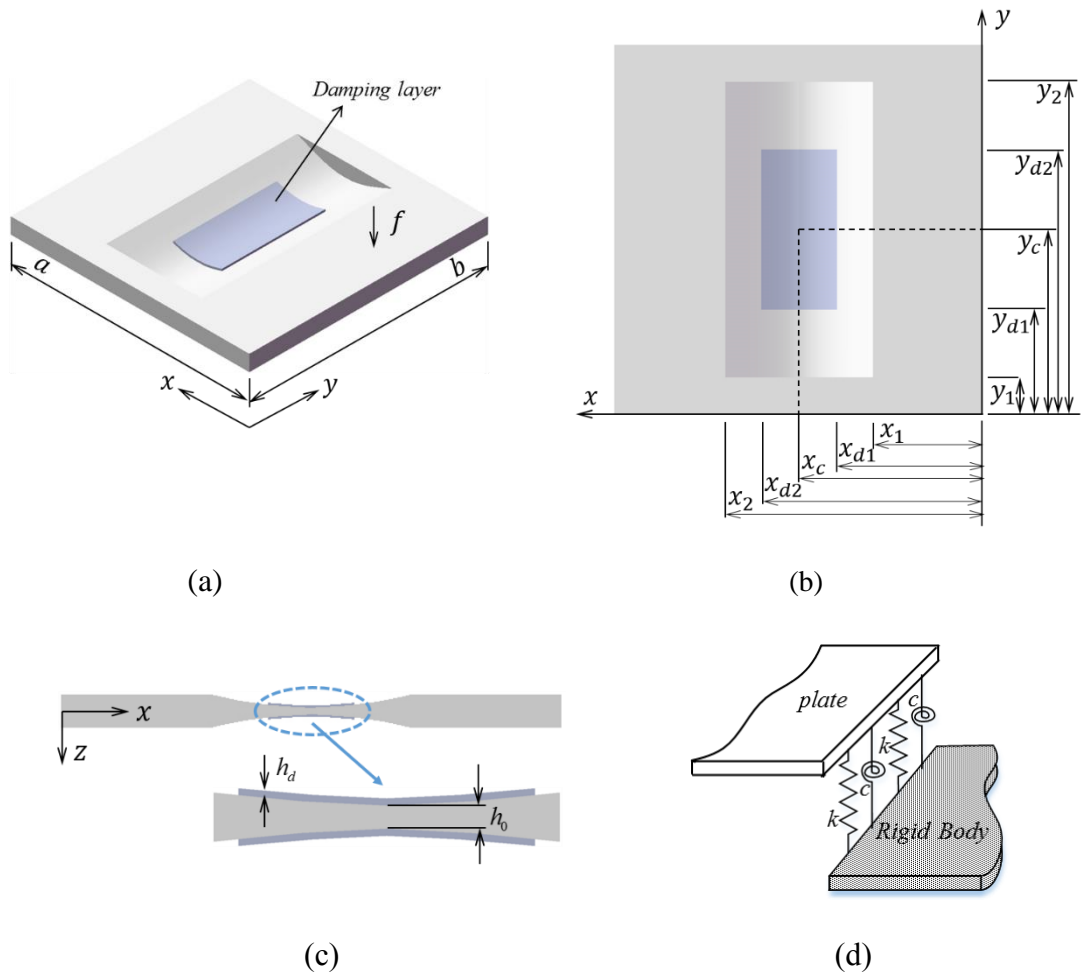


Figure 2.1 Plate model with a strip ABH indentation: (a) plate with symmetrical power-law thickness profiles; (b) ABH portion in vertical view; (c) cross-section of the ABH portion; (d) modeling of the boundary conditions.

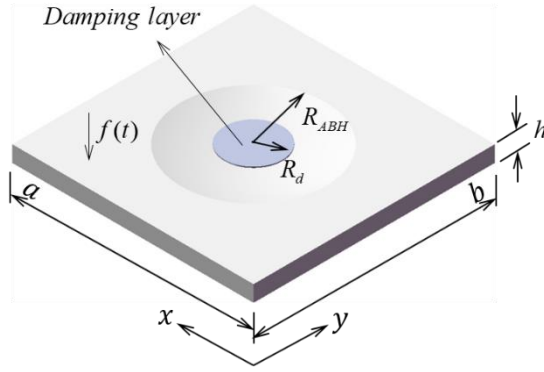


Figure 2.2 Plate model with a circular ABH indentation.

The system is assumed to be symmetrical with respect to the midplane of the plate. According to the Love-Kirchhoff thin plate theory, the displacement field of the system can be written as:

$$\{u, v, w\} = \left\{ -z \frac{\partial w}{\partial x}, -z \frac{\partial w}{\partial y}, w \right\} \quad (2.1)$$

in which vector $\{u, v, w\}$ contains the three displacements of a point, in either the plate or the damping layer.

Employing dimensionless coordinates $\bar{x} = x/a$ and $\bar{y} = y/b$, the transverse displacement w can be approximated by:

$$w = \sum_i^{\bar{p}} \sum_j^{\bar{q}} a_{ij}(t) \varphi_i(\bar{x}) \varphi_j(\bar{y}) \quad (2.2)$$

where $\varphi_i(\bar{x})$ and $\varphi_j(\bar{y})$ are the assumed admissible functions and $a_{ij}(t)$ are the unknown complex coefficients; \bar{p} and \bar{q} are the truncation order representing the number of terms of admissible functions to be kept in the computation; $a_{ij}(t)$ are the

generalized coordinates in the Euler-Lagrange equations which result from the stationary state of the system:

$$\frac{d}{dt} \left(\frac{\partial \mathcal{L}}{\partial \dot{a}_{ij}(t)} \right) - \frac{\partial \mathcal{L}}{\partial a_{ij}(t)} = 0 \quad (2.3)$$

where \mathcal{L} is the Lagrangian operator written as:

$$\mathcal{L} = E_k - E_p + W_f \quad (2.4)$$

in which E_k and E_p are the kinetic energy and the potential energy of the system, respectively; and W_f the work done by external forces. Neglecting small quantities of higher orders, these terms are expressed as:

$$\begin{aligned} E_k &= \frac{1}{2} \rho ab \iint h(\bar{x}) \left(\frac{\partial w}{\partial t} \right)^2 d\bar{x}d\bar{y} \\ E_p &= \frac{1}{2} \iint \frac{E[h(\bar{x})]^3}{12(1-\nu^2)} \left[\frac{b}{a^3} \left(\frac{\partial^2 w}{\partial \bar{x}^2} \right)^2 + \frac{a}{b^3} \left(\frac{\partial^2 w}{\partial \bar{y}^2} \right)^2 \right. \\ &\quad \left. + 2\nu \frac{1}{ab} \left(\frac{\partial^2 w}{\partial \bar{x}^2} \frac{\partial^2 w}{\partial \bar{y}^2} \right) + 2(1-\nu) \frac{1}{ab} \left(\frac{\partial^2 w}{\partial \bar{x} \partial \bar{y}} \right)^2 \right] d\bar{x}d\bar{y} \\ &\quad + \frac{b}{2} \int_0^1 \left\{ k_1 [w(0, \bar{y}, t)]^2 + k_2 [w(1, \bar{y}, t)]^2 \right. \\ &\quad \left. + c_1 \cdot \frac{1}{a^2} \left[\frac{\partial w(\bar{x}, \bar{y}, t)}{\partial \bar{x}} \Big|_{\bar{x}=0} \right]^2 + c_2 \cdot \frac{1}{a^2} \left[\frac{\partial w(\bar{x}, \bar{y}, t)}{\partial \bar{x}} \Big|_{\bar{x}=1} \right]^2 \right\} d\bar{y} \\ &\quad + \frac{a}{2} \int_0^1 \left\{ k_3 [w(\bar{x}, 0, t)]^2 + k_4 [w(\bar{x}, 1, t)]^2 \right. \\ &\quad \left. + c_3 \cdot \frac{1}{b^2} \left[\frac{\partial w(\bar{x}, \bar{y}, t)}{\partial \bar{y}} \Big|_{\bar{y}=0} \right]^2 + c_4 \cdot \frac{1}{b^2} \left[\frac{\partial w(\bar{x}, \bar{y}, t)}{\partial \bar{y}} \Big|_{\bar{y}=1} \right]^2 \right\} d\bar{x} \\ W_f &= f(t)w(\bar{x}_f, \bar{y}_f, t) \end{aligned} \quad (2.5)$$

where ρ is the density, ν the Poisson's ratio and (\bar{x}_f, \bar{y}_f) the location of the excitation force. k_1, k_2, k_3 and k_4 are the translation stiffness of the artificial springs along the plate edges with coordinates $(0, \bar{y}), (1, \bar{y}), (\bar{x}, 0)$ and $(\bar{x}, 1)$, respectively, and c_1, c_2, c_3

and k_4 are the rotation stiffness. Integrals in Equation (2.5) should be evaluated for the whole system, including both the plate and the damping layers. Application of Equations (2.4) and (2.5) to Equation (2.3) leads to a set of linear equations, expressed in a matrix form as:

$$\mathbf{M}\ddot{\mathbf{a}}(t) + \mathbf{K}\mathbf{a}(t) = \mathbf{F}(t) \quad (2.6)$$

where \mathbf{M} and \mathbf{K} represent the global mass and stiffness matrices (complex due to viscoelasticity of the material), respectively. For the strip ABH case, the entire structure is divided into five parts. The formation of \mathbf{K} and \mathbf{M} is given in Appendix A. Considering a harmonic excitation, the above Equation (2.6) can be cast into the standard matrix form

$$(\mathbf{K} - \omega^2\mathbf{M})\mathbf{A} = \mathbf{F} \quad (2.7)$$

Dropping the excitation terms yields a standard eigenvalue problem, whose solution gives the natural frequencies of the system along the corresponding mode shapes. As \mathbf{K} is complex, the natural angular frequencies are also in a complex form as:

$$\omega^2 = \omega_n^2(1 + i\eta_n) \quad (2.8)$$

where ω_n are the undamped natural angular frequencies and η_n the corresponding modal loss factor. η_n is an important parameter to characterize the energy dissipation of individual resonant modes resulting from the ABH effects, which will be described in Chapter 4.

2.2.2 Daubechies wavelet scaling functions

As shown in Appendix A, expressions of the stiffness matrix K and mass matrix M require the handling of some finite integral terms involving the DW scaling functions and their derivatives. This is worked out in this Section. For the benefit of the readership, Daubechies wavelets are briefly recalled and discussed. DWs are a compactly supported and orthogonal set which can be scaled to accommodate both localized and smooth variations [116]. Each DW member is governed by an even integer L and a set of wavelet filter coefficients $\{p_l, l = 0, 1, 2, \dots, L-1\}$ through a two-scale relation:

$$\varphi(x) = \sum_{l=0}^{L-1} p_l \varphi(2x-l) \quad (2.9)$$

and

$$\psi(x) = \sum_{l=2-L}^1 (-1)^l p_{1-l} \varphi(2x-l) \quad (2.10)$$

where $\varphi(x)$ is the scaling function and $\psi(x)$ the mother wavelet. Note $\varphi(x)$ and $\psi(x)$ are completely localized in the interval $[0, L-1]$ and $[1-L/2, L/2]$, respectively. The conditions that the coefficients p_j need to satisfy can be found in Ref. [116].

The constructed $\psi(x)$ possesses the following property:

$$\int_{-\infty}^{+\infty} x^k \psi(x) dx = 0 \quad k = 0, 1, \dots, L/2-1 \quad (2.11)$$

which indicates that the elements of the set $\{1, x, \dots, x^{L/2-1}\}$ can be a linear combination of $\varphi(x-k)$, translated from $\varphi(x)$ by k . Also, the n^{th} derivative of the scaling function $\varphi^{(n)}(x)$ exists for $n = 0, 1, \dots, L/2-1$. Employing Equation (2.9), an analogous form of the two-scale relation for $\varphi^{(n)}(x)$ can be obtained as:

$$\varphi^{(n)}(x) = 2^n \sum_{l=0}^{L-1} p_l \varphi^{(n)}(2x-l) \quad (2.12)$$

Equation (2.12) allows the calculations of the values of $\varphi^{(n)}(x)$ for all dyadic points at $x = k/2^j$, when $\varphi^{(n)}(k)$ are known at the integer points $k = 1, 2, \dots, L/2$. Substituting these integer points into Equation (2.12) gives a system of linear equations as:

$$2^{-n} \mathbf{X} = \mathbf{P} \mathbf{X} \quad (2.13)$$

where

$$\mathbf{X} = [\varphi^{(n)}(1), \varphi^{(n)}(2), \dots, \varphi^{(n)}(L-2)]^T \quad (2.14)$$

in which superscript T denotes the transpose and P is a $(L-2) \times (L-2)$ matrix:

$$\mathbf{P} = [p_{2l_1-l_2}]_{1 \leq l_1, l_2 \leq L-2} \quad (2.15)$$

with l_1 and l_2 being the row and column indices, respectively. Vector \mathbf{X} , the eigenvector, can be uniquely determined with the following normalization condition [116]:

$$\sum_{k=1}^{L-2} (-k)^n \varphi^{(n)}(k) = n! \quad (2.16)$$

Upon getting values of $\varphi^{(n)}(k)$ at $k = 1, 2, \dots, L-2$, values of $\varphi^{(n)}(x)$ at $x = k/2^j$ for $k = 1, 3, 5, \dots, 2^j(L-1) - 1$ and $j = 1, 2, \dots$ can be determined by using the relation:

$$\varphi^{(n)}\left(\frac{k}{2^j}\right) = 2^n \sum_{l=0}^{L-1} p_l \varphi^{(n)}\left(\frac{k}{2^{j-1}} - l\right) \quad (2.17)$$

knowing that $\varphi^{(n)}(x) = 0$ for $x \leq 0$ and $x \geq L - 1$. Subsequently, the values of the scaling function $\varphi(x)$ and its derivatives at any point can be recursively calculated.

2.2.3 Connection coefficients

Write the 2D wavelet base functions in the \bar{x} and \bar{y} directions as $\varphi_i(\bar{x}) = 2^{m/2}\varphi(2^m\bar{x} - i)$ and $\varphi_j(\bar{y}) = 2^{m/2}\varphi(2^m\bar{y} - j)$, respectively, where m is the resolution, i and j are the corresponding translation factors. To avoid the singularity when solving Equation (2.6), the integer translation factors i and j should be confined to the range $[-L + 2, \dots, 2^m - 1]$. This leads to a total of number of terms given by $\bar{p} = \bar{q} = 2^m + L - 2$. All the wavelet terms located within the interval $[0, L - 1]$ should be included in the displacement field.

For the purpose of illustration, $\varphi_i(\bar{x})$ with $m = 2$ and $i = -3, -2, \dots, 2, 3$ is shown in Figure 2.3.

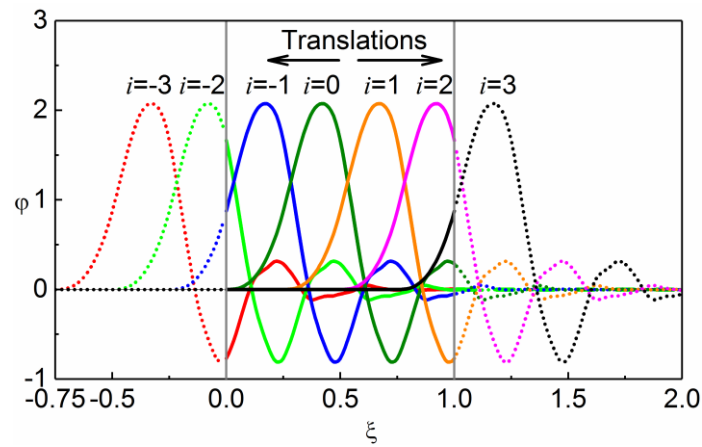


Figure 2.3 Daubechies scaling functions with $L=12$, $m=2$, $i=-3, -2, \dots, 2, 3$.

As shown in Appendix A, constructing K and M for each part of the plate (numbered by $q = 1, 2, \dots, 5$ in Appendix A) requires the calculations of 2-D connection coefficients which are the finite integrals involving admissible functions and their derivatives. The terminology of the so-called connection coefficients has been widely used in the literature on various applications of wavelets [111]. In the present case, the general form of 2D connection coefficients writes:

$$I_{r,i,s,j} = \int_{\bar{y}_{q1}}^{\bar{y}_{q2}} \int_{\bar{x}_{q1}}^{\bar{x}_{q2}} [h(\bar{x})]^n \varphi_r^{(\alpha_{\bar{x}})}(\bar{x}) \varphi_i^{(\beta_{\bar{x}})}(\bar{x}) \varphi_s^{(\alpha_{\bar{y}})}(\bar{y}) \varphi_j^{(\beta_{\bar{y}})}(\bar{y}) d\bar{x} d\bar{y} \quad (2.18)$$

where \bar{x}_{q1} and \bar{x}_{q2} are, respectively, the lower and upper limits in \bar{x} direction for a given part of the plate q ; and \bar{y}_{q1} and \bar{y}_{q2} in \bar{y} direction. n is equal to 1 for mass term and 3 for stiffness term. $\alpha_{\bar{x}}$, $\beta_{\bar{x}}$, $\alpha_{\bar{y}}$ and $\beta_{\bar{y}}$ are the order of derivatives of the scaling functions.

Due to the geometry of the strip ABH indentation, integrals in Equation (2.18) are separable. Recalling $\bar{x} = x/a$ and $\bar{y} = y/b$, $\varphi^{(\alpha)}(x) = (1/a)^\alpha \varphi^{(\alpha)}(\bar{x})$ and $\varphi^{(\alpha)}(y) = (1/b)^\beta \varphi^{(\beta)}(\bar{y})$. The general forms of 1D connection coefficients, I_x and I_y in the x and y directions, can be written as:

$$\begin{aligned} I_{x,r,i}^{\alpha,\beta} &= (1/a)^{\alpha-1} (1/b)^\beta 2^{(\alpha+\beta)m} \int_{\bar{x}_{q1}}^{\bar{x}_{q2}} [h(\bar{x})]^n \cdot 2^{m/2} [\varphi(2^m \bar{x} - r)]^{(\alpha)} \cdot 2^{m/2} [\varphi(2^m \bar{x} - i)]^{(\beta)} d\bar{x} \\ I_{y,s,j}^{\alpha,\beta} &= (1/a)^\alpha (1/b)^{\beta-1} 2^{(\alpha+\beta)m} \int_{\bar{y}_{q1}}^{\bar{y}_{q2}} 2^{m/2} [\varphi(2^m \bar{y} - s)]^{(\alpha)} \cdot 2^{m/2} [\varphi(2^m \bar{y} - j)]^{(\beta)} d\bar{y} \end{aligned} \quad (2.19)$$

where $\varphi^{(\alpha)}$ and $\varphi^{(\beta)}$ (with $\alpha, \beta=0, 1, 2$) are the derivatives of the scaling functions, which can be obtained by following the procedure described in [Section 2.2.2](#). Finally, the 2D connection coefficients are decomposed as a tensor product of their 1D counterparts I_x and I_y as:

$$\mathbf{I} = \mathbf{I}_x \otimes \mathbf{I}_y \quad (2.20)$$

where \otimes is the Kronecker tensor product symbol. Integrations in [Equation \(2.19\)](#) can then be carried out using 1D Gauss integration method.

It is relevant to note that the established formulation and the associated numerical scheme also apply to plates with circular ABH indentations. In that case, the thickness of the plate is a function of both \bar{x} and \bar{y} . Therefore, [Equation \(2.18\)](#) should be re-written as:

$$I_{r,i,s,j} = \int_{\bar{y}_{q1}}^{\bar{y}_{q2}} \int_{\bar{x}_{q1}}^{\bar{x}_{q2}} [h(\bar{x}, \bar{y})]^n \varphi_r^{(\alpha_\xi)}(\bar{x}) \varphi_i^{(\beta_\xi)}(\bar{x}) \varphi_s^{(\alpha_\eta)}(\bar{y}) \varphi_j^{(\beta_\eta)}(\bar{y}) d\bar{x} d\bar{y} \quad (2.21)$$

As a result, terms involving \bar{x} and \bar{y} are inseparable and the integral should be calculated by the 2-D Gauss integration method which takes the following standard form

$$\int_{-1}^1 \int_{-1}^1 f(\bar{x}, \bar{y}) d\bar{x} d\bar{y} = \sum_{i=1}^{M_0} \sum_{j=1}^{N_0} H_i H_j f(\bar{x}_i, \bar{y}_j) \quad (2.22)$$

where H_i and H_j are the weighting coefficients, $f(\bar{x}_i, \bar{y}_j)$ is the value of the integrand at the Gauss point (\bar{x}_i, \bar{y}_j) and M_0, N_0 the number of Gauss points.

2.2.4 Sound radiation model

The sound radiation of the ABH plate is characterized using radiated sound power, and sound radiation efficiency. The aforementioned vibration model is extended to accommodate this need under the wavelet-based framework.

2.2.4.1 Sound power and sound radiation efficiency

The acoustic model used in the analyses is shown in [Figure 2.4](#). The plate is assumed to be bounded by an infinitely large and rigid baffle. Setting the origin of the coordinates at the center of the plate, with $x - y$ plane coinciding with the mid-plane of the plate, Rayleigh integral [117] can be used to calculate the sound pressure radiated into the far field in an infinitely large half space as

$$\mathbf{p}(r) = \frac{j\omega\rho_a}{2\pi} \iint_S \mathbf{V}(r_0) \frac{\exp(-jk|r-r_0|)}{|r-r_0|} dS \quad (2.23)$$

where S represents the vibrating surface; ρ_a the density of air; ω the angular frequency and k the acoustic wavenumber. r is a position vector for a receiver position in the far field, r_0 is a position vector on the vibrating surface S . $\mathbf{V}(r_0)$ is the complex velocity normal to the plate surface. i is the imaginary unit which is the square root of -1.

In the harmonic case, the averaged acoustic intensity writes

$$\bar{\mathbf{I}} = \frac{1}{2} \text{Re}[\mathbf{p}(r)\vec{\mathbf{u}}^*(r)] \quad (2.24)$$

where $\mathbf{p}(r)$ and $\vec{\mathbf{u}}^*(r)$, are respectively the pressure and particle velocity. The superscript $*$ denotes complex conjugate and Re the real part.

The sound power can be calculated using either far field or near field methods. Adopting the far-field assumption and integrating the acoustic intensity in Equation (2.24) over a chosen hemispherical surface yield the total radiated sound power as

$$W_{rad} = \int_0^{2\pi} \int_0^{\pi/2} \frac{|\mathbf{p}(R_0, \theta, \phi)|}{2\rho_a c_a} r^2 \sin \theta d\theta d\phi \quad (2.25)$$

where θ is the polar angle, ϕ the azimuth angle, and c_a the speed of sound.

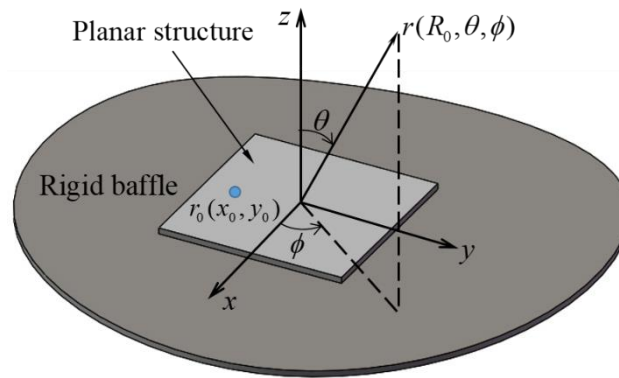


Figure 2.4 Coordinate system for the baffled plate.

For the near field calculation, the vibration velocity at a point (x_0, y_0) can be expressed as

$$v(x_0, y_0) = \sum_{i=1}^{\bar{p}} \sum_{j=1}^{\bar{q}} \dot{a}_{ij}(t) \varphi_i(\bar{x}) \varphi_j(\bar{y}) \quad (2.26)$$

Considering the ABH-specific strong wavelength variation over the plate and the need of reaching high frequency range, Daubechies wavelet scaling functions (DWs) are used as the admissible functions to capture the local details of the vibration field.

Based on Equation (2.26) and segmenting the plate into N cells as elementary radiators, a velocity vector \mathbf{V} can be constructed and expressed in a matrix form as

$$\mathbf{V} = \Phi \dot{\mathbf{A}} \quad (2.27)$$

in which Φ is a $N \times (2^m + L - 2)$ matrix whose elements are $\varphi_i(\bar{x})\varphi_j(\bar{y}) = 2^m \varphi(2^m \bar{x} - i)\varphi(2^m \bar{y} - j)$; $\dot{\mathbf{A}}$ is a vector of dimension $(2^m + L - 2) \times 1$ containing the time derivatives of $a_{ij}(t)$. Subsequently, the radiated sound power in the near field writes [118]

$$W_{rad} = \mathbf{V}^H \mathbf{R} \mathbf{V} = \dot{\mathbf{A}}^H (\Phi^H \mathbf{R} \Phi) \dot{\mathbf{A}} \quad (2.28)$$

in which the superscript H is the Hermitian transpose operator; and \mathbf{R} the radiation resistance matrix, expressed as

$$\mathbf{R} = \frac{\omega^2 \rho_0}{4\pi c_0} (\Delta S)^2 \begin{bmatrix} 1 & \frac{\sin(kr_{12})}{kr_{12}} & \dots & \frac{\sin(kr_{1n_0})}{kr_{1n_0}} \\ \frac{\sin(kr_{21})}{kr_{21}} & 1 & \dots & \frac{\sin(kr_{2n_0})}{kr_{2n_0}} \\ \vdots & \vdots & \ddots & \vdots \\ \frac{\sin(kr_{m_0 1})}{kr_{m_0 1}} & \frac{\sin(kr_{m_0 2})}{kr_{m_0 2}} & \dots & 1 \end{bmatrix} \quad (2.29)$$

where $\Delta S = S/N$ is the area of each elementary radiator on the plate; $m_0 = 1, 2, \dots, N$ and $n_0 = 1, 2, \dots, N$.

Upon obtaining the velocity \mathbf{V} in Equation (2.27) and the sound power W_{rad} in Equation (2.28), the sound radiation efficiency can also be calculated as [119]

$$\sigma = \frac{W_{rad}}{\rho_0 c_0 S \langle |\mathbf{V}|^2 \rangle} \quad (2.30)$$

where $\langle |\mathbf{V}|^2 \rangle$ represents the spatially averaged mean square velocity over the plate of a total area S . This definition applies to the entire plate, part of the plate or one particular structural mode. In the latter case, the terminology of modal radiation efficiency will be used.

To obtain the vibration velocity in Equation (2.27) and the sound power in Equation (2.28), \mathbf{A} should be calculated through Equation (2.7) in which M and K involves the calculation of the 2D connection coefficients that are the finite integrals of DWs and their derivatives.

2.3 Summary

A 2D semi-analytical wavelet plate model embedded with strip/circular indentations in the framework of the Rayleigh-Ritz method is proposed in this chapter. Calculations of connection coefficients that constitute the matrices of stiffness and mass

are described in detail. Theoretical modelling of vibration field in terms of eigen-frequencies, mode shapes, modal loss factors and forced vibration response, and sound radiation field in terms of radiated sound power (both in the far field and near field) and sound radiation efficiency are presented. Based on the proposed model, the vibration and sound radiation fields predicted by the proposed model will be fully validated in the following chapter.

Chapter 3

Model validations

3.1 Introduction

This Chapter validates the vibration and sound radiation model developed in [Chapter 2](#), through comparisons with FEM and experimental results. Emphasis is put on the latter through meticulous design, fabrication and experimental testing using an ABH plate. In a broader sense, comparisons with experimental results, in views of model validations, are scarce in the literature. Among a few existing examples, one can cite O'Boy *et al.* [\[54\]](#) who investigated the damping and mobility of a rectangular plate containing a wedge of power-law profile using a bending plate model. However, positions of resonant peaks showed significant differences with the results obtained from experiments. Experimental investigations into vibration characteristics of ABH plates have also been carried out in Refs. [\[13, 79\]](#). As opposed to vibration analyses, explorations into sound radiation properties of ABHs are scarce. Bowyer and Krylov [\[85\]](#) firstly experimentally investigated the sound radiation properties of rectangular plates containing multiple circular indentations. While demonstrating some typical ABH phenomena and their vibration and acoustic benefits, it is observed that the experimental setup may cause some errors at low frequencies because of acoustic short circuiting resulting from the free edges of the plate due to the absence of the acoustic baffle.

Simulation models are of vital importance for carrying out ABH design, analyses and optimization. However, there is still a lack of well-calibrated experimental benchmark solutions for their validations. This is probably due to the challenging task of manufacturing high-precision ABH indentations. In fact, as demonstrated by Bowyer *et al.* [77, 84], ABH effects depend on geometrical details. Although effective damping of ABH structures can still be obtained with the existence of imperfect geometrical and material parameters, albeit being reduced, such a variability can be a serious issue from the viewpoint of model validations. Therefore, it is imperative to establish well-controlled benchmark solutions, which motivates the present work.

This chapter primarily focuses on the full validations of the proposed 2D semi-analytical model. First, vibration characterizations of a rectangular plate embedded with a 1D ABH indentation (strip indentation) is validated against FE simulations. Furthermore, a rectangular plate embedded with a symmetric circular ABH indentation was meticulously manufactured using the Computer Numerical Control (CNC) milling. Structural properties of the manufactured sample, such as eigen-frequencies, mode shapes, forced vibration response and sound radiation into a baffled half-space were experimentally measured and compared with the predictions by a previously developed Daubechies wavelet (DW) model. The objective of this chapter is twofold: validating the previously developed model in [Chapter 2](#) along with the experimental assertion of

the revealed phenomena; and offering a useful set of experimental benchmark solutions for future ABH studies.

The rest of this chapter is structured as follows. In [Section 3.2](#), numerical analyses on the first one hundred eigen-frequencies of the plate with free edges are carried out using different support lengths L and resolutions m . In this regard, the suitable support length L and resolution m are determined for follow-up analyses of ABH plates in this thesis. Modal analyses and forced vibration analyses are then conducted in comparisons with the FEM simulations. [Section 3.4.1](#) gives a description of the high-precision ABH manufacturing process. In [Section 3.4.2](#), experimental setup used for vibration and sound radiation tests are introduced, followed by a brief description of the sound power measurement procedure [120]. Comparisons between the experimental results and DW model predictions are then conducted in [Section 3.4.3](#), in terms of eigen-frequencies of the first 120 modes, mode shapes, forced vibration response and radiated sound power. Finally, [Section 3.5](#) briefly summarizes this chapter.

3.2 Vibration validations by FE simulations

3.2.1 Determination of DW parameters and vibration validations

Using a rectangular plate embodied with a strip indentation (see [Figure 2.1](#)), the accuracy of the proposed model is first verified through comparisons with the FE simulations. Wavelet parameters are varied in order to determine a suitable combination to be used in the subsequent analyses for the maximum calculation efficiency and the

required accuracy. To this end, the eigen-frequencies of a typical ABH plate are calculated using different L and m values. Geometrical and material parameters of the plate as well as those of the strip ABH indentation are tabulated in [Table 3.1](#). The four edges of the plate are set to be free, by assigning a zero-stiffness value to all the boundary springs. The FE model using COMSOL software is densely meshed with an element size of 0.005 m to ensure the convergence of the solution. This gives a total of 12544 plate elements.

Table 3.1 Geometrical and material parameters of a plate embedded with a trip indentation

Geometry		Material
$a=0.56$ m	$y_1=0.056$ m	$E_0=200$ GPa
$b=0.56$ m	$y_2=0.504$ m	$\mu_0=0.3$
$h=6.4$ mm	$h_0=0.4$ mm	$\eta_0=0.01$
$x_1=0.16$ m	$\varepsilon=0.25$	$\rho_0=7800$ kg/m ³
$x_2=0.4$ m	$\gamma=2$	
$x_c=0.28$ m	$\delta_0=0.04$ m	
$y_c=0.28$ m		

Note that [Equation \(2.11\)](#) involves the derivative terms of the DWs up to an order of $L/2 - 1$. Therefore, L should be at least equal to or larger than 10 [\[111\]](#). Firstly, with

L fixed at 12, the influences of m are analyzed. Three typical m values, 6, 7 and 8, are used in the calculation which gives a total of 5476, 19044 and 70756 wavelet terms, respectively. The calculated eigen-frequencies of the first 100 modes are compared with those obtained by FEM in [Figure 3.1](#). It can be seen that results with $m = 7$ and 8 agree well with FEM results within the entire mode range, while more noticeable deviations in the higher-order modes appear when $m = 6$. To quantify the calculation accuracy, the relative error, defined as $|f_{model} - f_{FEM}| / f_{FEM} \times 100\%$, are calculated and shown in [Figure 3.2](#). Results confirm the same trend as the one observed in [Figure 3.1](#). Typically, $m = 7$ or 8 with $L = 12$ allows limiting the error below 3% for a large majority of modes. Clearly, a larger m (e.g. $m=8$) leads to a better accuracy for higher order modes, except for the first few modes. Similar phenomenon was also observed in a previous study using MH wavelets in 1D cases [\[46\]](#), which can be explained by the scaling properties of the wavelets. This suggests that a larger m is preferable for higher order mode prediction, which is the main frequency range of interest where systematic ABH effect is expected. Fixing m at 7 and varying L , the calculation errors against FEM results are given in [Figure 3.3](#). As can be seen, the three cases give very similar accuracy, except for the very low-order modes.

Apart from the accuracy, it is also relevant to consider the computation time which is mainly determined by the scaling factor m . For example, for a fixed L , the computation time for $m=8$ is four times that of $m=7$. Therefore, based on the above analyses, a calculation scheme using $L=12$ and $m=7$ is taken as a good compromise,

from both the accuracy and the computation time perspectives. This will be used in the subsequent analyses.

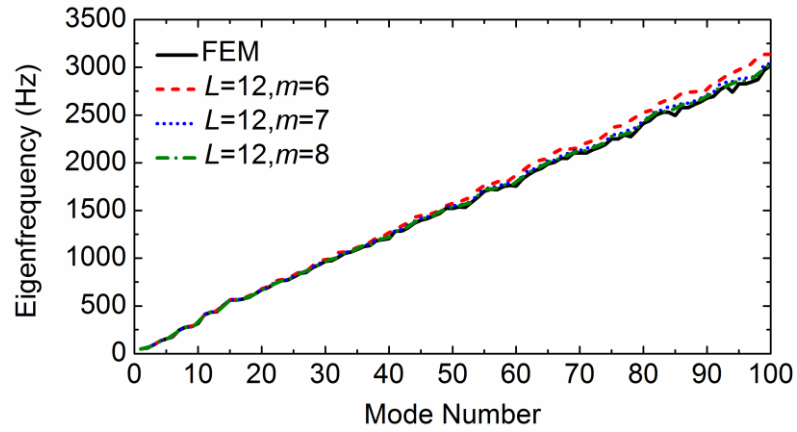


Figure 3.1 Comparisons with FEM analyses for the first 100 eigen-frequencies:
 FEM (solid line); $L=12, m=6$ (short dash line); $L=12, m=7$ (short dot line); $L=12, m=8$
 (short dash dot line).

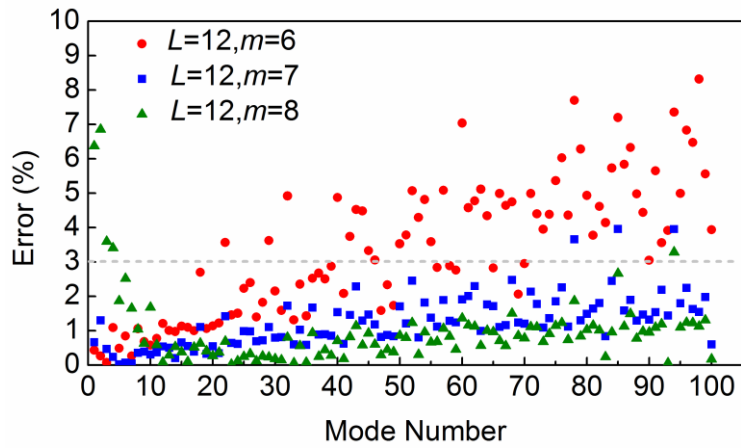


Figure 3.2 Percent errors for the first 100 eigen-frequencies obtained by the present model with $L=12$: $m=6$ (circle dot); $m=7$ (square dot) and $m=8$ (triangle dot).

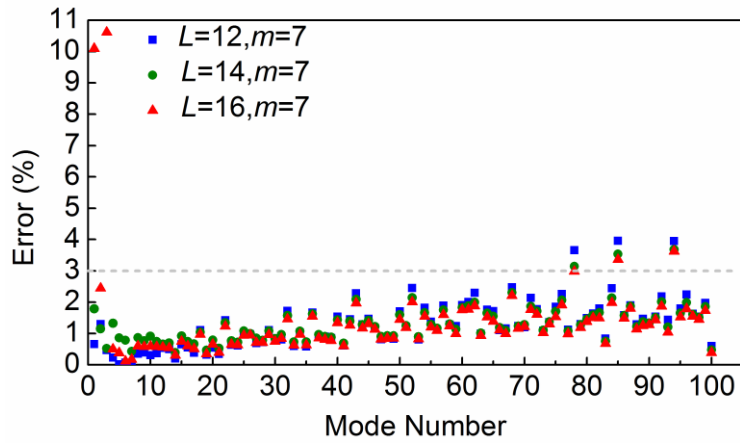
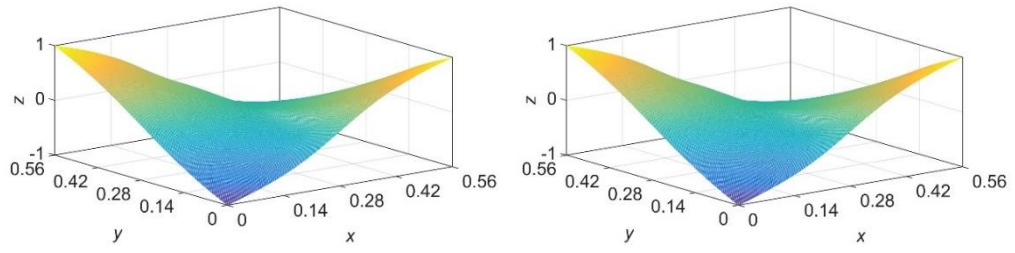
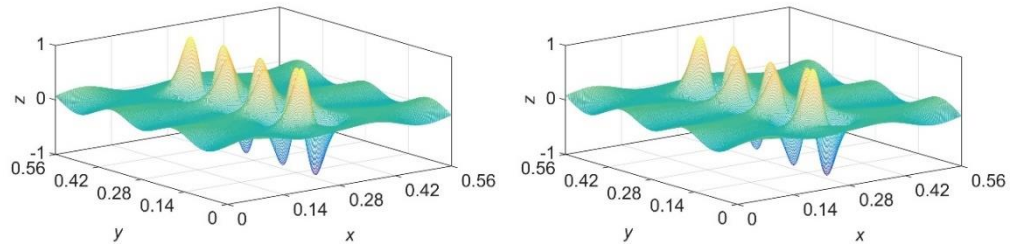


Figure 3.3 Percent errors for the first 100 eigen-frequencies obtained by the present model with $m=7$: $L=12$ (square dot); $L=14$ (circle dot) and $L=16$ (triangle dot).

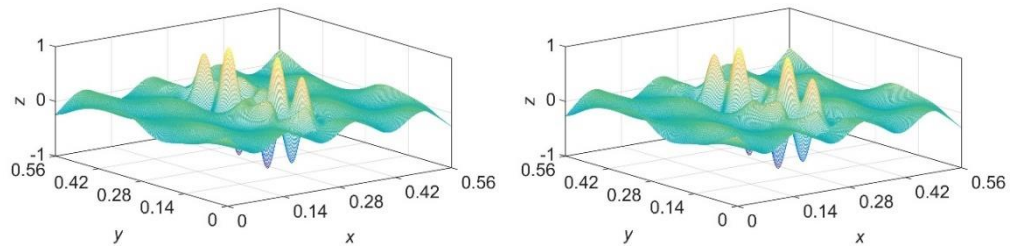
Figure 3.4 compares four arbitrarily chosen mode shapes, *i.e.*, the 1st, 50th, 79th and 98th modes, obtained by the present model and the FEM. It can be seen that, the proposed model allows a fine description of the vibrational details, including the local deformation within the ABH indentation area. Both sets of results seem to agree well, further confirming the remarkable ability of the proposed model in describing ABH-specific features even for higher-order modes.



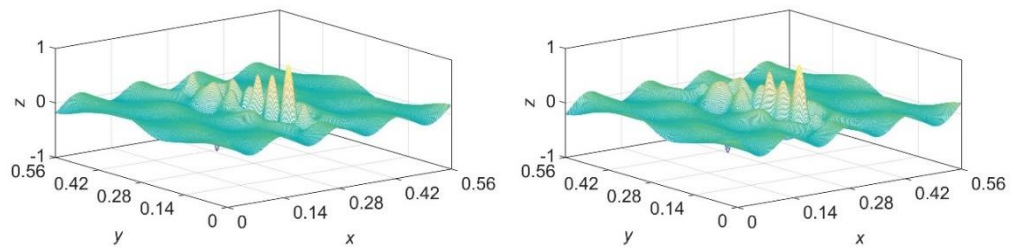
(a)



(b)



(c)



(d)

Figure 3.4 Mode shape comparisons: present model (left); FEM (right). (a) 1st mode; (b) 50th mode; (c) 79th mode; (d) 98th mode.

A forced vibration analysis is further carried out. A unit harmonic excitation force is applied at point $(\bar{x}_f, \bar{y}_f) = (1/7, 1/2)$ on the uniform portion of the plate. The mean square velocities, spatially averaged over the ABH portion and the uniform portion of the plate, respectively, are calculated and compared with the FEM results in Figure 3.5. It can be seen that, with the L and m combination suggested above, results calculated by the present model are in good agreement with those from the FEM analysis.

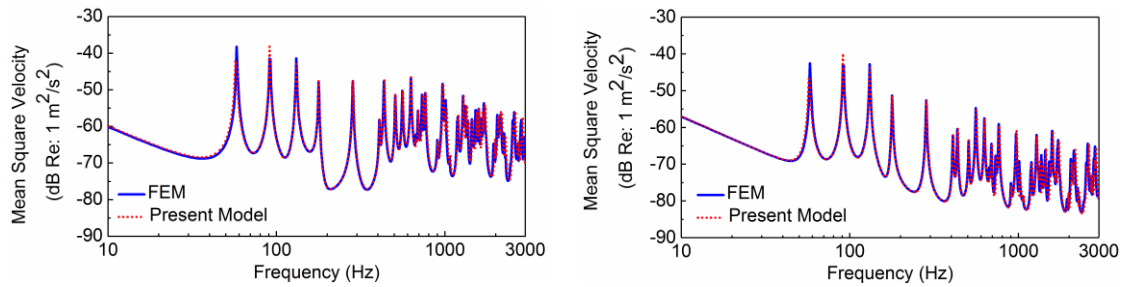


Figure 3.5 Mean square velocity: ABH portion (left); uniform portion (right).

To sum up, above comparisons show that the proposed model provides results which are consistent with FEM results, in terms of both modal characteristics and forced vibration responses. Most importantly, the model allows reaching the effective high frequency range, relevant to the ABH investigations. In fact, the frequency range outreach of the method well exceeds the conventionally reachable range using Rayleigh-Ritz models reported in the literature, demonstrating the attractiveness of the Daubechies scaling functions as a global basis.

3.3 Sound field Verifications by analytical solutions

As bending waves travel towards the center of the ABH indentation, structural wavelength gradually decreases. As demonstrated in the previous vibration study, a large number of decomposition terms are needed in Equation (2.2) to achieve an accurate description of vibration field in order to correctly capture the local structural details. For sound radiation analyses, acoustic waves should be further considered to determine various DW parameters to be used, especially above the critical frequency,

$$f_{critical} = \frac{c_a^2}{2\pi} \sqrt{\frac{12\rho_0(1-\mu_0^2)}{E_0h^2}},$$

where acoustic wavelength becomes smaller than their structural counterparts. A careful convergence study, though not detailed here, has been carried out to ensure the convergence of the solution. Specifically, the larger support length L and resolution m are, the more accurate the simulated vibration and sound field will be. However, more terms make the calculation cost ineffective. Finally, we still chose $m=7$ and $L=12$ for the subsequent analysis, in terms of convergence and computation time, this results in a total of 19044 terms to be used in the DWs.

The proposed calculation scheme on sound radiation detailed in Chapter 2 is validated against the benchmark solutions on a simply supported plate in terms of radiated sound power and the modal radiation efficiencies of lower-order modes. The values of ε and γ are adjusted (0.0045 and 0 respectively) so that the ABH plate degenerates into a flat plate which is 0.5 m in length, 0.45 m in width, and 4.7 mm in thickness. A unit harmonic excitation force is applied at (0.05, 0.315) m.

Using far field approach, Equation (2.25), the sound power is calculated with 5565 integration points uniformly distributed on a hemisphere with a radius of 10 m. Meanwhile, the radiated sound power is also calculated in the near field using Equation (2.28). The plate is divided into 50000 elementary radiators to make sure the sound field can be accurately estimated. Calculated sound power using the two different methods are compared with the analytical solutions in Figure 3.6. It can be seen that the DW sound radiation model yields consistent estimation of the radiated sound power with analytical solutions. In the entire frequency range up to 3000 Hz, using either the far field or the near field methods.

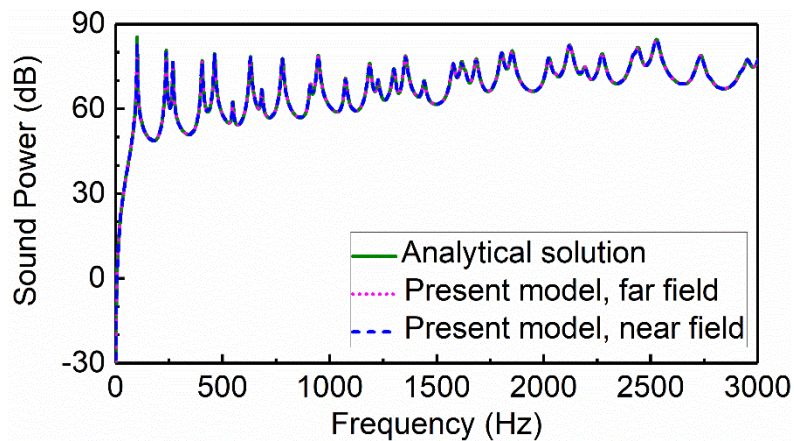


Figure 3.6 Radiated sound power obtained by the present theoretical model and analytical solution.

Furthermore, modal radiation efficiencies of six low-order modes of the abovementioned flat plate are also calculated. Plate parameters remain the same except that the width b is changed to 0.5 m to form a square plate, to allow a comparison with

the classical results obtained by Wallace [119]. The sound radiation efficiency for each structural mode, as a function of frequency, is expressed in terms of the acoustic wavenumber k normalized by the structural wavenumber k_b , calculated by

$$k_b = \sqrt{(p_0\pi/a)^2 + (q_0\pi/b)^2} \quad (3.1)$$

in which p_0 and q_0 represents the number of half waves. Modal radiation efficiencies of the six low-order modes of the plate are plotted as a function of k/k_b in Figure 3.7. Once again, a good agreement can be observed not only between the two calculation methods, but also with the standard solutions [119]. This further confirms the calculation accuracy of the proposed wavelet-based sound radiation model.

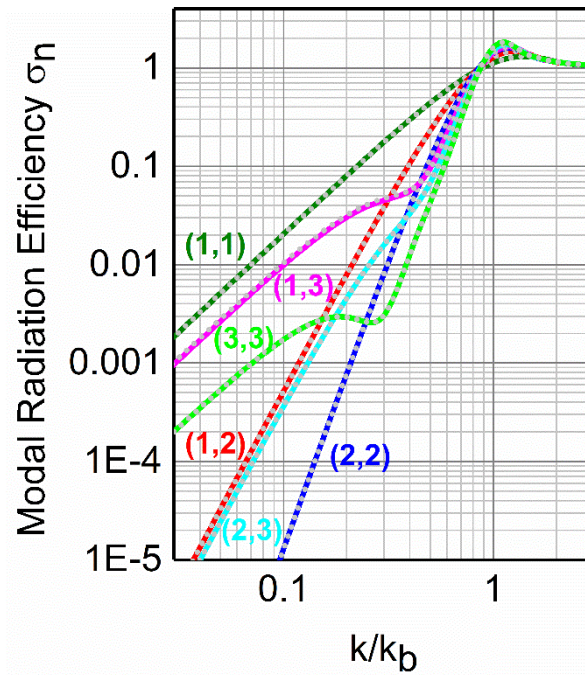


Figure 3.7 Radiation efficiencies of the first six low-order modes: present model (solid line); analytical solution (dash line).

It can be concluded that the extended 2D wavelet model can accurately predict the sound radiation field of a planar structure. For the subsequent sound radiation analyses on ABH plates, the calculation procedure will remain the same and will be validated experimentally.

3.4 Experimental validations

In this section, a rectangular plate embedded with a circular ABH indentation (see [Figure 2.2](#)) is manufactured. The successful manufacturing procedure and method are presented. The vibration field and sound radiation field predicted by the proposed model will be fully validated through experiments.

3.4.1 Manufacturing of ABH test sample

Manufacturing procedure for an ABH plate sample and the parameters that control the manufacturing process are reported as follows. To quantify the deviation of the manufactured thickness profile from its predesigned standard, the thickness at multiple points over the manufactured profile is measured using the Coordinate Measuring Machine (CMM).

The designed geometrical parameters of the test sample are shown in [Table 3.2](#). Material parameters of ABH sample and those of the damping layer (3MTM VHBTM adhesive transfer tape F9473PC) are tabulated in [Table 3.3](#). The damping material used in the tests are produced by 3M Company.

Table 3.2 Geometrical parameters of the experimental sample of an ABH plate

$a=0.6$ m	$x_c=0.3$ m	$\varepsilon=0.24/m$
$b=0.5$ m	$y_c=0.25$ m	$\gamma=2$
$h=6$ mm	$h_0=0.6$ mm	$R_{ABH}=0.15$ m

Table 3.3 Material parameters of experimental ABH sample and the damping layers

	Density	Elastic modulus	Loss factor	Poisson's ratio
ABH plate	$\rho_0=2800$ kg/m ³	$E_0=71$ GPa	$\eta_0=0.002$	$\nu_0=0.33$
F9473PC	$\rho_d=980$ kg/m ³	$E_d=30$ MPa	$\eta_d=0.9$	$\nu_d=0.499$

3.4.1.1 Manufacturing method

Manufacturing metallic structures with thin thickness is technically challenging, especially for an ABH plate that incorporates an indentation of power-law profile. The minimum thickness that can be reached in commonly used manufacturing techniques such as CNC milling and 3D printing is around 0.5 mm. In the present case, the targeted minimum thickness at the center of the indentation is chosen to be 0.6 mm. Meanwhile, the radius of the ABH indentation is relatively large, *i.e.*, 0.15 m. All in all, two main concerns arise. First, suffering from the mechanical stress from the milling cutter, the thin area of the ABH indentation is susceptible to tearing. Second, the resulting high-

temperature stress may deform the thin indentation area, thus compromising the accuracy of the thickness profile. Therefore, materials of the test sample and the milling cutter should be carefully selected. In the present case, top-grade aluminum 7075 which is widely used in aerospace industry is chosen. Aluminum 7075 has good machinability with high strength resistance to mechanical stress. Also, the sufficiently tough tungsten cutter with a ball end is a preferable choice for milling. The parameters that determine the manufacturing process should also be meticulously controlled. The rotation speed of the cutter is expected to be high, up to 10000 rpm. Also, the cutting volume and the cutting step of the milling cutter should be small, which are 0.5 mm and 0.15 mm, respectively.

The manufacturing procedure mainly consists of four steps. Firstly, a flat plate which has the same size as the test sample was machined out from an aluminum block and the burs were removed, with the flatness error of the surface on both sides controlled within an acceptable level, *e.g.* 0.05 mm for the present case. Secondly, the milling cutter produced the ABH indentation following a circular path around the center of the indentation, from outside to inside. Meanwhile, cooling liquid was used to alleviate the induced high-temperature stress. Finally, after completing the indentation on the top side of the plate, the sample was set aside for stress release for several days. Prior to manufacturing the symmetric indentation on the other bottom side, the finished indentation on the top side was fully filled with plaster to alleviate possible flapping of the cutter. Note the flapping effect frequently occurs when machining thin metals during

CNC milling, which can even lead to the tearing of the structure if not properly refrained. Meanwhile, sufficient machining allowance should be considered in each manufacturing step. Following the procedure described above, the symmetric indentation was successfully produced using a three-axis CNC milling machine (type VSC-1470).

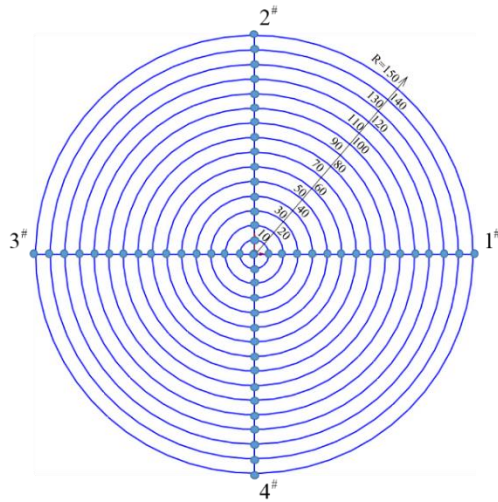
3.4.1.2 Measurement of the manufactured ABH profile

The manufactured test sample contains inevitable geometrical imperfections because of machining precision. Therefore, the deviation of the manufactured indentation from its predesigned profile is checked through measurement.

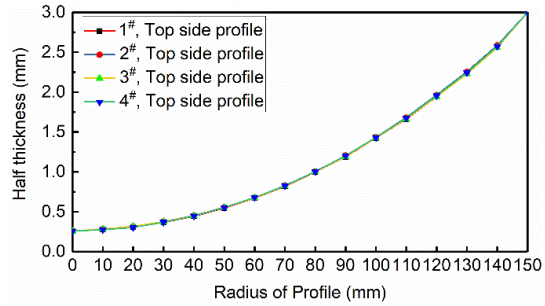
For illustration purposes, the half thickness, defined as the distance from a point at the surface of the indentation to the mid-plane of the test sample, is used to evaluate the error of the manufactured profile. On the top side, 31 measurement points (including the ABH center point) are uniformly distributed along two perpendicular lines intersecting at the ABH center, as shown in [Figure 3.8\(a\)](#). The thickness profile variations along these two perpendicular lines, for a total of four profiles (numbered 1[#], 2[#], 3[#], and 4[#]), were examined and deviations of them from the predesigned profile were assessed. The projection of these profiles and the points onto the mid-plane is shown in [Figure 3.8\(a\)](#). Half thickness profile of these 31 points was measured using CMM. Similar measurement was also carried out for the bottom side of the plate. The half

thickness variations obtained for both sides are respectively shown in [Figure 3.8\(b\)](#) and [Figure 3.8\(c\)](#), in comparison with that of the predesigned standard profile.

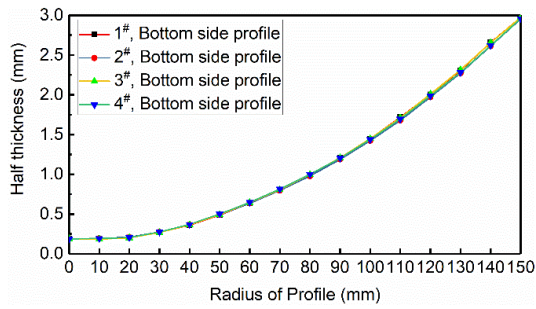
As can be seen from [Figure 3.8\(b\)](#), for the top side, the half thickness for points at the four measured profiles are very similar. This similarity can also be observed for the bottom side. Furthermore, the half thicknesses at four points located at the same circle are averaged, both for the top side and bottom side, and compared with their predesigned counterpart in [Figure 3.8\(d\)](#). It seems that, the half thickness on the top side shows a nice agreement with that of the predesigned profile, while a marginal deviation is observed for the bottom side, particularly at the central part (within a radius of 50 mm) of the indentation. However, this slight deviation is deemed to be acceptable, as will be further demonstrated by the agreement of vibration response between experimental tests and numerical simulations in [Section 3.4.3](#).



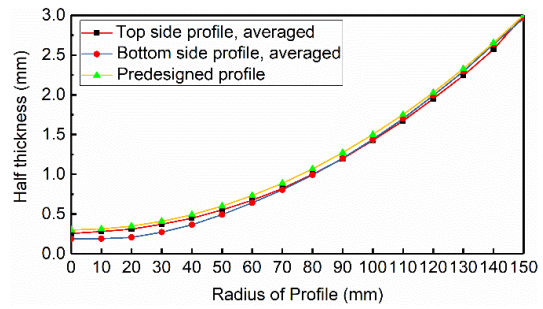
(a)



(b)



(c)



(d)

Figure 3.8 Half thickness profile: (a) measuring points; (b) top side; (c) bottom side; (d) averaged manufactured profile and predesigned profile.

3.4.2 Experimental setup

The vibrational properties of the manufactured sample and its radiated sound field were measured, inside a test room and a fully anechoic room, respectively. This section reports the experimental setup used for both tests.

3.4.2.1 Measurement of vibration characteristics

The test sample was vertically suspended onto a rigid frame using two flexible strings that introduce little damping, allowing for the vibration testing of the sample under free boundary conditions. The two strings pass through small holes (with a diameter of 4 mm) near the corner of the sample, as shown in [Figure 3.9\(a\)](#). The strings maintain adequate strength to support the weight of the sample plate (about 4.8 kilogram). The plate was excited by electromagnetic shaker (type 4809) through a small thin rod/stinger to filter out possible moment excitation. A force transducer (B&K 8200) was fastened to the end of the stinger to measure the input force. To reduce possible mass loading effect, adhesive glue was used to connect the force transducer to the test sample, as shown in [Figure 3.9\(b\)](#). The electromagnetic shaker was fed by a power amplifier (B&K 2706) with the periodic chirp signal. The input signal was converted to voltage signal via a charge amplifier (B&K 2635). A Polytec scanning laser vibrometer (PSV) 400 was used for signal generation and data acquisition. The vibration response signals were averaged over ten measurements to guarantee statistically representative results.

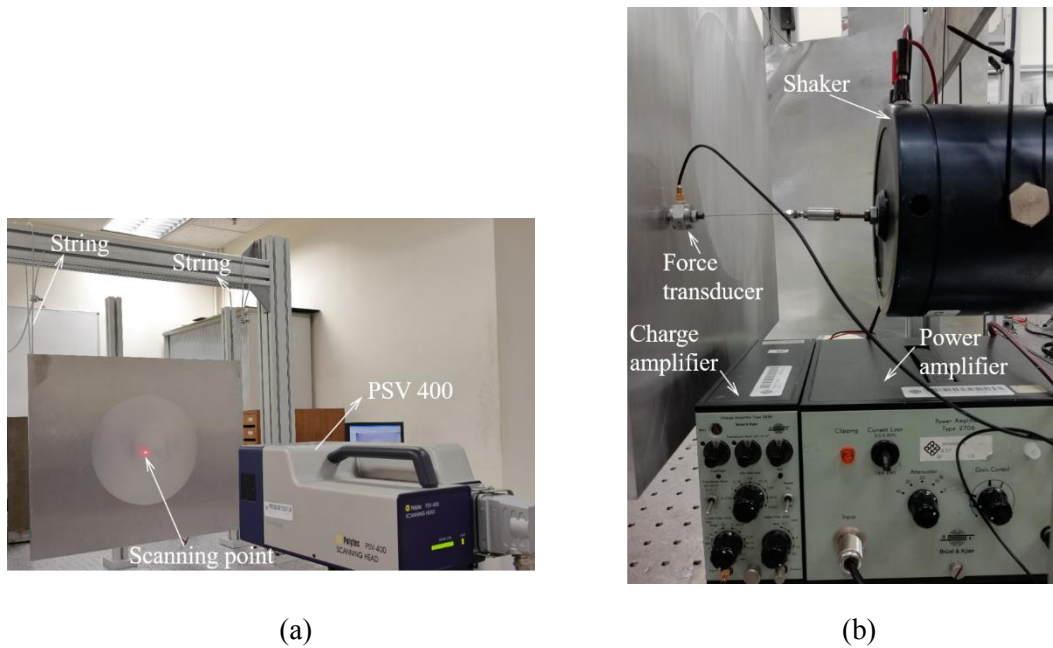


Figure 3.9 Experimental setup: (a) ABH test sample; (b) excitation with electromagnetic shaker and force transducer.

3.4.2.2 Measurement of the radiated sound power

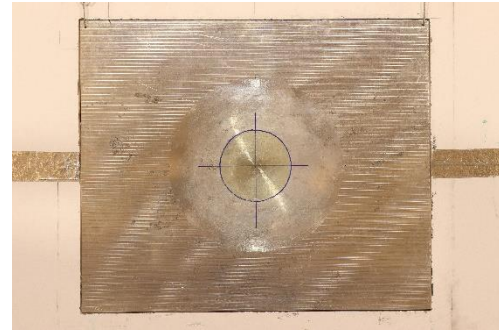
The measurement of the radiated sound power was carried out in a fully anechoic chamber with an inner dimension $6 \times 6 \times 3$ m. Walls of the chamber are covered with acoustic absorbing material (fiberglass) to meet the free field condition. The cut-off frequency of the chamber is roughly 90 Hz. A B&K Pulse system was utilized for signal generation and data acquisition instead of PSV 400, while other equipment remaining the same as for the vibration test. Thick large wooden panels (8 long \times 8 ft wide \times 0.75 inch thick) were used to surround the test sample and form a rigid acoustic baffle. Four smaller wooden panels, 4 ft long \times 4 ft wide \times 0.75 inch thick, were annexed to the four edges of the baffle to constitute a folded wall (see [Figure 3.10\(a\)](#)), which

allows for a larger effective sound wave blockage area. The test plate, flush-mounted with the surface of the baffle, was installed in the middle of the baffle, as shown in [Figure 3.10\(b\)](#). The gap between the wooden panel and the test sample was around 1 mm to avoid additional damping to the test sample caused by friction. The electromagnetic shaker was sealed inside a thick-walled box made of Polymethyl methacrylate to minimize its direct sound generation. The linearity of the system was ensured by checking the sound power outputs while doubling the input force level.

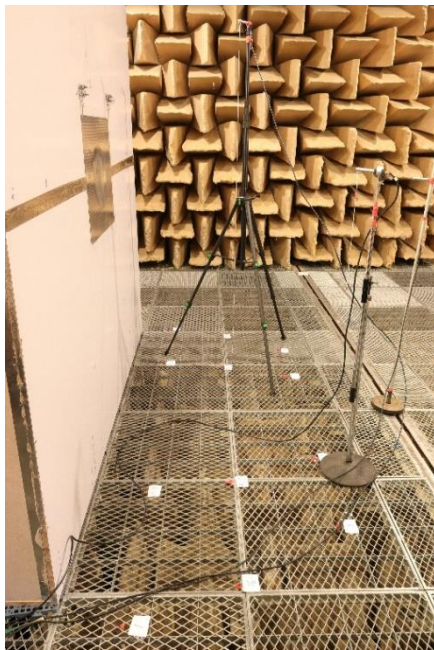
The sound power was obtained through sound pressure measurement in accordance with the international standard ISO 3744 [\[120\]](#). Twenty microphones were installed in the prescribed positions of an assumed hemispherical surface enclosing the front panel, as shown in [Figure 3.10\(d\)](#), with their projection on the floor of the chamber shown in [Figure 3.10\(c\)](#). The radius of the hemispherical surface is chosen to be larger than twice the characteristic source dimension of the test sample (1.78 m for the current case). In the current case, microphones were positioned on a hemispherical surface with a radius of 1.3 m due to the restriction of the height of the chamber.



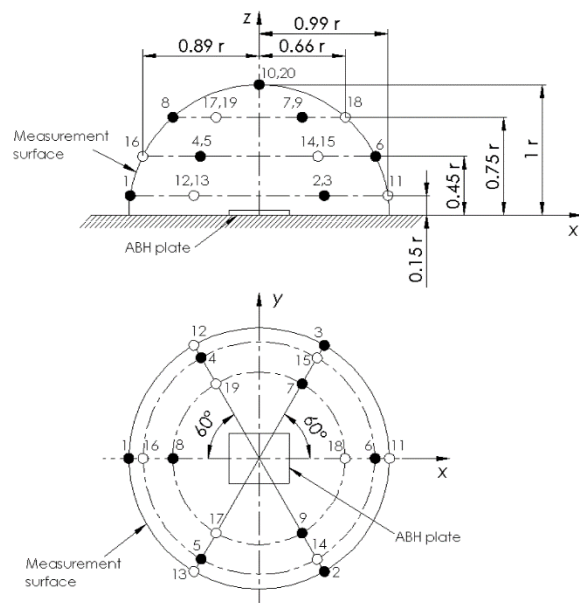
(a)



(b)



(c)



(d)

Figure 3.10 Anechoic chamber for radiated sound power tests: (a) position of the ABH test sample in relation to the rigid baffle; (b) coverage of the viscoelastic material F9473PC; (c) measuring points projected on the floor (red dot); (d) microphone positions over the hemispherical surface [120].

According to ISO 3744 [120], the pressure determined sound power can be obtained

by:

$$L_w = \bar{L}_p + 10 \lg(S/S_0) \quad (3.2)$$

in which $S = 2\pi r^2$ is the area of hemispherical surface, $S_0 = 1 \text{ m}^2$, and \bar{L}_p is the surface time-averaged sound pressure level which can be obtained by correcting the mean time-averaged sound pressure level $\bar{L}_{p(ST)}$ from background noise,

$$\bar{L}_p = \bar{L}_{p(ST)} - K_1 \quad (3.3)$$

where K_1 is the background noise correction. Assuming that the microphone positions are allocated with equal segment of areas, the mean time-averaged sound pressure level from arrays of microphones can be calculated as

$$\bar{L}_{p(ST)} = 10 \log_{10} \left(\frac{1}{N} \sum_{i=1}^N 10^{0.1 L_{pi(ST)}} \right) \quad (3.4)$$

where $L_{pi(ST)}$ is the time-averaged sound pressure level at i^{th} microphone position, and N the number of microphone positions which is 20 in the present case.

3.4.3 Experimental results

The eigen-frequencies of the first 120 modes and their corresponding mode shapes are first identified. Structural mobility and radiated sound power of the test sample subjected to a point harmonic force are then measured, for plates with/without damping materials. These results are compared against the numerically predicted ones. Additionally, reductions on structural vibration and sound power level are also observed.

3.4.3.1 Eigen-frequencies and mode shapes

Modal analyses of the manufactured ABH plate are carried out experimentally. Eigen-frequencies are identified based on the positions of resonant peaks observed from the frequency response curves measured by the laser-vibrometer. The obtained eigen-frequencies of the first 120 modes are present and compared with their numerically predicted counterparts from the DW model in Figure 3.11 showing a good agreement with each other. To quantify the agreement level, relative errors, defined as $(f_{test} - f_{model})/f_{test} \times 100\%$, are present in Figure 3.12, where f_{test} and f_{model} represent the eigen-frequency obtained from the experimental tests and the DW model, respectively. It can be seen that experimental values are slightly larger than the predicted ones due to shearing effect of the plate which is neglected in the DW model. Nevertheless, most of the errors are below 2% with the maximum one being 3.74%, which is deemed acceptable.

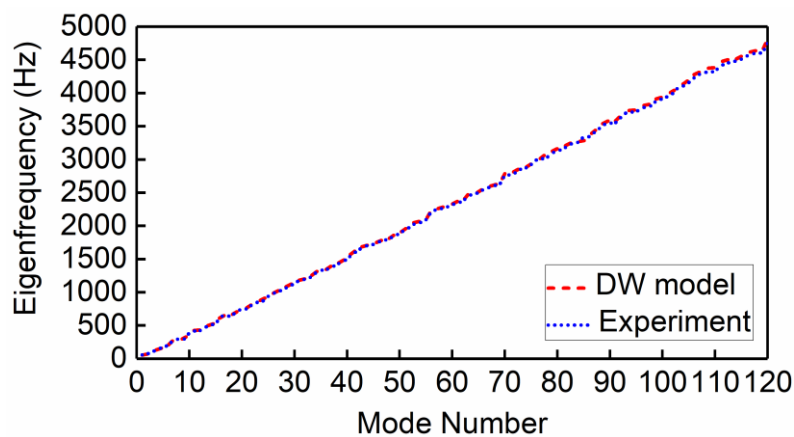


Figure 3.11 Eigen-frequencies of the first 120 modes: DW model (short dash line); experiment (short dot line).

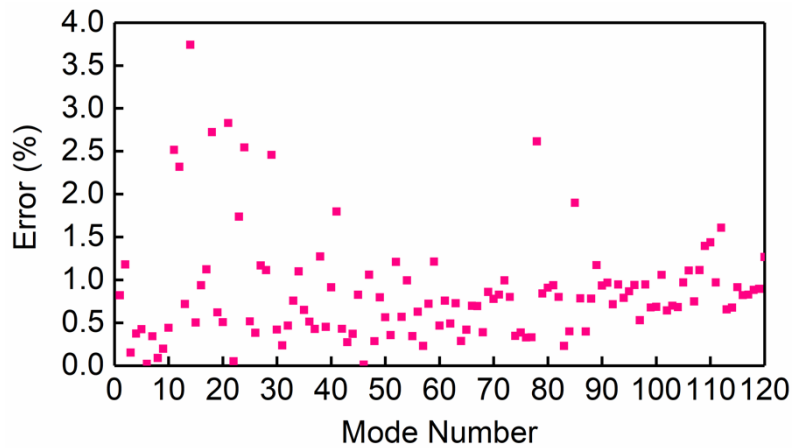


Figure 3.12 Relative errors of eigen-frequencies of the first 120 modes obtained from the DW model and experiments.

Further comparisons are performed in terms of mode shapes. Several arbitrarily chosen mode shapes (6th, 24th, 30th, 48th, 49th, 50th, 60th, 63rd, 74th, 79th, 83rd, 118th, 119th) are present in [Figures 13-25](#). To ensure a detailed comparison, different views (front view, side view, and vertical view) of these mode shapes are provided. To capture the local details inside ABH indentation, 75000 and 33233 points are respectively used to depict the mode shapes, obtained from numerical simulations and experiments. It is remarkable to see that experimentally measured mode shapes are in nearly perfect agreement with their numerically predicted counterparts, from low-order to high-order modes. Though signal to noise ratio is a bit low for high-order modes, details in deformation inside ABH indentation are clearly observable.

As previously mentioned, energy focalization is one of the unique features of ABH. This can be clearly observed from the measured vibration patterns of the high-order

modes, as shown in [Figures 13-25](#). The vibration amplitude inside ABH indentation is obviously larger than that of the uniform part of the plate, more evident around ABH center. Meanwhile, the highly compressed waves inside the indentation area can also be clearly observed.

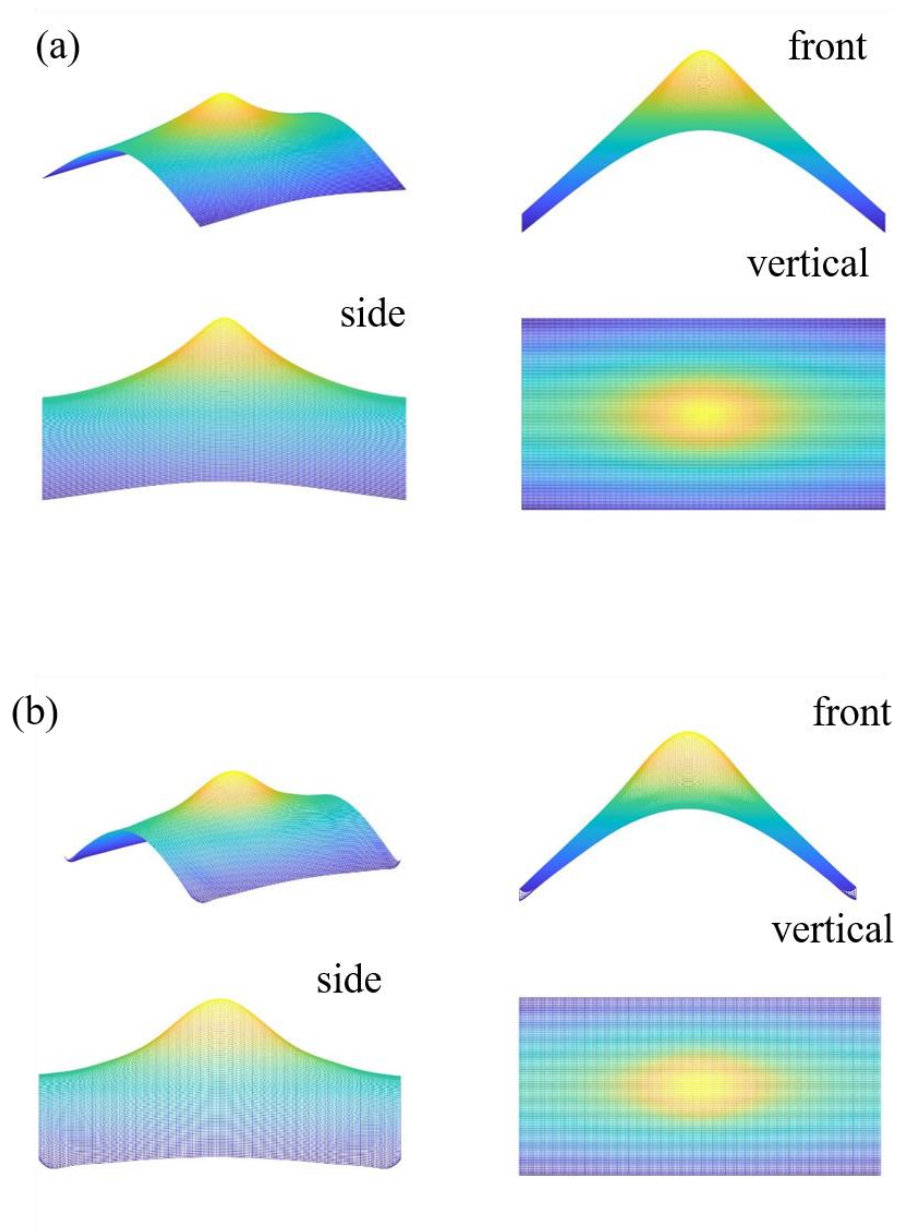


Figure 3.13 Comparison of 6th mode shape: (a) DW model (left), $f_n = 105.2$ Hz ;
 (b) experiment (right), $f_n = 105.0$ Hz .

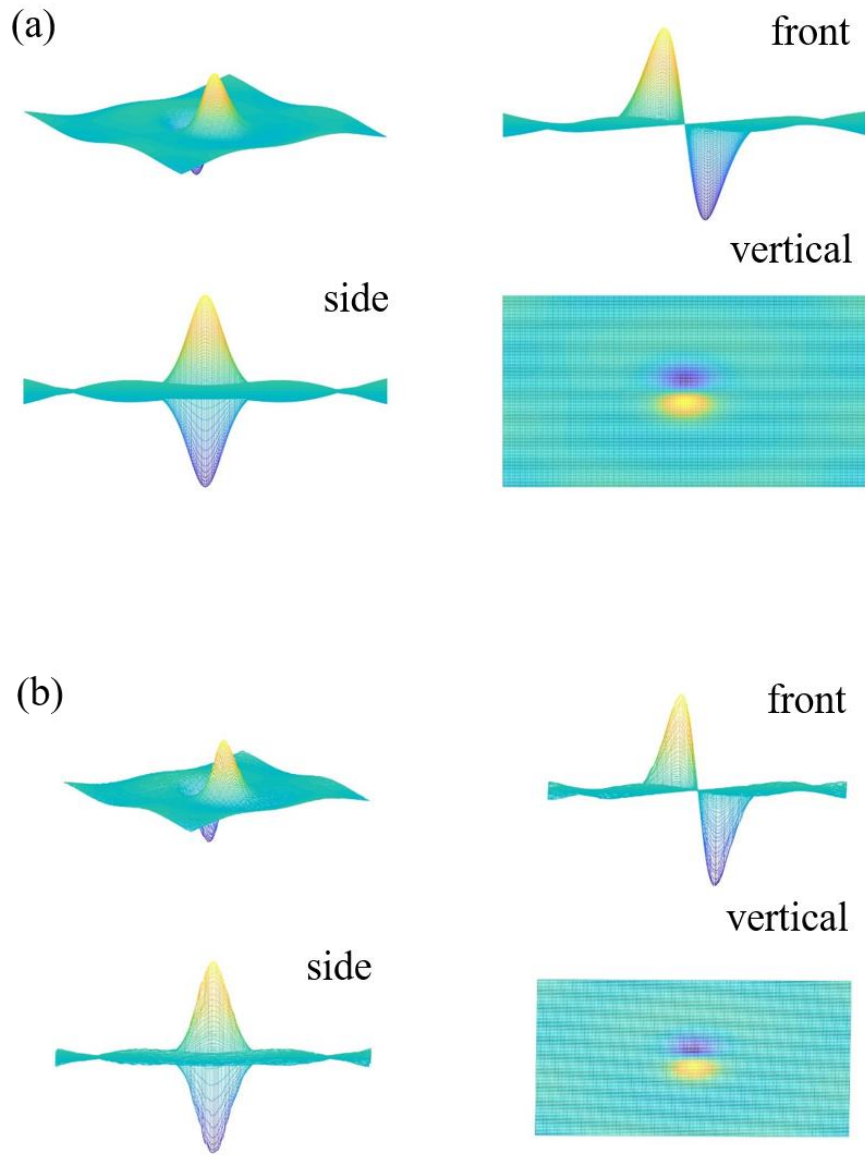


Figure 3.14 Comparison of 24th mode shape: (a) DW model (left),

$f_n = 767.7$ Hz; (b) experiment (right), $f_n = 746.6$ Hz.

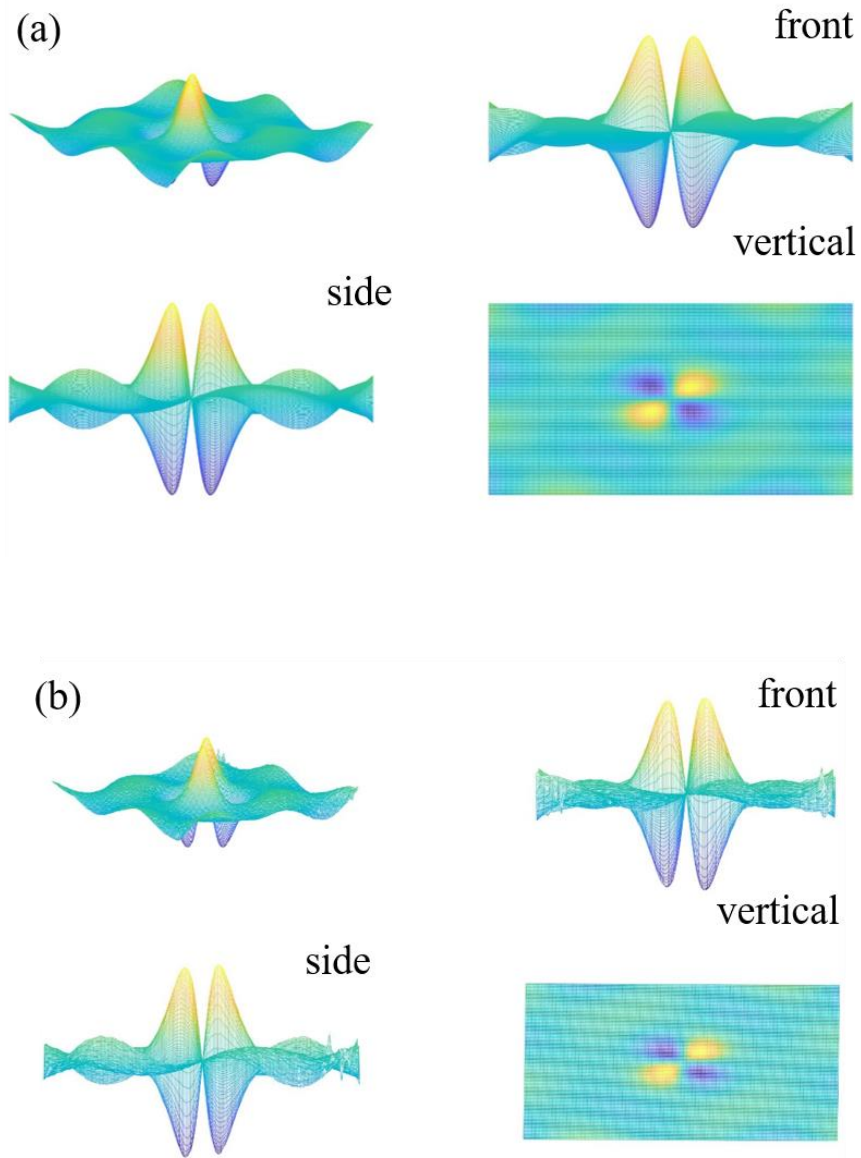


Figure 3.15 Comparison of 30th mode shape: (a) DW model (left),

$f_n = 1025.8$ Hz ; (b) experiment (right), $f_n = 1014.0$ Hz .

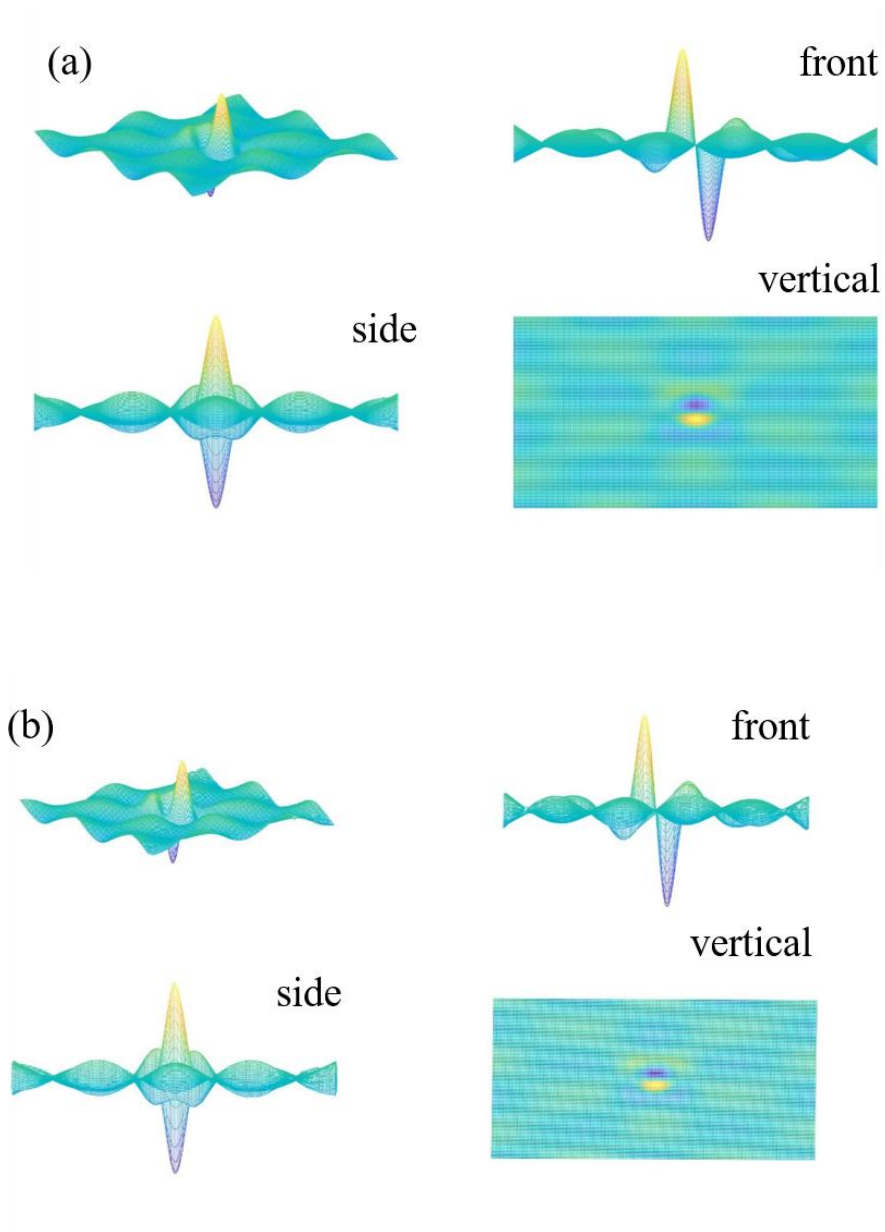


Figure 3.16 Comparison of 48th mode shape: (a) DW model (left),

$f_n = 1736.1$ Hz; (b) experiment (right), $f_n = 1721.9$ Hz.

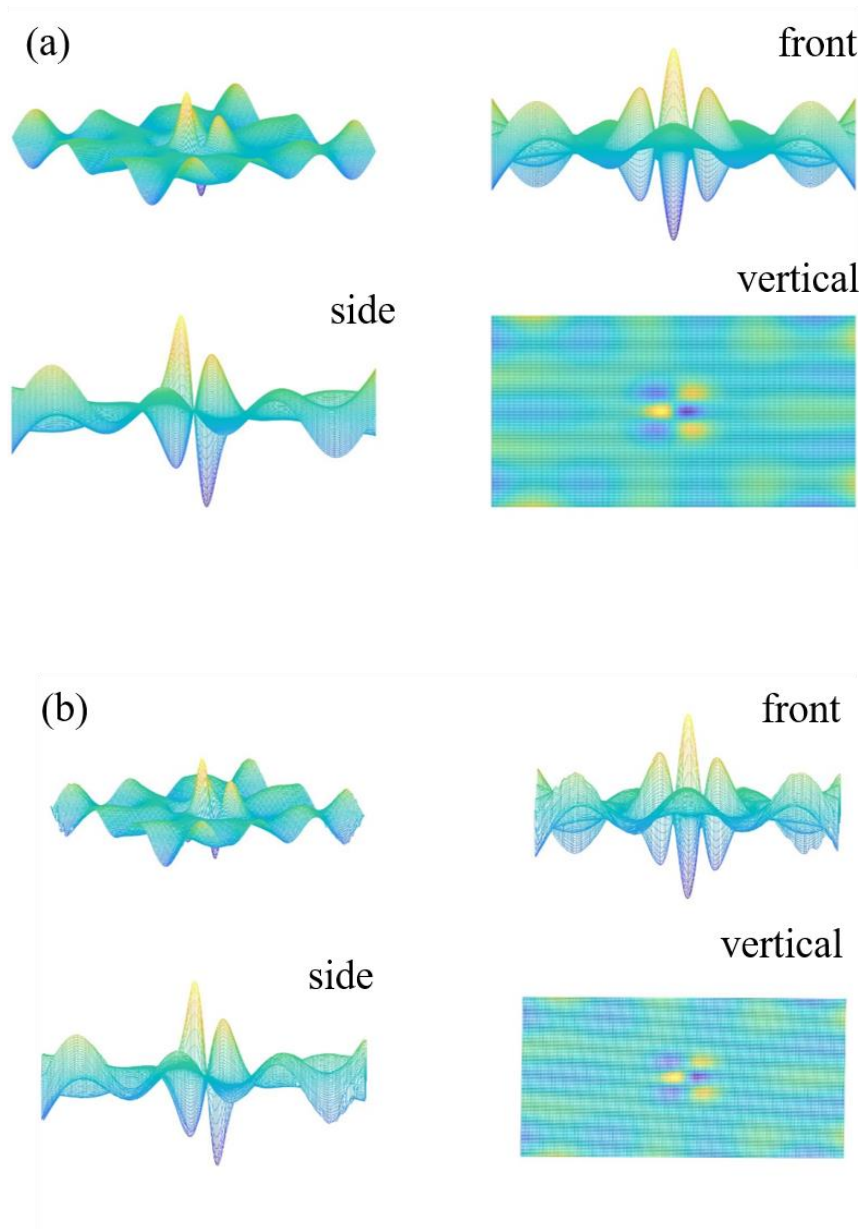


Figure 3.17 Comparison of 49th mode shape: (a) DW model (left),

$f_n = 1759.6$ Hz ; (b) experiment (right), $f_n = 1759.4$ Hz .

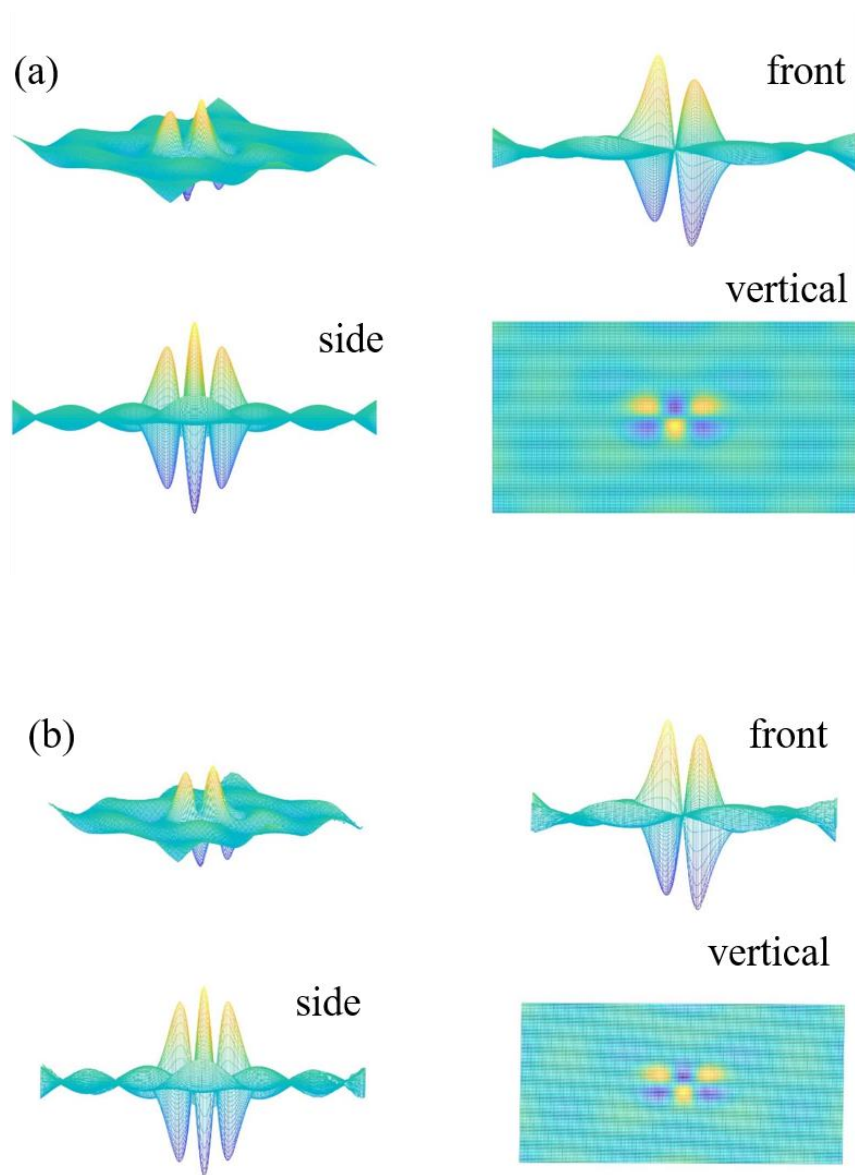


Figure 3.18 Comparison of 50th mode shape: (a) DW model (left),

$f_n = 1801.4$ Hz ; (b) experiment (right), $f_n = 1782.5$ Hz .

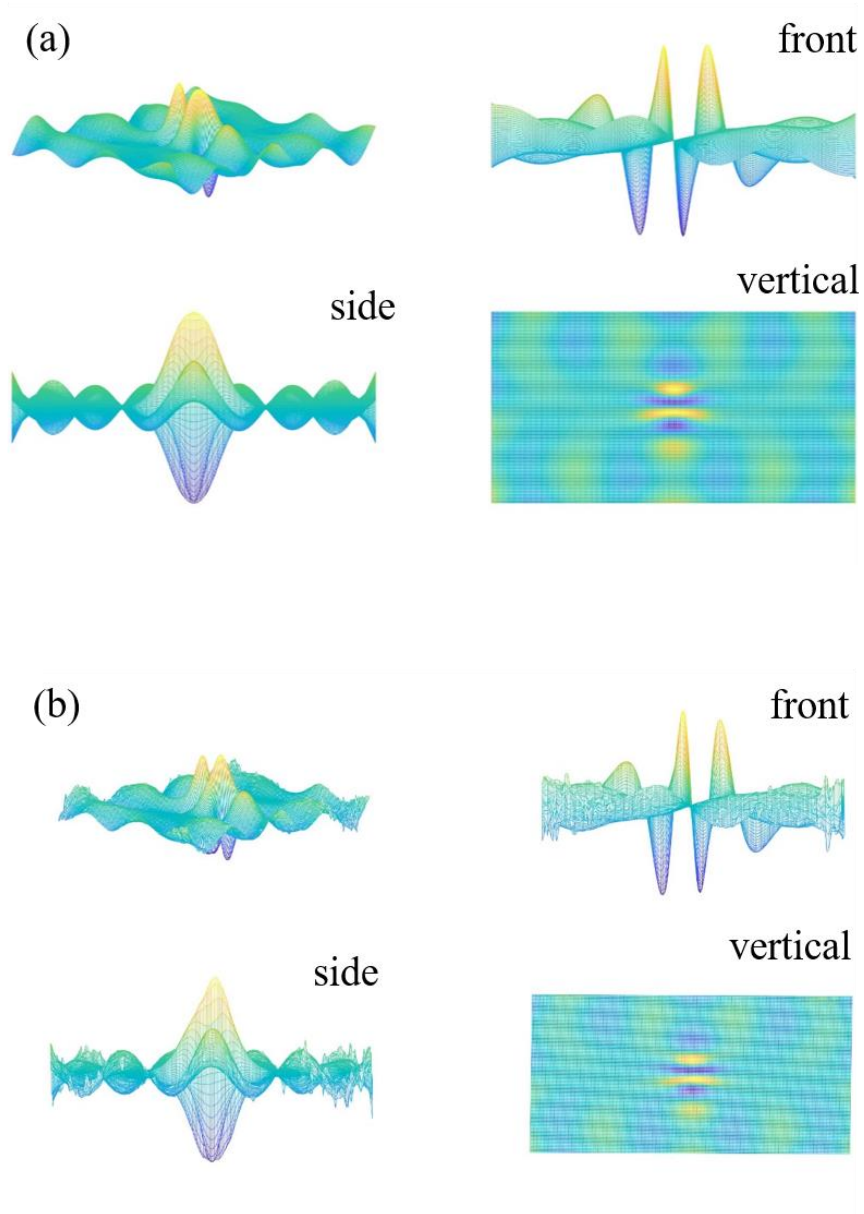


Figure 3.19 Comparison of 60th mode shape: (a) DW model (left),

$f_n = 2252.1$ Hz ; (b) experiment (right), $f_n = 2246.9$ Hz .

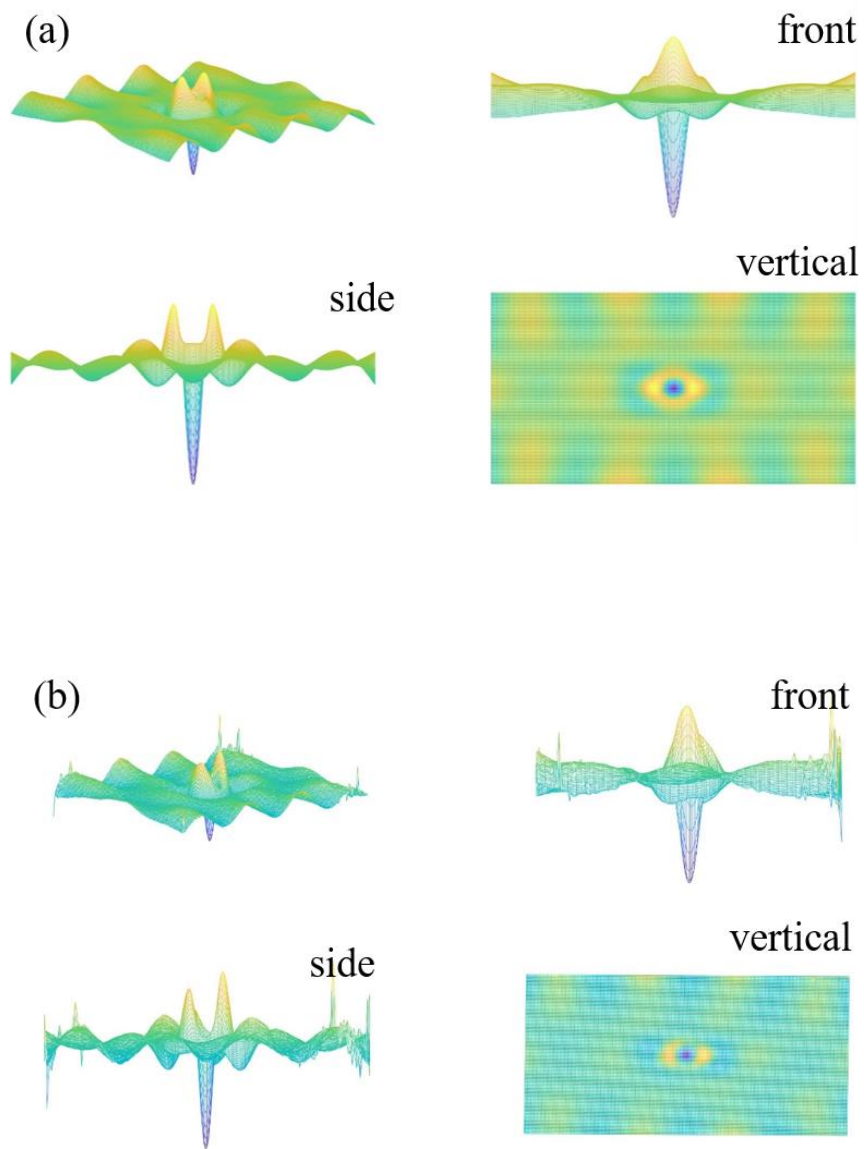


Figure 3.20 Comparison of 63rd mode shape: (a) DW model (left),

$f_n = 2329.6$ Hz; (b) experiment (right), $f_n = 2318.8$ Hz.

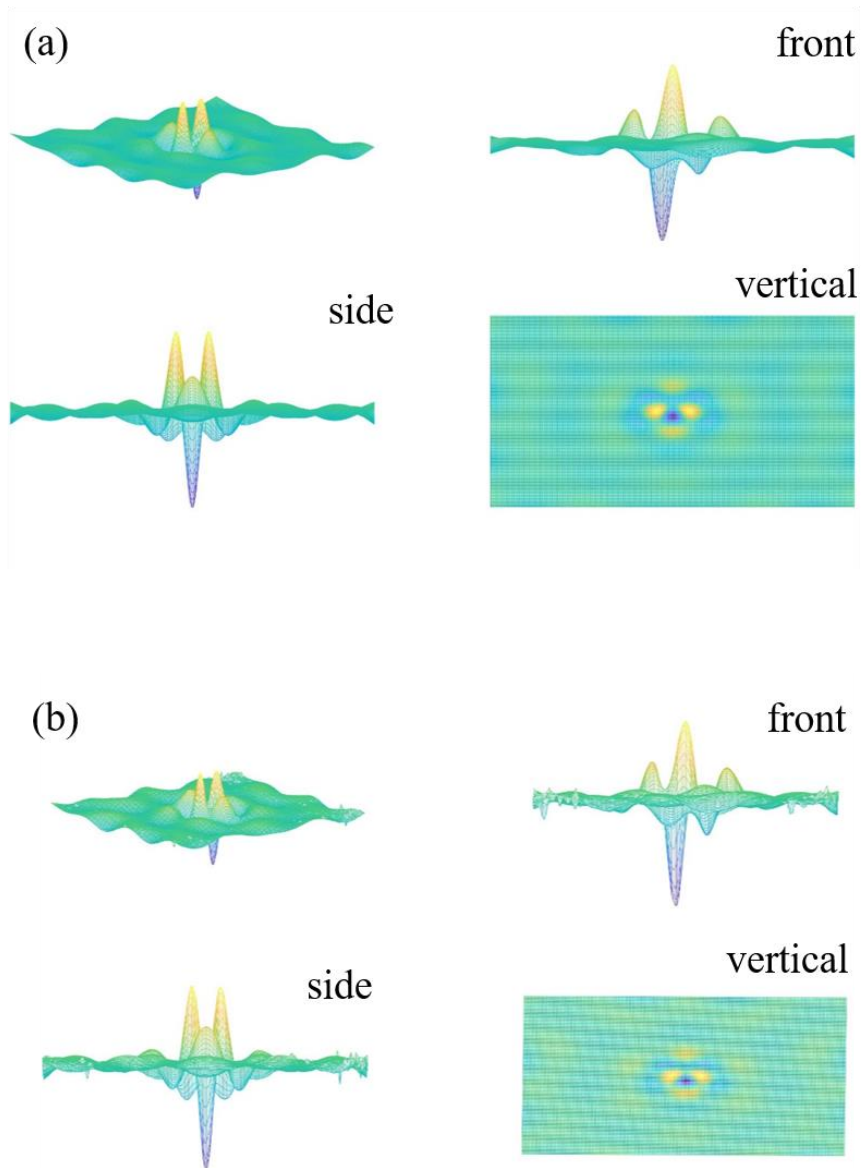


Figure 3.21 Comparison of 74th mode shape: (a) DW model (left),

$f_n = 2788.9$ Hz; (b) experiment (right), $f_n = 2766.0$ Hz.

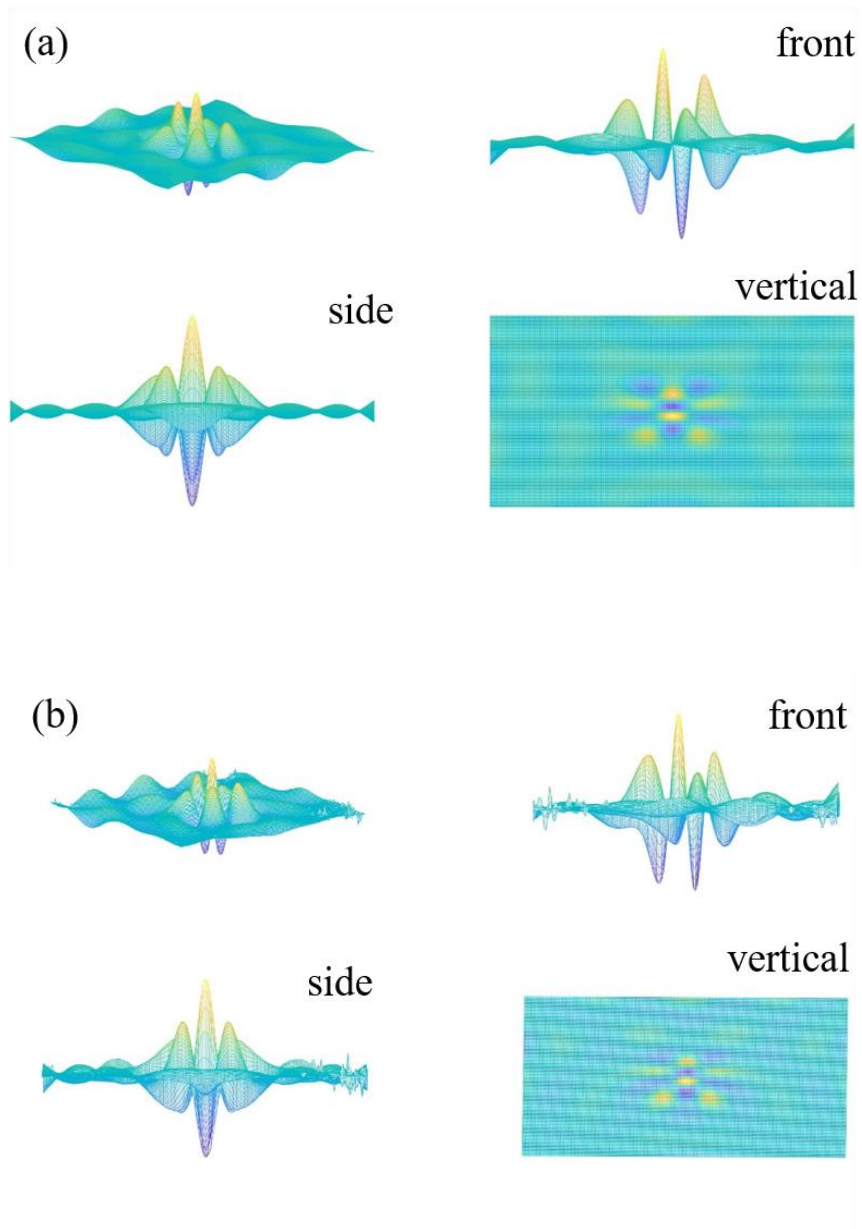


Figure 3.22 Comparison of 79th mode shape: (a) DW model (left),

$f_n = 3001.8$ Hz ; (b) experiment (right), $f_n = 2992.0$ Hz .

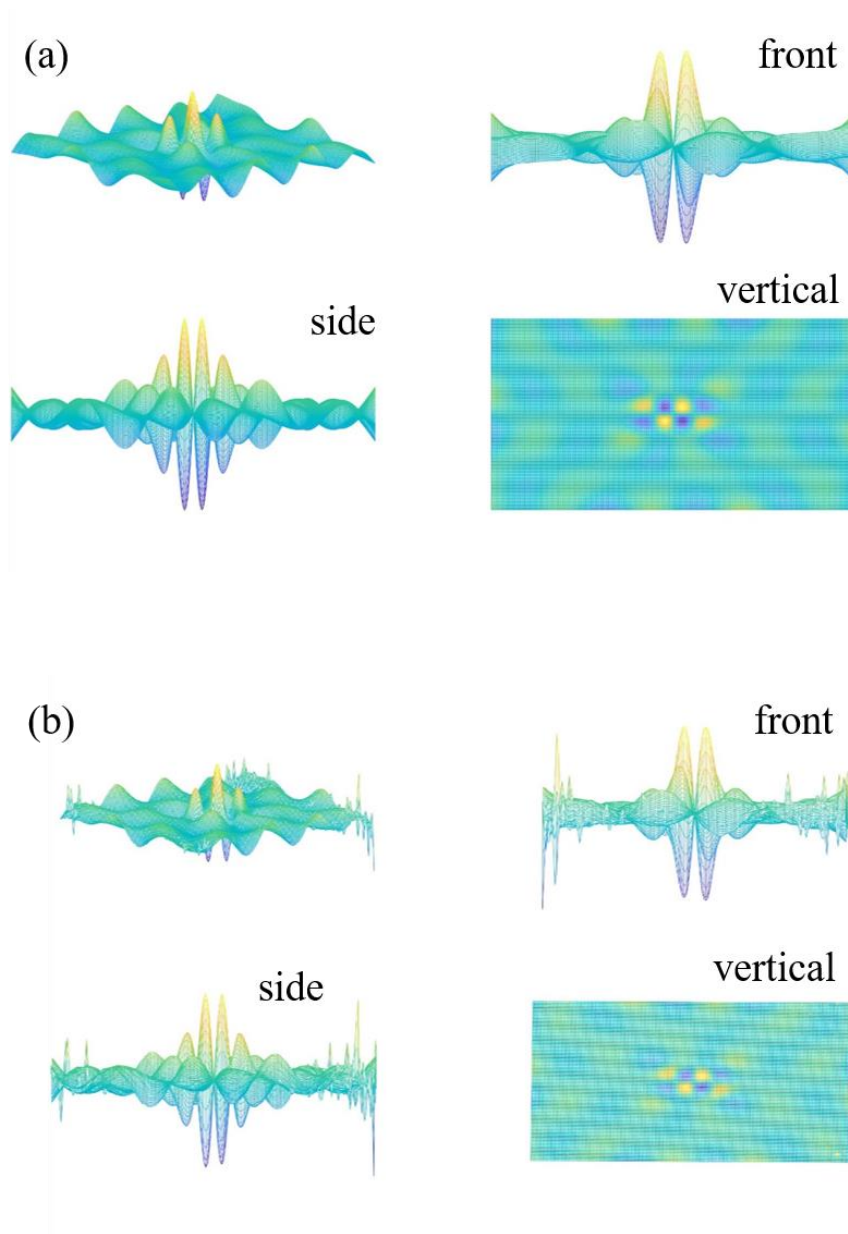


Figure 3.23 Comparison of 83rd mode shape: (a) DW model (left),

$f_n = 3163.5$ Hz ; (b) experiment (right), $f_n = 3135.0$ Hz .

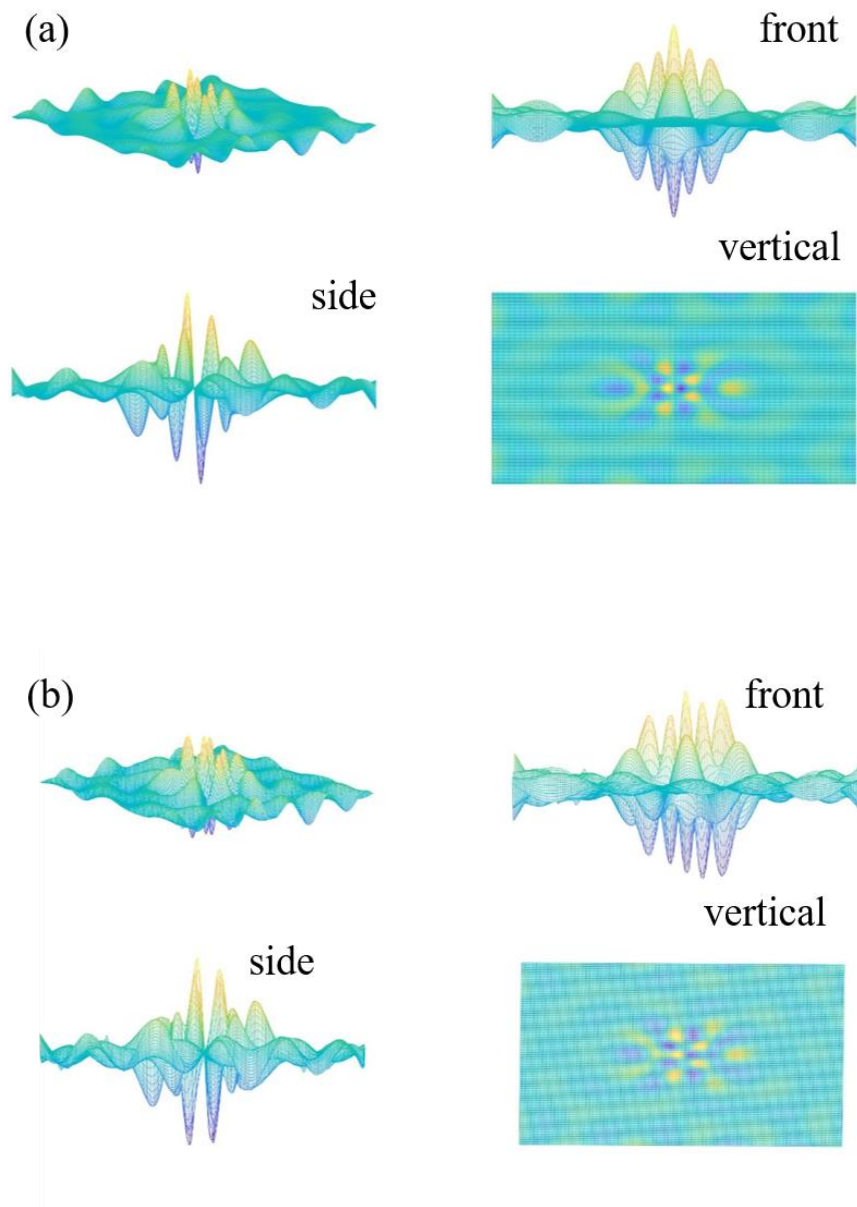


Figure 3.24 Comparison of 118th mode shape: (a) DW model (left),

$f_n = 4552.1$ Hz ; (b) experiment (right), $f_n = 4510.9$ Hz .

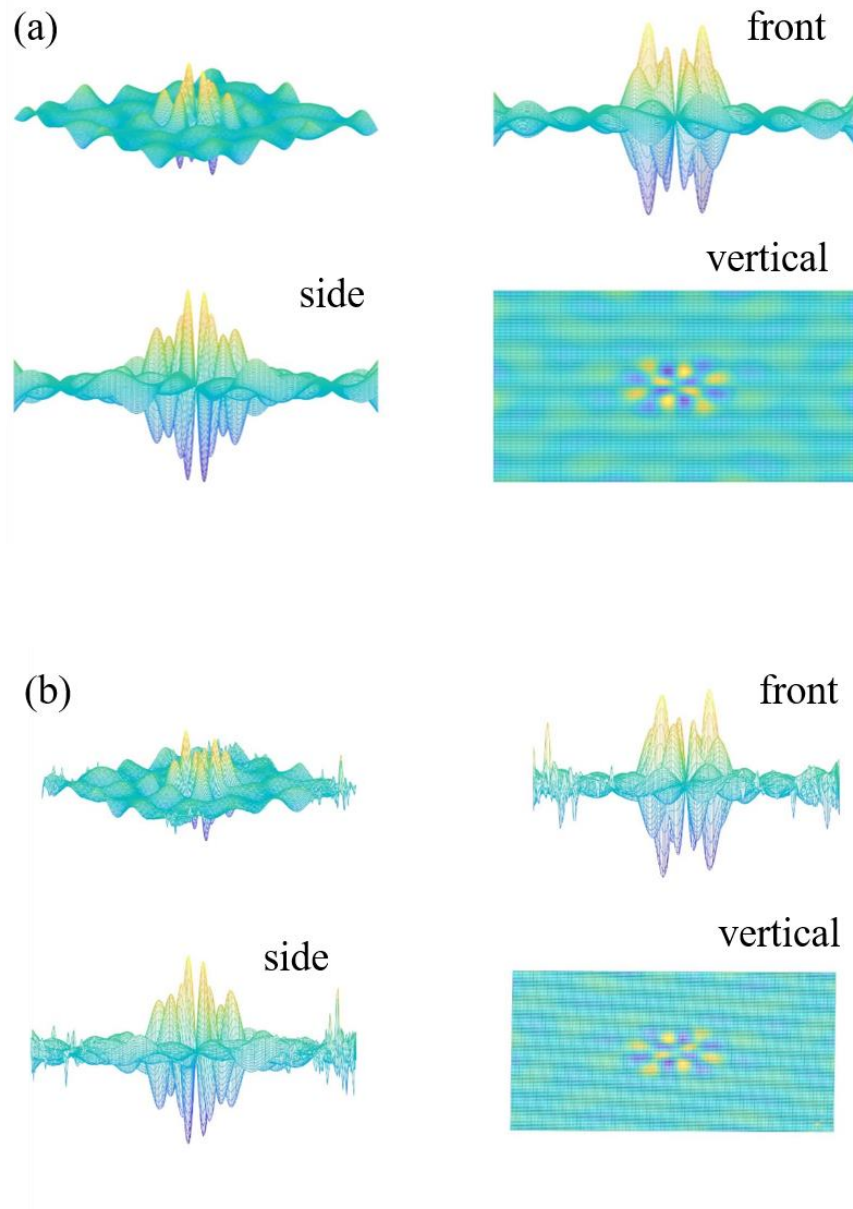


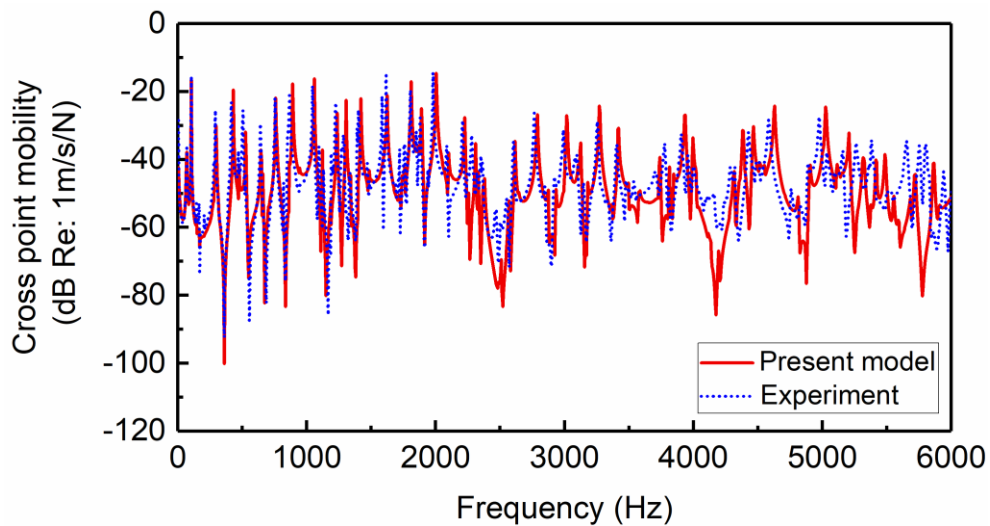
Figure 3.25 Comparison of 119th mode shape: (a) DW model (left),

$f_n = 4593.7$ Hz ; (b) experiment (right), $f_n = 4556.3$ Hz .

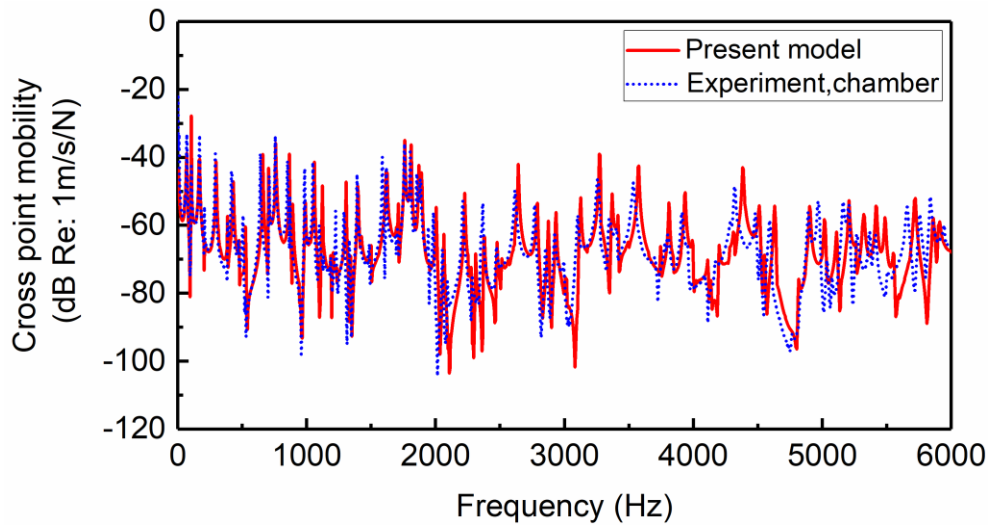
3.4.3.2 Cross point mobility

Forced vibration analyses were carried out on the test sample with a harmonic excitation applied at (0.518, 0.165) m over the uniform portion. The amplitude of vibration of several measured points over the surface of the test sample was measured

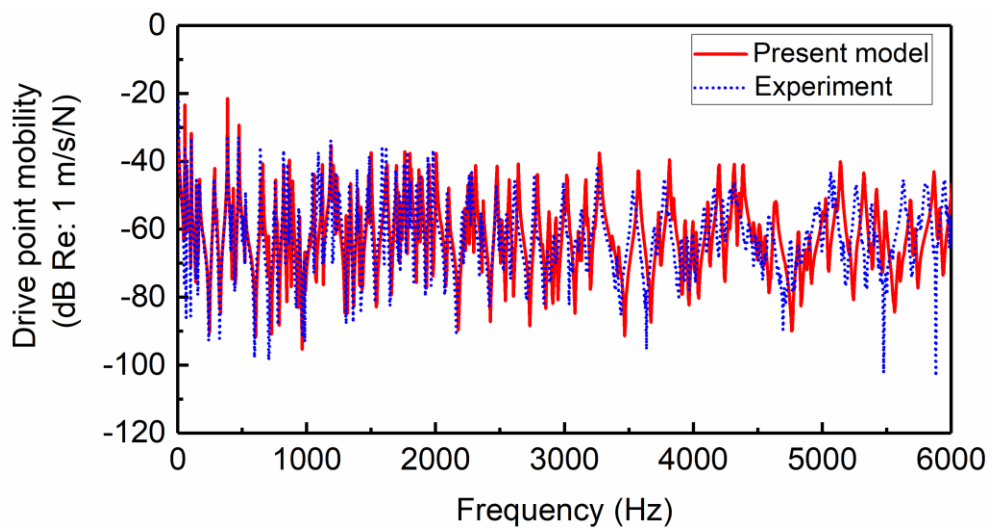
from 5 Hz to 6000 Hz with an increment of 5 Hz. Mobilities ($20 \lg(v/F)$) at three representative points over the test sample were extracted after 10 times averages. These three points include ABH center point (0.3, 0.25) m, a point (0.0375, 0.25) m on the uniform portion, and the driving point (0.518, 0.165) m. Figures 17(a)-(c) respectively illustrate the comparisons with numerical simulations. A good consistency can be observed in the entire frequency range, especially below 5500 Hz. Above 5500 Hz, differences begin to show; this presumably can be attributed to the deviation of manufactured ABH indentation from the predesigned profile, since the response at high frequencies is supposed to be more sensitive to local details. Nevertheless, it can be seen that the rich dynamics of the system, manifested by a large number of resonant peaks, can be truthfully reproduced by the DW simulation model, testifying the accuracy of the model on one hand, and the accuracy in manufacturing the test sample on the other hand.



(a)



(b)



(c)

Figure 3.26 Cross point mobility of the ABH plate: (a) ABH center (0.3,0.25) m; (b) an arbitrary point (0.0375, 0.25) m on the uniform portion; (c) drive point at (0.518, 0.165) m.

The deployment of damping layers inside the ABH indentation plays a crucial role in the realization of ABH effect. To illustrate the effect, the vibration response of the

ABH test sample with its central ABH portion covered with 3M™ VHB™ adhesive transfer tape F9473PC was experimentally measured. The density ρ_d , elastic modulus E_d and loss factor η_d of this material were evaluated at 4000 Hz [121] and tabulated in Table 3.3. In the present case, the central area of ABH indentation within a radius of $R_d = 60$ mm was covered with transfer tape F9473PC of a constant thickness $h_d = 0.75$ mm. Figure 3.27 shows the measured and predicted structural mobilities at (0.0375, 0.25) m, showing again a nice fit with each other. Compared with Figure 3.26(a), the overall mobility level of the damped plate shows a general decreasing trend with frequencies alongside a general reduction in the peak levels, which can be attributed to the ABH-induced enhancement in the overall system damping.

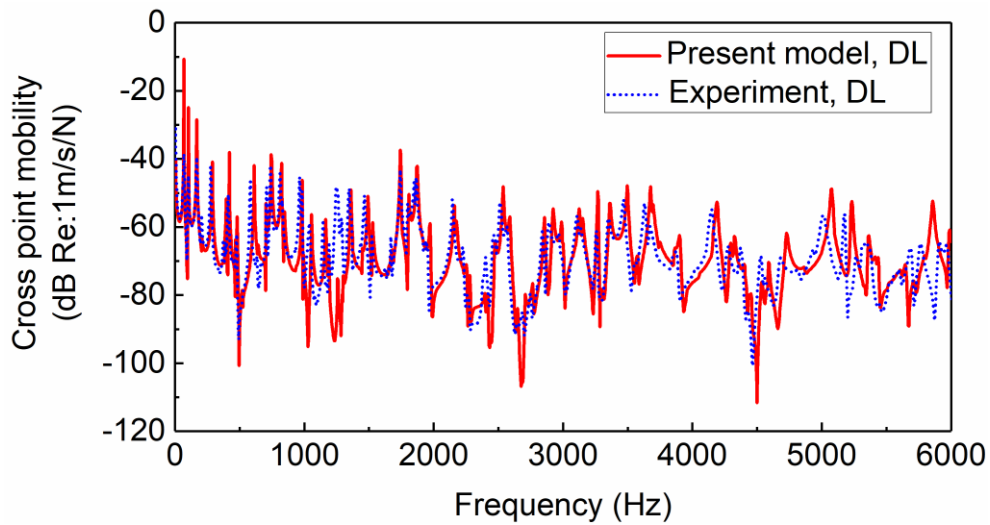
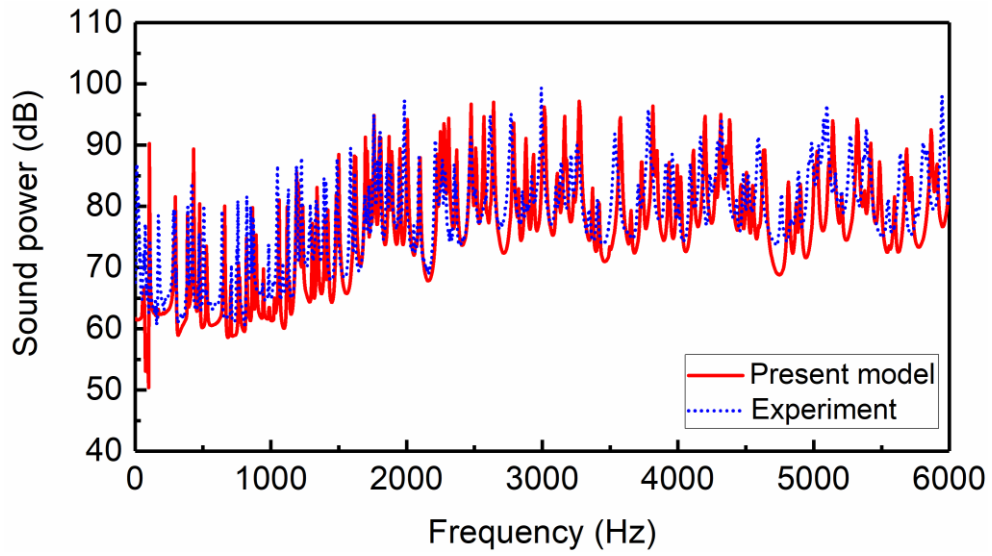


Figure 3.27 Comparison of cross point mobility at (0.0375, 0.25) m with damping layers: (a) present model (solid line); (b) experiment (dot line). DL denotes damping layer.

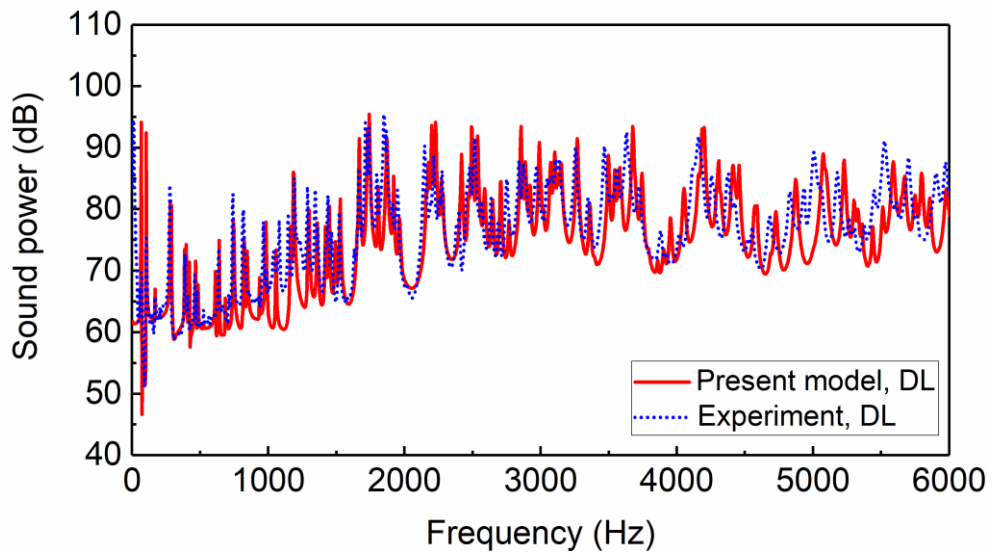
3.4.3.3 Radiated sound power

Following the procedure described in [Section 3.4.2.2](#), the sound power radiated from the baffled ABH test ample was measured. Using the same excitation as in the vibration test, the sound power radiated from test sample with/without damping materials was measured. For the sake of comparison, again, the measured sound pressure at each microphone position was normalized by the input force. Subsequently, substitution of averaged sound pressure level into [Equation \(3.2\)](#) yields the total sound power as shown in [Figure 3.28](#). Comparing the experimentally obtained sound power with that of model simulations, an agreement can be noticed between these two sets of results, both with ([Figure 3.28\(a\)](#)) and without ([Figure 3.28\(b\)](#)) damping layers.

The results also show that the signal to noise ratio is variable in the frequency range of interest. Due to the low signal to noise ratio in the frequency range between 1000 Hz and 1500 Hz, the observed sound power is larger than its numerical counterparts. Whereas for other frequency ranges, both sets of results match well. Interference from the shaker should be responsible for the discrepancy between 1000 Hz and 1500 Hz, as the noise from the shaker itself was detected and was difficult to be completely eliminated. Nevertheless, the overall agreement between the model and experiments is deemed satisfactory, especially for such a highly dynamic system exhibiting complex dynamic behaviors.



(a)



(b)

Figure 3.28 Radiated sound power: (a) without damping layer; (b) with damping layer. DL denotes damping layer.

3.5 Summary

Full validations of the proposed model through FEM simulations and by experiments are presented in this chapter. It mainly reports a systematic experimental investigation on a rectangular plate embodied with a symmetric circular ABH indentation. Upon a meticulous design and realization of the manufacturing process, a high-precision ABH plate is manufactured. Using the manufactured sample, its structural properties, in terms of eigen-frequencies, mode shapes, forced vibration response and radiated sound power, were experimental tested and compared with a previously developed semi-analytical model. Meanwhile, with realistic damping materials deposited at the central portion of the ABH indentation, ABH effects on reductions in vibration response and sound power are experimentally verified.

Through comparisons with FEM and experimental results,

1) The DW model has been shown to provide remarkable accuracy in characterizing the vibration response and sound radiation of the ABH plate which exhibits rich dynamics and complex dynamic behaviors. More specifically, most of the relative errors on the eigen-frequencies of the first 120 modes of the plate are below 2% (compared with experimental results), alongside a good match in the corresponding mode shapes. The cross-point mobility and the radiated sound power predicted by the DW model also show a good agreement with experimental measurement up to a high frequency range, both with and without deposition of damping materials. Meanwhile,

typical ABH phenomena such as wave compression, energy focalization and the effects of viscoelastic damping layers are also clearly observed in experiments, also in agreement with numerical predictions.

2) The proposed model, as well as the associated wavelet-based solution procedure, is shown to be able to overcome major technical difficulties which are specific to ABH structures: non-uniform wavelength distribution and ABH-induced wave compressions in the high frequency range in a realistic structure of finite size. The accuracy, as well as the frequency outreach well exceeds similar work reported in the literature. In that sense, this work offers a useful model which is conducive to the study of ABH phenomena.

3) Another important outcome of this work is the establishment of a feasible manufacturing procedure of an ABH plate, as well as a full set of well-controlled experimental benchmark solutions on some important vibrational and acoustic metrics. Considering the lack of experimental data in the literature, we believe this would serve as an invaluable data source for future ABH studies.

Chapter 4

A 2D Daubechies wavelet model on the vibration of rectangular plates containing strip indentations with a parabolic thickness profile

4.1 Introduction

Much work about vibration analyses of ABH beams and plates has been extensively studied through FEM simulations and experimental tests. However, explorations of vibration characteristics of 2D ABH plates using semi-analytical models are scarce, with the exception of a recent work by O'Boy and Krylov [50]. However, the frequency range that the model can reach is relatively low such that the ABH effect cannot systematically show.

In this chapter, the proposed model that has been fully validated in [Chapter 3](#) is utilized for vibration explorations of a rectangular plate embedded with a 1D ABH indentation (strip indentation). The same configuration used in O'Boy and Krylov [50] is adopted with an intention of improving that model to reach the effective ABH zone at much higher frequencies. Specifically, typical ABH phenomena such as wavelength compression and energy focalization are illustrated using the developed model. Vibration reduction effects of the ABH plates are investigated with comparisons against a reference uniform plate in [Section 4.2.1](#). Effect of different configurations of damping

layers over the surface of ABH indentations on structural damping increase is examined in [Section 4.2.2](#). Changes in the modal loss factors are investigated and linked up with typical ABH cell modes. The energy focalization capacities of a strip ABH and a circular ABH are investigated and compared in [Section 4.2.3](#). Finally, the vibration benefits of ABH plates are summarized in [Section 4.3](#).

4.2 Numerical Analyses and discussions

4.2.1 ABH phenomena and vibration benefit

Typical ABH phenomena, in terms of the compressed wavelength and increased vibration amplitude, are first analyzed using the same free plate. Note the issue of addressing other types of boundary conditions using Rayleigh-Ritz method has been extensively discussed in the literature [111]. The geometrical and material parameters of the plate embedded with a strip indentation is tabulated in [Table 3.1](#). It was observed (not shown here) that the boundary conditions do not fundamentally change the typical ABH phenomena that will be reported hereafter using a freely supported plate. In this case, the ABH strip covers the entire y direction of the plate. [Figure 4.1\(a\)](#) shows a cross sectional view along the x -axis of a typical mode shape (92th order) obtained by the present model. It can be seen that the wavelength begins to decrease at the interface between the uniform portion and the ABH portion. Meanwhile, the vibration amplitude gradually increases, typical of the expected ABH feature.

The concept of cut-on frequency [39], $f_{cuton} = \frac{\pi h}{2(R_{ABH})^2} \sqrt{\frac{E_0}{12\rho_0(1-\mu_0^2)}}$, means

that when the wavelength of incident flexural waves matches the characteristic dimension (length for 1D ABH and diameter for 2D circular indentation) of ABH tapers, the waves will well interact with ABH cell, leading to systematic ABH phenomena above the corresponding frequency. After ABH cell modes cut on, the ABH cell is expected to interact with the incident bending wave to create a significant vibration energy shift to the ABH portion. This is quantified by the ratio of the mean square velocity of the ABH portion to that of the uniform portion, defined as

$$\Gamma = 10 \log_{10} \left(\frac{\langle v_{ABH}^2 \rangle}{\langle v_{uniform}^2 \rangle} \right).$$

A larger Γ signifies a greater energy concentration in the

ABH portion. Figure 4.1(b) shows a clear vibration energy shift from the uniform portion to the ABH portion as a result of typical ABH effect, leading to a strong energy focalization within the ABH strip. This ABH-induced feature is conducive to energy harvesting and vibration reduction through local damping enhancement. Results also demonstrate that the present model correctly captures the main ABH-specific features of the plate.

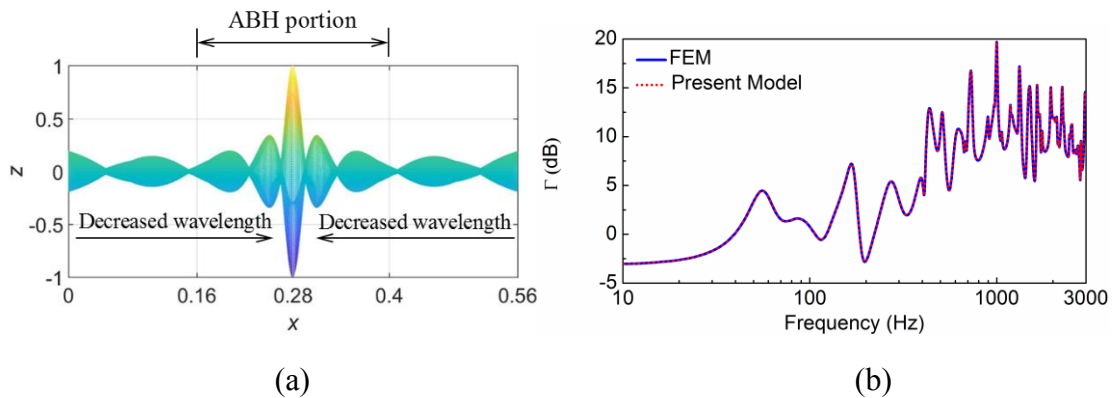


Figure 4.1 Typical ABH features: (a) decreased wavelength towards the center of ABH portion; (b) ratio of the mean square velocity between the ABH portion and that of the uniform portion.

To investigate the potential of using a strip ABH for vibration reductions, damping layers are symmetrically placed with respect to the central line of the strip (see [Figure 4.2\(b\)](#)), from $x_{d1}=0.25\text{m}$ to $x_{d2}=0.31\text{m}$ and from $y_{d1}=0$ to $y_{d2}=0.56\text{ m}$, with a constant thickness of $h_d = 2h_0$. The damping material has a Young's modulus $E_d=5\text{ GPa}$, a density $\rho_d=950\text{ kg/m}^3$ and a Poisson ratio $\nu_d=0.3$. Plate parameters are the same as those used before, tabulated in [Table 3.1](#). The total mass of the added damping layers is 0.26% that of the plate. For comparisons, a reference flat plate of the same size (coated with the same amount of damping layers at the same corresponding location, shown in [Figure 4.2\(a\)](#)) is also considered.



Figure 4.2 Reference plate and ABH plate coated with the same amount of damping layers. Coating area $x_{d1} \sim x_{d2}=0.25\sim 0.31\text{ m}$, $y_{d1} \sim y_{d2}=0\sim 0.56\text{ m}$ and thickness $h_d=2h_0$:

(a) Reference plate; (b) ABH plate. Dark gray area denotes the area coated with damping layers.

Under the same mechanical excitation, the mean square velocities averaged over the uniform portion of the two plates are compared in [Figure 4.3](#). It can be seen that the vibration level of the plate with the ABH indentation is generally much lower than that of its flat counterpart. Typically, peak levels differ by up to 12 dB. This shows the benefit of tailoring an ABH strip by removing materials from a flat panel to make the structure lighter and more vibration appealing at the same time, as far as the uniform part of the plate is concerned.

The aforementioned phenomena can be better explained by investigating the effects of the damping layers on each plate. [Figure 4.4](#) shows that, due to the rather uniform energy distribution in the flat plate, the use of the small amount of damping layers turn out to be insignificant, barely visible for some particular resonances. As to the ABH-featured plate, however, the same amount of damping leads to a much more visible vibration reduction, as demonstrated in [Figure 4.5](#). The vibration reduction is more obvious and systematic at higher frequencies, typically above the characteristic frequency of 500 Hz, where incident flexural waves interact more effectively with the ABH indentation due to their shorter wavelengths compared to the size of the ABH cell. This is also consistent with previous studies on 1D ABH wedges [\[7, 12\]](#) which showed that the impaired ABH effect caused by the thickness truncations can be well compensated by using a small piece of damping layer coated on the tapered ABH region. The presence of the damping layers largely reduces the reflection coefficient, thus

leading to a more significant energy concentration and dissipation in the tapered ABH region.

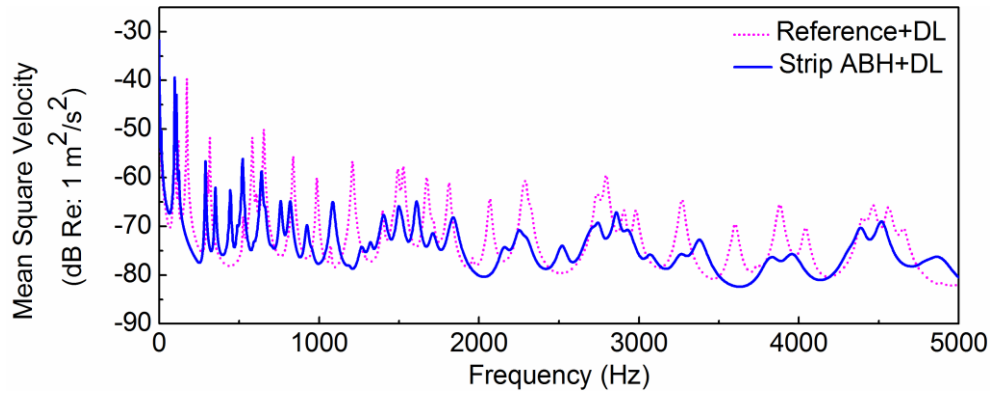


Figure 4.3 Mean square velocity of uniform portion: reference plate with damping layers (dot line); strip ABH plate with damping layers (solid line).

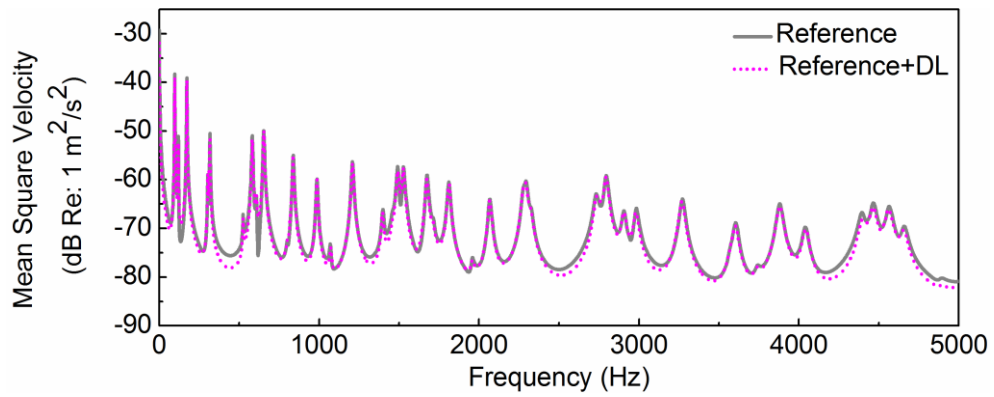


Figure 4.4 Mean square velocity of the uniform portion of reference plates: without damping layers (dot line); with damping layers (solid line).

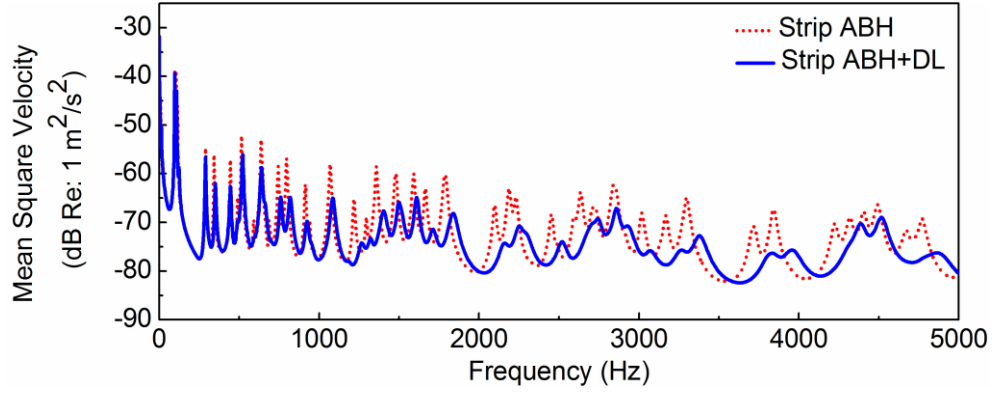
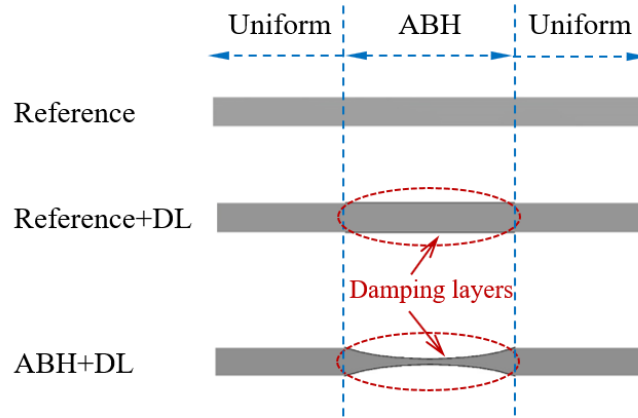


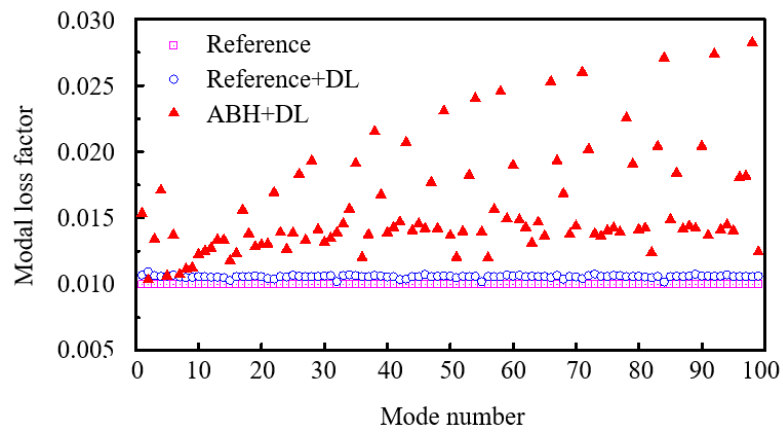
Figure 4.5 Mean square velocity of the uniform portion of strip ABH plates: without damping layers (dot line); with damping layers (solid line).

4.2.2 Modal loss factors

As the ABH tapered area features in strong energy focalization, a small amount of damping material coated at this area will visibly increase the structural damping of the system. To observe this, modal loss factors of an ABH plate embedded with a strip indentation are calculated. A uniform plate is used as reference. The whole ABH area is covered with a thin piece of damping layer whose thickness is as thin as $0.5 h_0$. The mass of the used damping layers merely accounts for 0.26% of the mass of the plate. For companions, the reference plate with the same amount of damping material coated at the corresponding ABH area is also investigated. The cross sections of the reference plate, reference plate coated with damping layers, and the ABH plate coated with damping layers are shown in [Figure 4.6\(a\)](#). Comparisons of modal loss factors of the first 100 modes of these three systems are illustrated in [Figure 4.6\(b\)](#).



(a)



(b)

Figure 4.6 Plates and modal loss factors: (a) bare reference plate (upper); reference plate with damping layers (middle); ABH plate with damping layers (lower); (b) reference plate (square dot); reference plate with damping layers (circular dot); ABH plate with damping layers (triangular dot).

It can be seen from [Figure 4.6\(b\)](#), modal loss factors slightly increased for reference plate coated with damping layers, in comparison to that of the reference plate. However, note that, for ABH plate coated with damping layers, as compared with the

inherent material damping (0.01 for the plate), one notices a significant damping increase for most modes, consistent with the observations made in 1D structures [46].

Furthermore, the bi-dimensionality of an ABH plate is expected to exhibit different features as compared to a 1D ABH beam taper [46]. This is scrutinized from the overall modal loss factors of the strip ABH plate. Upon the deployment of the damping layers over the strip ABH plate, same as Section 4.2.1, Figure 4.7 depicts the calculated modal loss factors for the first 100 structural modes. However, different from the 1D ABH beam [46] where damping enhancement is systematic for all modes with roughly the same enhancement level above the characteristic frequency, the current 2D plate exhibits a much more scattered pattern in terms of damping enhancement. More specifically, the cloud points in Figure 4.7 seem to regroup into different clusters, each following a different variation trend with respect to the increasing mode number/frequency. Typical mode shapes in each group are shown in Figure 4.7. The first group of modes seem to follow an obvious monotonically increasing trend with the frequency, with significantly topped-up damping. Mode shapes show that these modes share the common feature of having a half-wave along the x -direction (thickness tailoring direction) of the ABH strip, denoted as $(1, n)$ modes. The following group with a moderate damping increase consists of $(2, n)$ modes, with a full wave contained within the ABH strip in the x -direction. With the further increase in the structural deformation within the ABH cells along x -direction, the increase of the modal loss factors of the plate further diminishes. At the bottom of the cloud points are these modes involving a global

structural deformation of the plate. When this happens, the deployed damping layers within the small ABH region cannot generate meaningful damping increase in the overall structure. Therefore, the observed overall damping increase, brought up by the viscoelastic coating, as well as the vibration reduction phenomena observed in [Figure 4.5](#), is mainly attributed to the significant damping enhancement of the lower order local ABH modes, typically these involving a half and one wave in the direction in which the plate thickness profile is tailored.

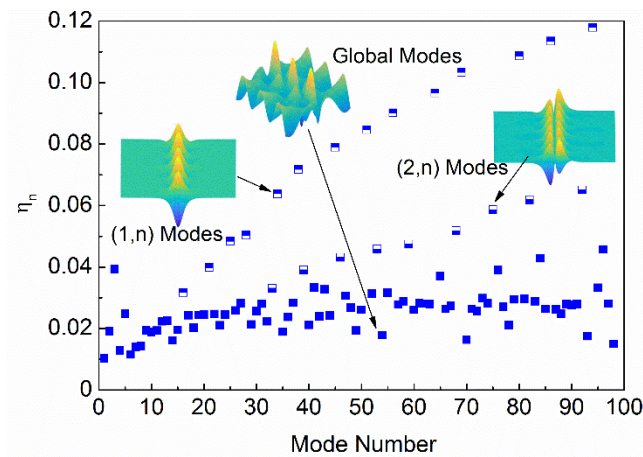


Figure 4.7 Modal loss factors of the strip ABH plate coated with damping layers:

(1, n) ABH cell modes (dots with hollow lower part); (2, n) ABH cell modes (dots with hollow upper part); global modes (solid dots).

4.2.3 Strip ABH versus circular ABH

It is surmised that bi-dimensionality properties of ABH plates would be better seen with a circular ABH indentation, since its local thickness variation might generate more pronounced coupling effects between the x and y directions of the plates. As aforementioned, apart from some mathematical treatments which are specific to the

calculation of the energy terms, the proposed modelling approach is also valid for plates embedded with a circular indentation, shown in [Figure 4.8](#). Using the model, a strip ABH plate and a circular ABH plate are compared in terms of energy concentration. While the local thickness variation of the strip ABH being $h(x) = \varepsilon(|x - x_c|)^\gamma + h_0$, that of the circular indentation follows $h(r) = \varepsilon r^\gamma + h_0$, where r is the radial coordinate of the circular ABH indentation. For comparisons, the dimensions of these two plates are chosen to be the same: $a = 0.5$ m, $b = 0.5$ m, $h = 4.7$ mm. Parameters for both ABH indentation are $\varepsilon = 0.2$, $\gamma = 2$ and $h_0 = 0.2$ mm. The circular indentation has a radius $R_{ABH} = 0.15$ m. To ensure the same area for both indentations, the dimension of the strip ABH is determined, covering an area from $x_1 = 0.1$ m to $x_2 = 0.4$ m in x direction and from $y_1 = 0.13225$ m to $y_2 = 0.36775$ m in y direction. Similarly, the same amount of damping material, 0.146% of the bare reference plate, is used around the center of both ABH indentations. For comparison purposes, the mean square velocity ratio Γ and the overall loss factors of each plate are calculated and compared.

In the absence of the damping layers, [Figure 4.9](#) shows that, above the characteristic frequency (500 Hz), the strip ABH plate seems to be generally superior to its circular counterpart in terms of energy focalization. The overall ABH effect is also confirmed by [Figure 4.10](#) in that, upon using the damping layers, the overall loss factors of most the strip ABH modes are also much larger than those of circular ABH.

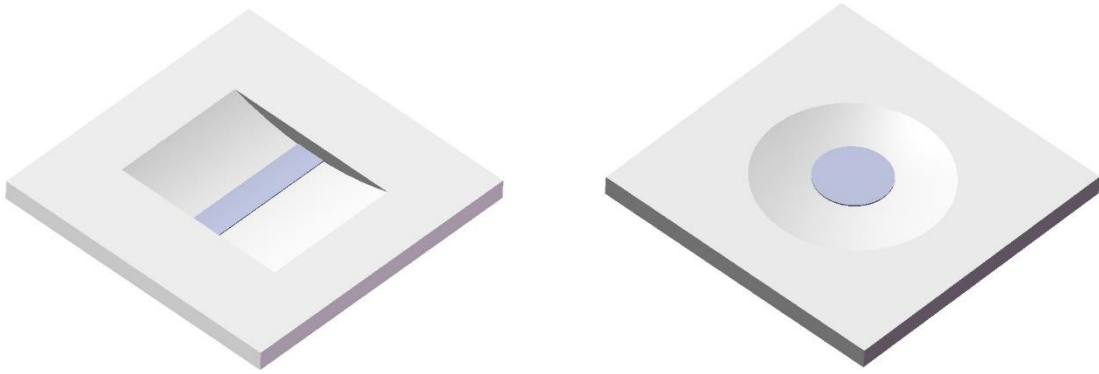


Figure 4.8 Plates with two types of ABH indentations: strip (left); circular (right).

Dark gray area denotes the area coated with damping layers.

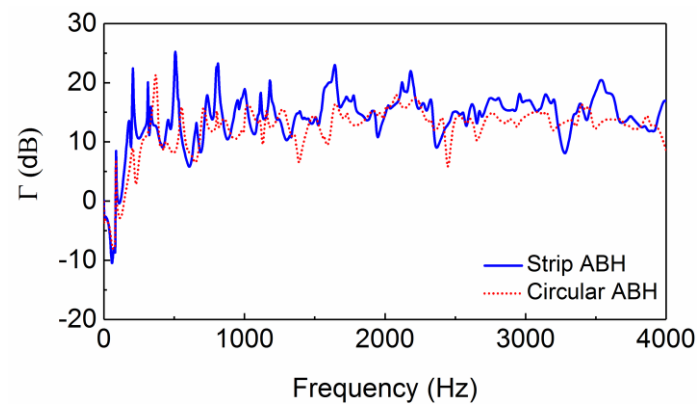


Figure 4.9 Comparison of the ratio of the mean square velocity between the ABH portion and that of the uniform portion without damping layers: strip ABH plate (solid line); circular ABH plate (dot line).

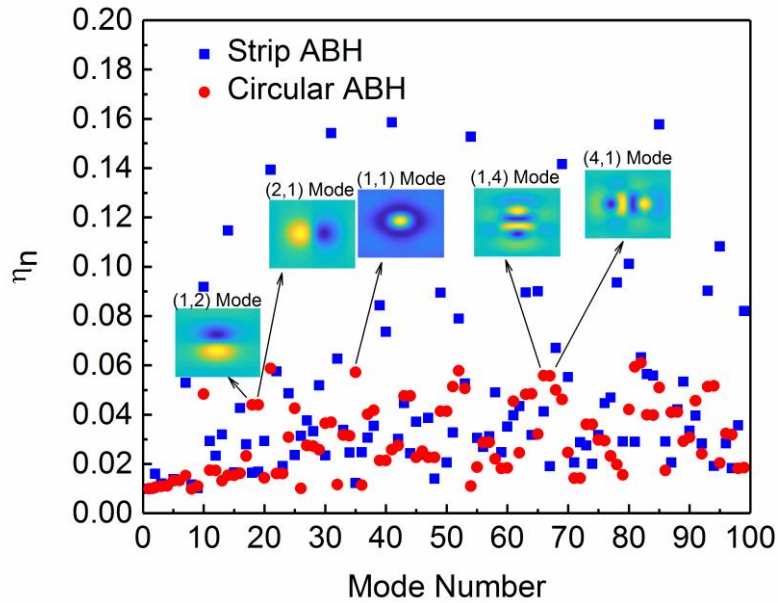


Figure 4.10 Comparison of the modal loss factors of the strip ABH plate and the circular ABH plate with damping layers: strip ABH plate (square dot); circular ABH plate (circular dot).

The dynamics of the circular ABH plate can be better understood by examining the local deformation of the ABH indentations. Having understood the relationship between the damping loss factor with the local mode shapes in the case of the strip ABH plate, the same analysis is now carried out for the circular one. Similar to the strip ABH plate, [Figure 4.10](#) shows that the largest damping increase also corresponds to the local ABH modes in the circular ABH plate. Different from the strip ABH plate, for which $(1, n)$ modes have larger modal loss factors than $(2, n)$ modes, for the circular ABH plate, local ABH $(1, 2)$ and $(2, 1)$ modes seem to provide very similar modal loss factors. Same applied to modes $(1, 4)$ and $(4, 1)$. This is naturally due to the bi-dimensionality of the circular ABH indentation. In the case of the circular ABH indentation, as opposed to the

strip case, mode classifications seem to be more difficult, although results still suggest that significant damping enhancement is governed by the lower order local ABH modes.

4.3 Summary

In this chapter, the proposed semi-analytical DW model is used for the vibration analyses of rectangular plates containing strip ABH indentations with a parabolic thickness profile. Numerical analyses lead to the following conclusions:

Numerical analyses show typical energy focalization and dissipation phenomena of a plate with an embedded ABH indentation covered by a small amount of damping materials, pointing at the possibility of designing lightweight structures with better vibration reduction performance. Study of different configurations of damping layers over the surface of the strip indentation shows that, the same amount of damping materials coated at the ABH central portion can significantly increase the modal loss factors, compared with a uniform plate. It is shown that, above the cut-on frequency of the panel, the ABH-induced damping enhancement phenomenon is mainly attributed to the local structural modes within the ABH indentation. These modes exhibit lower-order deformations (typically half and one wave along the thickness tailoring direction) for the strip indentation. Contributions to the damping increase by the higher-order local modes along the thickness tailoring direction and global modes are trivial and negligible. Owing to the high structural modal density, this turns out to be enough to produce an appreciable damping increase, and subsequent a vibration reduction of the entire

structure. A circular indentation basically follows the same trend, except that dominant local modes apply to both directions of the plate. For the same given indentation area, a strip indentation seems to outperform its circular counterpart, in terms of both energy focalization and the overall damping enhancement.

As a final remark, Daubechies wavelets, including both highly localized and highly smooth members, are compactly supported and orthogonal. These properties endow them with the ability to capture local structural changes and details, even when the ratio of ABH dimension to the overall structural dimension becomes small. In such cases, one should expect the effective range of the systematic ABH effects to be increased. For a given problem, a possible optimization could be conducted using the present model, such as finding the optimal distribution of the damping layers and the optimal ABH profile for reduced sound radiation and increased structural damping, as will be discussed in [Chapter 6](#) and [7](#).

Chapter 5

Sound radiation and transonic boundaries of a plate with a circular acoustic black hole indentation

5.1 Introduction

Apart from vibration benefits, lightweight structures with low sound radiation capability are also in great demand for various applications in aerospace, automobile and marine industries. The feasibility of making use of ABH concept for lightweight and quiet structure design is investigated in this Chapter. In particular, the proposed 2D semi-analytical ABH model is utilized to revisit some fundamental ABH-specific sound radiation issues.

This chapter aims to investigate and scrutinize the sound radiation properties of a plate with an embedded circular ABH indentation by employing the DW model. Particular attention is paid to the description and understanding of the underlying physical process of the sound radiation in different frequency ranges, with the help of relevant physical parameters such as changes of the transonic boundaries inside the ABH indentation and supersonic acoustic intensity [122, 123]. Results are expected to enrich the existing understanding on the sound radiation of ABH structures.

This chapter is organized as follows. [Section 5.2](#) introduces the procedures to calculate the supersonic acoustic intensity of the radiated sound in spatial domain. In [Section 5.3](#), investigations into the sound radiation of ABH plates are performed through examining the radiated sound power and sound radiation efficiency of the ABH plate in different frequency ranges. Reductions in vibration response and sound power were also experimentally observed. Subsequently, the observed reduction in the sound radiation is scrutinized and quantified by examining the ABH-induced structural stiffness changes in the low frequency range and the creation and evolution of the transonic boundary in the high frequency range. Supersonic acoustic intensity in spatial domain is validated using a simply supported uniform plate. Subsequently, supersonic intensity is exploited to identify the vibrating regions that are responsible for the effective sound radiation to the far field. Effect of the damping layers on sound radiation efficiency is also investigated, showing the non-negligible added stiffness effect for the investigated configuration. Finally, [Section 5.4](#) summarizes this chapter.

5.2 Supersonic acoustic intensity in spatial domain

The supersonic acoustic intensity is useful to identify the region of structures that effectively radiates sound into the far field. The sound radiation model is extended to accommodate this need under the wavelet-based framework. The supersonic acoustic intensity [\[124\]](#) can be calculated using a spatial domain approach [\[123\]](#). The supersonic pressure and supersonic normal velocity are defined as [\[124\]](#)

$$p^{(s)}(x, y, z) = \frac{1}{4\pi^2} \iint_{S_r} P(k_x, k_y, z) e^{-j(k_x x + k_y y)} dk_x dk_y \quad (5.1)$$

$$v^{(s)}(x, y, z) = \frac{1}{4\pi^2} \iint_{S_r} V(k_x, k_y, z) e^{-j(k_x x + k_y y)} dk_x dk_y \quad (5.2)$$

in which the superscript S denotes the supersonic quantity. S_r represents the integration area, defined within a circle, comprising all values of k_x and k_y such that $k_x^2 + k_y^2 \leq k^2$. Analogous to Equation (2.24), the supersonic acoustic intensity is defined as

$$I^{(s)}(x, y, z) = \frac{1}{2} \text{Re} \{ p^{(s)}(x, y, z) v^{(s)}(x, y, z)^H \} \quad (5.3)$$

In spatial domain, the calculation of the supersonic acoustic intensity is based on a two-dimensional convolution between the acoustic field and a radiation filter mask. Compared with wave number approach, the advantage of the direct convolution method is that it avoids a Fourier transformation in wave number domain and is relatively simple to implement. To this end, a unit circle function is defined with values transitioned from zero to one at the boundary of the circle.

The convolution theorem yields

$$p^{(s)}(x, y, z) = p(x, y, z) * h^{(s)}(x, y) \quad (5.4)$$

where $h^{(s)}(x, y)$ is the radiation filter mask, which can be expressed as [123]

$$h^{(s)}(x, y) = \frac{k}{2\pi\sqrt{x^2 + y^2}} J_1(k\sqrt{x^2 + y^2}) \quad (5.5)$$

where J_1 is the Bessel function of first kind. Equation (5.4) can then be discretized as

$$p^{(s)}(x, y, z) = \Delta S \sum_{n=1}^N p(x'_n, y'_n, z) \cdot h^{(s)}(x - x'_n, y - y'_n) \quad (5.6)$$

where ΔS is the area of each plate cell. Similar treatment also applies to the velocity terms. Subsequently, using Equation (5.3) allows the calculation of the supersonic acoustic intensity.

5.3 Model implementation and numerical analyses

Implementation of the simulation model requires the truncation of the decomposition series in Equation (2.2). As bending waves travel towards the center of the ABH indentation, structural wavelength gradually decreases. Therefore, a sufficiently large number of decomposition terms are needed to capture the local structural details. For sound radiation analyses, acoustic waves should be further considered to determine various DW parameters to be used in the computation, especially above the critical frequency where acoustic wavelength becomes smaller than their structural counterparts. For the subsequent sound radiation analyses on ABH plates, the same calculation procedure in Chapter 3 (in terms of integration scheme and number of elementary radiators) will be followed.

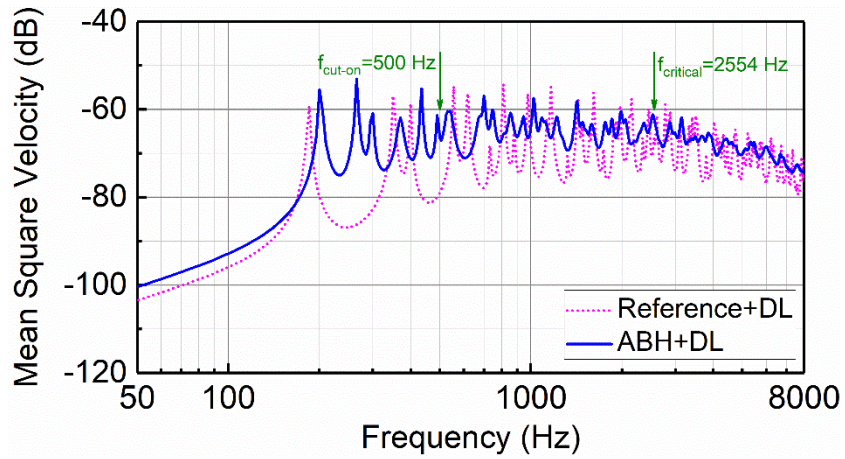
5.3.1 Vibration and sound fields of ABH plates

Using the model and the far field method described in [Section 2.2.4](#), the sound power radiated from ABH plate is examined. Parameters used in the calculations are tabulated in [Table 5.1](#), for both the ABH plate and its uniform counterpart. A unit harmonic excitation force is applied at (0.05, 0.315) m.

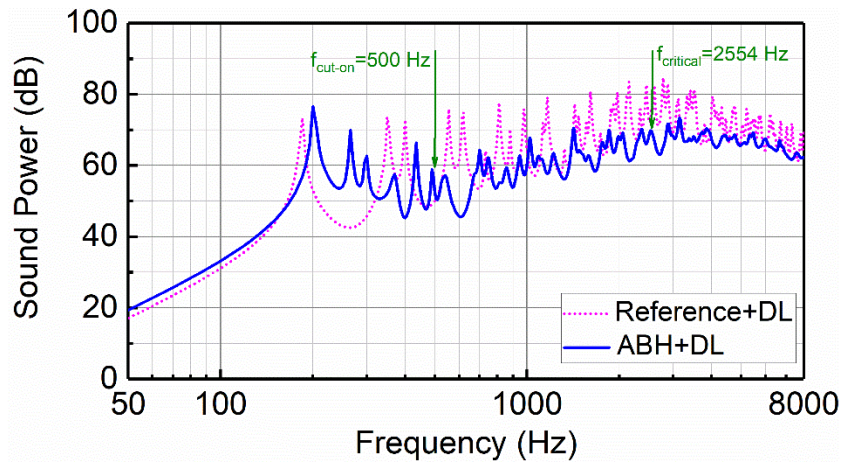
A partial damping treatment with a constant thickness $h_d = 0.3$ mm is applied within a radius of $R_d = 86.5$ mm in the central portion of the ABH cell (shown in [Figure 2.2](#)). The same damping treatment is also applied to the uniform plate for comparisons. Edges of both plates are assumed to be clamped. The space-averaged mean square velocity, with reference to $\langle |\mathbf{v}|^2 \rangle_{ref} = 1$ m/s, and the sound power radiated by both plates are compared in [Figure 5.1](#).

Table 5.1 Geometrical and material parameters of a plate with a circular ABH indentation

Geometry		Material	
$a=0.5$ m	$x_c=0.25$ m	$E_0=200$ GPa	$E_d=5$ GPa
$b=0.45$ m	$y_c=0.25$ m	$\nu_0=0.3$	$\nu_d=0.3$
$h=4.7$ mm	$\varepsilon=0.2/m$	$\eta_0=0.01$	$\eta_d=0.3$
$R_{ABH}=0.15$ m	$\gamma=2$	$\rho_0=7800$ kg/m ³	$\rho_d=950$ kg/m ³
$h_0=0.2$ mm			



(a)



(b)

Figure 5.1 Comparisons between the reference plate and the ABH plate: (a) space-averaged mean square velocity; (b) radiated sound power. DL denotes damping layers.

For the present case, the cut-on frequency [39] of the ABH plate is around 500 Hz. As illustrated in Figure 5.1, below 500 Hz, effects of the ABH on the plate vibration and sound power are not systematic in the sense that the inclusion of ABH indentation into

the plate cannot lead to any meaningful and systematic changes in neither structural vibration nor sound radiation. In the present case, it is rather the adverse effect that one can observe. However, above 500 Hz, reductions in the vibration amplitude begin to systematically show, with vibration peaks smoothed, especially at high frequencies as shown in [Figure 5.1\(a\)](#). Meanwhile, the ABH plate shows a significant reduction in the radiated sound power in the same frequency range. Note this is achieved by an ABH plate whose total mass is 88% that of the uniform plate due to the ABH indentation. These results demonstrate the potential and the benefit of using ABH principles to design lightweight structures. The observed sound reduction is definitely directly related to the typical ABH effect in terms of vibration energy localization and dissipation, leading to the reduced structural vibration. Meanwhile, a comparison between [Figure 5.1\(a\)](#) and [Figure 5.1\(b\)](#) indicates that the reduction in sound radiation seems to exceed that of the structural vibration. This points at the existence of other ABH-induced structural changes which contribute to the overall reduction of radiated sound power.

To explain this, the sound radiation efficiencies of ABH plates with/without damping layers are investigated. Again, results are compared against their uniform counterparts, as illustrated in [Figure 5.2](#). The critical frequency of the reference flat plate is 2554 Hz around which the radiation efficiencies peak for both plates with/without damping layers. Above this frequency, called supersonic region, the structural waves travel faster than acoustic waves, thus showing a consistently high efficiency in sound radiation, as one might expect from the basic sound radiation theory.

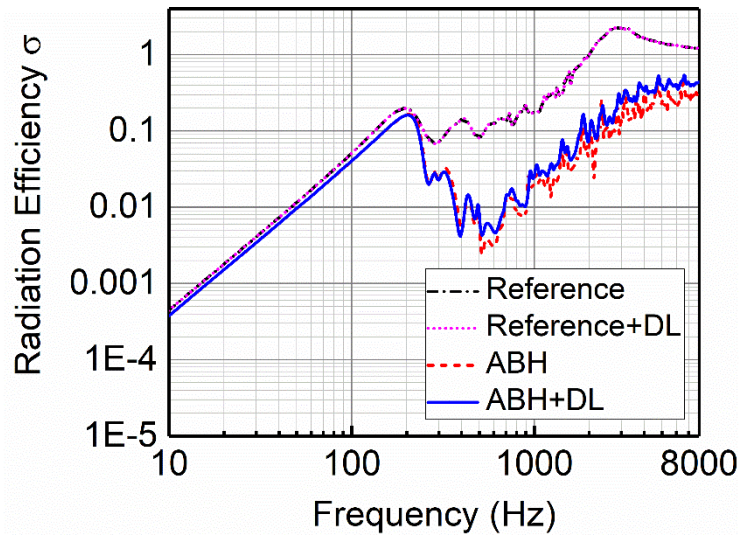


Figure 5.2 Comparisons of the sound radiation efficiencies between the reference plates and the ABH plates. DL denotes damping layers.

Figure 5.2 shows that the inclusion of the ABH indentation brings about significant changes in the sound radiation efficiency of the structure. 1). With or without damping, the radiation efficiencies of the ABH plates and the uniform reference plates are very similar before the first structural resonance. 2). Entering into the dynamic region and getting closer to the cut-on frequency (500 Hz), in this specific case, ABH plates show a significantly reduced radiation efficiency, compared with the uniform plates. 3). The same tendency maintains above the cut-on frequency. Above the critical frequency, the acoustically slow structural waves (also called subsonic structural waves) exist if the thinnest thickness is small enough. These waves lead to the reduced radiation efficiency, contributing to the overall reduction in the sound power of ABH plate as illustrated in Figure 5.1(b). It can also be observed from Figure 5.2 that the deployment of the

damping layers on the flat plate does not seem to alter much the radiation efficiency due to the small amount of coating used and the energy dispersive nature of the vibration energy over the plate. However, interestingly enough, the radiation efficiency of the ABH plate with the same coating is increased above the cut-on frequency in this particular case.

To ascertain this, influences of the stiffness and the mass of the damping layer are considered separately in the ABH plate and shown in Figure 5.3. As can be seen, the mass of the damping layer has negligible effect on the radiation efficiency. On the contrary, the effect of its stiffness is apparent. Note that the values of mass density and stiffness of damping layer used are realistic ones, consistent with those used in some reference papers [63, 125]. Therefore, the results call for a careful handling of damping layer in order to maximize the sound radiation reduction.

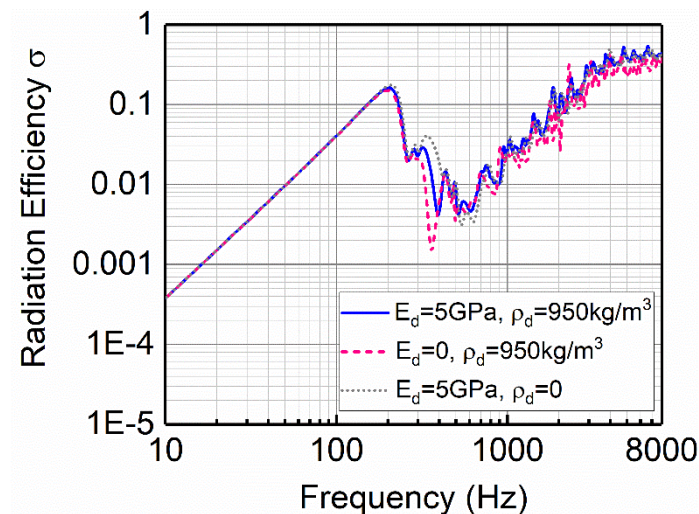


Figure 5.3 Effect of the stiffness and mass of the damping layers on the sound radiation efficiency of ABH plate.

5.3.2 Phenomena assertion by experiments

As aforementioned, damping layers coated around ABH center are indispensable for the realization of ABH effects and are beneficial to energy dissipation and vibration attenuation. This has been confirmed through experimental tests using the previous test sample. Note the mass of the damping material only accounts for 0.66% of the entire plate. Cross mobility at point (0.0375, 0.25) m over the uniform portion was measured. Compared with bare ABH test sample, the reduction of vibration peaks is visible. Similar trend is observed for sound power analyses. The parameters of experimental sample and the add-on damping layers are shown in Table 3.2 and Table 3.3.

The damping material FP9473 used in the experimental validation part in [Chapter 3](#) is relatively soft. For comparisons, another type of damping sheets, stiffer but also realistic, SD40PSA produced by 3M company were used for additional tests. While keeping the same coverage configuration as before, the thickness of the damping material SD40PSA was increased to 1.2 mm. The density of SD40PSA is 1682 kg/m^3 . Similarly, structural mobility and the radiated sound power of the test samples with the two different types of damping layers, alongside those of the bare ABH sample are compared in [Figure 5.4](#) and [Figure 5.5](#), respectively. It can be seen that a stiffer and more effective damping material enables significantly damped vibration peaks as

compared with the bare ABH plate, more obvious at high frequencies. Analogously, reduction in the sound power is also observed, especially above the critical frequency of 1995 Hz, estimated using the thickness of the uniform portion of the plate. The averaged reduction with respect to the bare plate can be up to 10 dB. The reduction of sound power is not only attributed to the suppressed vibration level but also to the reduced sound radiation efficiency of the ABH plate. Therefore, the utilization of realistic damping material deposited at the central portion of the ABH test sample allows for a substantial attenuation of structural vibration response and its radiated sound power, showing the great potential of ABH structures for vibration and noise control applications.

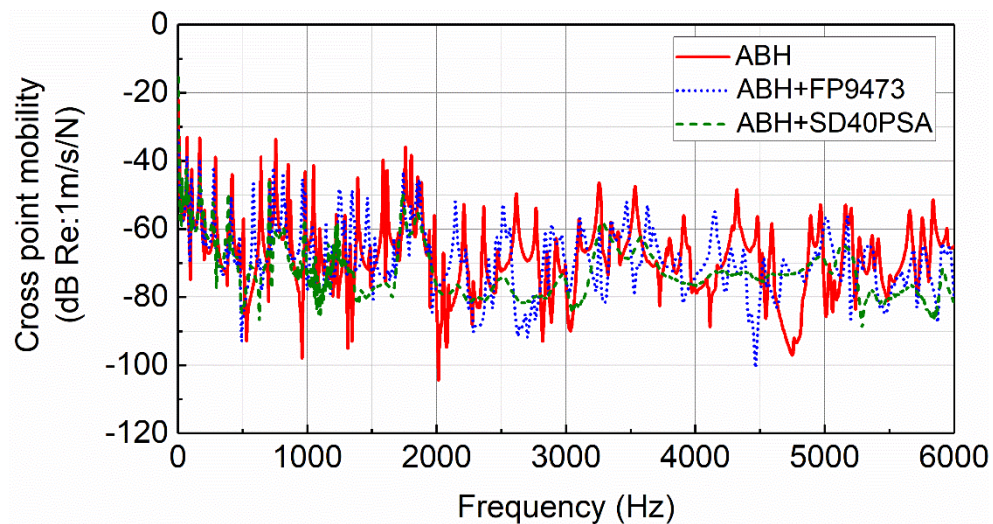


Figure 5.4 Measured cross point mobility at (0.0375, 0.25) m on the uniform portion of the test samples: (a) without damping material (solid line); (b) with damping material FP9473 (dot line); (c) with damping material SD40PSA (dash line).

DL denotes damping layer.

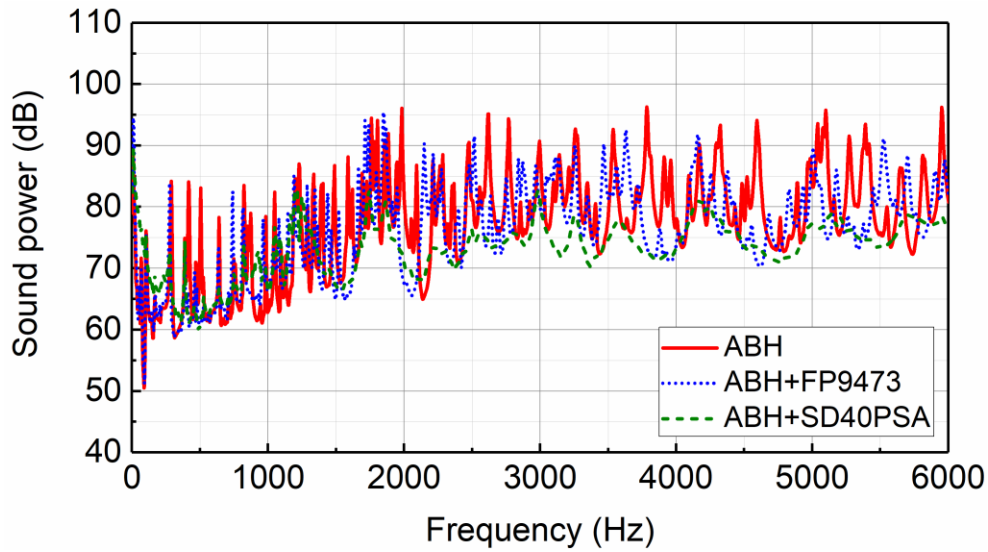


Figure 5.5 Measured radiated sound power of test samples: (a) without damping material (solid line); (b) with damping material FP9473 (dot line); (c) with Damping material SD40PSA (dash line). DL denotes damping layer.

5.3.3 Sound radiation mechanism analyses

5.3.3.1 Stiffness-controlled sound radiation efficiency

The observed reduction in the sound radiation efficiency below the cut-on frequency in [Section 5.3.1](#) can actually be attributed to the structural stiffness changes due to the inclusion of the ABH cell. This can be demonstrated by examining a uniform plate having the same mass, but with a reduced stiffness or thickness (not shown here). Results show that the observed reduction in the sound radiation efficiency of the ABH plate before the ABH cut-on is merely due to the overall stiffness reduction of the plate, instead of the intrinsic ABH feature. This explains the aforementioned increase in the sound radiation efficiency when damping layers are used over the ABH indentation, in

which case the added stiffness of the damping layers is non-negligible as compared to the thinnest part of the indentation.

5.3.3.2 *Sound radiation within the transonic boundary*

When bending waves travel across ABH boundary toward its center, with smoothly decreasing structural thickness, their phase velocity gradually reduces. For a given frequency above the critical frequency of the flat portion of the plate, a subsonic region may be created inside the ABH cell if the thickness of the ABH indentation is small enough. This subsonic region is delimited by a circle, referred to as the transonic boundary, whose radius is defined by

$$R_t = \left(c_a^2 \sqrt{12\rho_0(1-\mu_0^2)} / E_0 / (2\pi f \varepsilon) \right)^{1/3} \quad (5.7)$$

As an example, the sound power radiated from the area inside the transonic boundary corresponding to 4000 Hz ($R_t=118.4$ mm) is evaluated for three different plates: the reference flat plate and two ABH plates with/without damping layers.

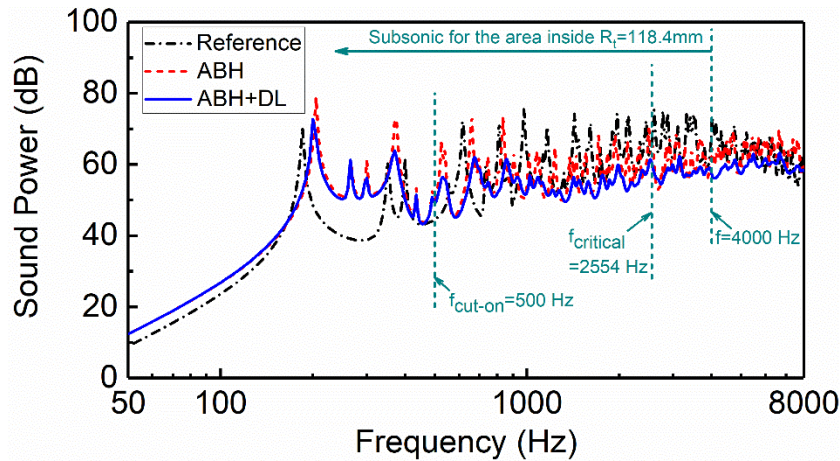


Figure 5.6 Sound power radiated from the region inside the area with a radius of 118.4 mm, corresponding to the transonic boundary at 4000Hz.

Figure 5.6 shows that, below the cut-on frequency (500 Hz), the investigated region (inside the transonic boundary) of the ABH plates (with and without damping layers) generates a higher sound power as compared with the reference plate. This is definitely due to the ABH-induced amplification of the vibration amplitude in the center area of the ABH cell, despite the aforementioned reduction in the radiation efficiency. Above 500 Hz, the ABH effect is cut-on, resulting in an obvious sound power reduction, especially when the frequency approaches the critical frequency at $f_{critical} = 2554 \text{ Hz}$. Up to 4000 Hz, the entire region inside the transonic boundary of ABH plates is subsonic. This results in the remarkably reduced sound power as compared with its counterpart in the reference panel. Above 4000 Hz, the transonic boundary starts to enter into the investigated area and keeps shrinking with the increase of the frequency, containing both subsonic and supersonic structural waves, along with greatly concentrated vibration

energy. When this happens, the sound power reduction, albeit clearly observable, becomes less significant due to the existence of acoustically fast structural waves.

5.3.3.3 *Sound radiation efficiency with transonic boundary changes*

Variations of the sound radiation efficiency along with transonic boundary changes are quantified. Specifically, the radiation efficiency of a series of concentric rings, moving from the inside to the outside of the transonic boundary are investigated. In each step, the width of the rings is kept constant, $\Delta R = 1/6 R_t$, as shown in Figure 5.7. The radiation efficiencies of the rings at different frequencies (from 4000 Hz to 8000 Hz) are compared in Figure 5.8(a). At each frequency, the inner ring radius R_{inner} is normalized by its corresponding transonic boundary radius. A uniform plate is also used as reference.

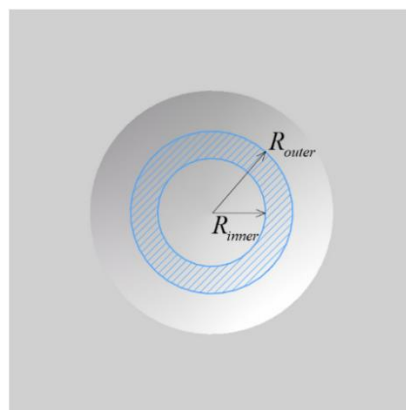
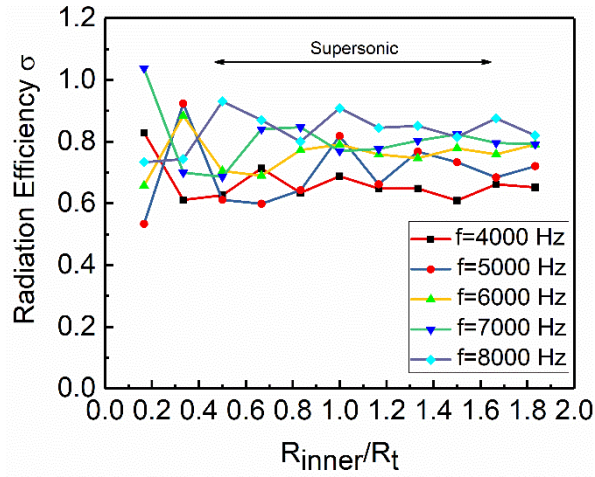
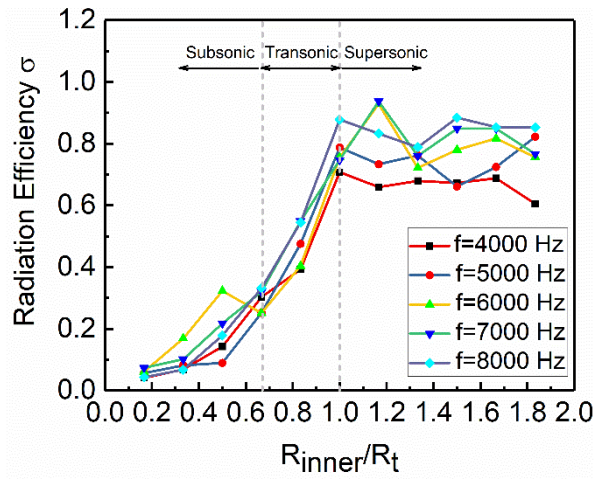


Figure 5.7 Diagram of investigated ring on the ABH plate.



(a)



(b)

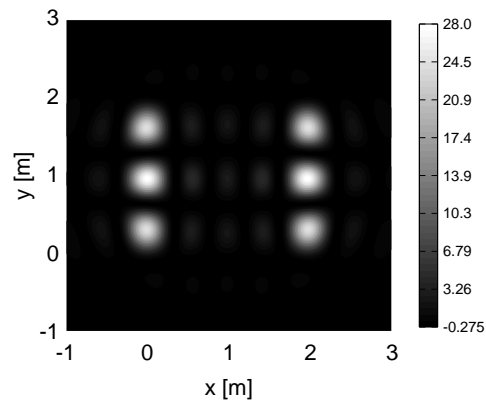
Figure 5.8 Radiation efficiency of rings around transonic boundary of ABH plate compared with those of reference plate at different frequencies: (a) Reference plate; (b) ABH plate.

For the flat plate, (Figure 5.8(a)) shows that, despite slight variations, the radiation efficiency for each calculated ring is consistently high and rather stable. As expected, with the increase of frequency, the radiation efficiency generally increases. For the ABH

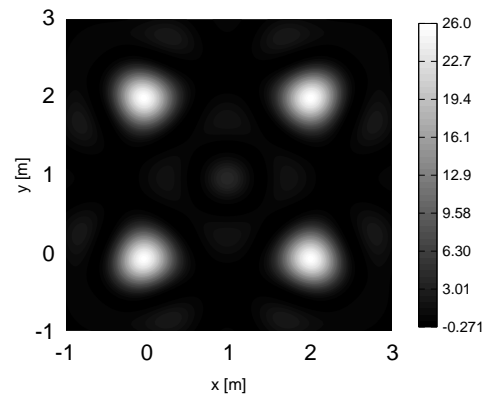
plate, similar phenomenon can be observed when $R_{inner} / R_t > 1.0$ (Figure 5.8(b)) when the ring moves outside the transonic boundary and enters into supersonic region; as a result, its radiation efficiency is consistently high. When the rings are inside their respective transonic boundaries, *e.g.* $R_{inner} / R_t < 1.0$, the sound radiation efficiency of the rings dwells at relatively low levels. While the rings passing through the transonic boundary, their corresponding radiation efficiencies undergo a sharp rise. This variation in the sound radiation efficiency is consistent with what one might expect from classical structural acoustic theory.

5.3.3.4 Verification of Supersonic acoustic intensity

To verify the procedures of supersonic intensity in a spatial domain in Section 5.2, the supersonic intensity of normal modes of a simply supported uniform square plate is first analyzed. The dimension of the plate is 2 m \times 2 m. The plate is surrounded by a rigid baffle. To compare the results obtained in spatial domain with those obtained by William [122] using Fourier transform analyses, two representative normal modes below the critical frequency are chosen: (11, 3) and (11, 9) modes, corresponding to ka amounting to 17.92 and 12 respectively. Figure 5.9 shows the supersonic intensity of these two modes. As expected, an edge mode and a corner mode are observed, in line with the classic structural radiation theory. Meanwhile, the obtained supersonic intensity matches well with that obtained in Ref. [122].



(a)



(b)

Figure 5.9 Supersonic intensity of normal modes: (a) (11, 3) mode at $ka=17.92$;

(b) (11, 9) mode at $ka=12$.

5.3.3.5 Numerical illustration of the supersonic acoustic intensity

To further illustrate the sound radiation properties of the ABH plate, various forms of acoustic intensity are calculated using the extended 2D Daubechies wavelet (DW) model, in comparison with its uniform counterpart for a few selected representative frequencies. The acoustic pressure over the vibrating surface and the baffle is calculated using Rayleigh integral in [Equation \(2.23\)](#). Supersonic acoustic intensity maps are

compared with the classical acoustic intensity maps. Variations of the supersonic acoustic intensity alongside the transonic boundary changes are also illustrated.

Figure 5.10(a) and Figure 5.10(b) show the supersonic acoustic intensity of the uniform plate and ABH plate, respectively, at 2000 Hz which is below the critical frequency. To facilitate the comparison, same scale is used for both plots. Supersonic acoustic intensity maps of the uniform plate in Figure 5.10(a) shows that effective sound radiation is basically from the two edges of the panel along y direction, which resembles the edge mode radiation, although the frequency is not a structural natural frequency to warrant perfect radiation cancellation as expected from the classical structural radiation theory. In comparison, the inclusion of the ABH indentation alters the radiation pattern as shown in Figure 5.10(b). Nevertheless, effective sound radiation still originates from the edge of the panel with a more scattered pattern and a reduced level as compared to the uniform plate. Classical acoustic intensity map of the ABH plate, Figure 5.10(c), shows that, because of the energy concentration, the energy level inside ABH cell is indeed very high, with both positive and negative values, specific to the near field feature of the sound radiation. With the circulating intensity being removed, supersonic acoustic intensity indeed allows for the identification of the hot spots over the plate, which are responsible for effective sound radiation into the far field. In this case, it is predominantly confined to the uniform part outside the ABH boundary, as shown in Figure 5.10(b).

Following the same procedure, evolutions of these intensity maps with increasing frequencies ($f=4200$ Hz and 7300 Hz) are illustrated from [Figure 5.10\(d\)](#) to [Figure 5.10\(i\)](#). Meanwhile, changes of the corresponding transonic boundary (marked by a dash circle inside the ABH boundary) are also shown for the three arbitrarily chosen frequencies, all above the critical frequency of the flat panel. For the flat plates ([Figure 5.10\(d\)](#) and [Figure 5.10\(g\)](#)), when the frequency increases, the sound radiation pattern shown by the supersonic intensity maps become more regular over the entire plate surface, similar to the surface radiation pattern. For the corresponding ABH plate, a transonic boundary appears and gradually reduces in size with the frequency. However, different from the uniform plate, the distribution of the effective sound radiation areas becomes less regular. More specifically, apart from the upper-left corner of the panel where the excitation force is applied, most energetic sound radiators gradually move into the ring between the ABH periphery and transonic boundaries when frequency increases ([Figure 5.10\(e\)](#) and [Figure 5.10\(h\)](#)). This ring area, being supersonic, exhibits high radiation efficiency and contains a considerable amount of vibration energy at the same time. In terms of intensity level, judged by the darkness of the maps (or by the colors on-line), it is also obvious that the flat plates radiate much more efficiently than the ABH plate does, even though the near field acoustic intensity could be high ([Figure 5.10\(f\)](#) and [Figure 5.10\(i\)](#)) inside the subsonic region of the ABH plate. These results agree with the sound radiation properties along with transonic boundary changes analyzed in [Section 5.3.3.2](#).

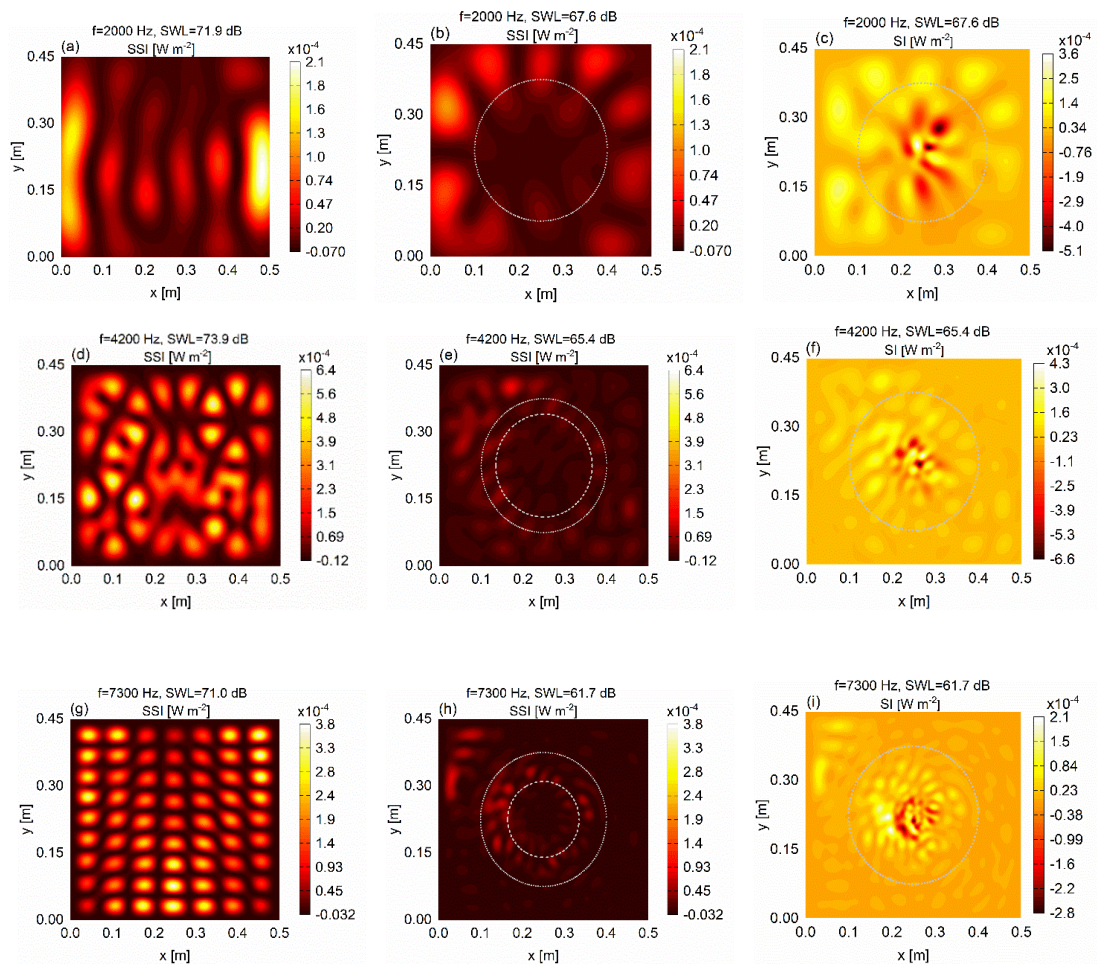


Figure 5.10 (Color on-line) Acoustic intensity maps: (a-b-c) $f=2000$ Hz; (d-e-f) $f=4200$ Hz; (g-h-i) $f=7300$ Hz. (a-d-g) supersonic acoustic intensity of the reference plate; (b-e-h) supersonic acoustic intensity of the ABH plate; (c-f-i) acoustic intensity of the ABH plate. The dot circle denotes the ABH periphery and the dash circle the transonic boundary. SSI indicates the supersonic acoustic intensity; SI the acoustic intensity and SWL the total radiated sound power.

5.4 Summary

As an alternative to conventional FEM, the proposed 2D Daubechies wavelet (DW) model is utilized to explore the sound radiation mechanisms of a plate embedded with a circular ABH indentation. The model allows the exploration of ABH-specific sound radiation features in relation to the transonic boundary changes. Supersonic acoustic intensity in spatial domain is used to visualize the sound radiation pattern and identify the dominant sound radiation areas on the vibrating surface of the ABH plate. Numerical analyses lead to the following main conclusions:

- 1) The investigated ABH plate is shown to exhibit a significantly reduced sound radiation efficiency in a broad dynamic frequency range as compared to its uniform counterpart. Physical mechanisms in different frequency ranges are revealed. Before the cut-on of the ABH effect, this is mainly due to the weakening of the overall structural stiffness, which persists until the critical frequency. Above the critical frequency, the subsonic region within the transonic boundary results in an impaired sound radiation efficiency of the plate due to the subsonic structural waves. Supersonic acoustic intensity maps show that the regularly distributed supersonic waves over the flat plate are altered by the presence of the ABH indentation. As a result, the far field acoustic energy is mainly generated by the ring area between the ABH periphery and the corresponding transonic boundary.

2) For the investigated configuration, an increase in the sound radiation efficiency of the ABH panel is observed, which is caused by the added stiffness effect of the damping layer. This points at the need of striking a balance between the dual effects of the damping layers: damping enhancement and stiffness-induced increase in the sound radiation efficiency of the structure.

The present work attempts to claim a three-fold novelty: 1). A wavelet-based model is established for the acoustic radiation prediction as an alternative to the FE/BE. 2). ABH effect on the sound radiation is demonstrated and physically explained using parameters such as supersonic acoustic intensity and transonic boundary changes. This allows the visualization of the sound radiation in spatial domain and hopefully enriches the existing understanding on the sound radiation of ABH structures. 3). The stiffness effect of damping layers on the increase of the sound radiation efficiency calls for a careful handling of the viscoelastic coating for sound radiation applications.

Chapter 6

Topological optimization of damping layers

6.1 Introduction

Controlling sound radiation of vibrating structures is an important research topic for many engineering applications. ABH structures have shown great potential in reduction of sound radiation, as demonstrated in [Chapter 5](#). As a counter measure for impaired wave reflections caused by truncation thickness, the deposition of a thin layer of viscoelastic damping materials over the ABH portion has been shown to be necessary to draw energy away from the system [\[12\]](#), a phenomenon which was later confirmed in other works [\[39, 46, 50\]](#). Therefore, the use of the damping layers constitutes an indispensable part in the realization of the ABH effect.

However, it was also observed that an excessive use of the damping layers could cause adverse effects. For example, it was noted that the coating layer may generate non-negligible added stiffness effect to the host structure [\[46\]](#), which in turn would affect the expected ABH effect. Meanwhile, the intuitive way of coating the center of the indentation in an imperfect ABH plate with a modified ABH thickness profile would increase its minimum thickness and then offset the focal point of energy localization [\[26\]](#). Using a laser excitation and wave decomposition technique, the existence of an optimal thickness for the damping layer which leads to minimum wave reflections was

experimentally determined. It was observed that the excessive use of the coating may compromise or even jeopardize the expected energy focalization due to its dynamic interference with the host structure, leading to an impaired energy dissipation [70]. Also, it was discovered in Chapter 5 that the use of damping layers could be responsible for the increase of sound radiation efficiency of an ABH panel due to the additional stiffness effect. All these observations point at the need for a meticulous design and optimization of the layout of the damping layers in order to strike a balance between their dual effects: damping enhancement and stiffness-induced increase in the wave reflection and sound radiation efficiency. However, systematic investigations of the issue, as well as the development of the required topological optimization tools, are still lacking.

Topological optimization of sound radiation requires the provision of two major components: an efficient vibro-acoustic solver and an adaptive optimizer. For the former, the commonly used FE/BE discretizes the solution domain into meshes, a process that needs to be repeated in every optimization loop, which is very computationally intensive and cumbersome. In that regard, the semi-analytical sound radiation model, detailed previously, shows its advantages. The model provides an ideal platform to incorporate the add-on damping layers and accommodate the changing topology incurred during the optimization process. In fact, due to the energy-based and modular nature of the model, the coating area to be optimized can be discretized into a number of elementary sections. Employing the Solid Isotropic Material with Penalization (SIMP) method [126], the stiffness and mass matrices for each section, and the complex normal velocity of the

plate are readily available for sensitivity analysis of the objective function with respect to design variables.

As another important component, structural topology optimization has been widely studied for various vibration problems such as the optimization of fundamental eigenfrequencies [127-129], band gaps [130, 131], system loss factors [132] and dynamic compliance [133] *etc.* Minimization of structural vibrations [134-137] and their sound radiation under harmonic excitations is another important topic for topology optimization. So far, much work has focused on the topology optimization of structures to achieve better acoustical properties. Using a mixed finite element formulation, Yoon *et al.* [138] minimized the averaged sound pressure of 2D vibro-acoustic structures within a frequency interval. Du and Olhoff [139] topologically optimized vibrating bi-material structures to minimize their radiated sound power. Meanwhile, optimization of damping layers to minimize vibration response and sound radiation has also attracted the attention of many researchers. Employing the complex mode superposition method, damping layers in shell structures were optimized to minimize the vibration amplitude at specific points [135, 140]. Zhang and Kang [141] also optimized the layout of damping layers in a square plate and a hollow box to achieve minimized sound pressure at specific points under harmonic excitations. Yan *et al.* [142] topologically optimized the damping layer for minimized residual vibration under impact loads.

So far, topological optimization design of ABH structures for sound radiation minimization has not been dealt with in the literature. The only remotely related paper is the one by Rothe *et al.* [100], in which the position of acoustic black holes was optimized for sound radiation of ABH plates using evolutionary optimization algorithm. As previously discussed, damping layer plays an important role in achieving ABH effect for the mitigation of vibration and sound radiation. Considering the dual conflicting effects of the damping layers, *e.g.* enhancing system damping and increasing its sound radiation efficiency, and the lack of analysis and understanding on the topic, we explore the issue in this Chapter by proposing a general methodology for the topological optimization of the layout of damping layers on an acoustic black hole (ABH) plate. By combining the previous semi-analytical wavelet plate model, the Solid Isotropic Material with Penalization method (SIMP) and the Optimality Criteria (OC) method [143], the sound radiation into a free space by ABH plates is minimized at either a given frequency or within a frequency band.

This Chapter is organized as follows. Section 6.1.1 formulates the topology optimization. As an important component in the optimization process, a sensitivity analysis of the objective function with respect to design variables is derived using adjoint variable method (AVM), under the wavelet framework in Section 6.1.2. The adopted optimization method is validated using a square uniform plate in Section 6.1.3. Numerical results and analyses are presented in Section 6.2. Main focus is put on the minimization of the radiated sound power of ABH plates. Effects of damping layers

deposited at the central area of the ABH indentation are first analyzed. With the same amount of damping material, optimal placement of the damping layers is then topologically searched at a given frequency or within a frequency band. For comparison, minimization of the mean square velocity of the plates is also conducted. Wavenumber analyses are performed on different configurations to illustrate the underlying physical process as a result of the optimization. Finally, [Section 6.3](#) summarizes this chapter.

6.1.1 Formulation of topological optimization

The layout of the damping layers is to be optimized within a pre-defined search/design space, which is divided into a number of elementary sections. [Figure 6.1](#) schematically shows an example of the optimized configuration, in which the segmented elements are denoted either by 1 or 0, indicating that the corresponding area is either fully coated or not coated by damping layer, respectively. Note during the optimization process, however, values associated to each element evolve from 0 to 1, before reaching the final optimized configuration, as detailed later.

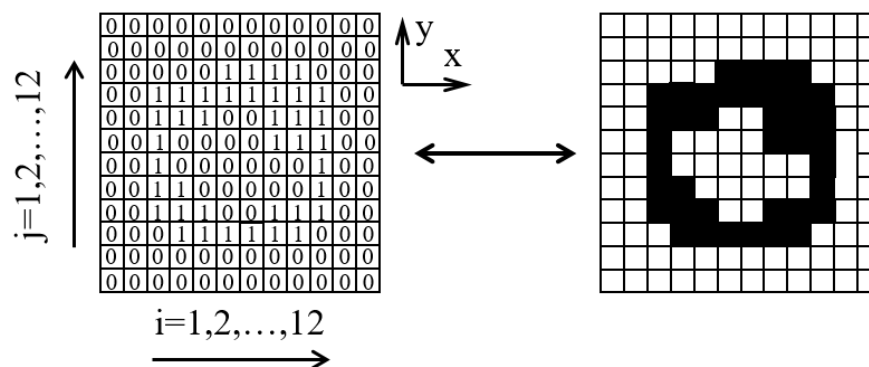


Figure 6.1 Optimized layout of damping layers.

The model described in [Chapter 2](#) is used to topologically optimize the layout of a given amount of damping material to minimize various physical quantities such as the plate vibration or the radiated sound power. In the latter case, assuming $\mathbf{S} = \mathbf{K} - \omega^2 \mathbf{M}$, the optimization problem within a frequency band, from f_l to f_u , can be mathematically defined as

$$\begin{aligned}
\min. \quad & C = \int_{f_l}^{f_u} \mathbf{V}^H \mathbf{R} \mathbf{V} df \\
\text{s.t.} \quad & \mathbf{S} \mathbf{A} = \mathbf{F} \\
& \sum_{e=1}^{N_e} \rho_e v_e - f_v \sum_{e=1}^{N_e} v_e \leq 0 \\
& 0 < \rho_{\min} \leq \rho_e \leq 1
\end{aligned} \tag{6.1}$$

in which C is the objective function; min. is the abbreviation of *minimize*; and s.t. the abbreviation of *subject to*. The constraint condition [Equation \(6.1\)](#) imposes a restriction on the volume of the damping material used in the optimization process. f_v represents the prescribed volume fraction. N_e is the total number of segmented elements within the design area. v_e is the volume of damping material for element e . Note ρ_e is an important control parameter defining the degree of fulfillment of an element e by the damping material, which can be regarded as a relative density term of the damping layer. The constraint condition $0 < \rho_{\min} \leq \rho_e \leq 1$ in [Equation \(6.1\)](#) indicates that the relative density changes within 0 and 1 in the process of iteration. Usually, a lower limit ρ_{\min} , a small positive value, should be assigned in the calculation procedure.

With the aforementioned topology representation, the global stiffness and mass matrices of the system are assembled as

$$\begin{aligned}\mathbf{K} &= \mathbf{K}^{plate} + \sum_{e=1}^{N_e} \mathbf{K}_e^{damp} \\ \mathbf{M} &= \mathbf{M}^{plate} + \sum_{e=1}^{N_e} \mathbf{M}_e^{damp}\end{aligned}\quad (6.2)$$

where \mathbf{K}^{plate} and \mathbf{M}^{plate} are the stiffness and mass matrices of the base plate respectively; \mathbf{K}_e^{damp} and \mathbf{M}_e^{damp} are those of the damping layers for section e , respectively. Employing the Solid Isotropic Material with Penalization (SIMP) method [126], \mathbf{K}_e^{damp} and \mathbf{M}_e^{damp} can be expressed as

$$\begin{aligned}\mathbf{K}_e^{damp} &= (\rho_e)^{\tilde{p}} \tilde{\mathbf{K}}_e^{damp} \\ \mathbf{M}_e^{damp} &= (\rho_e)^{\tilde{q}} \tilde{\mathbf{M}}_e^{damp}\end{aligned}\quad (6.3)$$

in which $\tilde{\mathbf{K}}_e^{damp}$ and $\tilde{\mathbf{M}}_e^{damp}$ are respectively the stiffness and mass matrices for section e when $\rho_e = 1$. \tilde{p} and \tilde{q} are the penal factors that are selected to be 3 in this study.

With given initial values, the design variable ρ_e for each section e will be updated during the optimization process. When the iteration terminates to reach a complete converged result, ρ_e will be either 0 or 1, corresponding to an empty and fully coated element, respectively.

6.1.2 Sensitivity analysis for optimization

The minimization problem defined in Equation (6.1) requires the calculation of the sensitivity of the objective function C with respect to the design variable ρ_e . The sensitivity of the objective function is derived using adjoint variable method (AVM) [135]. To make the paper self-contained, some key equations related to AVM are recalled from Ref. [135], cast into the present modelling framework and briefly

presented below. Recall Equation (2.27), $\mathbf{V} = \mathbf{\Phi}\mathbf{\dot{A}}$, it seems that the objective function C depends on the complex coefficients \mathbf{A} . To derive the sensitivity expression, C is written as:

$$C = C(\mathbf{A}) + \boldsymbol{\mu}_1^T (\mathbf{S}\mathbf{A} - \mathbf{F}) + \boldsymbol{\mu}_2^T (\bar{\mathbf{S}}\bar{\mathbf{A}} - \bar{\mathbf{F}}) \quad (6.4)$$

where $\boldsymbol{\mu}_1^T$ and $\boldsymbol{\mu}_2^T$ are the adjoint vectors.

Differentiating Equation (6.4) with respect to ρ_e yields

$$\frac{dC}{d\rho_e} = \boldsymbol{\mu}_1^T \frac{\partial \mathbf{S}}{\partial \rho_e} \mathbf{A} + \boldsymbol{\mu}_2^T \frac{\partial \bar{\mathbf{S}}}{\partial \rho_e} \bar{\mathbf{A}} + \left(\frac{\partial C}{\partial \mathbf{A}^R} + \boldsymbol{\mu}_1^T \mathbf{S} + \boldsymbol{\mu}_2^T \bar{\mathbf{S}} \right) \frac{\partial \mathbf{A}^R}{\partial \rho_e} + \left(\frac{\partial C}{\partial \mathbf{A}^I} + i\boldsymbol{\mu}_1^T \mathbf{S} - i\boldsymbol{\mu}_2^T \bar{\mathbf{S}} \right) \frac{\partial \mathbf{A}^I}{\partial \rho_e} \quad (6.5)$$

Assuming

$$\boldsymbol{\mu}_1^T \mathbf{S} = -\frac{1}{2} \left(\frac{\partial C}{\partial \mathbf{A}^R} - i \frac{\partial C}{\partial \mathbf{A}^I} \right) \quad (6.6)$$

and $\boldsymbol{\mu}_2^T = \boldsymbol{\mu}_1^T$, where i is the imaginary unit, Equation (6.5) can be written as

$$\frac{dC}{d\rho_e} = 2 \operatorname{Re} \left(\boldsymbol{\mu}_1^T \frac{\partial \mathbf{S}}{\partial \rho_e} \mathbf{A} \right) \quad (6.7)$$

Discretizing the integration in Equation (6.1) and considering Equation (2.27) yield

$$\begin{aligned} \frac{\partial C}{\partial \mathbf{A}^R} &= \omega^2 \sum_{i=1}^N \frac{\partial C}{\partial \mathbf{W}_i^R} \frac{\partial \mathbf{W}_i^R}{\partial \mathbf{A}^R} = 2\omega^2 \mathbf{W}_R^T \mathbf{R}\boldsymbol{\Phi} \\ \frac{\partial C}{\partial \mathbf{A}^I} &= \omega^2 \sum_{i=1}^N \frac{\partial C}{\partial \mathbf{W}_i^I} \frac{\partial \mathbf{W}_i^I}{\partial \mathbf{A}^I} = 2\omega^2 \mathbf{W}_I^T \mathbf{R}\boldsymbol{\Phi} \end{aligned} \quad (6.8)$$

where \mathbf{W} is the complex displacement vector of the plate with subscripts R and I indicating the real part and imaginary part, respectively. N is the number of vibrating points on the investigated system. Substituting Equation (6.6) and Equation (6.8) into Equation (6.7) yields

$$\begin{aligned}\frac{dC}{d\rho_e} &= 2\text{Re}\left(\mathbf{\mu}_1^T \frac{\partial \mathbf{S}}{\partial \rho_e} \mathbf{A}\right) \\ &= -2\sum_{j=1}^J \omega_j^2 \text{Re}\left(\mathbf{W}^H \mathbf{R} \Phi \mathbf{S}^{-1} \frac{\partial \mathbf{S}}{\partial \rho_e} \mathbf{A}\right) \Delta f\end{aligned}\quad (6.9)$$

in which J is the number of discretized frequencies. Optimizations at a single frequency can be treated as a special case of the above defined optimization problem.

In that case, Equation (6.9) degenerates to

$$\frac{dC}{d\rho_e} = -2\omega^2 \text{Re}\left(\mathbf{W}^H \mathbf{R} \Phi \mathbf{S}^{-1} \frac{\partial \mathbf{S}}{\partial \rho_e} \mathbf{A}\right)\quad (6.10)$$

Meanwhile, if the focus is on the minimization of the plate vibrational response in terms of mean square velocity, a parallel formulation can be easily established by following the same procedure. In that case, Equation (6.9) and Equation (6.10) still hold by simply replacing the radiation resistance matrix \mathbf{R} by a unit matrix. Using the above sensitivity expressions, the relative density ρ_e for each section e is updated using an optimizer based on Optimality Criteria (OC) method [143] by

$$\rho_e^{\delta+1} = \left(B_e^\delta\right)^\zeta \rho_e^\delta\quad (6.11)$$

where $\tilde{\delta}$ is the number of iteration; ζ the numerical damping coefficient [143] and $B_e^\delta = \max\left(0, -(dC/d\rho_e)/\lambda\right)$, where λ is a Lagrangian multiplier which can be

obtained using bi-sectioning algorithm. During the process of iteration, a mesh-independency filter [144] is used to avoid the checkboard pattern.

6.1.3 Validation examples

The proposed topology optimization procedure involves two modules: a numerical solver of the physical system (vibration and sound radiation model) and an optimizer. The former has been thoroughly validated in a previous work, in terms of both vibration and sound radiation prediction. Hereafter, the optimizer is to be validated. To that end, the test case used in [135] is considered, in which damping layers coated on a simply supported square plate are topologically optimized. The plate is made of aluminum and has a dimension of $3 \times 3 \times 0.02$ m. Using the same set of geometrical and material parameters, the current model differs slightly from [135] in two aspects: 1) a structural damping model via complex Young's modulus is used for the damping layer in the present model, instead of a Rayleigh damping model used in [135]; 2) the plate is symmetrically covered on both sides in the current model, whilst in Ref. [135], the same amount of damping was applied on only one side of the plate.

The damping layers are discretized into 30×30 meshes, in contrast to 60×60 meshes used in the Ref. [135]. Same as in [135], a point force excitation is applied at the center of the plate. The square of the amplitude of vibration displacement at the excitation point is chosen as the objective function. The iteration process terminates

when the convergence criteria $(|\rho_e^{\delta+1} - \rho_e^\delta| / \rho_e^\delta)_{\max} < 0.01\%$ is satisfied. Using the optimization method described in Sections 6.1.1 and 6.1.2, the resulting optimal damping layout is compared with the results given in [135] using mathematical programming algorithm (MMA). Among several frequencies being tested, three typical ones are shown in Figure 6.2 for $f=30, 60, 90$ Hz, respectively. It can be seen that both set of results agree in terms of coverage topology. The present model uses a smaller number of elements which inevitably affects the resolution of the image. Meanwhile the aforementioned differences in the model also contribute to the observed differences. Nevertheless, the proposed optimization algorithm gives the optimized configurations, consistent with results from [135], thus validating the established optimization approach.

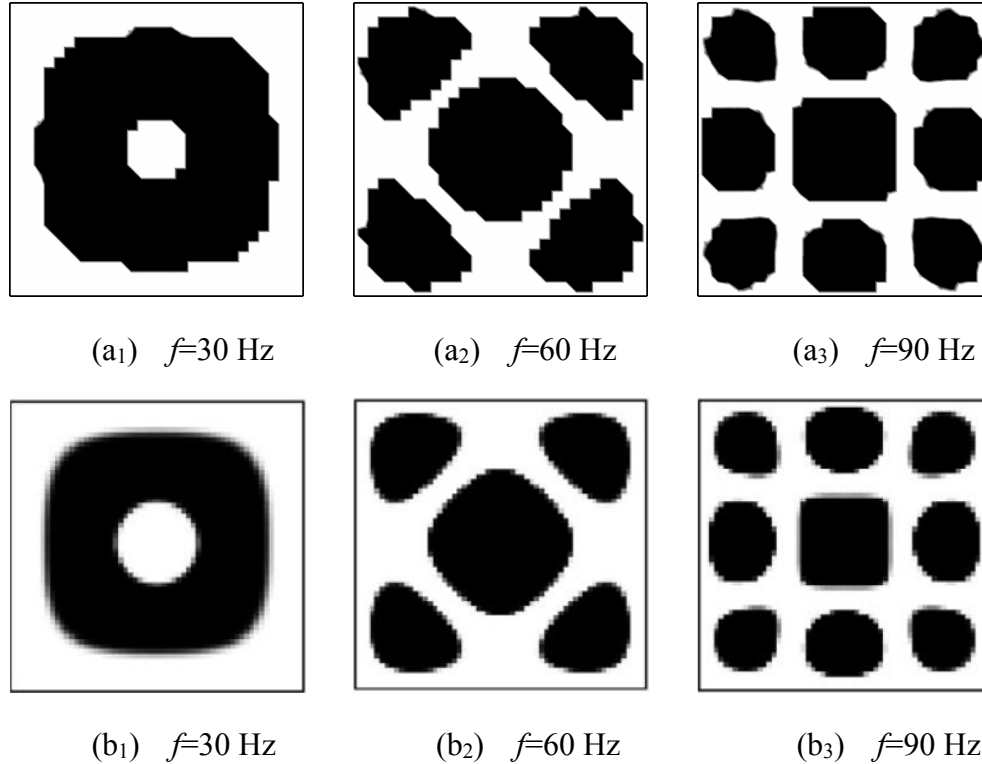


Figure 6.2 Optimal layout of damping layers at different frequencies: Present model with OC method (a₁-a₂-a₃); Results from [135] with MMA method ((b₁-b₂-b₃)).

6.2 Numerical analyses

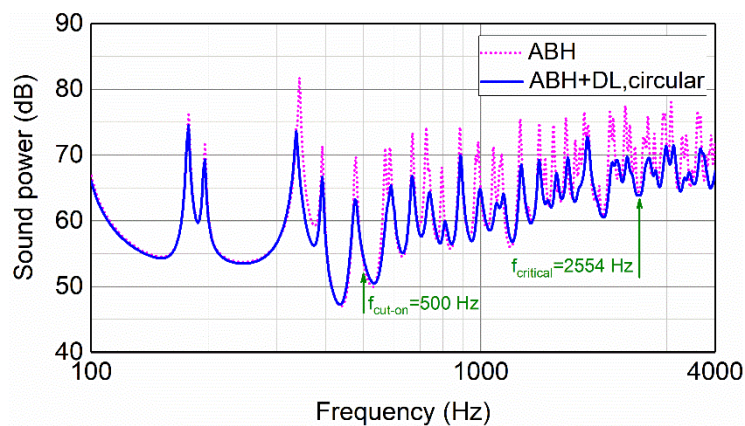
Numerical examples and analyses use a simply supported ABH plate with geometrical and material parameters the same as in Table 5.1. Apart from those previously defined parameters, additional ones include the densities ρ_0 , ρ_d and Poisson's ratios ν_0 , ν_d for the plate and the damping layers, respectively. The reference case is defined as the one with central part of the ABH indentation fully coated inside a circle with a radius of $R_d = 86.5$ mm. In this reference case, referred to as circular case hereafter, the damping layer has a uniform thickness $h_d = 0.3$ mm on each side of the plate. The basic sound radiation phenomena of this reference case, in particular the effect of the damping layers, will first be illustrated. Then, topological optimization will be applied to determine the optimal coating layout which allows the minimization of the radiated sound power, by using the same amount of damping material, at either a given frequency or within a pre-defined frequency band. A harmonic point force is applied at (0.05, 0.315) m over the uniform portion.

6.2.1 Effect of damping layers on the vibration and sound radiation of ABH plates

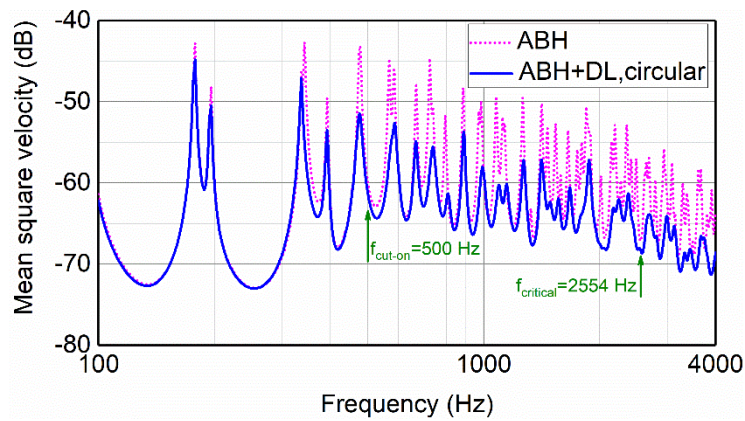
Using the previously developed DW model, the effect of the damping layers (reference case with central circular coating) on the vibration of the ABH plates and

their radiated sound field are first analyzed to show the necessity of the optimization. A bare ABH plate without any damping treatment is taken as comparison basis. Some important comparative results between the ABH plates with/without central circular coating are recapped here, as shown in [Figure 6.3](#). [Figure 6.3 \(a\)](#) and [Figure 6.3 \(b\)](#) show the comparisons in terms of the radiated sound power level and the corresponding mean square velocity level (referenced to $1 \text{ m}^2/\text{s}^2$) of the plates, averaged over their entire surface. It can be seen that, compared with the bare plate, the use of the damping layers obviously reduces the resonance peaks as well as the overall level of the both the plate vibration level and the radiated sound power, especially above the cut-on frequency [\[39\]](#). The so-called cut-on frequency is an indicative frequency at which the wavelength of the incident bending waves starts to be equal to the characteristic dimension (the diameter of the circular indentation in the present case) of the ABH indentation. It is commonly accepted that the bending waves interact more effectively with the ABH indentation above this frequency, thus producing systematic ABH effects. In the present case, the cut-on frequency is 500 Hz. Above the cut-on frequency, these aforementioned phenomena are obviously due to the coating-enhanced ABH effects in terms of energy focalization and dissipation towards the indentation center. A less known phenomenon, however, is the coating-induced changes in the sound radiation efficiency of the plate as shown in [Figure 6.3\(c\)](#). In fact, the deployment of the damping layers generates an obvious increase in the sound radiation efficiency of the plate, again more obvious and systematic after the ABH cut-on. The increase in the radiation efficiency is attributed to the additional stiffness of the damping layers rather than their

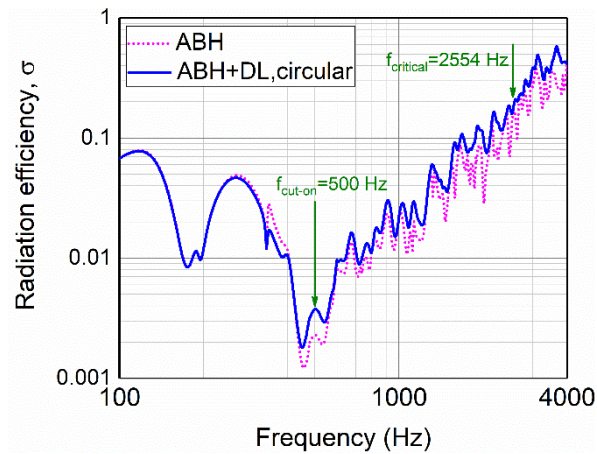
mass, as demonstrated in Section 5.3.1. The trend continues even after the critical frequency of the plate calculated based on the thickness of the uniform portion of the plate. Above critical frequency $f_{critical}$, the length of the bending waves inside the plate becomes larger than that of the acoustic waves. In another word, structural waves travel faster than their acoustic counterparts, thus producing the so-called supersonic structural waves, which are shown to be efficient in sound radiation by classical structural acoustic theory. Thanks to the gradually decreased thickness of the ABH indentation, at a given frequency above $f_{critical}$, a so-called transonic circular boundary with a radius in Equation (5.7) is created, which demarcates a subsonic region inside the circle with a supersonic region outside. Therefore, the inside region within R_t is less efficient in sound radiation. These observations point at the need for a meticulous design and optimization of the layout of the damping layers in order to strike a balance between their dual effects: damping enhancement and stiffness-induced increase in the sound radiation efficiency.



(a)



(b)



(c)

Figure 6.3 Comparison between ABH plate (dot line) and ABH plate with damping layers (solid line): (a) Radiated sound power; (b) Mean square velocity; (c) Radiation efficiency. DL denotes damping layer.

6.2.2 Topological optimization for the minimization of sound power

The optimization method is employed to seek solutions to the minimization of the radiated sound power of a plate defined in Section 6.2.1. at single frequencies. The design area is a square which frames the ABH external peripheral circle and is

discretized into 12×12 elements. The volume fraction f_v is restricted to 0.2618 to make sure that the total volume of damping layer is the same as the reference case with a circular coverage, as discussed in [Section 6.2.1](#).

An arbitrary frequency of 3480 Hz is chosen to show the typical evolution of the objective function (the radiated sound power level in the present case) during the iteration process in [Figure 6.4](#). It can be seen that the objective function undergoes a continuous decrease from 67.1 dB to approach a converged value of 64.9 dB after roughly 10 iterations. Meanwhile, the layout of the damping layer also evolves accordingly, starting from the initial uniform coverage to gradually converge to a stable and fully converged optimal configuration. The grey color shown in the map of configuration of damping layers at step 1 indicates that, at the beginning of iteration, the relative density, ρ_e , is quite different from either 0 or 1. With the increase of iteration loop, ρ_e gradually gets closer to 0 or 1. It is interesting to note that, at this particular frequency, the initially covered central area of the ABH indentation (step 4) tends to be gradually emptied, until reaching the final optimal layout in which the central portion of ABH indentation is not fully coated (steps 9-18), in contrast to the intuitive guess that one might have to simply cover the central area.

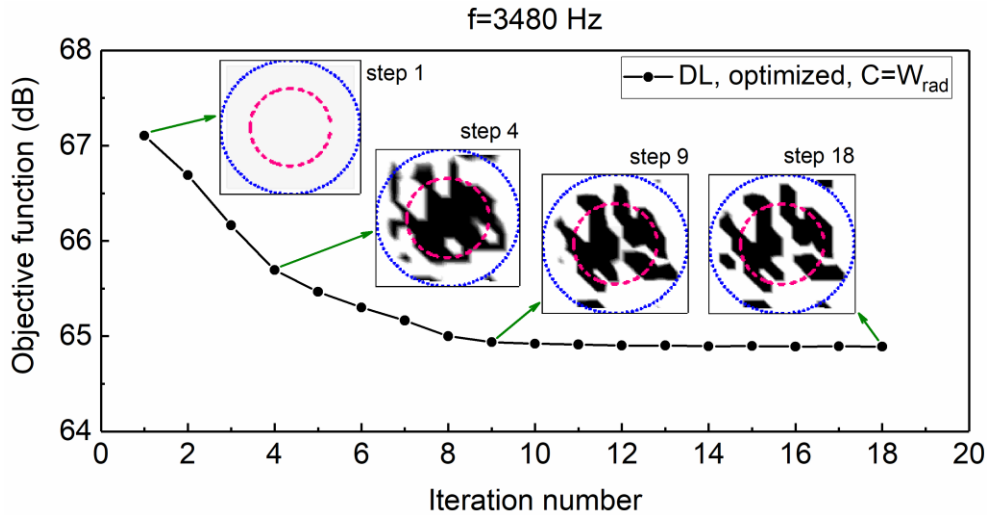
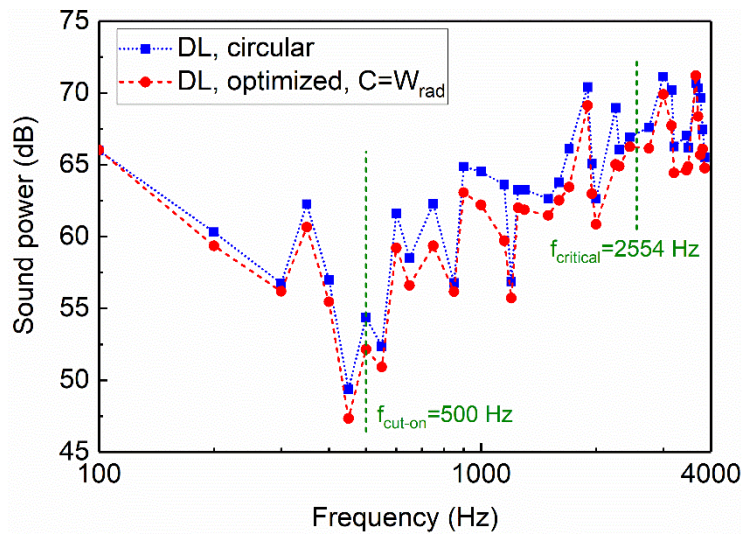


Figure 6.4 Convergence of iteration process at $f = 3480$ Hz. The outer dot circle represents the ABH peripheral circle, and the inner dash circle represents the circular coverage of damping layers. DL denotes damping layer and W the radiated sound power. Step 1 is the initial starting configuration.

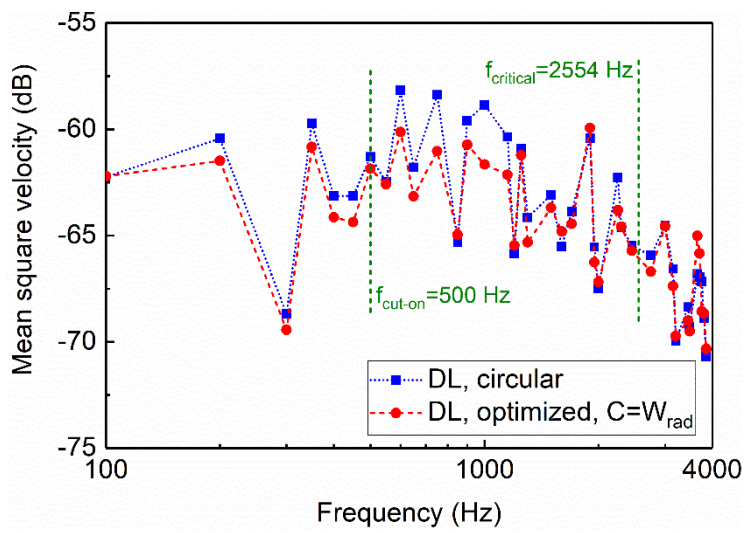
The same process can be followed for every given frequency of interest. The outcome of the optimization is shown in Figure 6.5(a)-(c) in terms of sound power level, mean square velocity level as well as the sound radiation efficiency, respectively. Again, results are compared with their reference counterparts with the circular coating using the same amount of damping materials.

Figure 6.5(a) shows that, compared with the circular case, the optimal damping layout results in a reduced radiated sound power of different level, which may go up to roughly 4 dB in the present case. Below the cut-on frequency (500 Hz), the effect of the optimization is trivial. The same observation also applies to the mean square velocity of

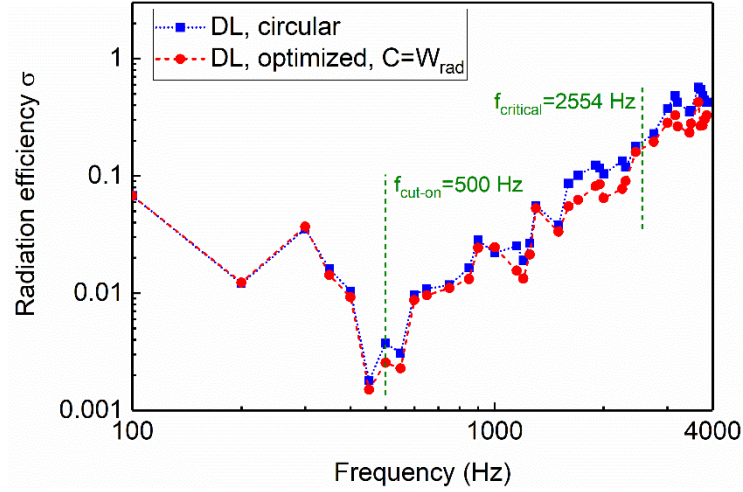
the plate (Figure 6.5(b)), as well as the sound radiation efficiency (Figure 6.5(c)). This is understandable since ABH effect is absent in this low frequency range so that the room for optimization is basically non-existent. In fact, as to be demonstrated later on, the finally reached optimized layout in the low-frequency range is basically the same as the central coverage case. Above the cut-on frequency, a systematic reduction in the radiated sound power starts to show as a result of the optimization. The mean square velocity level, however, though generally following the same reduction trend but to a less degree, exhibits an increase at some frequencies. Note that when approaching and exceeding the critical frequency (2554 Hz), changes in the vibration level becomes even smaller. The above observation suggests that the observed systematic reduction in the sound radiation cannot be totally attributed to the changes in the vibration level of the system. Instead, a possible change in the sound radiation properties of the structure due to the different coating layouts is expected. This is further confirmed by examining the corresponding changes in the sound radiation efficiency of the plate before and after optimization, as shown in Figure 6.5(c). It seems that, though not being directly used as the objective function, the sound radiation efficiency of the plate is almost systematically reduced by the optimization, more significantly at higher frequencies. This shows that the optimization impacts on the physical system in a way that its sound radiation properties are altered through a more reasonable design of the damping layer layout.



(a)



(b)



(c)

Figure 6.5 Comparison between initial case (square symbol) and the case of optimized sound power (circular symbol) at single frequencies: (a) Sound power; (b) Mean square velocity; (c) Radiation efficiency. DL denotes damping layer, and W the radiated sound power.

Meanwhile, the reduction in the radiation efficiency indicates that the plate is less effective in radiating sound. To better show the underlying physical process, a wavenumber transform analysis [87] is performed on the vibration velocity field of the ABH plates at 3480 Hz, with the circular and the optimized damping layout, respectively. To this end, the vibration velocity is transformed from spatial domain to wavenumber domain as:

$$\mathbf{V}(k_x, k_y, f) = \iint \mathbf{V}(x, y, f) e^{-j(k_x x + k_y y)} dx dy \quad (6.12)$$

where k_x and k_y are the wavenumbers in x and y directions, respectively, and $\mathbf{V}(k_x, k_y, f)$ is the vibration velocity in wavenumber domain. Figure 6.6 shows a plot

of the two normalized wavenumber components \bar{k}_x and \bar{k}_y of $\mathbf{V}(k_x, k_y, f)$, i.e., k_x and k_y are normalized with respect to $k = 2\pi f/c_a$, where c_a is the speed of sound. The circle on each figure denotes a unit radiation circle which demarcates the vibrational supersonic components of the plates (inside the circle) from the subsonic ones (outside the circle).

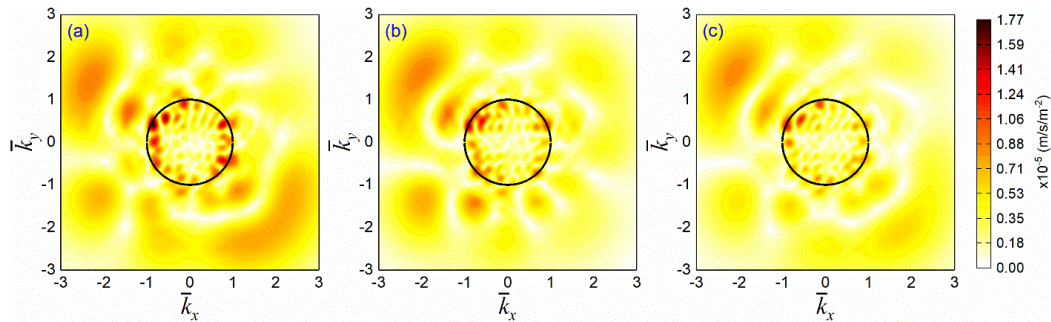


Figure 6.6 Wavenumber spectra of ABH plates at 3480 Hz: (a) ABH plate with no damping layers; (b) ABH plate with damping layers coated inside a central circle; (c) ABH plate with optimized damping layers. The solid circle indicates the normalized radiation circle with radius of $r=1$.

It can be seen from Figure 6.6 that for the bare plate (Figure 6.6(a)), energetic vibration components are mainly located inside the radiation circle. This is understandable since the frequency under investigation is above the critical frequency of the flat plate; therefore, supersonic components exist in the system. With circular damping coverage (Figure 6.6(b)), supersonic components inside the radiation circle is reduced. This trend is further accentuated with the optimal damping layout, as shown in Figure 6.6(c). Therefore, the wavenumber analysis further confirms the fact that the optimal layout of the damping layer changes the sound radiation properties of the plate

by reducing the supersonic components in the plate vibration, thus resulting in a minimized radiated sound power.

6.2.3 Vibration minimization versus sound power minimization

The previously established optimization methodology applies to the optimization of both sound radiation and structural vibration. Since the excessive use of the damping layer may affect both the wave reflection and sound radiation, probably in different ways, it is relevant to examine the issue to understand its impact on the final optimized system topology. To this end, the optimal damping layer layouts based on vibration minimization (using the mean square velocity, MSV, of the plate) and sound radiation minimization (using radiated sound power, W_{rad}) are compared at three representative frequencies: 100 Hz (before the ABH cut-on), 1700 Hz (after cut-on) and 3150 Hz (above the critical frequency). Results are tabulated in [Table 6.1](#) for comparisons. $C=MSV$ and $C=W_{rad}$ means that the objective functions are taken as the mean square velocity and radiated sound power, respectively.

It can be seen that, at the low-frequency of 100 Hz, which is below the cut-on frequency and around the first natural frequency (92 Hz) of the plate, both optimization problems lead to basically the same optimal damping layout with a central coverage. With the increase of frequency (above the ABH cut-on), differences between the two cases start to be noticeable. Specifically, compared with the structural vibration minimization, optimized coated area based on sound radiation tends to be further away

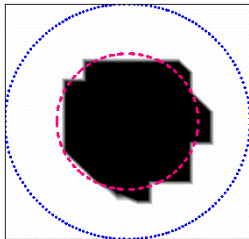
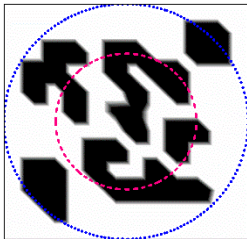
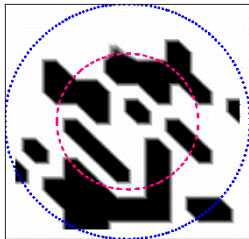
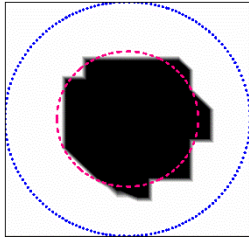
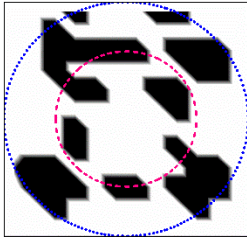
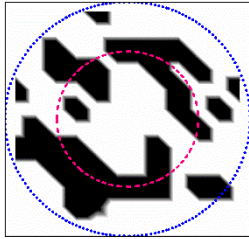
from the central portion of the ABH indentation. This is an indication that the adverse effect of the coating, which is presumably more significant at the ABH center, is more significant on sound radiation (e.g. increased sound radiation efficiency) than on structural vibration (increased wave reflections). To quantify this phenomenon and also to examine its applicability to other frequencies, a Coverage Ratio (CR) is used to quantify the fulfillment level of the central area of the ABH indentation. CR is defined as the ratio between the coated area inside the inner dash circle depicted in [Table 6.1](#) (corresponding to the periphery of the circular coverage) and the total area inside the circle.

CR curves for both the MSV and W_{rad} optimization within the entire frequency range of interest are compared in [Figure 6.7](#). It shows that, with only a few exceptions, CR based on W_{rad} optimization is smaller than its MSV-based counterpart at almost all frequencies, especially above the ABH cut-on frequency. This confirms the general character of the optimal damping layout observed before.

As can be seen from [Table 6.1](#), in contrast to the vibration optimization, damping layers tend to spread more towards the periphery region of the ABH indentation as a result of acoustic optimization. This is understandable since, as shown in [Figure 6.5\(c\)](#), damping layers coated at the central portion of the ABH indentation (with very thin thickness and therefore weak stiffness) would increase the radiation efficiency of the structure. This observation further confirms the fact that, among the dual adverse effect

of the damping in terms of the increased wave reflection and radiation efficiency, the latter seems to be more dominant. While the vibration optimization only needs to cope with the former, acoustic optimization has to deal with both. Therefore, through the optimized damping layout, the acoustic benefit is achieved as a result of balanced consideration of both aspects, predominantly through a reduced radiation efficiency.

Table 6.1 Comparison of optimal layouts of damping layers under different objective functions. The outer dot circle represents the ABH peripheral circle, and the inner dash circle represents the circular coverage of damping layers.

Optimal layout	$f=100$ Hz	$f=1700$ Hz	$f=3150$ Hz
Objective function, $C=MSV$.			
Objective function, $C=W_{rad}$.			

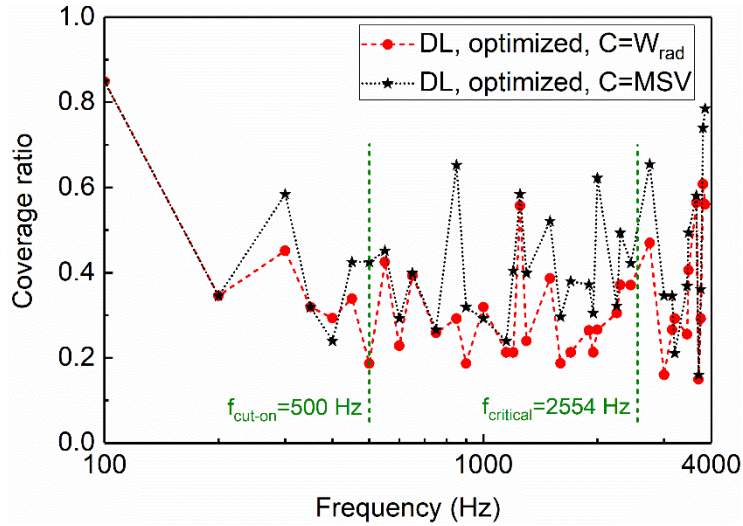


Figure 6.7 Comparison of the coverage ratios W_{rad} : Sound power optimization (circular dot); MSV: mean square velocity optimization (star dot).

6.2.4 Minimization of sound power within a frequency band

Possible variations in the excitation frequencies can be dealt with by considering a frequency band instead of discrete frequencies. To investigate the issue, minimizations of the radiated sound power within a prescribed frequency band, mathematically defined in Equation (6.1), is investigated. To this end, an arbitrary frequency band of 50 Hz is chosen as an example. It should be noted that the proposed methodology and tools can be applied to any frequency range. The reason why we choose a 50Hz band is to accommodate a typical engineering scenario in which relatively stable excitation is exerted onto the structure, but with slight variations. Four representative frequency bands are selected for analyses: one below cut-on frequency (175-225 Hz), two between the cut-on frequency and the critical frequency (1675-1725 Hz and 2225-2275 Hz, respectively), and the third one above the critical frequency (3725-3775 Hz). For

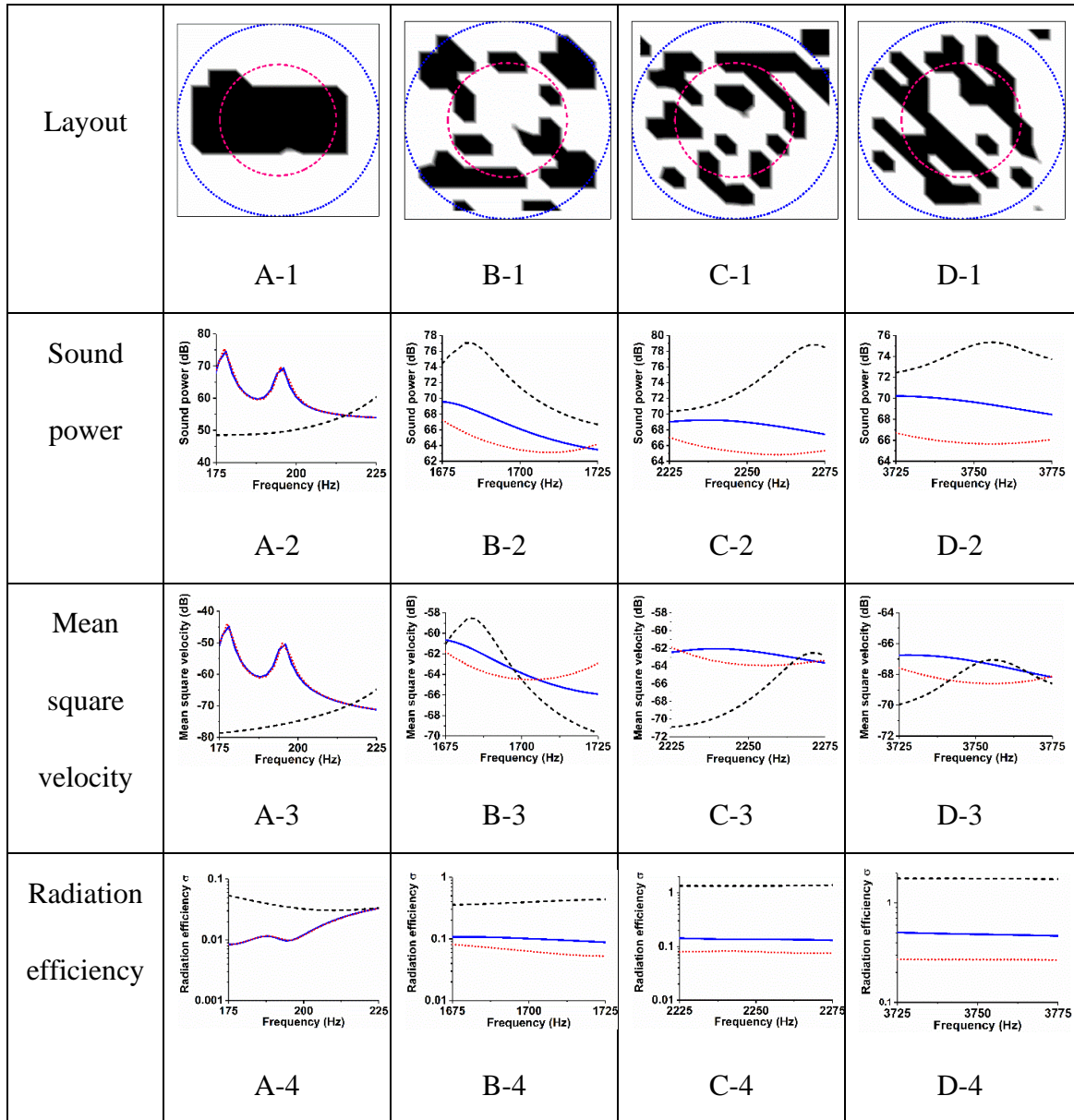
comparison purposes, central circular coverage configuration is taken as reference to quantify the changes in various physical parameters: sound power variation as well as the overall reduction within the band, alongside the corresponding mean square velocity and the radiation efficiency of the plate. Results are shown in [Table 6.2](#). The optimal coating layouts for each frequency bands are also presented.

This comparison allows to revisit and confirm the general character of several observations that are previously made using particular discrete frequencies. Again, optimizations allow to determine the optimal layout towards the minimization of the structural sound radiation for any given frequency band. The reduction level resulting from the optimal layout, as compared to the central coverage case using the same amount of damping materials, varies depending on the frequency band of interest, trivial in the non-dynamic low frequency range, and more appreciable at higher frequencies after the ABH effect is cut-on. Effect of the optimization is quasi-unobservable on any physical parameters of the system at the low frequency, typically below the ABH cut-on. When frequency increases, however, the reduction ΔW in the radiated sound power does not always go hand in hand with the variation in the vibration level of the plate. A typical example is the case corresponding to the B-column of [Table 6.2](#), where vibration level of the plate increases while the radiated sound is reduced within a portion of the frequency band. Having said that, a remarkably consistent phenomenon is that, in all cases considered in [Table 6.2](#), the sound radiation efficiency of the plate with optimal damping layout is systematically reduced above the ABH cut-on. This further

consolidates the conclusion that the reduced sound radiation of the optimized ABH plate roots in an improved sound radiation property of the structure as a result of the optimization. Meanwhile, the optimal damping coverage is not always concentrated on the central ABH indentation area, consistent with the previous observations made on single frequency cases. It is also relevant to compare the coated cases against a bare plate (with corresponding quantities shown by black dotted lines in Table 6.2). Below the cut-on frequency, the effect of ABH plate on sound power is not obvious as expected, compared with that of a uniform plate. Above the cut-on frequency, however, as can be seen in column B-2, C-2, and D-2, the reduction in the radiated sound power can be up to 8-10 dB.

Table 6.2 Characteristics of sound radiation under different frequency bands. Solid line represents the reference circular case, the dot line the optimized case, and the dash line the uniform plate

Frequency band	$f < f_{cut-on}$	$f_{cut-on} < f < f_{critical}$		$f > f_{critical}$
ΔW	$\Delta W = 0$ dB	$\Delta W = 2.31$ dB	$\Delta W = 3.25$ dB	$\Delta W = 3.60$ dB



6.3 Summary

A general topological optimization methodology is proposed in this Chapter to achieve a minimized vibration or sound radiation of an acoustic black hole (ABH) plate through optimizing the layout of the damping layers coated on its surface. The proposed tool encompasses a 2D semi-analytical Daubechies Wavelet (DW) model with an adaptive optimizer based on the Solid Isotropic Material with Penalty (SIMP) method

and the Optimality Criteria (OC) method. System optimization can be performed at either a given frequency or within a prescribed frequency band. The work aims at providing a solution to address the conflicting role that damping layers play in a typical ABH structure in terms of energy dissipation versus degraded structural properties. Based on numerical analyses, the main conclusions are summarized as follows.

- 1) The developed DW model is shown to be flexible and versatile to deal with the topological evolutions incurred during the optimization process. Its energy-based, modular and additive properties in relation to the handling of damping layers make it conducive for topological optimizations.

- 2) The optimization allows a reduction of the radiated sound power at either a given frequency or within a prescribed frequency band. For the configuration investigated in the paper, the reduction level can be up to 4 dB compared with its reference plate with standard damping coating at the ABH center using the same amount of materials. At low frequencies before the ABH cut-on, the reduction in the sound radiation is insignificant due to the absence of the ABH effect, while at high frequencies, the optimization warrants a systematic reduction in the sound radiation efficiency of the plate, which is the dominant factor leading to the reduced sound radiation. Along with this is an impaired energy level of the supersonic vibration components in the plate.

3) The optimal damping layout, irrespective of the minimization parameters (sound power or mean square velocity), is basically the same as the central coverage configuration below the cut-on frequency of the plate. Above the ABH cut-on, however, the two optimization problems end up with different optimal configurations, which shows that the best coating area may not necessarily be the center of the ABH indentation center. The optimized layout based on sound radiation optimization draws damping material further away from the central portion of the ABH indentation, as compared to the vibration-based optimization does. This shows that the adverse effect of the excessive use of the coating impacts more on the sound radiation than structural vibration.

It is relevant to note that the optimization results reported obviously depend on numerous parameters of the system such as structural details, excitation as well as the frequencies of interest. The focus of the work is placed on 1) showing a general design methodology by providing the necessary tools and 2) revealing the underlying physical changes in the structural properties alongside the topological evolution of the damping treatment. In that sense, striving for the maximum performance was not the main objective of this work. Should this be the main objective, the proposed methodology could be extended to also consider other factors such as coating with non-uniform thickness or other non-perfect ABH profiles, for which the system is shown to be more sensitive to the deployment of the damping layers [26, 46].

Chapter 7

Optimization for alternative ABH profiles

7.1 Introduction

Apart from the reflection coefficient that described in [Chapter 1](#), structural damping is another intrinsic indicator for evaluating the overall effects of an ABH structure. Analyses have demonstrated that ABH structures combined with damping materials entail significant damping enhancement, as compared with uniform ones with the same damping treatment [\[50\]](#). Recently, most works on damping enhancement of ABH structures focus on the layout of the damping layer deployment. For example, using an Euler-Bernoulli beam, Tang *et al.* [\[46\]](#) investigated the influences of the shape and the location of damping layers coated over the surface of an ABH taper on system loss factors. Feurtado and Conlon [\[43\]](#) investigated the effect of the damping layer thickness and that of the coverage on modal loss factors. Results show that coating over the central portion of an ABH indentation can largely increase the modal loss factors of the entire structure, and that an enlarged coverage of damping layer cannot necessarily result in an improvement of the system damping. It is relevant to recall that, as aforementioned, damping layer imposes the dual effects of increasing both energy dissipation and wave reflections, especially when the thickness becomes excessively large.

Different from the existing studies on damping layer for structural damping enhancement, in this chapter, we focus on seeking alternative ABH profiles to achieve enhanced system damping through optimizing the structural thickness. This would lead to an ABH thickness profile which is, in principle, different from the classical ABH profiles defined by the standard power-law relationship. For a standard ABH profile, the taper power index can be any integer larger than 2, but usually less than 4 to satisfy the smoothness conditions required [12, 102]. Therefore, in this chapter, we would seek an optimized new thickness profile, which takes the form of a combination of power-law profiles with different power indices. The optimization is achieved using a fast and elitist genetic algorithm: Nondominated Sorting Genetic Algorithm II (NSGA II).

The rest of this chapter is organized as follows. In [Section 7.2](#), the optimization problem is defined. The constraint-handling NSGA II adopted for the thickness profile optimization is briefly introduced, as well as the Lagrange interpolation polynomials. In [Section 7.3](#), the optimization is performed based on the previously established 2D semi-analytical wavelet model. Numerical analyses of a clamped plate embedded with an optimized ABH indentation are then conducted. Issues like system loss factors, their relationship with structural deformation depicted by mode shapes, energy distribution as well as the vibration and sound radiation properties are scrutinized. Meanwhile, vibration response is analyzed using a wave number transform analysis to explain the improved ABH effects resulting from the optimized ABH profile. Results are also

compared with those of a standard ABH plate (with a taper power index of 4). Finally, a summary is given in [Section 7.4](#).

7.2 Formulation and procedures of the optimization

7.2.1 Objective function and constraints

The structure under investigation is a rectangular plate embedded with a symmetric circular indentation. While the thickness profile of standard ABH indentations follows a power-law relationship, an alternative ABH thickness profile is attempted for improving the overall ABH effect of the plate. To define the searching scope, the diameter ($2R_{ABH}$) of the indentation, the minimum thickness h_0 and the maximum thickness h of the thickness profiles are kept constant, as shown in [Figure 7.1](#).

Structural damping is a direct and intrinsic descriptor of the ABH effect, which is independent of external excitations. As a quantitative measure, structural damping is used to construct the objective function for the optimization. More specifically, the sum of the first 100 modal loss factors in the plate is maximized. The fitness function in the optimization problem is the reciprocal of the objective function, which will be minimized. Thickness profiles of individuals in the initial population are represented by polynomials, up to a given order, which are determined by several distinct points (shown in [Figure 7.1](#)) using the polynomial interpolation functions that will be introduced in [Section 7.2.3](#).

The optimization problem can be mathematically defined as

$$\begin{aligned}
 fitness &= \frac{1}{\sum_{i=1}^{100} \eta_i} \\
 \text{s.t.} \quad & h_0 \leq h(x) \leq h \\
 & 0 \leq x_{\min} < R_{ABH} \\
 & \int_0^{R_{ABH}} k_{opt}(x) dx > \int_0^{R_{ABH}} k_{std}(x) dx
 \end{aligned} \tag{7.1}$$

in which η_i stands for the modal loss factor of the i^{th} mode and x_{min} the position of the minimum thickness; k_{opt} and k_{std} are the wavenumbers of the propagating waves inside the optimized profile and the standard profile, respectively. The first constraint $h_0 \leq h(x) \leq h$ defines the variation range of the thickness. The second constraint $0 \leq x_{\min} < R_{ABH}$ stipulates that the position of the minimum thickness can be at any location within the indentation, rather than at the indentation center like the case of a standard ABH profile. The last constraint $\int_0^{R_{ABH}} k_{opt}(x) dx > \int_0^{R_{ABH}} k_{std}(x) dx$ ensures that the accumulated phase of the bending waves inside the optimized ABH indentation is larger than that of the standard indentation, which imposes that the propagating waves would take more time to travel inside the indentation, thus resulting in a better ABH effect.

Rotating the 1D profile $h(x)$ around z axis, as shown in [Figure 7.1](#), yields a 2D circular indentation expressed as $h(r) = a_0 + a_1r + a_2r^2 + a_3r^3 + a_4r^4$. The thickness profile of the ABH indentation will be optimized to achieve the maximum structural damping of the plate using the NSGA II that will be described in [Section 7.2.2](#).

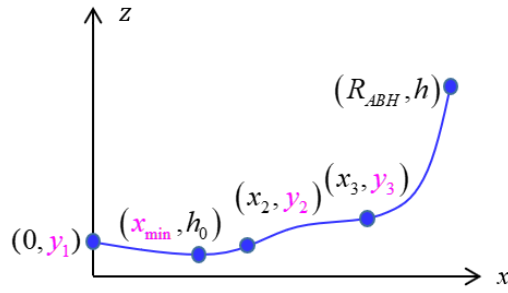


Figure 7.1 The design variables (shown in pink color) that determine the ABH profile.

7.2.2 Constraint-handling NSGA II

Nondominated sorting genetic algorithm II (NSGA-II) is a fast and elitist genetic algorithm developed by Deb [145]. Herein a brief description of the procedure for selecting the best solution is presented. Initially, a population P_t of size N_p is randomly generated, with each individual being assigned a fitness value that is equal to its nondominant level (in a decreasing order from level 1 being the best, level 2 being the next-best and so on). Then the following procedures are performed to minimize the fitness.

1) An offspring Q_t of size N_p is created through binary tournament selection, recombination and mutation operators.

2) Combining the parent population and the offspring leads to a combined population \tilde{R}_t of size $2N_p$; this combination guarantees the elitism of the population.

3) Sorting the combined population \tilde{R}_t using nondomination (more details can be found in Ref. [145]).

4) Assembling a new population P_{t+1} of size N_p . Individuals belonging to the first dominated set \mathcal{F}_1 are the best solutions which should be emphasized more than other individuals. If the number of individuals in \mathcal{F}_1 is smaller than N_p , all individuals in \mathcal{F}_1 will be selected as the new population P_{t+1} . The remaining individuals in P_{t+1} will be chosen from \mathcal{F}_2 , and so on. To exactly choose a population of size N_p , the best individuals in the last dominated front \mathcal{F}_l will be chosen using the crowded-comparison operator \prec_n [145] to fill the population P_{t+1} .

5) Finally, the new population P_{t+1} will be used to create next generation, and the above steps will be repeated till the convergence of the fitness function.

The flow chart of getting the converged solutions is shown in [Figure 7.2](#).

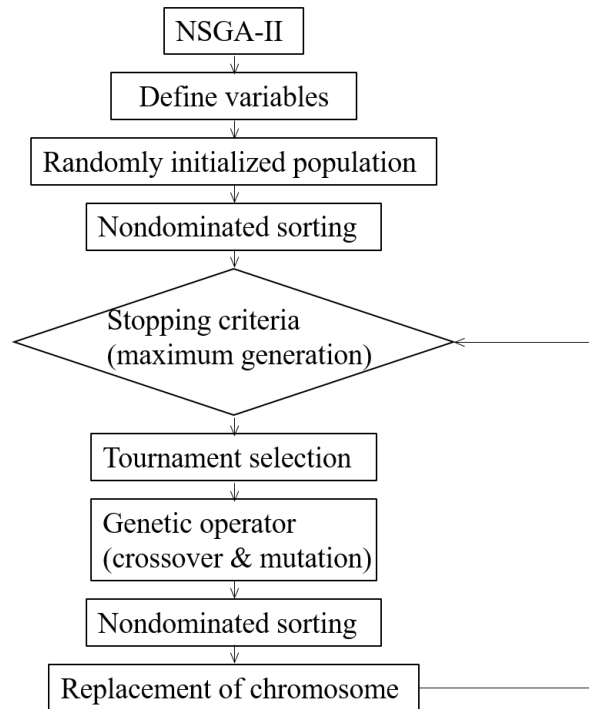


Figure 7.2 The flow chart of NSGA-II.

A simple strategy for handling constraints [145] is necessary for implementations. The constraint-handling approach uses the tournament selection, *i.e.*, two individuals are picked from the population and the better one is selected. Each individual can be feasible or infeasible in the presence of constraints. Considering the single objective optimization nature of the current problem, the following simple rule is used for the tournament selection:

- 1) If both individuals are feasible, the one with a better objective function will be chosen;
- 2) If one individual is feasible and the other one is not, choose the feasible one;
- 3) If none of the individuals is feasible, choose the one with smaller overall constraint violation.

7.2.3 Lagrange interpolation polynomials for profile generation

We first discuss the description of the thickness profile. Lagrange interpolation polynomials are very useful and important in numerical analyses, because they can uniformly approximate any defined and continuous functions within a bound. If there are $\tilde{n}+1$ distinct data points, $x_0, x_1, \dots, x_{\tilde{n}}$, and \tilde{f} is a function whose values are given at these points, there is a unique polynomial $P(x)$ of degree at most \tilde{n} with

$$\tilde{f}(x_k) = P(x_k) \quad (7.2)$$

in which $k=0, 1, 2, \dots, \tilde{n}$. The polynomial is given by

$$P(x) = \sum_{k=0}^{\tilde{n}} \tilde{f}(x_k) l_k \quad (7.3)$$

where l_k is the Lagrange interpolation operator which is written as

$$l_k = \prod_{\substack{j=0 \\ j \neq k}}^{\tilde{n}} \left(\frac{x - x_j}{x_k - x_j} \right) \quad (7.4)$$

Based on the above, the Lagrange interpolation polynomials are used to create the thickness profiles in the population for the optimization. To satisfy the smoothness condition required by realization of ABH effect, the taper power of the ABH profiles should be equal to or less than 4. Therefore, five distinct points are used to create the polynomials for thickness profiles.

In the example to be discussed hereafter, the diameter and the minimum thickness of the ABH indentation remain the same as the values used in the experiment tests in

Chapter 3, with parameters tabulated in Table 3.1. Five points, $(0, y_1)$, (x_{min}, h_0) , (x_2, y_2) , (x_3, y_3) and (R_{ABH}, h) as shown in Figure 7.1, are taken as variables to depict the ABH thickness profile. The x -coordinates of the points for creating the polynomials in Equation (7.3) can be nonuniformly distributed. In the current case, $x_2=1/3R_{ABH}$ and $x_3=2/3R_{ABH}$, and the corresponding thickness y_2, y_3 , and y_1 at the indentation center are undetermined. The minimum thickness of the indentation is set to be $h_0=0.6$ mm. This value is chosen in consideration of the manufacturing capability that is readily achievable by traditional manufacturing methods such as CNC milling. Meanwhile, this might also be the minimum thickness that can be acceptable for practical applications. However, the position of the minimum thickness, x_{min} , is not fixed *a priori*. The thickness at the junction between the uniform portion and the ABH portion of the plate should be continuous, *i.e.*, the point (R_{ABH}, h) is given *a priori*. As a result, there are 4 design variables: the thickness y_1 at the indentation center, the thicknesses y_2 and y_3 at two fix positions and the position of the minimum thickness, x_{min} . The variable bounds for y_1, y_2, y_3 and x_{min} are $[h_0, h]$ and $[0, R_{ABH})$, respectively.

An initial population containing 96 individuals are randomly generated in compliance with Equation (7.3) to start the optimization process. As an example, the first 8 individuals are shown in Figure 7.3.

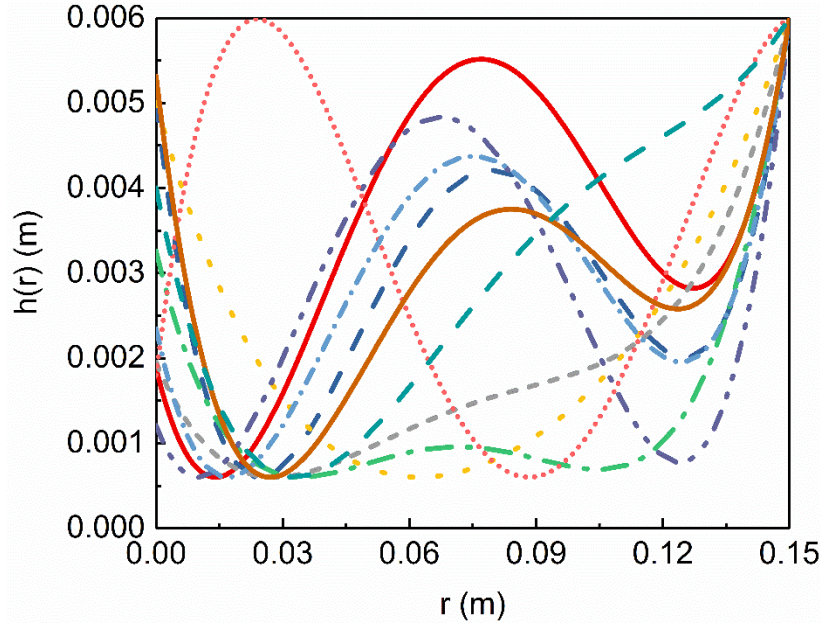


Figure 7.3 The first 8 individuals in the randomly generated initial population.

7.3 Numerical analyses and discussions

7.3.1 Damping performance

Exploiting the NSGA-II described in [Section 7.2.2](#), the minimization problem defined in [Equation \(7.1\)](#) is investigated using the previously 2D semi-analytical wavelet model. In the present case, the geometrical and material parameters of the plate and those of the add-on damping layer remain the same as those used in the experiment tests, as listed in [Table 3.1](#) and [Table 3.2](#), respectively. Note that the entire ABH indentation, rather than the central ABH portion, is covered with soft damping layers. The supported length L and resolution m used in the wavelet series are selected to be 12 and 5, respectively. Distribution indices [\[146\]](#) are used for crossover and mutation operators as $\eta_c = 20$ and $\eta_m = 20$, respectively. After 153 generations, the fitness function converges. For comparisons, the values of the objective function for the initial

population before optimization are presented in Figure 7.4. Best values of the initial population in each generation are shown in Figure 7.5(a).

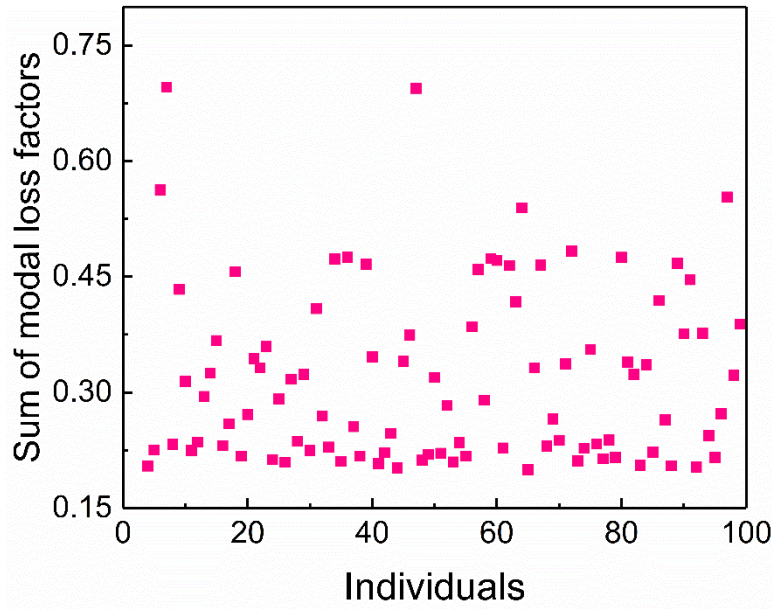
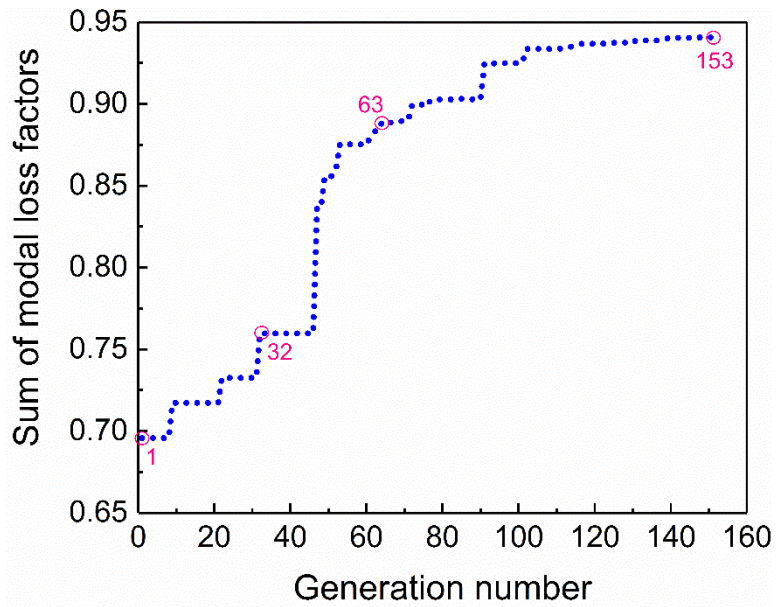
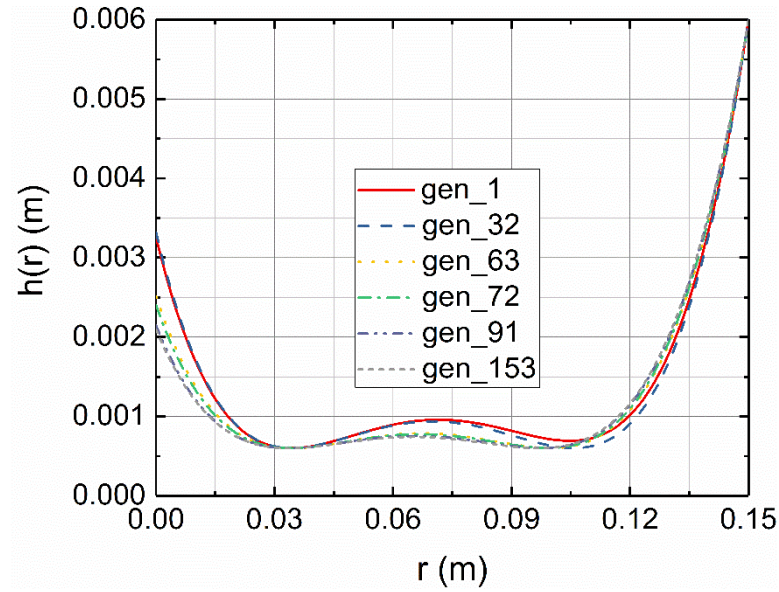


Figure 7.4 Objective values for the initial population.



(a)



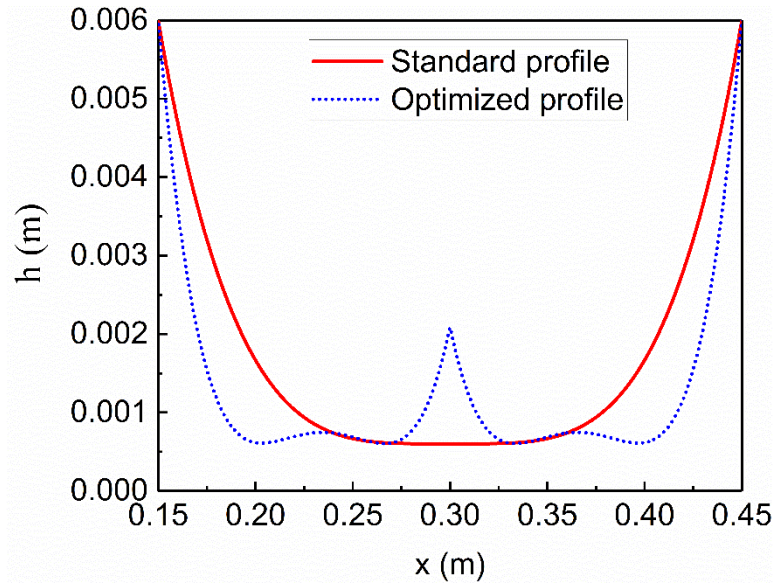
(b)

Figure 7.5 Steps of optimization process: (a) objective values of the best individual in each step; (b) optimal profile in each step.

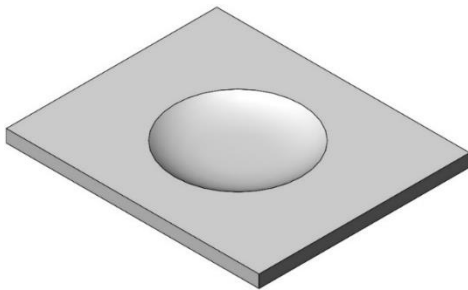
Figure 7.5(a) shows that the objective value of the best individual in each generation experiences a rising trend with the number of the generation. Though most of the objective values for the initial population are relatively low (shown in Figure 7.4), the one with the largest value is actually very close to the final optimal one. To illustrate the evolution process, the profiles of the best individuals at a few generation steps (1st, 32nd, 63rd, 72nd, 91st, 153rd) are illustrated in Figure 7.5(b). It can be seen that the thickness of the portion of the thickness profile close to the outer junction with the uniform part of the plate gradually reduces (from 1st to 32nd generation) and then becomes thicker (from 32nd to 153rd generation), while the thickness of the other parts of the thickness profile show a decreasing trend with the number of generation. Finally,

the optimization result converges to the best individual without noticeable further changes.

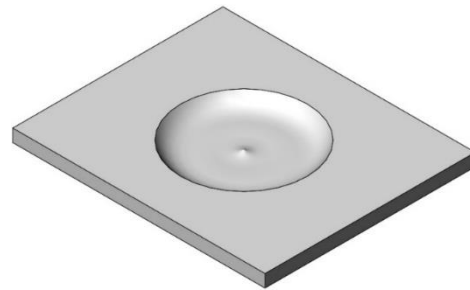
The finally achieved ABH thickness profile, described in a polar coordinate system writes: $h_{opt} = (0.0021) + (-0.12)r + (3.3243)r^2 + (-36.85)r^3 + 141.23r^4$. For comparison, a standard thickness profile expressed as $h_{std} = (0.6e-3) + 10.67r^4$ is presented and compared with the optimized profile in [Figure 7.6](#). [Figure 7.6\(a\)](#) shows both profiles in 1D view along the radial direction of the indentation. Different from the standard profile, the optimized one undergoes a sharp decrease in thickness when entering the ABH indentation from the outer junction with the uniform part of the plate, dwells into a thin plateau and then undergoes a raise-up at the indentation center. The position of the minimum thickness is 0.0336 m away from the indentation center instead of at the indentation center. The thickness at the indentation center of the optimized profile is around 2.1 mm. Three-dimensional schematic views of both the standard and optimized indentations are shown in [Figure 7.6\(b\)](#) and [Figure 7.6\(c\)](#), respectively.



(a)



(b)

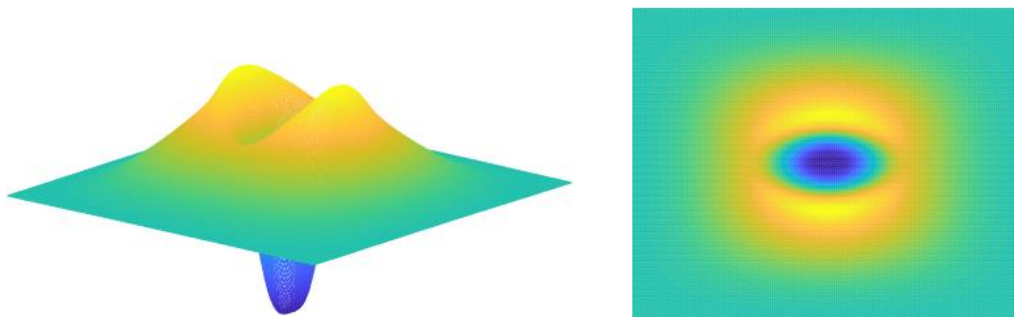


(c)

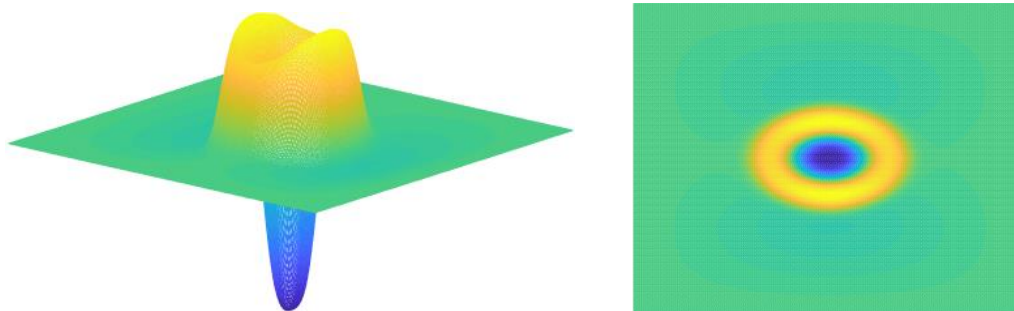
Figure 7.6 Plates with different ABH profiles: (a) the standard profile and optimized profile in 1D view; (b) a plate with an indentation of standard ABH profile; (c) a plate with an indentation of optimized profile.

Numerical analyses of both plates are conducted with resolution $m=7$ to ensure a better accuracy up to a high frequency range. Firstly, mode shapes of a clamped plate embedded with the optimized indentation are investigated. Several typical mode shapes (*i.e.*, 4th, 9th, 52nd, 67th, 148th) from low to high orders are presented in [Figure 7.7](#). It can be observed that, ABH local modes occur at relatively low orders such as 9th mode.

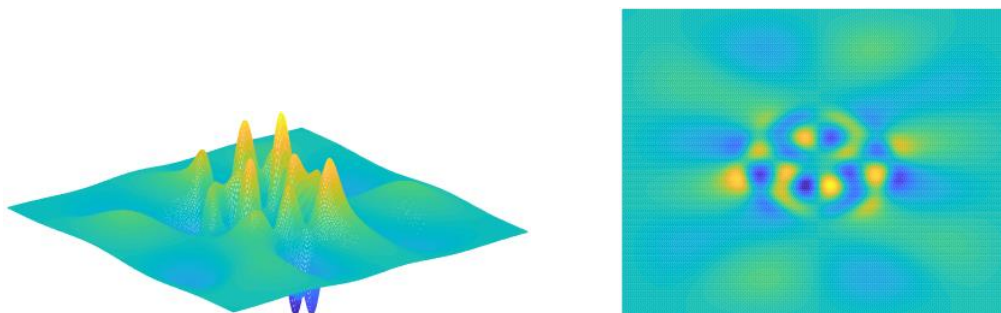
Similar phenomena can also be observed for the standard ABH plate. However, different from the standard ABH plate, local ABH $(n, 1)$ and $(n, 2)$ modes inside ABH indentation are clearly observed. The $(n, 1)$ and $(n, 2)$ modes here represent mode shapes that exhibit n half waves in the circumferential direction and one or two half waves in the radial direction of the indentation, *e.g.*, 67th and 148th mode shapes depicted in [Figure 7.7\(d\)-\(e\)](#).



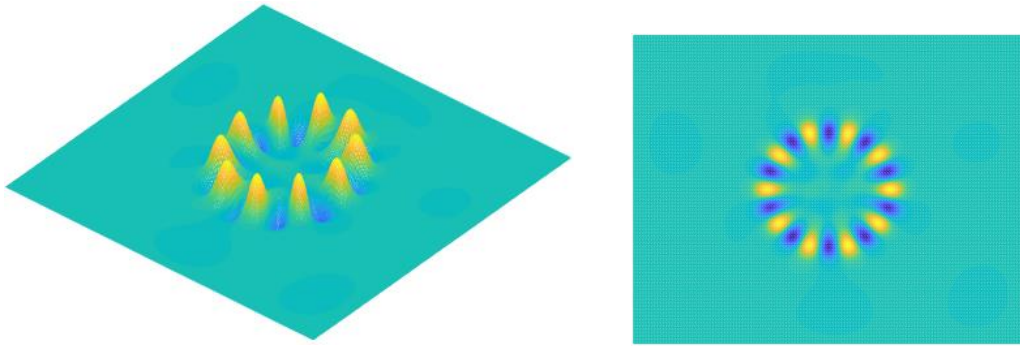
(a) 4th mode



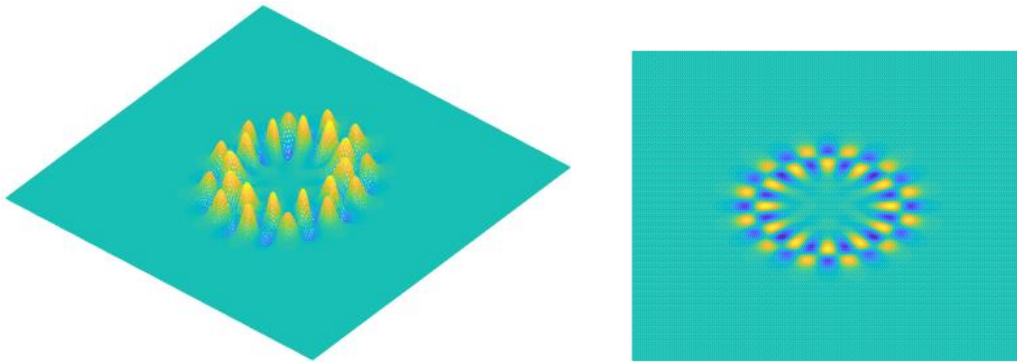
(b) 9th mode



(c) 52nd mode



(d) 67th mode



(e) 148th mode

Figure 7.7 Mode shapes of a plate embedded with an indentation of optimized profile.

An examination on the modal loss factors shows that, the optimized profile leads to a significantly increased structural damping compared with the standard ABH one. More specifically, the overall damping enhancement for the first 100 modes amounts to around 39.5%.

To gain insights into the underlying phenomena induced by the optimized profile, the first 150 modal loss factors are shown in [Figure 7.8](#). It can be seen that, for the standard ABH case, the loss factors dwell in the interval (0.004, 0.01). For the optimized

ABH case, the loss factors are primarily scattered from 0.004 to 0.016, with their averaged value increasing by 43.7%, compared with that of the standard ABH case. Typical mode shapes corresponding to the loss factors of low, medium and high levels are also presented. It seems that, the low-value loss factors mostly correspond to global modes, *e.g.*, 52nd mode; in agreement with the analyses of the modal loss factors reported in [Section 4.2.2](#). Also, two representative modes (18th and 113th) for the standard ABH case with high and low loss factors are presented. Relationships between the loss factors and the mode shapes are very similar to those observed for a standard ABH plate in [Section 4.2.3](#), which will not be repeated here. It can be seen from [Figure 7.8](#) that, the loss factors of most modes of the optimized ABH case are larger than those of the standard ABH case. Further explorations into modes with high loss factors, *i.e.*, above the level of 0.012, shows that, these modes are primarily local ABH ($n, 1$) and ($n, 2$) modes such as the 67th mode and the 148th mode depicted in [Figure 7.7\(d\)-\(e\)](#).

The occurrence of the local ABH ($n, 1$) and ($n, 2$) modes which give high loss factors in the optimized ABH case is attributed to the unique feature of the optimized thickness profile. In fact, because the minimum thickness is away from the indentation center in the optimized ABH profile, a ring-shaped area (from radius 0.0336 m to 0.0972 m) is formed inside the indentation, which is conducive to further reducing the structural stiffness along the circumferential direction and promoting energy focalization. For the standard ABH plate, however, only the central area of the indentation is effective in energy focalization. From wave propagation perspective, it can be surmised that the

extended thin thickness plateau between the center and the outer boundary of the optimized ABH indentation (or the valley area of the ring) would probably create a bi-directional ABH effect so that wave energy is trapped from both sides (incoming waves or the residual waves reflected by the indentation center).

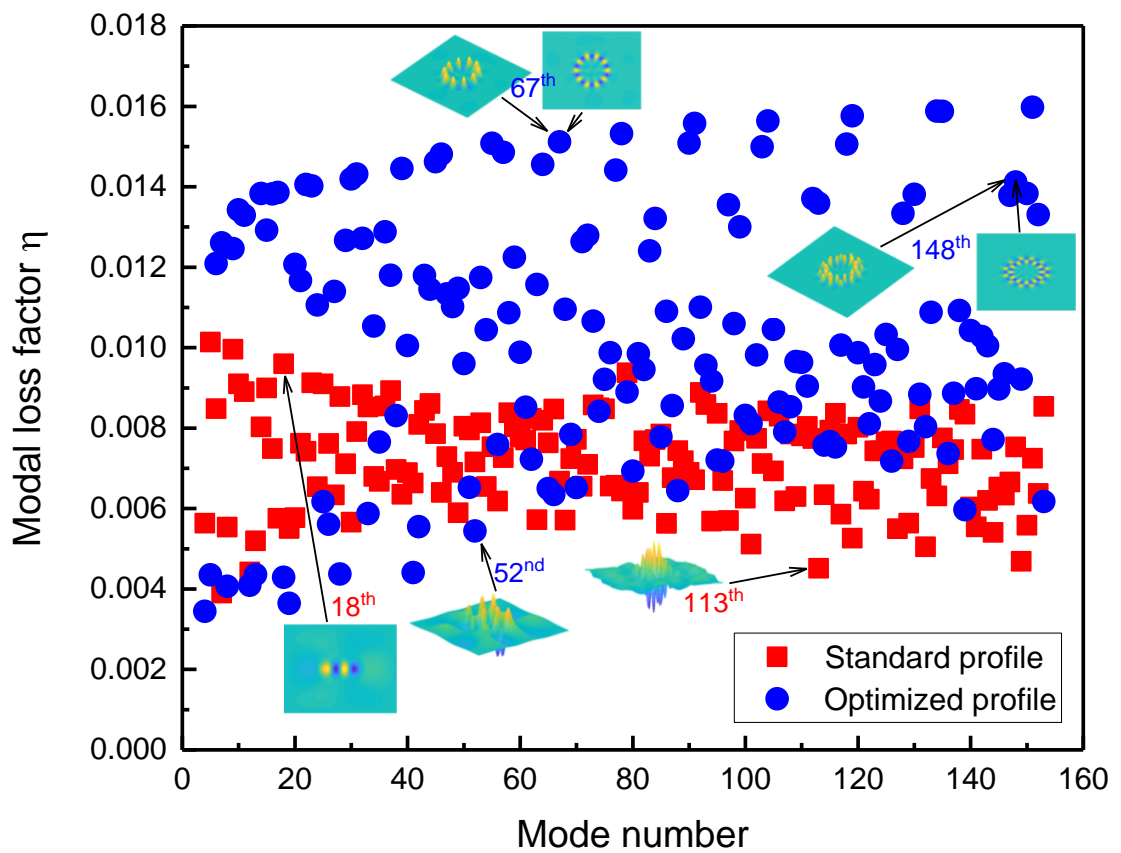


Figure 7.8 Comparison of modal loss factors: (a) standard profile (square dot); (b) optimized profile (circular dot).

An energy density ratio between the ABH portion and the uniform portion of the plate, defined as $10\lg\left[\left(\frac{1}{V_{ABH}}\int_{V_{ABH}}\mathbf{V}\mathbf{V}^*dV\right)\left/\left(\frac{1}{V_{uni}}\int_{V_{uni}}\mathbf{V}\mathbf{V}^*dV\right)\right.\right]$, is utilized to further assess the energy focalization ability of the optimized indentation. A harmonic point excitation force is applied at (0.518, 0.165) m over the uniform portion of the plate. Comparisons between the standard ABH plate and the optimized ABH plate are illustrated in [Figure 7.9](#). It can be observed that, above the critical frequency of 1995 Hz (calculated using parameters of the uniform portion of the plate), the optimized ABH plate exhibits a significantly larger energy density ratio than the standard ABH plate. This indicates that the optimized profile indeed exhibits enhanced energy focalization.

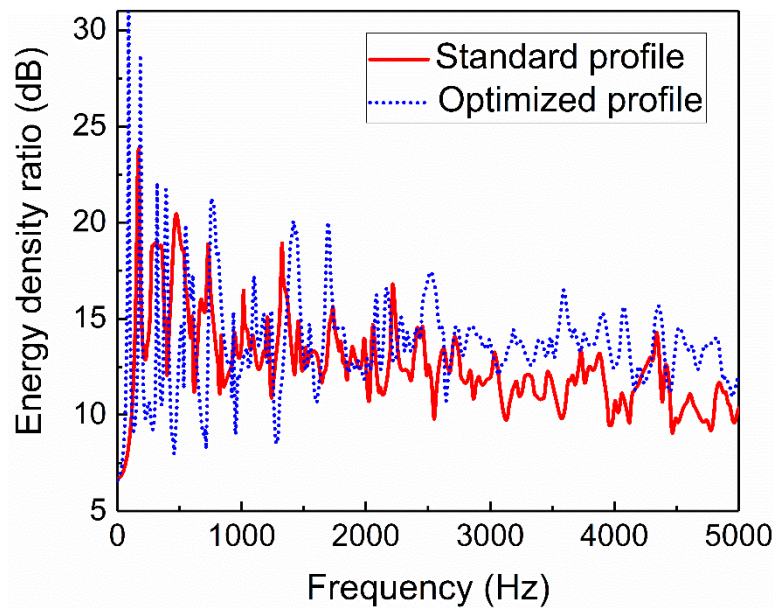
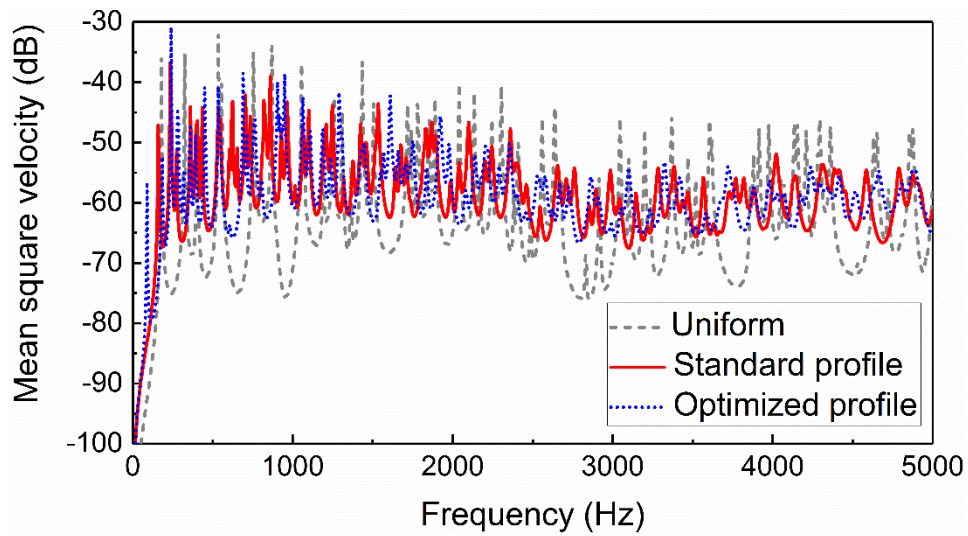


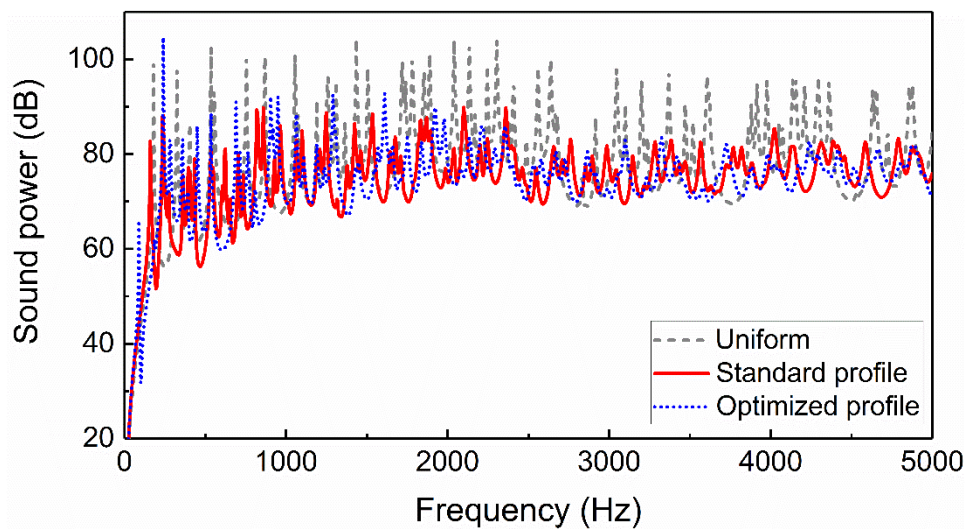
Figure 7.9 Ratio of energy density between the ABH portion and the uniform portion: (a) standard profile (solid line); (b) optimized profile (dot line).

7.3.2 Vibration response and sound radiation characterizations

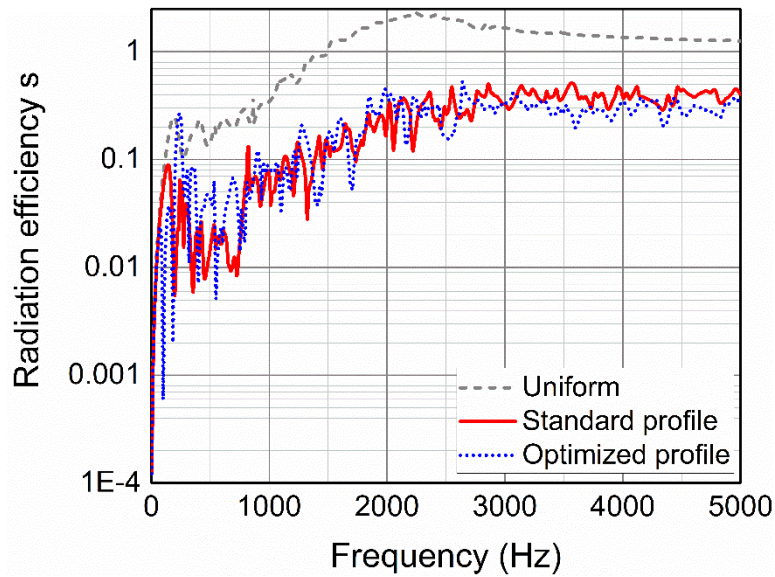
The vibration response and sound radiation characteristics of the optimized ABH plate are investigated. Comparisons with their counterparts of the standard ABH plate are shown in Figure 7.10(a)-(c), in terms of the mean square velocity, radiated sound power and radiation efficiency. To facilitate the comparison, a uniform plate of the same dimension is also included as reference.



(a)



(b)

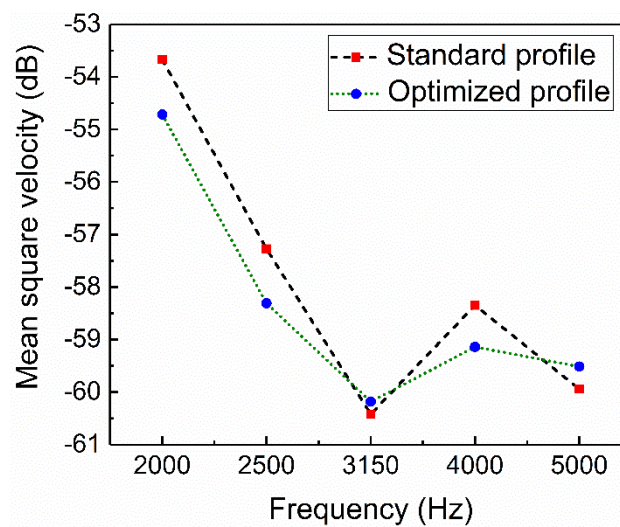


(c)

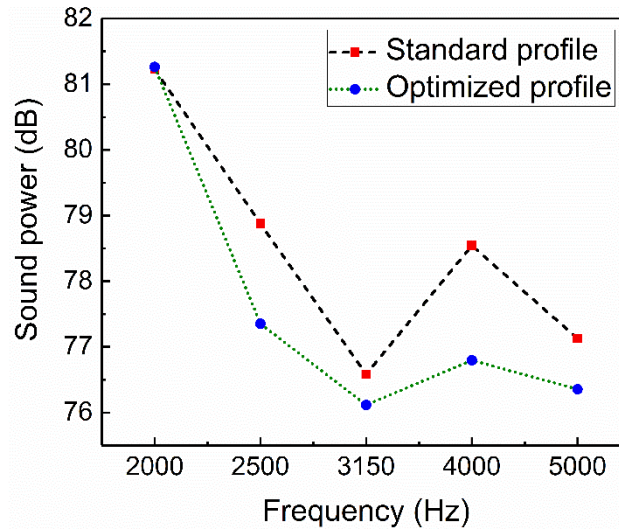
Figure 7.10 Comparisons between a plate of uniform thickness (dash line) and plates embedded with an indentation of standard ABH profile (solid line) and optimized profile (dot line): (a) space-averaged mean square velocity; (b) radiated sound power; (c) sound radiation efficiency.

Compared with the uniform plate, it is not surprising that both the standard ABH and the optimized ABH plates show drastic reductions in the mean square velocity, radiated sound power and radiation efficiency, especially above the cut-on frequency of 644 Hz, as expected. Meanwhile, a noticeable reduction in the peak levels of the mean square velocity (roughly 1.7dB), radiated sound power (2.5dB) and the radiation efficiency of the optimized ABH plate is also observed above the critical frequency of 1995 Hz, in comparison with the standard ABH plate.

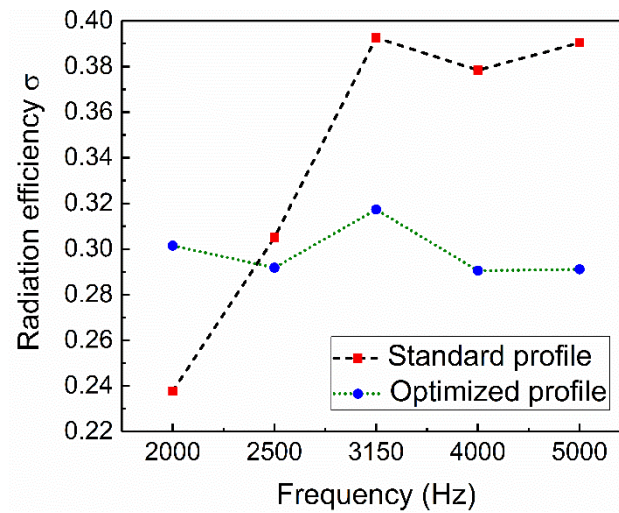
To better evaluate the global improvement of the optimized ABH plate over the standard ABH plate, results above the critical frequency are averaged into one-third octave bands and shown in Figure 7.11. It can be seen that, the averaged mean square velocity of the optimized ABH plate experiences a downward trend, in contrast to that of the standard ABH plate, with reductions around 1 dB at frequency bands centered at 2000, 2500 and 4000 Hz. Meanwhile, the averaged sound power is reduced by 1.5~2 dB in the frequency bands centered at 2500, 3150, 4000 and 5000 Hz. The reduction of the sound power observed in Figure 7.11(b) is attributed to the reduction in the vibration response and the radiation efficiency shown in Figure 7.11(c). Additionally, the calculated radiation efficiencies in the last four frequency bands are evidently reduced, which is justifiable considering the constraint in Equation (7.1). Another explanation of the reduced radiation efficiency is due to the weakened stiffness of the plate; which can be seen from the reduced eigen-frequencies (not shown here).



(a)



(b)



(c)

Figure 7.11 Comparisons between the standard ABH plate and the optimized ABH plate in one third octave band: (a) space-averaged mean square velocity; (b) radiated sound power; (c) sound radiation efficiency.

Wavenumber transform analyses are carried out for the illustration of the improved ABH effect of the optimized ABH plate. Again, the uniform plate is used as reference. Employing Equation (6.12), the spatial variations of the vibration velocity are

transformed into wavenumber domain. Comparisons between the uniform plate, plates with the standard ABH profile and the optimized one are conducted at representative frequencies (2250 Hz around the critical frequency and 3390 Hz above the critical frequency) with results shown in Figure 7.12.

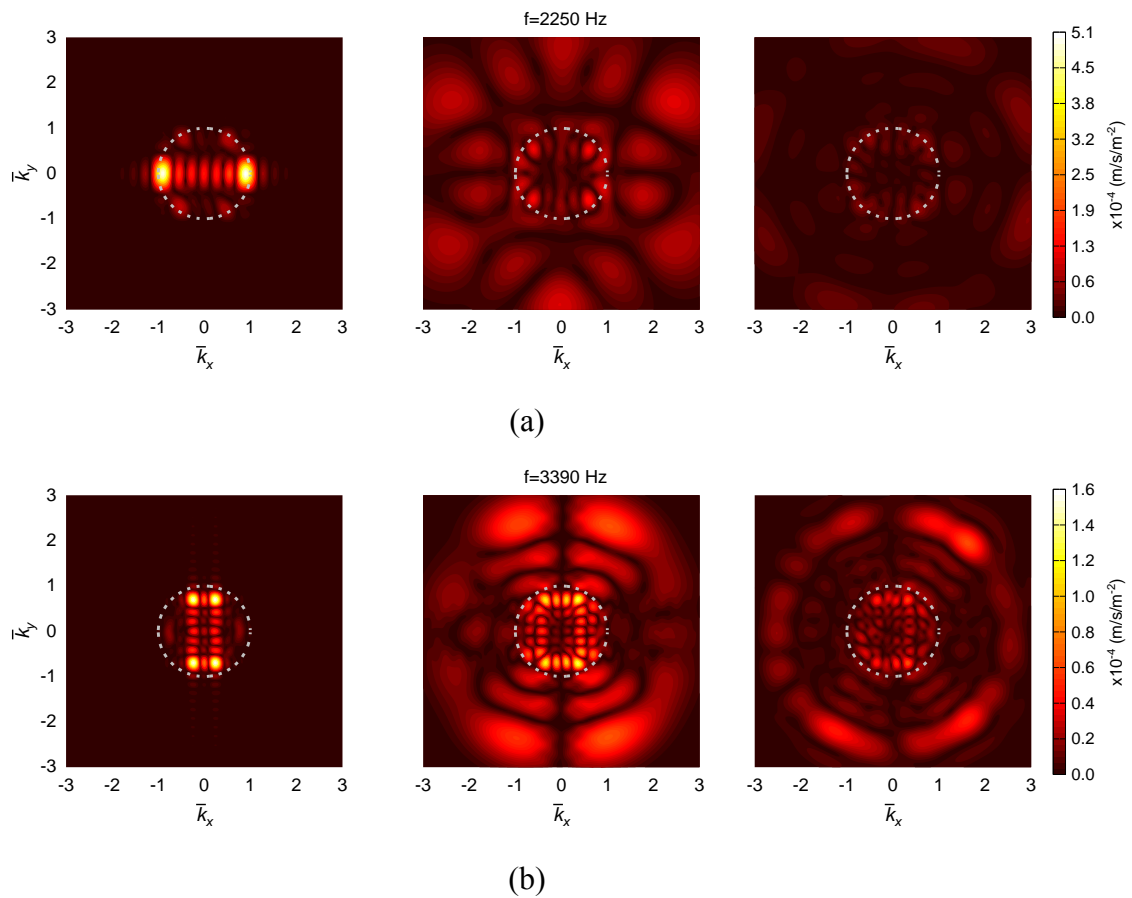


Figure 7.12 Wavenumber spectra of uniform plate (left), ABH plates embedded with an indentation of standard profile (middle) and optimized profile (right) at different frequencies: (a) 2250 Hz; (b) 3390 Hz. The dash circle indicates the normalized radiation circle with radius $r=1$.

Figure 7.12(a) shows the vibration velocity at 2250 Hz in the wavenumber domain. It seems that for the uniform plate (left column), the high-amplitude vibration velocity mainly locates at the periphery of the normalized radiation circle. As to the standard ABH plate (middle column), the vibration velocity inside the normalized radiation circle is significantly reduced, as expected. A further reduction in the vibration velocity with supersonic components is observed for the optimized ABH plate (right column). Similarly, Figure 7.12(b) compares the vibration velocity at 3390 Hz, which is above the critical frequency of 1995 Hz. For the uniform plate, the high-amplitude vibration velocity resides inside the normalized radiation circle, as expected. However, for the standard ABH plate and the optimized ABH plate, the vibration velocity with supersonic components is reduced, and the high-amplitude vibration velocity also spreads outside the normalized radiation circle. Compared with the standard ABH plate, the optimized one shows a significant reduction in the vibration velocity with supersonic components. These analyses confirm the improved ABH effect of the optimized ABH plate in terms of sound radiation.

7.4 Summary

In this chapter, based on the previously established 2D semi-analytical wavelet model, an optimal ABH profile is proposed through a systematic optimization procedure using NSGA II. Maximization of the structural damping is taken as the objective function. Performance comparisons between the standard and the optimized ABH plates

are conducted to show the superiority of the latter in terms of the ABH effects, as reflected by the overall enhancement of the structural damping, and a general reduction of major vibration and sound radiation metrics. Main conclusions are summarized as follows:

1) Employing the NSGA II, an optimized thickness ABH profile which is different from the standard ABH profile is proposed. The optimized ABH thickness profile entails improved ABH effects. More specifically, the sum of the first 100 modal loss factors (taken as the objective function) is increased by 39.5% in the optimized configuration, as compared with the standard one.

2) Mode shape analyses of the optimized ABH plate show that local ABH ($n, 1$) and ($n, 2$) modes feature relatively high loss factors. The occurrence of these modes is attributed to the unique feature of the optimized ABH profile for which the minimum thickness is away from the center of the indentation, thus forming a flexible ring which is beneficial to energy focalization. This is further confirmed by the energy density ratio between the ABH portion and the uniform portion of the optimized plate, which allows increased structural damping with the use of the same amount of damping materials.

3) Compared with the standard ABH plate, vibration response and sound radiation analyses on the optimized ABH plate also show a reduction in the mean square velocity, sound power and sound radiation efficiency above the critical frequency of 1995 Hz.

For the investigated case, the averaged reductions in the peak values of the mean square velocity and sound power above the critical frequency is about 1.7 dB and 2.5 dB, respectively, or 1 dB and 1.5~2 dB in the one-third Octave bands. Wavenumber transform analyses confirm the reduced vibration velocity with the supersonic components, which is mainly responsible for the far-field sound radiation.

Chapter 8

Conclusions and future research

8.1 Conclusions

This thesis establishes an efficient, flexible and versatile semi-analytical model for the simulation of vibration and sound radiation of a 2D Acoustic Black Hole (ABH) structure of finite size. The model is based on the Love-Kirchhoff thin plate theory under the framework of Rayleigh-Ritz method. Daubechies wavelet scaling functions are used as the admissible functions to approximate the transverse displacement of the plate. The proposed model allows for the accommodation of add-on damping layers in a fully coupled manner. As an alternative to the conventional FEM, the proposed 2D Daubechies wavelet (DW) model is utilized to explore the vibration and sound radiation mechanisms of a plate embedded with an ABH indentation shows its efficacy for structural analysis and optimization. In addition, the energy-based, modular and additive properties of the proposed model allow the inclusion of other add-on components that may be required by particular applications, and in particular entail topological optimization of damping layouts and the searching of alternative ABH thickness profiles.

Major conclusions out of this work are summarized as follows:

1) The DW model is shown to provide remarkable accuracy in characterizing the vibration response and sound radiation of the ABH plate which exhibits rich dynamics and complex dynamic behaviors. More specifically, most of the relative errors on the eigen-frequencies of the first 120 modes of the investigated plate are below 2% (compared with experimental results), alongside a good match in the corresponding mode shapes. The cross-point mobility and the radiated sound power predicted by the DW model also show a good agreement with experimental measurement up to a high frequency range, both with and without deposition of damping materials. Meanwhile, considering the lack of experimental data in the literature, the reported experimental results would serve as an invaluable data source for future ABH studies.

2) The proposed model, as well as the associated wavelet-based solution procedure, is shown to be able to overcome major technical difficulties which are specific to ABH structures: non-uniform wavelength distribution and ABH-induced wave compressions in the high frequency range in a realistic structure of finite size. The accuracy, as well as the frequency outreach well exceeds similar work reported in the literature. In that sense, this work offers a unique and useful model which is conducive to the study of ABH phenomena.

3) Studies on different damping configurations over the surface of a strip/circular ABH indentation shows that, the same amount of damping materials coated at the central portion of standard ABH indentation can significantly increase the modal loss

factors, compared with a uniform plate of the same thickness and dimension. Subsequently, a significant reduction in the vibration response is achieved. Investigations into the modal loss factors show that, above the cut-on frequency of the panel, the ABH-induced damping enhancement phenomenon is mainly attributed to the local structural modes within the ABH indentation. These modes exhibit lower-order deformations (typically half and one wave along the thickness tailoring direction). Contributions to the damping increase by the higher-order local modes along the thickness tailoring direction and global modes are trivial and negligible.

4) ABH plates exhibit significantly reduced sound power and sound radiation efficiency in a broad dynamic frequency range as compared to its uniform counterpart. The reduction in the radiated sound power is attributed to a reduction in both the vibration response of the plate and its sound radiation efficiency. Physical mechanisms for the reduced radiation efficiency in different frequency ranges are revealed. Before the cut-on of the ABH effect, this is mainly due to the weakening of the overall structural stiffness, which persists until the critical frequency. Above the critical frequency, the subsonic region within the transonic boundary results in an impaired sound radiation efficiency of the plate due to the subsonic structural waves. Supersonic acoustic intensity maps show that the regularly distributed supersonic waves over the flat plate are altered by the presence of the ABH indentation. As a result, the far field acoustic energy is mainly generated by the ring area between the ABH periphery and the corresponding transonic boundary.

5) The topological optimization of the damping layout over the surface of standard ABH indentations allows a reduction of the radiated sound power either at a given frequency or within a prescribed frequency band. For the configuration investigated in this thesis, the reduction level can be up to 4 dB compared with its reference plate with standard damping coating at the ABH center using the same amount of materials. At low frequencies before the ABH cut-on, the reduction in the sound radiation is insignificant due to the absence of the ABH effect, while at high frequencies, the optimization warrants a systematic reduction in the sound radiation efficiency of the plate, which is the dominant factor leading to the reduced sound radiation.

6) Damping layer coated over the standard ABH indentation creates dual effects. On one hand, they are conducive to energy focalization and dissipation; on the other hand, they would increase the sound radiation efficiency due to their additional stiffness. Topological optimization of damping layout shows that, irrespective of the minimization parameters (sound power or mean square velocity), optimization is meaningless below the cut-on frequency of the plate. Above the ABH cut-on, however, the two optimization problems (vibration reduction or sound radiation reduction) end up with different optimal configurations, while all pointing at a common conclusion that the best coating area may not necessarily be the center of the ABH indentation center. The optimized layout based on sound radiation optimization tends to draw damping material further away from the central portion of the ABH indentation, as compared to

the vibration-based optimization does. This testifies that the adverse effect of the excessive use of the coating impacts more on the sound radiation than the structural vibration.

7) An alternative ABH thickness profile that is different from the standard ABH profiles is proposed through system optimization. The optimized ABH thickness profile entails improved ABH effects. More specifically, the sum of the modal loss factors of the first 100 modes (taken as the objective function) is increased by 39.5% in the configuration studied in this thesis, as compared with the standard case. Mode shape analyses of the optimized ABH show the dominance of local ABH $(n, 1)$ and $(n, 2)$ modes with relatively high loss factors. The occurrence of these modes is attributed to the unique feature of the optimized profile, namely the area with the minimum thickness is away from the center of the indentation, thus forming a flexible ring which is beneficial to energy focalization. This is further confirmed by the energy density ratio between the ABH portion and the uniform portion of the optimized plate, which allows increased structural damping with the use of the same amount of damping materials.

8.2 Suggestions for future research

This thesis mainly focuses on vibration and sound radiation mitigation of ABH plates. Numerical analyses are conducted using the proposed 2D semi-analytical wavelet model. The research findings provide inspirations for further exploration in future research:

1) The proposed semi-analytical wavelet model is based on the Love-Kirchhoff thin plate theory which requires that the investigated plate should be symmetric with respect to its midplane. In this regard, the ABH indentation should also be asymmetric on both sides of the plate. This brings a great challenge for the manufacturing of ABH indentations in thin-walled structures. Efficient manufacturing methods of ABH structures and their real-world applications constitute a significant and important research direction. Meanwhile, possible nonlinear effects due to the large amplitude vibration of the ABH indentation, as well as its impact on the expected ABH effects should be further evaluated.

2) The realization of ABH effect requires that the local thickness is tailored according to a power-law relationship. Up to now, most of the work about ABH is conducted on relatively thick beams and plates. However, in many branches of industries such as household appliances, the commonly used panels are as thin as 1-2 mm. The realization of the ABH effect in such thin panels is a real issue which has not been investigated in the literature. Undoubtedly, this issue is of practical significance for the implementations of ABH structures for real-world applications.

3) In terms of structural strength, plates embedded with ABH indentations on one side or with double-layer ABH indentations are superior to those embedded with symmetric ABH indentations investigated in this thesis. In this regard, modelling and

investigations of these kind of ABH structures of relatively high strength is of practical significance.

4) Apart from the simple ABH indentations investigated in this thesis, ABH plates embedded with indentations on one side and with doubled-layer indentations are also

5) ABH structures feature locally tailored thickness profile that warrants the slowing-down of the propagating bending waves. By the same token, the reduced thickness would weaken the stiffness and integrity of the structures, making them vulnerable and easy to be damaged. More innovative design of new types of ABH structures is highly desirable.

Appendix A

Formulas for \mathbf{M} , \mathbf{K} , and \mathbf{F} for a plate embedded with a strip ABH indentation

The plate structure is divided into five parts: uniform parts from 1 to 4 and an ABH part 5.

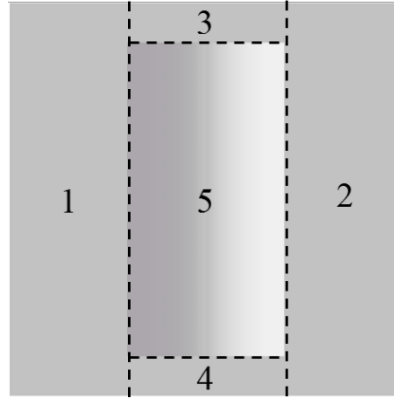


Figure A.1 Division of a strip ABH plate.

$$\mathbf{M} = \mathbf{M}^{Uniform} + \mathbf{M}^{ABH} + \mathbf{M}^{Damping}$$

$$\mathbf{K} = \mathbf{K}^{Uniform} + \mathbf{K}^{ABH} + \mathbf{K}^{Spring}$$

$$\begin{aligned} \mathbf{M}^{Uniform} &= \rho hab \left(\sum_{q=1}^4 \int_{\bar{y}_{q1}}^{\bar{y}_{q2}} \int_{\bar{x}_{q1}}^{\bar{x}_{q2}} \varphi_r(\bar{x}) \varphi_i(\bar{x}) \varphi_s(\bar{y}) \varphi_j(\bar{y}) d\bar{x} d\bar{y} \right) \\ &= \rho hab \sum_{q=1}^4 \left(\mathbf{I}_{\bar{x}_q}^{00} \otimes \mathbf{I}_{\bar{y}_q}^{00} \right) \end{aligned}$$

$$\begin{aligned} \mathbf{M}^{ABH} &= \rho ab \left(\int_{\bar{y}_{51}}^{\bar{y}_{52}} \int_{\bar{x}_{51}}^{\bar{x}_{52}} h(\bar{x}) \varphi_r(\bar{x}) \varphi_i(\bar{x}) \varphi_s(\bar{y}) \varphi_j(\bar{y}) d\bar{x} d\bar{y} \right) \\ &= \rho ab \left(\mathbf{I}_{\bar{x}_5}^{00} \otimes \mathbf{I}_{\bar{y}_5}^{00} \right) \end{aligned}$$

$$\begin{aligned}\mathbf{M}^{Damping} &= \rho ab \left(\int_{\bar{y}_{d1}}^{\bar{y}_{d2}} \int_{\bar{x}_{d1}}^{\bar{x}_{d2}} h_d \varphi_r(\bar{x}) \varphi_i(\bar{x}) \varphi_s(\bar{y}) \varphi_j(\bar{y}) d\bar{x} d\bar{y} \right) \\ &= \rho ab (\mathbf{I}_{x_d}^{00} \otimes \mathbf{I}_{y_d}^{00})\end{aligned}$$

$$\begin{aligned}\mathbf{K}^{Uniform} &= D \cdot \frac{b}{a^3} \left(\sum_{q=1}^4 \int_{\bar{y}_{q1}}^{\bar{y}_{q2}} \int_{\bar{x}_{q1}}^{\bar{x}_{q2}} \varphi_r''(\bar{x}) \varphi_i''(\bar{x}) \varphi_s(\bar{y}) \varphi_j(\bar{y}) d\bar{x} d\bar{y} \right) + D \cdot \frac{a}{b^3} \left(\sum_{q=1}^4 \int_{\bar{y}_{q1}}^{\bar{y}_{q2}} \int_{\bar{x}_{q1}}^{\bar{x}_{q2}} \varphi_r(\bar{x}) \varphi_i(\bar{x}) \varphi_s''(\bar{y}) \varphi_j''(\bar{y}) d\bar{x} d\bar{y} \right) \\ &+ \frac{\mu_0 D}{ab} \left(\sum_{i=1}^4 \int_{\bar{y}_{q1}}^{\bar{y}_{q2}} \int_{\bar{x}_{q1}}^{\bar{x}_{q2}} \varphi_r''(\bar{x}) \varphi_i(\bar{x}) \varphi_s(\bar{y}) \varphi_j'(\bar{y}) d\bar{x} d\bar{y} \right) + \frac{2(1-\mu_0)D}{ab} \left(\sum_{q=1}^4 \int_{\bar{y}_{q1}}^{\bar{y}_{q2}} \int_{\bar{x}_{q1}}^{\bar{x}_{q2}} \varphi_r'(\bar{x}) \varphi_i'(\bar{x}) \varphi_s(\bar{y}) \varphi_j'(\bar{y}) d\bar{x} d\bar{y} \right) \\ &= D \cdot \frac{b}{a^3} \left(\sum_{q=1}^4 \mathbf{I}_{x_q}^{22} \otimes \mathbf{I}_{y_q}^{00} \right) + D \cdot \frac{a}{b^3} \left(\sum_{q=1}^4 \mathbf{I}_{x_q}^{00} \otimes \mathbf{I}_{y_q}^{22} \right) + \mu_0 D \cdot \frac{1}{ab} \left(\sum_{q=1}^4 \mathbf{I}_{x_q}^{20} \otimes \mathbf{I}_{y_q}^{02} \right) + 2(1-\mu_0) D \cdot \frac{1}{ab} \left(\sum_{q=1}^4 \mathbf{I}_{x_q}^{11} \otimes \mathbf{I}_{y_q}^{11} \right)\end{aligned}$$

$$\begin{aligned}\mathbf{K}^{ABH} &= \frac{E_0}{12(1-\mu_0^2)} \left\{ \int_{\bar{y}_{s1}}^{\bar{y}_{s2}} \int_{\bar{x}_{s1}}^{\bar{x}_{s2}} [h(\bar{x})]^3 \left(\begin{aligned} &\frac{b}{a^3} \varphi_r''(\bar{x}) \varphi_i''(\bar{x}) \varphi_s(\bar{y}) \varphi_j(\bar{y}) + \frac{a}{b^3} \varphi_r(\bar{x}) \varphi_i(\bar{x}) \varphi_s''(\bar{y}) \varphi_j''(\bar{y}) \\ &+ \frac{\mu_0}{ab} \varphi_r''(\bar{x}) \varphi_i(\bar{x}) \varphi_s(\bar{y}) \varphi_j''(\bar{y}) + \frac{2(1-\mu_0)}{ab} \varphi_r'(\bar{x}) \varphi_i'(\bar{x}) \varphi_s(\bar{y}) \varphi_j'(\bar{y}) \end{aligned} \right) d\bar{x} d\bar{y} \right\} \\ &= \frac{E_0}{12(1-\mu_0^2)} \left\{ \frac{b}{a^3} (\mathbf{I}_{x_s}^{22} \otimes \mathbf{I}_{y_s}^{00}) + \frac{a}{b^3} (\mathbf{I}_{x_s}^{00} \otimes \mathbf{I}_{y_s}^{22}) + \frac{\mu_0}{ab} (\mathbf{I}_{x_s}^{20} \otimes \mathbf{I}_{y_s}^{02}) + \frac{2(1-\mu_0)}{ab} (\mathbf{I}_{x_s}^{11} \otimes \mathbf{I}_{y_s}^{11}) \right\}\end{aligned}$$

$$\begin{aligned}\mathbf{K}^{Damping} &= \frac{E_d}{12(1-\mu_d^2)} \left\{ \int_{\bar{y}_{d1}}^{\bar{y}_{d2}} \int_{\bar{x}_{d1}}^{\bar{x}_{d2}} \left\{ [2h_d + h(\bar{x})]^3 - [h(\bar{x})]^3 \right\} \left(\begin{aligned} &\frac{b}{a^3} \varphi_r''(\bar{x}) \varphi_i''(\bar{x}) \varphi_s(\bar{y}) \varphi_j(\bar{y}) \\ &+ \frac{a}{b^3} \varphi_r(\bar{x}) \varphi_i(\bar{x}) \varphi_s''(\bar{y}) \varphi_j''(\bar{y}) \\ &+ \frac{\mu_d}{ab} \varphi_r''(\bar{x}) \varphi_i(\bar{x}) \varphi_s(\bar{y}) \varphi_j''(\bar{y}) \\ &+ \frac{2(1-\mu_d)}{ab} \varphi_r'(\bar{x}) \varphi_i'(\bar{x}) \varphi_s(\bar{y}) \varphi_j'(\bar{y}) \end{aligned} \right) d\bar{x} d\bar{y} \right\} \\ &= \frac{E_d}{6(1-\mu_d^2)} \left\{ \frac{b}{a^3} (\mathbf{I}_{x_d}^{22} \otimes \mathbf{I}_{y_d}^{00}) + \frac{a}{b^3} (\mathbf{I}_{x_d}^{00} \otimes \mathbf{I}_{y_d}^{22}) + \frac{\mu_d}{ab} (\mathbf{I}_{x_d}^{20} \otimes \mathbf{I}_{y_d}^{02}) + \frac{2(1-\mu_d)}{ab} (\mathbf{I}_{x_d}^{11} \otimes \mathbf{I}_{y_d}^{11}) \right\}\end{aligned}$$

$$\begin{aligned}\mathbf{K}^{Spring} &= k_1 b \varphi_- \otimes \mathbf{I}^{00} + k_2 b \varphi_+ \otimes \mathbf{I}^{00} + c_1 \frac{b}{a^2} \varphi_-' \otimes \mathbf{I}^{00} + c_2 \frac{b}{a^2} \varphi_+' \otimes \mathbf{I}^{00} \\ &+ k_3 a \mathbf{I}^{00} \otimes \varphi_- + k_4 a \mathbf{I}^{00} \otimes \varphi_+ + c_3 \frac{a}{b^2} \mathbf{I}^{00} \otimes \varphi_-' + c_4 \frac{a}{b^2} \mathbf{I}^{00} \otimes \varphi_+' \end{aligned}$$

$$\text{where } \mathbf{I}^{00} = \int_0^1 \varphi_r(\bar{x}) \varphi_i(\bar{x}) d\bar{x}$$

$$\varphi_- = [\varphi_r(0)\varphi_i(0)]$$

$$\varphi_+ = [\varphi_r(1)\varphi_i(1)]$$

$$\varphi'_- = [\varphi'_r(0)\varphi'_i(0)]$$

$$\varphi'_+ = [\varphi'_r(1)\varphi'_i(1)]$$

$$\mathbf{f}(\mathbf{t}) = \mathbf{F}e^{i\omega t}$$

$$\mathbf{F}_{r,s} = \mathbf{F}\varphi_r(\bar{x})\varphi_s(\bar{y})$$

where

$$r = -L+2, -L+1, \dots, 2^m-2, 2^m-1$$

$$i = -L+2, -L+1, \dots, 2^m-2, 2^m-1$$

$$s = -L+2, -L+1, \dots, 2^m-2, 2^m-1$$

$$j = -L+2, -L+1, \dots, 2^m-2, 2^m-1$$

$D = \frac{E_0 h^3}{12(1-\mu_0^2)}$ is the bending rigidity of uniform portion of the plate.

Appendix B

Formulas for \mathbf{M} and \mathbf{K} for a plate embedded with a circular ABH indentation

The plate structure is divided into five parts: uniform parts from 1 to 4 and an ABH part 5. The part coated with damping layers is number 6.

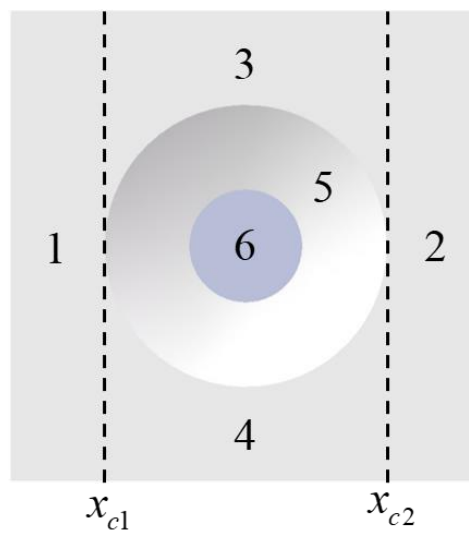


Figure B.1 Division of a circular ABH plate.

$$\mathbf{M} = \mathbf{M}^{Uniform} + \mathbf{M}^{ABH} + \mathbf{M}^{Damping}$$

$$\mathbf{K} = \mathbf{K}^{Uniform} + \mathbf{K}^{ABH} + \mathbf{K}^{Spring}$$

$$\begin{aligned}
\mathbf{M}^{Uniform} &= \rho hab \left(\int_0^1 \int_0^{\bar{x}_{c1}} \varphi_r(\bar{x}) \varphi_i(\bar{x}) \varphi_s(\bar{y}) \varphi_j(\bar{y}) d\bar{x} d\bar{y} + \int_0^1 \int_{\bar{x}_{c2}}^1 \varphi_r(\bar{x}) \varphi_i(\bar{x}) \varphi_s(\bar{y}) \varphi_j(\bar{y}) d\bar{x} d\bar{y} \right. \\
&+ \int_{\bar{y}_r - \frac{1}{b} \sqrt{(R_{ABH})^2 - a^2(\bar{x} - \bar{x}_r)^2}}^1 \int_{\bar{x}_{c1}}^{\bar{x}_{c1}} \varphi_r(\bar{x}) \varphi_i(\bar{x}) \varphi_s(\bar{y}) \varphi_j(\bar{y}) d\bar{x} d\bar{y} \\
&+ \left. \int_0^{\bar{y}_r + \frac{1}{b} \sqrt{(R_{ABH})^2 - a^2(\bar{x} - \bar{x}_r)^2}} \int_{\bar{x}_{c1}}^{\bar{x}_{c1}} \varphi_r(\bar{x}) \varphi_i(\bar{x}) \varphi_s(\bar{y}) \varphi_j(\bar{y}) d\bar{x} d\bar{y} \right) \\
&= \rho hab \sum_{q=1}^4 \left(\mathbf{I}_{x_q}^{00} \otimes \mathbf{I}_{y_q}^{00} \right)
\end{aligned}$$

$$\begin{aligned}
\mathbf{M}^{ABH} &= \rho ab \left(\int_{\bar{y}_r - \frac{1}{b} \sqrt{(R_{ABH})^2 - a^2(\bar{x} - \bar{x}_r)^2}}^{\bar{y}_r + \frac{1}{b} \sqrt{(R_{ABH})^2 - a^2(\bar{x} - \bar{x}_r)^2}} \int_{\bar{x}_{c1}}^{\bar{x}_{c2}} h(\bar{x}, \bar{y}) \varphi_r(\bar{x}) \varphi_i(\bar{x}) \varphi_s(\bar{y}) \varphi_j(\bar{y}) d\bar{x} d\bar{y} \right) \\
&= \rho ab \left(\mathbf{I}_{5,risj}^{0000} \right)
\end{aligned}$$

$$\begin{aligned}
\mathbf{M}^{Damping} &= \rho ab \left(\int_{\bar{y}_r - \frac{1}{b} \sqrt{(R_d)^2 - a^2(\bar{x} - \bar{x}_r)^2}}^{\bar{y}_r + \frac{1}{b} \sqrt{(R_d)^2 - a^2(\bar{x} - \bar{x}_r)^2}} \int_{\bar{x}_{d1}}^{\bar{x}_{d2}} h_d \varphi_r(\bar{x}) \varphi_i(\bar{x}) \varphi_s(\bar{y}) \varphi_j(\bar{y}) d\bar{x} d\bar{y} \right) \\
&= \rho ab \mathbf{I}_{x_d}^{00} \otimes \mathbf{I}_{y_d}^{00}
\end{aligned}$$

$$\begin{aligned}
\mathbf{K}^{Uniform} &= D \cdot \frac{b}{a^3} \left(\int_0^1 \int_0^{\bar{x}_{c1}} \varphi_r''(\bar{x}) \varphi_i''(\bar{x}) \varphi_s(\bar{y}) \varphi_j(\bar{y}) d\bar{x} d\bar{y} + \int_0^1 \int_{\bar{x}_{c2}}^1 \varphi_r''(\bar{x}) \varphi_i''(\bar{x}) \varphi_s(\bar{y}) \varphi_j(\bar{y}) d\bar{x} d\bar{y} \right. \\
&\quad + \int_{\bar{y}_r - \frac{1}{b} \sqrt{(R_{ABH})^2 - a^2(\bar{x} - \bar{x}_r)^2}}^1 \int_{\bar{x}_{c1}}^{\bar{x}_{c1}} \varphi_r''(\bar{x}) \varphi_i''(\bar{x}) \varphi_s(\bar{y}) \varphi_j(\bar{y}) d\bar{x} d\bar{y} \\
&\quad \left. + \int_0^{\bar{y}_r + \frac{1}{b} \sqrt{(R_{ABH})^2 - a^2(\bar{x} - \bar{x}_r)^2}} \int_{\bar{x}_{c1}}^{\bar{x}_{c1}} \varphi_r''(\bar{x}) \varphi_i''(\bar{x}) \varphi_s(\bar{y}) \varphi_j(\bar{y}) d\bar{x} d\bar{y} \right) \\
&+ D \cdot \frac{a}{b^3} \left(\int_0^1 \int_0^{\bar{x}_{c1}} \varphi_r(\bar{x}) \varphi_i(\bar{x}) \varphi_s''(\bar{y}) \varphi_j''(\bar{y}) d\bar{x} d\bar{y} + \int_0^1 \int_{\bar{x}_{c2}}^1 \varphi_r(\bar{x}) \varphi_i(\bar{x}) \varphi_s''(\bar{y}) \varphi_j''(\bar{y}) d\bar{x} d\bar{y} \right. \\
&\quad + \int_{\bar{y}_r - \frac{1}{b} \sqrt{(R_{ABH})^2 - a^2(\bar{x} - \bar{x}_r)^2}}^1 \int_{\bar{x}_{c1}}^{\bar{x}_{c1}} \varphi_r(\bar{x}) \varphi_i(\bar{x}) \varphi_s''(\bar{y}) \varphi_j''(\bar{y}) d\bar{x} d\bar{y} \\
&\quad \left. + \int_0^{\bar{y}_r + \frac{1}{b} \sqrt{(R_{ABH})^2 - a^2(\bar{x} - \bar{x}_r)^2}} \int_{\bar{x}_{c1}}^{\bar{x}_{c1}} \varphi_r(\bar{x}) \varphi_i(\bar{x}) \varphi_s''(\bar{y}) \varphi_j''(\bar{y}) d\bar{x} d\bar{y} \right) \\
&+ \frac{\mu_0 D}{ab} \left(\int_0^1 \int_0^{\bar{x}_{c1}} \varphi_r''(\bar{x}) \varphi_i(\bar{x}) \varphi_s(\bar{y}) \varphi_j''(\bar{y}) d\bar{x} d\bar{y} + \int_0^1 \int_{\bar{x}_{c2}}^1 \varphi_r''(\bar{x}) \varphi_i(\bar{x}) \varphi_s(\bar{y}) \varphi_j''(\bar{y}) d\bar{x} d\bar{y} \right. \\
&\quad + \int_{\bar{y}_r - \frac{1}{b} \sqrt{(R_{ABH})^2 - a^2(\bar{x} - \bar{x}_r)^2}}^1 \int_{\bar{x}_{c1}}^{\bar{x}_{c1}} \varphi_r''(\bar{x}) \varphi_i(\bar{x}) \varphi_s(\bar{y}) \varphi_j''(\bar{y}) d\bar{x} d\bar{y} \\
&\quad \left. + \int_0^{\bar{y}_r + \frac{1}{b} \sqrt{(R_{ABH})^2 - a^2(\bar{x} - \bar{x}_r)^2}} \int_{\bar{x}_{c1}}^{\bar{x}_{c1}} \varphi_r''(\bar{x}) \varphi_i(\bar{x}) \varphi_s(\bar{y}) \varphi_j''(\bar{y}) d\bar{x} d\bar{y} \right) \\
&+ \frac{2(1 - \mu_0) D}{ab} \left(\int_0^1 \int_0^{\bar{x}_{c1}} \varphi_r'(\bar{x}) \varphi_i'(\bar{x}) \varphi_s'(\bar{y}) \varphi_j'(\bar{y}) d\bar{x} d\bar{y} + \int_0^1 \int_{\bar{x}_{c2}}^1 \varphi_r'(\bar{x}) \varphi_i'(\bar{x}) \varphi_s'(\bar{y}) \varphi_j'(\bar{y}) d\bar{x} d\bar{y} \right. \\
&\quad + \int_{\bar{y}_r - \frac{1}{b} \sqrt{(R_{ABH})^2 - a^2(\bar{x} - \bar{x}_r)^2}}^1 \int_{\bar{x}_{c1}}^{\bar{x}_{c1}} \varphi_r'(\bar{x}) \varphi_i'(\bar{x}) \varphi_s'(\bar{y}) \varphi_j'(\bar{y}) d\bar{x} d\bar{y} \\
&\quad \left. + \int_0^{\bar{y}_r + \frac{1}{b} \sqrt{(R_{ABH})^2 - a^2(\bar{x} - \bar{x}_r)^2}} \int_{\bar{x}_{c1}}^{\bar{x}_{c1}} \varphi_r'(\bar{x}) \varphi_i'(\bar{x}) \varphi_s'(\bar{y}) \varphi_j'(\bar{y}) d\bar{x} d\bar{y} \right) \\
&= D \cdot \frac{b}{a^3} \left(\sum_{q=1}^4 \mathbf{I}_{x_q}^{22} \otimes \mathbf{I}_{y_q}^{00} \right) + D \cdot \frac{a}{b^3} \left(\sum_{q=1}^4 \mathbf{I}_{x_q}^{00} \otimes \mathbf{I}_{y_q}^{22} \right) + \mu_0 D \cdot \frac{1}{ab} \left(\sum_{q=1}^4 \mathbf{I}_{x_q}^{20} \otimes \mathbf{I}_{y_q}^{02} \right) + 2(1 - \mu_0) D \cdot \frac{1}{ab} \left(\sum_{q=1}^4 \mathbf{I}_{x_q}^{11} \otimes \mathbf{I}_{y_q}^{11} \right)
\end{aligned}$$

$$\begin{aligned}
\mathbf{K}^{ABH} &= \frac{E_0}{12(1-\mu_0^2)} \left\{ \int_{\bar{y}_r - \frac{1}{b}\sqrt{(R_{ABH})^2 - a^2(\bar{x}-\bar{x}_r)^2}}^{\bar{y}_r + \frac{1}{b}\sqrt{(R_{ABH})^2 - a^2(\bar{x}-\bar{x}_r)^2}} \int_{\bar{x}_{c1}}^{\bar{x}_{c1}} [h(\bar{x}, \bar{y})]^3 d\bar{x}d\bar{y} \right. \\
&\quad \left. \begin{aligned} &\left(\frac{b}{a^3} \varphi_r''(\bar{x})\varphi_i''(\bar{x})\varphi_s(\bar{y})\varphi_j(\bar{y}) \right. \\ &+ \frac{a}{b^3} \varphi_r(\bar{x})\varphi_i(\bar{x})\varphi_s''(\bar{y})\varphi_j''(\bar{y}) \\ &+ \frac{\mu_0}{ab} \varphi_r''(\bar{x})\varphi_i(\bar{x})\varphi_s(\bar{y})\varphi_j''(\bar{y}) \\ &\left. + \frac{2(1-\mu_0)}{ab} \varphi_r'(\bar{x})\varphi_i'(\bar{x})\varphi_s'(\bar{y})\varphi_j'(\bar{y}) \right) \end{aligned} \right\} \\
&= \frac{E_0}{12(1-\mu_0^2)} \left\{ \frac{b}{a^3} (\mathbf{I}_{5,risj}^{2200}) + \frac{a}{b^3} (\mathbf{I}_{5,risj}^{0022}) + \frac{\mu_0}{ab} (\mathbf{I}_{5,risj}^{2002}) + \frac{2(1-\mu_0)}{ab} (\mathbf{I}_{5,risj}^{1111}) \right\}
\end{aligned}$$

$$\begin{aligned}
\mathbf{K}^{Damping} &= \frac{E_d}{12(1-\mu_d^2)} \left\{ \int_{\bar{y}_r - \frac{1}{b}\sqrt{(R_d)^2 - a^2(\bar{x}-\bar{x}_r)^2}}^{\bar{y}_r + \frac{1}{b}\sqrt{(R_d)^2 - a^2(\bar{x}-\bar{x}_r)^2}} \int_{\bar{x}_{d1}}^{\bar{x}_{d2}} \left\{ [2h_d + h(\bar{x})]^3 - [h(\bar{x})]^3 \right\} d\bar{x}d\bar{y} \right. \\
&\quad \left. \begin{aligned} &\left(\frac{b}{a^3} \varphi_r''(\bar{x})\varphi_i''(\bar{x})\varphi_s(\bar{y})\varphi_j(\bar{y}) \right. \\ &+ \frac{a}{b^3} \varphi_r(\bar{x})\varphi_i(\bar{x})\varphi_s''(\bar{y})\varphi_j''(\bar{y}) \\ &+ \frac{\mu_d}{ab} \varphi_r''(\bar{x})\varphi_i(\bar{x})\varphi_s(\bar{y})\varphi_j''(\bar{y}) \\ &\left. + \frac{2(1-\mu_d)}{ab} \varphi_r'(\bar{x})\varphi_i'(\bar{x})\varphi_s'(\bar{y})\varphi_j'(\bar{y}) \right) \end{aligned} \right\} \\
&= \frac{E_d}{6(1-\mu_d^2)} \left\{ \frac{b}{a^3} (\mathbf{I}_{6,risj}^{2200}) + \frac{a}{b^3} (\mathbf{I}_{6,risj}^{0022}) + \frac{\mu_d}{ab} (\mathbf{I}_{6,risj}^{2002}) + \frac{2(1-\mu_d)}{ab} (\mathbf{I}_{6,risj}^{1111}) \right\}
\end{aligned}$$

Calculations of the stiffness of artificial springs and force remain the same as in

[Appendix A.](#)

References

- [1] D. Ross, E.E. Ungar, E.M. Kerwin Jr., Damping of plate flexural vibrations by means of viscoelastic laminae, *Structural damping*, (1959) 49-97.
- [2] A.D. Nashif, D.I.G. Jones, J.P. Henderson, *Vibration damping*, John Wiley & Sons, Inc., New York, 1985.
- [3] D.J. Mead, *Passive vibration control*, John Wiley & Sons, Chichester, England, 1998.
- [4] L. Cremer, M. Heckl, B.A.T. Petersson, *Structure-borne sound: structural vibrations and sound radiation at audio frequencies*, Springer Science & Business Media, Germany, 2013.
- [5] G.S. Cole, A.M. Sherman, *Lightweight materials for automotive applications*, *Mater. Charact.*, 35 (1995) 3-9.
- [6] C. Vemula, A.N. Norris, Attenuation of waves in plates and bars using a graded impedance interface at edges, *J. Sound Vib.*, 196 (1996) 107-127.
- [7] V.V. Krylov, New type of vibration dampers utilising the effect of acoustic 'black holes', *Acta Acust. united Ac.*, 90 (2004) 830-837.
- [8] C. Montgomery, W. Orchiston, I. Whittingham, Heritage, Michell, Laplace and the origin of the black hole concept, *J. Astron. Hist. Herit*, 12 (2009) 90-96.
- [9] C.L. Pekeris, Theory of propagation of sound in a half-space of variable sound velocity under conditions of formation of a shadow zone, *J. Acoust. Soc. Am.*, 18 (1946) 295-315.
- [10] M.A. Mironov, Propagation of a flexural wave in a plate whose thickness decreases smoothly to zero in a finite interval, *Sov. Phys. Acoust.*, 34 (1988) 318-319.
- [11] V.V. Krylov, A.L. Shuvalov, Propagation of localised flexural vibrations along plate edges described by a power law, in: *Proceedings of the Institute of Acoustics, Moscow, Russia, 2000*.
- [12] V.V. Krylov, F.J.B.S. Tilman, Acoustic 'black holes' for flexural waves as effective vibration dampers, *J. Sound Vib.*, 274 (2004) 605-619.
- [13] V.B. Georgiev, J. Cuenca, M.A. Moleron Bermudez, F. Gautier, L. Simon, V.V. Krylov, Numerical and experimental investigation of the acoustic black hole effect for vibration damping in beams and elliptical plates, in: *Proceedings of Euronoise 2009, Proceedings of the European Conference on Noise Control, Edingburgh, UK, 2009*.
- [14] V.B. Georgiev, J. Cuenca, F. Gautier, L. Simon, V.V. Krylov, Damping of structural vibrations in beams and elliptical plates using the acoustic black hole effect, *J. Sound Vib.*, 330 (2011) 2497-2508.
- [15] F. Gautier, J. Cuenca, V.V. Krylov, L. Simon, Experimental investigation of the acoustic black hole effect for vibration damping in elliptical plates, in: *Acoustics, Paris, 2008*, pp. 3318.
- [16] V.V. Krylov, Geometrical-acoustics approach to the description of localized vibrational modes of an elastic solid wedge, *Sov. Phys. Tech. Phys.*, 35 (1990) 137-140.
- [17] V.V. Krylov, Conditions for validity of the geometrical-acoustics approximation in application to waves in an acute-angle solid wedge, *Sov. Phys. Acoust.*, 35 (1989) 176-180.

- [18] V.V. Krylov, Damping of resonant vibrations utilising the acoustic black hole effect, in: Proceedings of the International Conference on Noise and Vibration Emerging Technologies (NOVEM 2005), Saint Raphael, France, 2005.
- [19] V.V. Krylov, Localized acoustic modes of a quadratic solid wedge, *Mosc. Univ Phys. Bull.*, 45 (1990) 65-69.
- [20] V.V. Krylov, Propagation of plate bending waves in the vicinity of one-and two-dimensional acoustic ‘black holes’, in: Proceedings of the First International ECCOMAS Thematic Conference on Computational Methods in Structural Dynamics and Earthquake Engineering (COMPDYN 2007), Rethymno, Crete, Greece, 2007.
- [21] M.A. Mironov, V.V. Pislyakov, One-dimensional acoustic waves in retarding structures with propagation velocity tending to zero, *Acoust. Phys.*, 48 (2002) 347-352.
- [22] A. Karlos, S. Elliott, J. Cheer, Reflection from elastic wedges of different thickness profiles, in: Proceedings of ISMA 2018 and USD 2018, 2018.
- [23] A. Karlos, S.J. Elliott, J. Cheer, Higher-order WKB analysis of reflection from tapered elastic wedges, *J. Sound Vib.*, 449 (2019) 368-388.
- [24] O. Guasch, M. Arnela, P. Sánchez-Martín, Transfer matrices to characterize linear and quadratic acoustic black holes in duct terminations, *J. Sound Vib.*, 395 (2017) 65-79.
- [25] W. Huang, H. Ji, J. Qiu, L. Cheng, Analysis of ray trajectories of flexural waves propagating over generalized acoustic black hole indentations, *J. Sound Vib.*, 417 (2018) 216-226.
- [26] W. Huang, H. Ji, J. Qiu, L. Cheng, Wave energy focalization in a plate with imperfect two-dimensional acoustic black hole indentation, *J. Vib. Acoust.*, 138 (2016) 061004.
- [27] J.Y. Lee, W. Jeon, Exact solution of Euler-Bernoulli equation for acoustic black holes via generalized hypergeometric differential equation, *J. Sound Vib.*, 452 (2019) 191-204.
- [28] K. Hook, J. Cheer, S. Daley, A parametric study of an acoustic black hole on a beam, *J. Acoust. Soc. Am.*, 145 (2019) 3488-3498.
- [29] J. Yang, D.J. Thompson, A non-reflecting boundary for use in a finite element beam model of a railway track, *J. Sound Vib.*, 337 (2015) 199-217.
- [30] C.R. Steele, L.A. Taber, Comparison of WKB calculations and experimental results for three-dimensional cochlear models, *J. Acoust. Soc. Am.*, 65 (1979) 1007-1018.
- [31] S. Foucaud, G. Michon, Y. Gourinat, A. Pelat, F. Gautier, Artificial cochlea and acoustic black hole travelling waves observation: Model and experimental results, *J. Sound Vib.*, 333 (2014) 3428-3439.
- [32] T. Zhou, L. Cheng, A resonant beam damper tailored with Acoustic Black Hole features for broadband vibration reduction, *J. Sound Vib.*, 430 (2018) 174-184.
- [33] L. Tang, L. Cheng, Ultrawide band gaps in beams with double-leaf acoustic black hole indentations, *J. Acoust. Soc. Am.*, 142 (2017) 2802-2807.
- [34] N. Gao, Z. Wei, H. Hou, A.O. Krushynska, Design and experimental investigation of V-folded beams with acoustic black hole indentations, *J. Acoust. Soc. Am.*, 145 (2019) EL79-EL83.
- [35] H. Zhu, F. Semperlotti, Two-dimensional structure-embedded acoustic lenses based on periodic acoustic black holes, *J. Appl. Phys.*, 122 (2017) 065104.

- [36] H. Zhu, F. Semperlotti, Phononic thin plates with embedded acoustic black holes, *J. Phys. Rev. B*, 91 (2015) 104304.
- [37] H. Zhu, F. Semperlotti, Improving the performance of structure-embedded acoustic lenses via gradient-index local inhomogeneities, *Int. J. Smart Nano Mater.*, 6 (2015) 1-13.
- [38] A. Climente, D. Torrent, J. Sánchez-Dehesa, Gradient index lenses for flexural waves based on thickness variations, *J. Appl. Phys. Lett.*, 105 (2014) 064101.
- [39] S.C. Conlon, J.B. Fahnlne, F. Semperlotti, Numerical analysis of the vibroacoustic properties of plates with embedded grids of acoustic black holes, *J. Acoust. Soc. Am.*, 137 (2015) 447-457.
- [40] S.C. Conlon, J.B. Fahnlne, F. Semperlotti, P.A. Feurtado, Enhancing the low frequency vibration reduction performance of plates with embedded Acoustic Black Holes, in: *INTER-NOISE and NOISE-CON Congress and Conference Proceedings*, Institute of Noise Control Engineering, Melbourne, Australia, 2014, pp. 175-182.
- [41] J.J. Bayod, Application of elastic wedge for vibration damping of turbine blade, *J. Syst. Des. Dyn.*, 5 (2011) 1167-1175.
- [42] P.A. Feurtado, S.C. Conlon, Experimental analysis of vibration and radiated sound power reduction using an array of acoustic black holes, in: *ASME 2015 Noise Control and Acoustics Division Conference at InterNoise 2015*, American Society of Mechanical Engineers, San Francisco, CA, USA, 2015, pp. V001T001A012-V001T001A012.
- [43] P.A. Feurtado, S.C. Conlon, An experimental investigation of acoustic black hole dynamics at low, mid, and high frequencies, *J. Vib. Acoust.*, 138 (2016) 061002.
- [44] L. Zhao, F. Semperlotti, Embedded Acoustic Black Holes for semi-passive broadband vibration attenuation in thin-walled structures, *J. Sound Vib.*, 388 (2017) 42-52.
- [45] X. Jia, Y. Du, K. Zhao, Vibration Control of variable thickness plates with embedded Acoustic Black Holes and dynamic vibration absorbers, in: *ASME 2015 Noise Control and Acoustics Division Conference at InterNoise 2015*, American Society of Mechanical Engineers, 2015, pp. V001T001A008-V001T001A008.
- [46] L. Tang, L. Cheng, H. Ji, J. Qiu, Characterization of acoustic black hole effect using a one-dimensional fully-coupled and wavelet-decomposed semi-analytical model, *J. Sound Vib.*, 374 (2016) 172-184.
- [47] L. Tang, L. Cheng, Enhanced Acoustic Black Hole effect in beams with a modified thickness profile and extended platform, *J. Sound Vib.*, 391 (2017) 116-126.
- [48] L. Tang, L. Cheng, Loss of acoustic black hole effect in a structure of finite size, *Appl. Phys. Lett.*, 109 (2016) 014102.
- [49] L. Tang, L. Cheng, Broadband locally resonant band gaps in periodic beam structures with embedded acoustic black holes, *J. Appl. Phys.*, 121 (2017) 194901.
- [50] D.J. O'Boy, V.V. Krylov, Vibration of a rectangular plate with a central power-law profiled groove by the Rayleigh–Ritz method, *Appl. Acoust.*, 104 (2016) 24-32.
- [51] J. Deng, L. Zheng, P. Zeng, Y. Zuo, O. Guasch, Passive constrained viscoelastic layers to improve the efficiency of truncated acoustic black holes in beams, *Mech. Syst. Signal Proc.*, 118 (2019) 461-476.

- [52] J. Deng, L. Zheng, O. Guasch, H. Wu, P. Zeng, Y. Zuo, Gaussian expansion for the vibration analysis of plates with multiple acoustic black holes indentations, *Mech. Syst. Signal Proc.*, 131 (2019) 317-334.
- [53] Y. Wang, J. Du, L. Cheng, Power flow and structural intensity analyses of Acoustic Black Hole beams, *Mech. Syst. Signal Proc.*, 131 (2019) 538-553.
- [54] D.J. O'Boy, V.V. Krylov, V. Kralovic, Damping of flexural vibrations in rectangular plates using the acoustic black hole effect, *J. Sound Vib.*, 329 (2010) 4672-4688.
- [55] D.J. O'Boy, V.V. Krylov, Damping of flexural vibrations in circular plates with tapered central holes, *J. Sound Vib.*, 330 (2011) 2220-2236.
- [56] X. Li, Q. Ding, Sound radiation of a beam with a wedge-shaped edge embedding Acoustic Black Hole feature, *J. Sound Vib.*, 439 (2019) 287-299.
- [57] J. Cuenca, A. Pelat, F. Gautier, Vibration damping in polygonal plates using the acoustic black hole effect: model based on the image source method, in: *Congrès français de mécanique*, AFM, Maison de la Mécanique, 39/41 rue Louis Blanc, 92400 Courbevoie, France, Besancon France, 2011.
- [58] X. Zhou, D. Yu, Acoustic energy absorption and dissipation characteristic of Helmholtz resonator enhanced and broadened by acoustic black hole, *J. Aerosp. Sci. Technol.*, 81 (2018) 237-248.
- [59] L. Zhao, S.C. Conlon, F. Semperlotti, Broadband energy harvesting using acoustic black hole structural tailoring, *Smart Mater. Struct.*, 23 (2014) 065021.
- [60] L. Zhao, F. Semperlotti, S.C. Conlon, Enhanced vibration based energy harvesting using embedded acoustic black holes, in: *Sensors and Smart Structures Technologies for Civil, Mechanical, and Aerospace Systems 2014*, International Society for Optics and Photonics, 2014, pp. 90610L.
- [61] L. Zhao, S.C. Conlon, F. Semperlotti, An experimental study of vibration based energy harvesting in dynamically tailored structures with embedded acoustic black holes, *Smart Mater. Struct.*, 24 (2015) 065039.
- [62] V. Denis, F. Gautier, A. Pelat, J. Poittevin, Measurement and modelling of the reflection coefficient of an Acoustic Black Hole termination, *J. Sound Vib.*, 349 (2015) 67-79.
- [63] V. Denis, A. Pelat, F. Gautier, B. Elie, Modal overlap factor of a beam with an acoustic black hole termination, *J. Sound Vib.*, 333 (2014) 2475-2488.
- [64] X. Wang, X. Liu, J. Tai, T. He, Y. Shan, A novel method of reducing the acoustic emission wave reflected by boundary based on acoustic black hole, *Ultrasonics*, 94 (2019) 292-304.
- [65] V. Kralovic, V.V. Krylov, Damping of flexural vibrations in tapered rods of power-law profile: Experimental studies, *Proceedings of the Institute of Acoustics*, 29 (2007).
- [66] V. Kralovic, V.V. Krylov, Some new methods of damping impact-induced vibrations in badminton racquets, *Proceedings of the Institute of Acoustics*, 30 (2008) 155-162.
- [67] H. Li, C. Touzé, A. Pelat, F. Gautier, X. Kong, A vibro-impact acoustic black hole for passive damping of flexural beam vibrations, *J. Sound Vib.*, 450 (2019) 28-46.
- [68] T. Zhou, L. Tang, H. Ji, J. Qiu, L. Cheng, Dynamic and static properties of double-layered compound acoustic black hole structures, *Int. J. Appl. Mech.*, 9 (2017) 1750074.

- [69] V.V. Krylov, R.E.T.B. Winward, Experimental investigation of the acoustic black hole effect for flexural waves in tapered plates, *J. Sound Vib.*, 300 (2007) 43-49.
- [70] H. Ji, J. Luo, J. Qiu, L. Cheng, Investigations on flexural wave propagation and attenuation in a modified one-dimensional acoustic black hole using a laser excitation technique, *Mech. Syst. Signal Proc.*, 104 (2018) 19-35.
- [71] E. Bowyer, V. Krylov, D. O'Boy, Damping of flexural vibrations in rectangular plates by slots of power-law profile, in: *Proceedings of the Acoustics 2012 Nantes Conference*, Nantes, France, 2012, pp. 2193-2198.
- [72] E.P. Bowyer, V.V. Krylov, Slots of power-law profile as acoustic black holes for flexural waves in metallic and composite plates, *Structures*, 6 (2016) 48-58.
- [73] E. Bowyer, J. Lister, V. Krylov, D. O'Boy, Experimental study of damping flexural vibrations in tapered turbofan blades, in: *Proceedings of the Acoustics 2012 Nantes Conference*, Nantes, France, 2012, pp. 2207-2212.
- [74] E.P. Bowyer, V.V. Krylov, Damping of flexural vibrations in turbofan blades using the acoustic black hole effect, *Appl. Acoust.*, 76 (2014) 359-365.
- [75] V.V. Krylov, R.E.T.B. Winward, Experimental evidence of the acoustic black hole effect for flexural waves in tapered plates, in: *Proceedings of the 12th International Congress on Sound and Vibration*, Lisbon, Portugal, 2005.
- [76] V. Kralovic, E.P. Bowyer, V.V. Krylov, D.J. O'Boy, Experimental study on damping of flexural waves in rectangular plates by means of one-dimensional acoustic 'Black Holes', in: *Proceedings of the 14th International Acoustic Conference*, 14th International Acoustic Conference, Kocovce, Slovak Republic, 2009.
- [77] E.P. Bowyer, D.J. O'Boy, V.V. Krylov, J.L. Horner, Effect of geometrical and material imperfections on damping flexural vibrations in plates with attached wedges of power law profile, *Appl. Acoust.*, 73 (2012) 514-523.
- [78] J.J. Bayod, Experimental study of vibration damping in a modified elastic wedge of power-law profile, *J. Vib. Acoust.*, 133 (2011) 061003.
- [79] E.P. Bowyer, D.J. O'Boy, V.V. Krylov, F. Gautier, Experimental investigation of damping flexural vibrations in plates containing tapered indentations of power-law profile, *Appl. Acoust.*, 74 (2013) 553-560.
- [80] E.P. Bowyer, D.J. O'Boy, V.V. Krylov, Damping of flexural vibrations in plates containing ensembles of tapered indentations of power-law profile, in: *Proceedings of Meetings on Acoustics*, ASA, 2012, pp. 030003.
- [81] V.V. Krylov, E.P. Bowyer, Acoustic black holes: A new approach to vibration damping in light-weight structures, in: *Proceedings of the Institute of Acoustics*, Institute of Acoustics, 2013, pp. 184-191.
- [82] E.P. Bowyer, V.V. Krylov, Experimental investigation of damping flexural vibrations in glass fibre composite plates containing one-and two-dimensional acoustic black holes, *Compos. Struct.*, 107 (2014) 406-415.
- [83] E.P. Bowyer, P. Nash, V.V. Krylov, Damping of flexural vibrations in glass fibre composite plates and honeycomb sandwich panels containing indentations of power-law profile, in: *Proceedings of Meetings on Acoustics*, ASA, 2012, pp. 030004.

- [84] E.P. Bowyer, Acoustic black hole manufacturing for practical applications and the effect of geometrical and material imperfection, in: INTER-NOISE and NOISE-CON Congress and Conference Proceedings, Institute of Noise Control Engineering, Hamburg, 2016, pp. 2411-2421.
- [85] E.P. Bowyer, V.V. Krylov, Experimental study of sound radiation by plates containing circular indentations of power-law profile, *Appl. Acoust.*, 88 (2015) 30-37.
- [86] P. Feurtado, Assessing acoustic black hole performance via wavenumber transforms, in: INTER-NOISE and NOISE-CON Congress and Conference Proceedings, Institute of Noise Control Engineering, Hamburg, 2016, pp. 2381-2385.
- [87] P.A. Feurtado, S.C. Conlon, Wavenumber transform analysis for acoustic black hole design, *J. Acoust. Soc. Am.*, 140 (2016) 718-727.
- [88] P.A. Feurtado, S.C. Conlon, Transmission loss of plates with embedded acoustic black holes, *J. Acoust. Soc. Am.*, 142 (2017) 1390-1398.
- [89] H. Brody, *Tennis science for tennis players*, University of Pennsylvania Press, Philadelphia, PA, 2010.
- [90] H. Brody, R. Cross, C. Lindsey, *The physics and technology of tennis*, Racquet Tech Publishing, Solana Beach, 2002.
- [91] E.P. Bowyer, V.V. Krylov, Experimental investigations into the acoustic black hole effect and its applications for reduction of flexural vibrations and structure-borne sound, in: *Proceedings of the AIA-DAGA 2013 Conference on Acoustics*, Merano, Italy, 2013.
- [92] E.P. Bowyer, V.V. Krylov, A review of experimental investigations into the acoustic black hole effect and its applications for reduction of flexural vibrations and structure-borne sound, in: *Inter-Noise 2015 the 44th International Congress and Exposition on Noise Control Engineering*, San Francisco, USA, 2015.
- [93] J.Y. Lee, W. Jeon, Vibration damping using a spiral acoustic black hole, *J. Acoust. Soc. Am.*, 141 (2017) 1437-1445.
- [94] B.E. Anderson, M.C. Remillieux, P.-Y. Le Bas, T.J. Ulrich, L. Pieczonka, Ultrasonic radiation from wedges of cubic profile: Experimental results, *Ultrasonics*, 63 (2015) 141-146.
- [95] M.C. Remillieux, B.E. Anderson, P.-Y. Le Bas, T.J. Ulrich, Improving the air coupling of bulk piezoelectric transducers with wedges of power-law profiles: A numerical study, *Ultrasonics*, 54 (2014) 1409-1416.
- [96] M.C. Remillieux, B.E. Anderson, T.J. Ulrich, P.-Y. Le Bas, M.R. Haberman, J. Zhu, Review of air-coupled transduction for nondestructive testing and evaluation, *Acoust. Today*, 10 (2014) 36-45.
- [97] P.-Y. Le Bas, T.J. Ulrich, B.E. Anderson, J.J. Esplin, A high amplitude, time reversal acoustic non-contact excitation (trance), *J. Acoust. Soc. Am.*, 134 (2013) EL52-EL56.
- [98] V. Denis, A. Pelat, C. Touzé, F. Gautier, Improvement of the acoustic black hole effect by using energy transfer due to geometric nonlinearity, *Int. J. Nonlin. Mech.*, 94 (2017) 134-145.
- [99] V.E. Gusev, C. Ni, A. Lomonosov, Z. Shen, Propagation of flexural waves in inhomogeneous plates exhibiting hysteretic nonlinearity: Nonlinear acoustic black holes, *Ultrasonics*, 61 (2015) 126-135.

- [100] S. Rothe, V. Ghaffari Mejelej, S.C. Langer, T.J.P. Vietor, Optimal adaptation of acoustic black holes by evolutionary optimization algorithms, *Proc. Appl. Math. Mech.*, 16 (2016) 625-626.
- [101] M.R. Shepherd, P.A. Feurtado, S.C. Conlon, Multi-objective optimization of acoustic black hole vibration absorbers, *J. Acoust. Soc. Am.*, 140 (2016) EL227-EL230.
- [102] P.A. Feurtado, S.C. Conlon, F. Semperlotti, A normalized wave number variation parameter for acoustic black hole design, *J. Acoust. Soc. Am.*, 136 (2014) EL148-EL152.
- [103] C. Zhao, M. Prasad, Studies on influence of geometrical parameters of an Acoustic Black Hole, in: *INTER-NOISE and NOISE-CON Congress and Conference Proceedings*, Institute of Noise Control Engineering, Hong Kong, 2017, pp. 670-677.
- [104] J. Cuenca, A. Pelat, F. Gautier, N. Ferguson, Improving the acoustic black hole effect for vibration damping in one-dimensional structures, in: *Acoustics 2012*, Nantes, France, 2012.
- [105] B.S. Beck, K.A. Cunefare, Improved negative capacitance shunt damping with the use of acoustic black holes, in: *Active and Passive Smart Structures and Integrated Systems 2014*, International Society for Optics and Photonics, San Diego, California, USA, 2014, pp. 90571Z.
- [106] W. Huang, H. Zhang, D.J. Inman, J. Qiu, C.E. Cesnik, H. Ji, Low reflection effect by 3D printed functionally graded acoustic black holes, *J. Sound Vib.*, 450 (2019) 96-108.
- [107] L. Zhao, Low-frequency vibration reduction using a sandwich plate with periodically embedded acoustic black holes, *J. Sound Vib.*, 441 (2019) 165-171.
- [108] C. Zhao, M.G. Prasad, Acoustic Black Holes in Structural Design for Vibration and Noise Control, *Acoustics*, 1 (2019) 220-251.
- [109] B.M.P. Chong, L.B. Tan, K.M. Lim, H.P. Lee, A review on Acoustic Black-Holes (ABH) and the experimental and numerical study of ABH-featured 3D printed beams, *Int. J. Appl. Mech.*, 9 (2017) 1750078.
- [110] V.V. Krylov, Acoustic black holes: Recent developments in the theory and applications, *IEEE Trans. Ultrason., ferroelectr., Freq. Control*, 61 (2014) 1296-1306.
- [111] S. Zhang, L. Cheng, Wavelet decompositions for high frequency vibrational analyses of plates, *Int. J. Appl. Mech.*, 9 (2017) 1750088.
- [112] S. Ilanko, L. Monterrubio, Y. Mochida, *The Rayleigh-Ritz method for structural analysis*, John Wiley & Sons, Hoboken, 2014.
- [113] P. Ruta, Application of Chebyshev series to solution of non-prismatic beam vibration problems, *J. Sound Vib.*, 227 (1999) 449-467.
- [114] S. Zhang, L. Cheng, On the efficacy of the wavelet decomposition for high frequency vibration analyses, *J. Sound Vib.*, 380 (2016) 213-223.
- [115] L. Cheng, R. Lapointe, Vibration attenuation of panel structures by optimally shaped viscoelastic coating with added weight considerations, *Thin Walled Struct.*, 21 (1995) 307-326.
- [116] M.Q. Chen, C. Hwang, Y.P. Shih, The computation of wavelet - Galerkin approximation on a bounded interval, *Int. J. Numer. Methods Eng.*, 39 (1996) 2921-2944.
- [117] B.K. Wada, J.L. Fanson, E.F. Crawley, Adaptive structures, *J. Intell. Mater. Syst. Struct.*, 1 (1990) 157-174.

- [118] Z. Xu, Q. Huang, The study of three-dimensional structural acoustic radiation using FEM and BEM, *Adv. Theor. Appl. Mech.*, 3 (2010) 189-194.
- [119] C.E. Wallace, Radiation resistance of a rectangular panel, *J. Acoust. Soc. Am.*, 51 (1972) 946-952.
- [120] I.O.f. Standardization, ISO 3744: Acoustics-Determination of sound power levels of noise sources using sound pressure – engineering method in an essentially free field over a reflecting plane, in, Brussels, 2009.
- [121] W. Liu, M.S. Ewing, Experimental and analytical estimation of loss factors by the power input method, *AIAA J.*, 45 (2007) 477-484.
- [122] E.G. Williams, *Fourier acoustics: sound radiation and nearfield acoustical holography*, Academic Press, Cambridge, 1999.
- [123] E. Fernandez-Grande, F. Jacobsen, Q. Leclere, Direct formulation of the supersonic acoustic intensity in space domain, *J. Acoust. Soc. Am.*, 131 (2012) 186-193.
- [124] E.G. Williams, Supersonic acoustic intensity on planar sources, *J. Acoust. Soc. Am.*, 104 (1998) 2845-2850.
- [125] S.Y. Kim, D. Lee, Numerical analysis of wave energy dissipation by damping treatments in a plate with acoustic black holes, *J. Mech. Sci. Technol.*, 32 (2018) 3547-3555.
- [126] M.P. Bendsøe, Optimal shape design as a material distribution problem, *Struct. Optimization*, 1 (1989) 193-202.
- [127] A.R. Díaz, N. Kikuchi, Solutions to shape and topology eigenvalue optimization problems using a homogenization method, *Int. J. Numer. Methods Eng.*, 35 (1992) 1487-1502.
- [128] Z.-D. Ma, N. Kikuchi, H.-C. Cheng, Topological design for vibrating structures, *Comput. Method Appl. M.*, 121 (1995) 259-280.
- [129] N.L. Pedersen, Maximization of eigenvalues using topology optimization, *Struct. Multidiscip. Optim.*, 20 (2000) 2-11.
- [130] O. Sigmund, J. Søndergaard Jensen, Systematic design of phononic band-gap materials and structures by topology optimization, *Philos. Trans. R. Soc. Lond. Ser. A-Math. Phys. Eng. Sci.*, 361 (2003) 1001-1019.
- [131] Y. Li, X. Huang, F. Meng, S. Zhou, Topology optimization of 2D phononic band gap crystals based on BESO methods, in: *Proc. 11th World Congr. Struct. Multidisciplinary Optim.*, 2015, pp. 157-161.
- [132] M. Ansari, A. Khajepour, E. Esmailzadeh, Application of level set method to optimal vibration control of plate structures, *J. Sound Vib.*, 332 (2013) 687-700.
- [133] N. Olhoff, J. Du, Topological design for minimum dynamic compliance of structures under forced vibration, in: *Topology optimization in structural and continuum mechanics*, Springer, 2014, pp. 325-339.
- [134] M. Alvelid, Optimal position and shape of applied damping material, *J. Sound Vib.*, 310 (2008) 947-965.
- [135] Z. Kang, X. Zhang, S. Jiang, G. Cheng, On topology optimization of damping layer in shell structures under harmonic excitations, *Struct. Multidiscip. Optim.*, 46 (2012) 51-67.
- [136] L. Shu, M.Y. Wang, Z. Fang, Z. Ma, P. Wei, Level set based structural topology optimization for minimizing frequency response, *J. Sound Vib.*, 330 (2011) 5820-5834.

- [137] H. Zheng, C. Cai, G. Pau, G. Liu, Minimizing vibration response of cylindrical shells through layout optimization of passive constrained layer damping treatments, *J. Sound Vib.*, 279 (2005) 739-756.
- [138] G.H. Yoon, J.S. Jensen, O. Sigmund, Topology optimization of acoustic–structure interaction problems using a mixed finite element formulation, *Int. J. Numer. Methods Eng.*, 70 (2007) 1049-1075.
- [139] J. Du, N. Olhoff, Minimization of sound radiation from vibrating bi-material structures using topology optimization, *Struct. Multidiscip. Optim.*, 33 (2007) 305-321.
- [140] X. Zhang, Z. Kang, Vibration suppression using integrated topology optimization of host structures and damping layers, *J. Vib. Control*, 22 (2016) 60-76.
- [141] X. Zhang, Z. Kang, Topology optimization of damping layers for minimizing sound radiation of shell structures, *J. Sound Vib.*, 332 (2013) 2500-2519.
- [142] K. Yan, G. Cheng, B. Wang, Topology optimization of damping layers in shell structures subject to impact loads for minimum residual vibration, *J. Sound Vib.*, 431 (2018) 226-247.
- [143] O. Sigmund, A 99 line topology optimization code written in Matlab, *Struct. Multidiscip. Optim.*, 21 (2001) 120-127.
- [144] O. Sigmund, On the design of compliant mechanisms using topology optimization, *J. Struct. Mech.*, 25 (1997) 493-524.
- [145] K. Deb, A. Pratap, S. Agarwal, T. Meyarivan, A fast and elitist multiobjective genetic algorithm: NSGA-II, *IEEE T. Evolut. Comput.*, 6 (2002) 182-197.
- [146] K. Deb, R.B. Agrawal, Simulated binary crossover for continuous search space, *Complex Syst.*, 9 (1995) 115-148.